

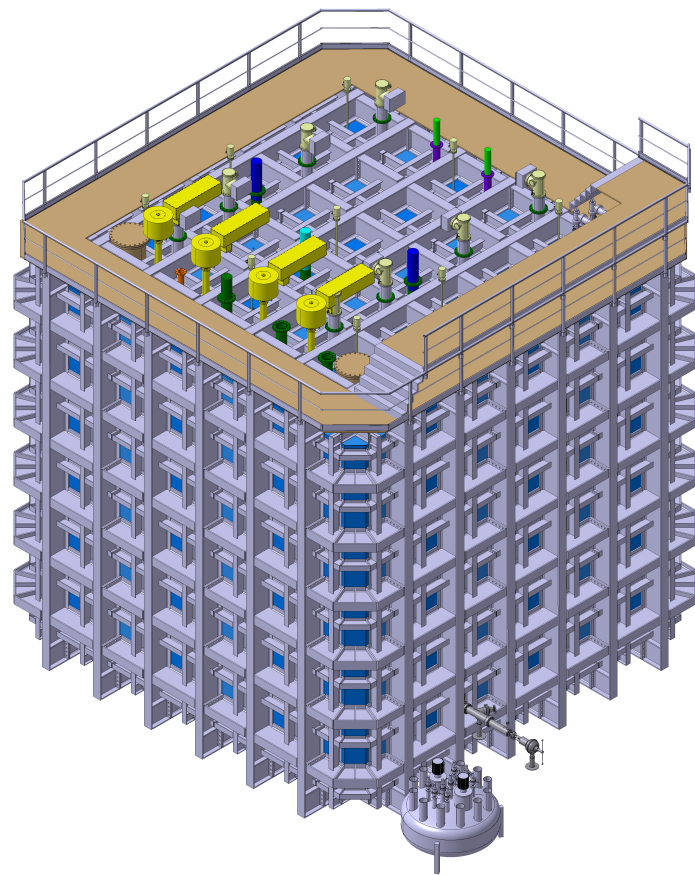
¹

The Single-Phase ProtoDUNE

²

DRAFT Technical Design Report

³



⁴

October 7, 2016

1 Contents

2	Contents	i
3	List of Figures	iv
4	List of Tables	vii
5	Acronyms, Abbreviations and Terms	viii
6	1 Introduction	2
7	1.1 ProtoDUNE-SP in the context of DUNE/LBNF	2
8	1.2 The ProtoDUNE-SP detector	3
9	1.3 Goals of ProtoDUNE-SP	5
10	1.3.1 Detector engineering validation	6
11	1.3.2 Physics	8
12	1.4 Run plan	9
13	2 Detector components	13
14	2.1 Overview of detector components	13
15	2.2 Anode Plane Assemblies (APA)	13
16	2.2.1 Scope and requirements	13
17	2.2.2 APA design overview	16
18	2.2.3 Wire properties	19
19	2.2.4 APA frame and mesh	20
20	2.2.5 Anchoring elements and wire boards	21
21	2.2.6 Interconnection features	27
22	2.3 Cathode Plane Assembly (CPA)	28
23	2.3.1 Scope and requirements	28
24	2.3.2 Design considerations	30
25	2.3.3 CPA design	30
26	2.3.4 Mechanical and electrical interconnections between modules	35
27	2.4 Field Cage (FC)	36
28	2.4.1 Scope and requirements	36
29	2.4.2 Mechanical design	37
30	2.4.3 Electrical design	39
31	2.4.4 Top/bottom FC assemblies and GP modules	40
32	2.4.5 Interfaces to other TPC components	42
33	2.5 TPC high-voltage (HV) components	45

1	2.5.1 Scope and requirements	45
2	2.5.2 HV feedthrough design, power supply and cabling	47
3	2.5.3 HV monitoring	49
4	2.6 TPC Front-end Electronics	49
5	2.6.1 Scope and requirements	49
6	2.6.2 Grounding and shielding	54
7	2.6.3 Distribution of APA wire-bias voltages	55
8	2.6.4 Front-End Mother Board	57
9	2.6.5 CE feedthroughs and cold cables	63
10	2.6.6 Warm interface electronics	68
11	2.6.7 External Power and Cables	71
12	2.7 Photon Detection System (PDS)	72
13	2.7.1 Scope and requirements	73
14	2.7.2 Photon detector modules	73
15	2.7.3 Sensors	75
16	2.7.4 Mechanical design and installation	76
17	2.7.5 Alternative photo detector under development	78
18	2.7.6 Photon detector UV-light monitoring system	79
19	2.8 PDS electronics	81
20	2.9 Data Acquisition (DAQ)	83
21	2.9.1 Scope and requirements	83
22	2.9.2 Timing, trigger and beam interface	85
23	2.9.3 TPC data readout	88
24	2.9.4 RCE-based readout	88
25	2.9.5 FELIX-based readout	89
26	2.9.6 PDS and beam instrumentation data readout	89
27	2.9.7 Event-building software	89
28	2.9.8 Control, configuration and operational monitoring	90
29	2.9.9 Interface of the DAQ to the online storage	91
30	2.9.10 Data-quality monitoring	92
31	2.10 Cryostat and feedthroughs	93
32	2.10.1 Scope and requirements	93
33	2.10.2 Storage characteristics	94
34	2.10.3 Cold GTT vessel	95
35	2.10.4 Temporary Construction Opening (TCO)	96
36	2.10.5 LAr pump penetration	96
37	2.10.6 Beam window penetration	97
38	2.10.7 Roof signal, services and supports penetrations	98
39	2.10.8 Detector Support Structure (DSS)	98
40	2.11 Installation	99
41	2.11.1 Anode Plane Assemblies (APAs)	99
42	2.11.2 Photon Detection System (PDS)	100
43	2.11.3 Cold Electronics (CE)	101
44	2.11.4 Cathode Plane Assemblies (CPAs)	103
45	2.11.5 Field Cage (FC)	103
46	2.12 Cryogenics and LAr purification systems	105
47	2.12.1 Overview, Overall planning and ES&H	105

1	2.12.2 Cryogenics Layout	107
2	2.12.3 Modes of operation	110
3	2.12.4 Features	112
4	2.12.5 Cryostat pressure control	116
5	2.13 Detector monitoring and slow control	118
6	2.13.1 Monitoring devices and sensors	118
7	2.13.2 Slow Control System	121
8	3 Software and Computing	124
9	3.1 Overview	124
10	3.2 Data storage and management system	124
11	3.2.1 Data characteristics	124
12	3.2.2 Raw data flow	125
13	3.3 Offline data processing	125
14	3.3.1 Production processing	126
15	3.3.2 Prompt processing	127
16	3.4 The LArSoft framework for simulation and reconstruction	128
17	3.5 Event simulation	129
18	3.6 Event reconstruction algorithms and performance	131
19	3.6.1 Reconstruction	131
20	3.6.2 Performance	132
21	4 Space and infrastructure	140
22	5 Test beam specifications	144
23	5.1 Beam requirements	144
24	5.2 Beamlne	146
25	5.2.1 H4 beamlne layout and optics	146
26	5.2.2 Beam properties	147
27	5.2.3 Muon halo	149
28	5.3 Beamlne instrumentation	150
29	5.3.1 Beam profile monitoring, particle tracking and momentum measurements	150
30	5.3.2 Particle identification	152
31	5.3.3 Material budget and discussion	156
32	5.3.4 Trigger and data acquisition	157
33	References	158

List of Figures

1.1	The major components of the ProtoDUNE-SP TPC	4
1.2	Energy at interaction	10
2.1	The TPC components	13
2.2	The field cages	14
2.3	APA Diagram	17
2.4	APA dimensions	20
2.5	APA Bolted Joint Drawing	21
2.6	APA Full-Size Mesh Drawing	22
2.7	APA Board Stack	22
2.8	APA wire board connection to electronics	24
2.9	APA Side Board Model	25
2.10	APA Side Board Photo	25
2.11	APA Support Comb Model	27
2.12	Solid model of modular CE boxes	28
2.13	APA Interconnect Drawing	29
2.14	Resistive surface CPA concept	31
2.15	CPA geometry	33
2.16	Views of various parts of a CPA	34
2.17	CPA and FC module hinged connection	35
2.18	Model of the HV bus	36
2.19	An end-wall field cage assembly	38
2.20	The field cage with ground planes	39
2.21	Field cage schematic diagram	40
2.22	Top/bottom FC panel with endwall frame	41
2.23	3D model of one fully assembled FC+GP module	41
2.24	CPA to field cage connection	42
2.25	Beam plug	44
2.26	Beam plug component-level view	44
2.27	Beam plug electrodes	45
2.28	Beam plug electrode	46
2.29	Beam plug to CPA connection	46
2.30	Beam plug to CPA connection	47
2.31	TPC HV circuit	48
2.32	HV feedthrough	50
2.33	The front-end electronics mounted on an APA	51

1	2.34 Connections between signal flange and APA	52
2	2.35 APA wire bias schematic diagram	56
3	2.36 Measured pulse response with details	58
4	2.37 Measured ENC vs filter time constant	59
5	2.38 The layout of the 16-channel ADC ASIC	60
6	2.39 The CE Architecture	61
7	2.40 The Front End Mother Board (FEMB), as used in an early set of tests	62
8	2.41 Faraday box for the FEMB	63
9	2.42 Conceptual design of CE feedthrough	64
10	2.43 Conceptual design of CE feedthrough	64
11	2.44 TPC cable routing scheme	65
12	2.45 Results from cable validation testing	67
13	2.46 LV power feed wire specifications	67
14	2.47 Conceptual design of signal flange	68
15	2.48 PTC and timing	69
16	2.49 WIB and LV power	69
17	2.50 Warm Interface Board	70
18	2.51 Bottom of the fuse PCB	72
19	2.52 Photon detection system overview	74
20	2.53 Radiator Plate Mounting Blocks	75
21	2.54 Diagram of PDS installation into APA frame and installed SiPM mounting board	76
22	2.55 Photo of PD mock installation	77
23	2.56 SiPM mounting board with 12 SiPMs and with Rj-45 connector	77
24	2.57 Cables in APA frame	78
25	2.58 ARAPUCA array installed in a APA frame	79
26	2.59 UV-light monitoring system	80
27	2.60 SSP Photograph	82
28	2.61 SSP Block Diagram	82
29	2.62 DAQ Overview	84
30	2.63 Warm vessel layout	94
31	2.64 Cryostat overall dimensions	95
32	2.65 Cross section of insulation layers on membranes	96
33	2.66 Front view of the cryostat with the TCO for the NP04 cryostat	97
34	2.67 Detector support system	99
35	2.68 DSS showing full set of beams	100
36	2.69 The APA with the special tooling attached	101
37	2.70 PDS installation	101
38	2.71 CE installation	102
39	2.72 Cold test stand	103
40	2.73 Top/bottom FC assembly	104
41	2.74 FC end wall panel	104
42	2.75 Process Flow Diagram	108
43	2.76 3D model of the installation	109
44	2.77 Detail of the internal cryogenics	109
45	2.78 A purity monitor from ICARUS T600	119
46	2.79 DCS design	123

1	3.1	Conceptual diagram of the flow of raw data in ProtoDUNE-SP	126
2	3.2	The reconstructed invariant masses of π^0 candidates in MC	133
3	3.3	Performance of the PANDORA reconstruction algorithm for single muons with momentum between 300 MeV/c and 5 GeV/c.	134
4	3.4	Performance of the PMA reconstruction algorithm for single muons with momentum between 300 MeV/c and 5 GeV/c.	135
5	3.5	Vertex resolution for inelastic interaction of π^\pm on Ar where a π^0 is produced	136
6	3.6	Reconstructed event of simulated proton with initial momentum 2 GeV/c	137
7	3.7	Example of reconstructed cosmic muons in ProtoDUNE-SP	137
8	3.8	Comparison of imaging recon qualities with and without charge information	139
9	3.9	Reconstructed image for one neutrino interaction event; comparison to MC	139
10	4.1	ProtoDUNE-SP cryostat in EHN1	141
11	4.2	Conventions for labeling the four sides of the cryostat	141
12	4.3	Elevation section view of the cryostat	142
13	4.4	Layout of rails in clean room and dimensions	143
14	4.5	Locations of activities in clean room	143
15	5.1	Beam window locations	145
16	5.2	H4 beamline layout	146
17	5.3	H4 beam optics	148
18	5.4	Beam momentum uncertainty	150
19	5.5	Muon halo intensity at the cryostat face	151
20	5.6	CERN threshold Cherenkov counter	153
21	5.7	Cherenkov gases	153
22	5.8	Required ToF resolution	154
23	5.9	pLAPPD	155
24	5.10	Material budget	156

List of Tables

1	1.1	Preliminary run plan for ProtoDUNE-SP hadron beam	11
2	1.2	Preliminary run plan for ProtoDUNE-SP electron beam	12
3	2.1	TPC detection components, dimensions and quantities	14
4	2.2	APA Physics Requirements	15
5	2.3	APA Design Parameters	18
6	2.4	Baseline bias voltages for APA wire layers	18
7	2.5	CuBe wire tensile strength and CTE	20
8	2.6	Electronics components and quantities	53
9	2.7	Physics requirements for the PDS electronics	81
10	2.8	Parameters defining data rate and volume in the “most likely” scenario	85
11	2.9	Cryostat penetrations, roof	98
12	2.10	List of engineering parameters for cryogenics installation	113
13	2.11	Estimated heat loads within the cryostat	114
14	2.12	Cryostat pressures during normal operations	117
15	5.1	Particle beam requirement	145
16	5.2	Beam composition	147
17	5.3	Particle rate	149
18			

Acronyms, Abbreviations and Terms

¹	O(n)	of order n
³	3D	3 dimensional (also 1D, 2D, etc.)
⁴	ADC	analog to digital converter
⁵	APA	anode plane assembly
⁶	ASIC	application-specific integrated circuit
⁷	BGR	band-gap reference
⁸	CASTOR	Cern Advanced STORage system, a hierarchical storage management system developed at CERN
⁹		
¹⁰	CC	charged current (interaction)
¹¹	CE	Cold Electronics
¹²	CMOS	complementary metalâŠoxideâŠsemiconductor
¹³	COB	cluster on-board (motherboards)
¹⁴	CP	product of charge and parity transformations
¹⁵	CPA	cathode plane assembly
¹⁶	CPT	product of charge, parity and time-reversal transformations
¹⁷	CPV	violation of charge and parity symmetry
¹⁸	CR	capacitance-resistance (board)
¹⁹	CTE	coefficient of thermal expansion

¹	DAQ	data acquisition
²	DCS	
³	DIS	deep inelastic scattering
⁴	DOE	U.S. Department of Energy
⁵	DP	dual-phase
⁶	DRAM	dynamic random access memory
⁷	DSS	detector support system
⁸	DUNE	Deep Underground Neutrino Experiment
⁹	DUNE-DP	dual-phase far detector module for DUNE
¹⁰	DUNE-SP	single-phase far detector module for DUNE
¹¹	EHN1	extension to hall in North Area at CERN, building that houses ProtoDUNE-SP
¹²		
¹³	ENC	electronic noise charge
¹⁴	ESH	Environment, Safety and Health
¹⁵	eV	electron-Volt, unit of energy (also keV, MeV, GeV, etc.)
¹⁶	FC	field cage
¹⁷	FD	far detector
¹⁸	FE	front end (electronics)
¹⁹	FELIX	Front-End-Link-EXchange
²⁰	FEMB	front-end mother board
²¹	Fermilab (also FNAL)	Fermi National Accelerator Laboratory (in Batavia, IL, the Near Site)
²²	FNAL	see Fermilab
²³	FPGA	field programmable gate array
²⁴	FR4	a composite material composed of woven fiberglass cloth with an epoxy resin binder that is flame resistant (Wikipedia)
²⁵		

1	FRP	fiberglass-reinforced plastic
2	FSI	final-state interactions
3	GAr	gaseous argon
4	GEANT4	GEometry ANd Tracking, a platform for the simulation of the passage of particles through matter using Monte Carlo methods
5		
6	GENIE	Generates Events for Neutrino Interaction Experiments (an object-oriented neutrino Monte Carlo generator)
7		
8	GP	ground plane
9	H4	H4 beamline, extended to ProtoDUNE-SP
10	HV	high voltage
11	L	level, indicates depth in feet underground at the DUNE far site, e.g., 4850L
12	LAr	liquid argon
13	LArTPC	liquid argon time-projection chamber
14	LBNF	Long-Baseline Neutrino Facility
15	LN2	liquid nitrogen
16	LV	low voltage
17	MC	Monte Carlo (detector simulation methods)
18	MH	mass hierarchy
19	MIP	minimum ionizing particle
20	MPOD	a multi-channel LV/HV power supply system from Wiener™
21	MUX	multiplex
22	NP04	the cryostat for ProtoDUNE-SP ???
23	PDS	photon detection (system)
24	pLAPPD	a time-of-flight system from Argonne Nat'l Laboratory
25	POT	protons on target

¹	ProtoDUNE-DP	dual-phase ProtoDUNE
²	ProtoDUNE-SP	single-phase ProtoDUNE
³	QA/QC	quality assurance/quality control
⁴	QE	quasi-elastic (interaction)
⁵	RCE	reconfigurable computing element
⁶	RIO	reconfigurable input output
⁷	RT	room temperature
⁸	S/N	signal-to-noise (ratio)
⁹	SiPM	silicon photomultiplier
¹⁰	SP	single-phase
¹¹	SSP	SiPM signal processor
¹²	t	metric ton, written <i>tonne</i> (also kt)
¹³	TCO	temporary cryostat opening
¹⁴	TDR	Technical Design Report
¹⁵	ToF	time of flight
¹⁶	TPB	tetraphenyl-butadiene
¹⁷	TPC	time-projection chamber
¹⁸	UHMW PE	ultra-high-molecular-weight polyethylene
¹⁹	WEC	warm electronics crate
²⁰	WIB	warm interface board
²¹	WLS	wavelength shifting
²²	ZS	zero suppression

²³

¹ Todo list

2	FR4 definition ok?	1
3	add “of n ppb or ppt”	2
4	and has in place?	3
5	Asia?	3
6	can we give rough percentages of the photons emitted into the bar and then internally reflected?	5
7	independent of DUNE itself?	5
8	check previous paragraph. Anne	6
9	not sure what prev sentence is trying to convey	6
10	can we drop prev pgraph?	7
11	want to leave this as is?	7
12	next pgraph seems like too much 35-t info; can we just say what pdune-sp will do to improve this?	7
13	The separation of physics vs engr goals may not be quite right yet	8
14	check 8 weeks	8
15	I don't see relationship between this sentence and next. Maybe need a “therefore” in next sentence?	9
16	the ‘wherever possible’ makes the sentence meaningless; please clarify	9
17	This whole last paragraph is somehow not gripping me; could it be clarified and then maybe put above the previous paragraph (which would make a better conclusion)	9
18	May need some intro/transition content here since this section was just moved in from a different part of the document	9
21	cite fluka05,Fluka15	10
22	we haven't define the coordinate system; is x along the drift direction?	16
23	^{fig:tpc_apo_boardstack} figure 2.7 needs labeling	21
24	checking: X and U, not U and V?	23
25	this figure could use some labelling	23
26	checking: X and U, not U and V?	23
27	Eric has question mark on the temp range	24
28	Eric has question on ‘longitudinal’ is it vertical X and G plane?	26
29	Eric has question on ‘longitudinal’ is it vertical X and G plane?	26
30	dissipation?	27
31	check prev pgraph	31
32	are the “buttons” called something else in the figures?	35
33	need some reference with details for this requirement	43
34	still?	43
35	citation to doc describing limit would be good	45
36	^{fig:hv-feed-through} Figure 2.32 is for DP not SP!	49
37	^{fig:tpc_FFBonAPA} Figure 2.33: APA fin is not defined	49

tab:ce-components	
1 check Table 2.6 ; there are some missing numbers	53
2 what's the Common plane? not defined. And why is "Common" capitalized (twice)?	54
3 write out	71
4 define MPOD	71
5 Missing this citation in common/pdune-tdr-citedb.bib"	73
6 ?	75
7 check if right figure ref	76
8 A bunch of content removed from here; but then gap in (paper) pages received from Flavio 9 (missing 4-147 to 4-180); not sure what to do with remainder of this file. Anne	80
10 How long do these monitoring run take ? When would they be taken (relative to beam and 11 comics running) ? Some interference with light from comics is expected; how will this be 12 addressed ? Time of a flash will be known much better than 1us, so not much overlap with 13 random cosmic events at 1ms	80
14 FEE = front end electronics? fig:daq-overview	81
15 Figure 2.62 requires significant zooming to read. Need a simpler diagram initially to show the 16 major pieces, and only the DAQ pieces. Also some descriptive text; relate the physical 17 components to data rates and such.	83
18 List components: timing, trigger, throttle systems, FPGA-based master, etc.	83
19 needs citation	85
20 is this part of the DAQ?	86
21 define	86
22 packet of data output?	86
23 what does the 'both' refer to?	87
24 separate from the actual data?	87
25 here 'both' seems to refer to 3 things	87
26 crate vs crate assembly?	88
27 define	88
28 This could use a bit of introduction, so I'm moving things around a bit, e.g., start with	91
29 end Anne's intro	91
30 prev sentence is awkward	92
31 This may need some massaging to put 'scope and req' at the beginning of this section	93
32 what are the ext constraints? Also, the text on the figure is too small; is it intended to indicate 33 what each color is? Can you clarify and make sure each part/color is labeled?	93
34 next to?	100
35 FLC: it would be desirable to have a picture of the CPA here	103
36 Jack needs to remake the fc end wall panel picture	104
37 shown in some figure?	104
38 shown in some figure?	105
39 again, figure?	105
40 This implies that N2 is at the level of 30-35 ppm - way too bad for the Scintillation Light .. 41 practically unacceptable, as it would imply a loss of 70% of the light due to N2 quenching.	113
42 A short section on requirements here would be useful	118
43 Can't find citation in bib file fig:lcaPrM	119
44 Figure 2.78 was not referenced; I added one. It's pretty, but not very informative. It could use 45 more description like "the 16(?) divisions in the device are the whatever, and the connection 46 on the right is ..." Or we could take it out.	119

1 the temp gradient device provides “coarse” measurement, but this device provides “reliable”	120
2 measurement, not “precise” measurement. Pls clarify	
3 operation of the?	121
4 relating ‘control the experiment’ and ‘monitor behavior of experiment,’ it seems out of order. Can	
5 you start with monitor and then say control?	121
6 Where is this shown?	121
7 logic or logistics?	121
8 still ‘will be developed?’	122
9 what’s EOS?	125
10 typically has?	126
11 creating derived data and	126
12 dcache reference needed	127
13 cross check with description in DAQ section; there is some tolerable (?) overlap	128
14 give some adjective before ‘file’ e.g., ‘output’?	128
15 need citation in bib file	128
16 therefore?	129
17 The prev sentence replaces this: The electrons are propagated by LArSoft-specific tools including	
18 an integral over the distributions created by longitudinal and transverse diffusion, and the	
19 wire locations on which to record the charge passing or collecting are looked up from the	
20 geometry assuming uniform spacing.	130
21 that affects the lifetime?	130
22 I took this out because I don’t think it’s discussed in this document. Anne “Space charge effects	
23 and resulting field distortions for protoDUNE are discussed in Section ??”. <small>REMOVED: SCEN intro</small>	130
24 prev sentence in parens sounds like it’s for a particular expt	131
25 prev sentence replaces: A drawback of this procedure is that signals also arrive on neighboring	
26 channels at the same time, and this procedure reduces the signal as well as the noise, in a	
27 manner that depends on the angle of a track or shower with respect to the drift field.	131
28 THEIR cold electronics?	131
29 No longer in doc? “as described in Section ??.”	131
30 choices?	132
31 What is the type of performance discussed in the first pgraph? (as opposed to particle- and	
32 event-level)	132
33 ILC - int’l linear collider?	133
34 increase size of stat box entries; if possible remove “temp” header	136
35 Something like the following could go into a summary of the document; the other chapters don’t	
36 include a summary like this.	138
37 define SAS	140
38 Is STiC defined?	155
39 need to get proper link	159
40 need to get proper link	159

1 FR4 definition ok?

¹ Chapter 1

² Introduction

³ 1.1 ProtoDUNE-SP in the context of DUNE/LBNF

⁴ ProtoDUNE-SP is the single-phase DUNE Far Detector prototype that is under construction and
⁵ will be operated at the CERN Neutrino Platform (NP) starting in 2018. It was proposed to the
⁶ CERN SPSC in June 2015 (SPSC-P-351), and following positive recommendations by SPSC and
⁷ the CERN Research Board in December 2015, was approved at CERN as experiment NP-04 (Pro-
⁸ toDUNE). The Fermilab Director and the CERN Director of Research and Scientific Computing
⁹ signed a Memorandum of Understanding (MoU) for this experiment in December 2015 that is
¹⁰ initially valid until December 2022, and may be extended by mutual agreement.

¹¹ ProtoDUNE-SP, a crucial part of the DUNE effort towards the construction of the first DUNE
¹² 10-kt fiducial mass far detector module (17 kt total LAr mass), is a significant experiment in its
¹³ own right. With a total liquid argon (LAr) mass of 0.77 kt, it represents the largest monolithic
¹⁴ single-phase LArTPC detector to be built to date. It is housed in an extension to the EHN1 hall in
¹⁵ the North Area, where the CERN NP is providing a new dedicated charged-particle test beamline.
¹⁶ ProtoDUNE-SP aims to take its first beam data before the LHC long shutdown (LS2) at the end
¹⁷ of 2018.

¹⁸ ProtoDUNE-SP prototypes the designs of most of the single-phase DUNE far detector module
¹⁹ (DUNE-SP) components at a 1:1 scale, with an extrapolation of about 1:20 in total LAr mass.
²⁰ This is similar to the scaling factor adopted by ICARUS; its T600 detector, split into two half-
²¹ modules of about 375 t total LAr mass each, was preceded by the 14-t “10-m³” prototype.

²² The detector elements, consisting of the time projection chamber (TPC), the cold electronics (CE),
²³ and the photon detection system (PDS), are housed in a cryostat that contains the LAr target
²⁴ material. The cryostat, a free-standing steel-framed vessel with an insulated double membrane, is
²⁵ based on the technology used for liquefied natural gas (LNG) storage and transport. A cryogenics
²⁶ system maintains the LAr at a stable temperature of about 89 K and at the required purity level

1 add “of n ppb or ppt”

2 through a closed-loop process that recovers the evaporated argon, recondenses and filters it, and
3 returns it to the cryostat.

4 The construction and operation of ProtoDUNE-SP will serve to validate the membrane cryostat
5 technology and associated cryogenics, and the networking and computing infrastructure that will
6 handle the data and simulated data sets. A charged-particle beam test will enable critical calibra-
7 tion measurements necessary for precise calorimetry. It will also enable the collection of invaluable
8 data sets for optimizing the event reconstruction algorithms – i.e., for finding interaction vertices
9 and for particle identification – and ultimately for quantifying and reducing systematic uncertain-
10 ties for the DUNE far detector. These measurements are expected to significantly improve the
11 physics reach of the DUNE experiment.

12 Given its technical challenges, its importance to the DUNE experiment and the timeframe in which
13 it must operate, ProtoDUNE-SP requires

14 and has in place?

15 a strong organizational structure and a collaborative effort from most of the DUNE collaboration
16 including U.S. National laboratories and university groups, CERN and international partners in
17 the EU and Latin America.

18 Asia?

19 **1.2 The ProtoDUNE-SP detector**

20 The ProtoDUNE-SP TPC, illustrated in Figure 1.1 comprises two drift volumes, defined by a
21 central cathode plane that is flanked by two anode planes, each at a distance of 3.6 m, and a field
22 cage (FC) that surrounds the entire active volume. The active volume is 6 m high, 7 m wide and
23 7.2 m deep (along the drift direction). Each anode plane is constructed of three adjacent Anode
24 Plane Assemblies (APAs) that are each 6 m high by 2.3 m wide in the installed position. Each
25 APA consists of a frame that holds three parallel planes of sense and shielding wires; the wires of
26 each plane are oriented at different angles with respect to those on the other planes to enable 3D
27 reconstruction. The wire pitch for all wire planes is 4.5 mm, and each APA holds a total of 2,560
28 wires.

29 The cathode plane, called the Cathode Plane Assembly (CPA) is an array of 18 (six wide by three
30 high) CPA modules, which consist of flame-retardant FR4 frames, each 1.18 m wide and 2 m
31 high, that hold thin panels with a resistive coating on both sides. The CPA is held at -180 kV
32 providing the 500-V/cm drift field in the 3.6-m-deep drift regions. Uniformity of the electric field
33 is guaranteed by the surrounding FC.

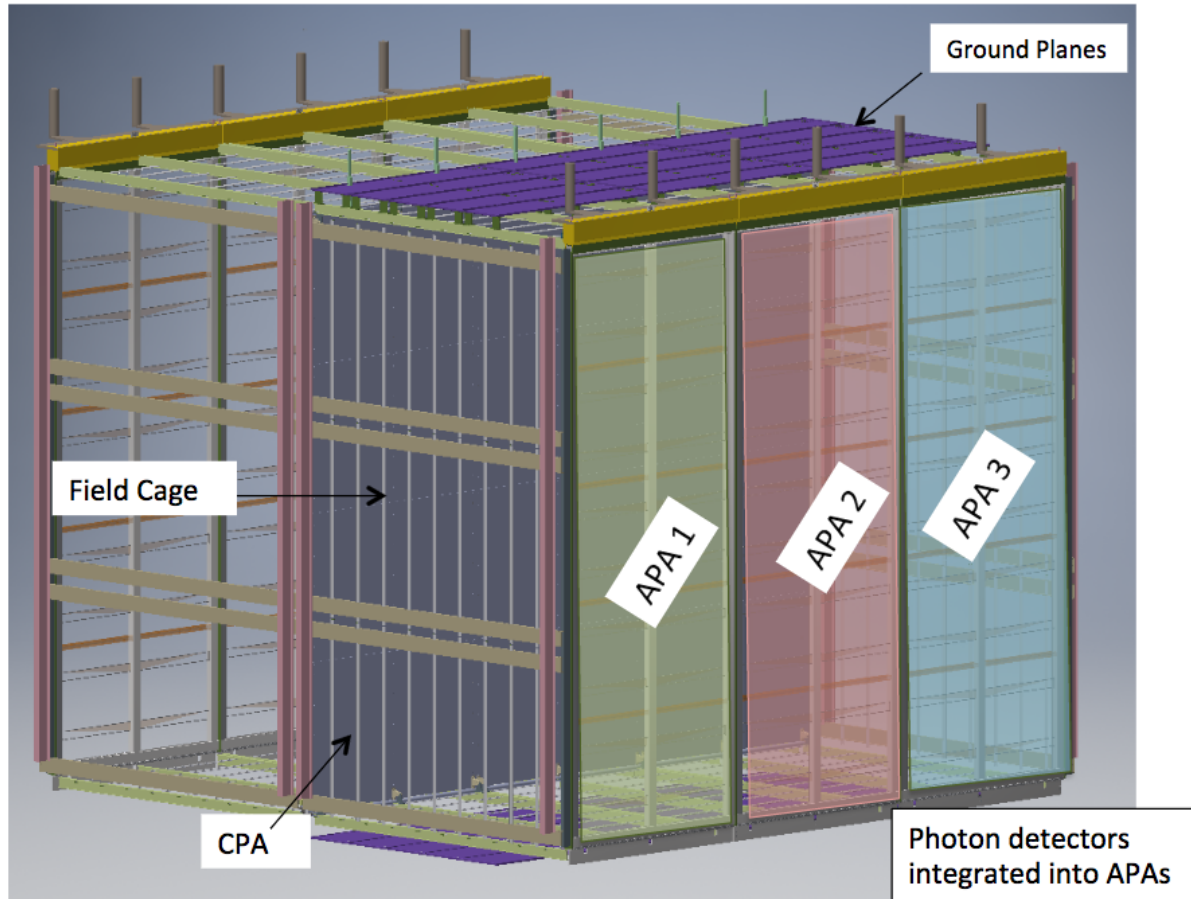


Figure 1.1: The major components of the ProtoDUNE-SP TPC. Note that the field cage shows a vertical stack of three FC assemblies; the design now calls for a stack of four.

fig:prot

- 1 The CE, mounted onto the APA frame, and thus immersed in LAr, amplifies and continuously
2 digitizes the induced signals on the sense wires at several MHz, and transmits these waveforms to
3 the Data Acquisition system (DAQ). From the DAQ the data are transmitted through the buffer
4 to disk, then to the central CERN Tier-0 Computing Center, and finally to other partner sites for
5 processing and analysis.
- 6 The modular PDS is integrated into the APAs. Each PDS module (referred to as a PD) consists
7 of a thin, wavelength-shifting radiator plate mounted on a wavelength-shifting, bar-shaped light
8 guide. The plates are coated with a layer of tetraphenyl-butadiene (TPB) that converts incoming
9 VUV (128 nm) scintillation photons to longer-wavelength photons, in the visible blue range. Some
10 of the converted photons are emitted into the bar, a fraction of which are then internally reflected
11 to the bar’s end where they are detected by silicon photomultipliers (SiPMs). Each APA frame
12 is designed with ten bays into which PDs are inserted after the TPC wires have been strung.
13 This allows for final assembly at the integration area (in a clean room) at the CERN NP prior to
14 installation inside the cryostat.

15 can we give rough percentages of the photons emitted into the bar and then internally re-
flected?

16 **1.3 Goals of ProtoDUNE-SP**

co:goals

17 The ProtoDUNE-SP test program at CERN has two very clear primary goals. First, it will
18 benchmark the principal technical solutions for the DUNE SP far detector components and, if
19 they are found to be fully adequate, to endorse them. Operating the detector in real experimental
20 conditions and for an extended period will allow for a full characterization of the components,
21 including the membrane cryostat and the cooling and purification circuit, the APA design and
22 the layout of its cold read-out electronics, the HV system, and the PDS and its warm read-out
23 electronics. Secondly, ProtoDUNE-SP will perform the measurements needed to understand, and
24 quantify to the extent possible, the systematic uncertainties that will affect the DUNE oscillation
25 measurements. This second goal anticipates physics outcomes that will be relevant independent
26 of the Far Detector.

27

independent of DUNE itself?

28 The construction and operation of ProtoDUNE-SP are thus indispensable steps toward the first
29 DUNE Far Detector module, DUNE-SP. ProtoDUNE-SP will allow the collaboration to validate
30 and benchmark the far detector engineering, to test and validate associated infrastructure require-
31 ments, and ultimately to extend the physics reach of the experiment.

1.3.1 Detector engineering validation

2 ProtoDUNE-SP is designed such that it will provide information on the actual far detector performance in as close as possible a configuration to the actual far detector layout, given the practical
3 considerations imposed by time, space, and cost. To achieve this, the cold components are identical
4 to the components proposed for the far detector, to the extent possible.

5 The APAs are full-scale pre-production modules for the far detector. The ground connections
6 between the electronics, the APA mechanical structure, the photon detectors, and the detector
7 support structure are the same as those proposed for DUNE-SP. ProtoDUNE-SP is instrumented
8 with three APAs along each wall; this will test for cross talk between the middle APA and its
9 neighbors. Whereas DUNE-SP is designed with a 12-m-high TPC, based on a two-APA-high
10 layout, ProtoDUNE-SP TPC is one APA high, due to practical limitations. The collaboration
11 will test the mechanical process of installing the two-APA detector configuration, along with the
12 related cabling, separately.

13 The cold readout electronics design is based on the DUNE-SP cryogenic front-end pre-amp/shaper
14 chip and ADC. The dedicated ASIC for serializing the data and providing a 1-GB/s link is not
15 yet available, therefore an FPGA emulating its functionality is used; it is mounted on a dedicated
16 mezzanine board. All the analog components, the conversion to digital, and the grounding/power
17 distribution for the final electronics can be tested in this configuration.

18 ProtoDUNE-SP will be the largest experiment to date to take data with cold electronics, allowing
19 high-statistics detailed studies of the performance. In the event further optimization of the ASICs
20 is required based on the ProtoDUNE-SP findings, it can be implemented before the start of pro-
21 duction in 2020. Since there is no charge amplification in the liquid, the electronics is required
22 to be extremely sensitive. The grounding and shielding are therefore critical, and the designs are
23 as similar as is practical to those of DUNE-SP. The building ground in ENH1, with the intercon-
24 nected rebar in the concrete floor connected to the building ground bus, will provide a fairly good
25 ground. The cryostat itself is isolated from the building ground, and all the mechanical/electrical
26 connections have dielectric breaks. DUNE-SP, in contrast, will be installed a mile underground in
27 a very dry mine, and better isolation from the environment is expected. ProtoDUNE-SP will test
28 the ground isolation and shielding under conservative conditions.

30 check previous paragraph. Anne

31 The FC and cathode planes are full-scale prototypes, with the same maximum drift distance and
32 corresponding high voltage. This allows ProtoDUNE-SP to use the same HV feedthrough and
33 drift-field configuration as is planned for DUNE-SP. The cryostat dimensions are selected to be
34 the same for both ProtoDUNEs to leverage the same cryostat and cryogenics system designs. In
35 order to fit the ProtoDUNE-SP TPC in the cryostat, the wall-to-cathode plane distance is slightly
36 smaller than in DUNE-SP, making this setup a conservative test of the HV design. The ground
37 planes above and below the detector make the actual mechanical geometry inside the cryostat on
38 the top and bottom irrelevant for issues related to high voltage.

1 not sure what prev sentence is trying to convey

- 2 This preserves the freedom to tailor the DUNE-SP far detector cryogenics system as needed in
3 order to optimize the purification without compromising the validity of the ProtoDUNE-SP results.
- 4 Testing these components under nominal operating conditions is extremely important, as this is
5 the first instance of LArTPCs operating with a resistive cathode and FC construction with metal
6 profiles and fiberglass I-beam support. If ProtoDUNE-SP wishes a second run with a shorter drift
7 distance in order to reduce the effects of space charge, the FC can be shortened to set a 2.5-m
8 maximum drift distance.

9 can we drop prev pgraph?

- 10 ProtoDUNE-SP offers a unique platform to validate and possibly optimize the cryogenics design
11 for DUNE-SP. The DUNE 35-t prototype was the first membrane cryostat to achieve high-purity
12 operation, but it was limited to roughly $3e^{-\text{lifetime}}$ ms. This is substantially worse than the Micro-
13 BooNE experiment's ~ 10 ms or the lifetimes seen at ICARUS at the end of its last run.

14 want to leave this as is?

15 next pgraph seems like too much 35-t info; can we just say what pdune-sp will do to improve
this?

- 16 There are several possible causes for a shorter electron lifetime. A third of the 35-t cryostat roof is
17 covered with a hatch that is not insulated, but designed with radiation shields. As the dominant
18 source of contamination is the transfer of impurities in the gas ullage to the liquid, the gas circu-
19 lation in the ullage and the impact of the hatch are important factors in the cryostat/cryogenics
20 design. The purity monitors inside the 35-t cryostat also indicated that the liquid was not well
21 mixed; it exhibited substantially higher purity at the bottom of the cryostat, indicating that the
22 liquid feed and temperature need to be optimized.

- 23 As the dominant source of contamination is the transfer of impurities in the gas ullage to the
24 liquid, the gas circulation in the ullage and the impact of the hatch are important factors in the
25 cryostat/cryogenics design. Several design improvements are in place. First, Proto-DUNE-SP
26 replaces the hatch in the ullage with a temporary construction opening (TCO) in the side of the
27 cryostat. All cryostat penetrations are designed with gas purge to prevent contaminates from
28 migrating from warm surfaces to the ullage volume, and the the liquid and gas flows inside the
29 cryostat are being modeled. This is expected to provide an excellent test bed to validate the
30 cryogenics design for DUNE-SP.

- 31 ProtoDUNE-SP will prototype the tooling and procedures for transporting APAs and transferring
32 them to a suspended rail system. Similarly, the assembly and transport processes of the CPAs and
33 top/bottom FC assemblies are being developed. ProtoDUNE-SP will not have the capability to
34 test the hanging of one APA/CPA from another or the of moving a 12-m-tall stacked module. Due
35 to the tight space inside the cryostat, the rail structure on which the detector is hung will most

¹ likely be different for DUNE-SP. Despite these differences, the experience gained in installing the
² ProtoDUNE-SP detector will be invaluable in planning the DUNE-SP installation.

³ Integration of the test beam with ProtoDUNE-SP is quite different from the neutrino beam inte-
⁴ gration planned for DUNE-SP. To minimize the material interactions of the particle beam in the
⁵ ProtoDUNE-SP cryostat upstream of the TPC, a volume of LAr along the beam path (between
⁶ the cryostat membrane and the FC) is displaced, and replaced by a less dense volume of dry ni-
⁷ trogen gas. This requires a penetration into the cryostat to install a beam plug. To ensure that
⁸ the displacement plug does not compromise the ProtoDUNE-SP operation, a dedicated HV test
⁹ at Fermilab is planned that will test the final beam plug in the exact field configuration planned
¹⁰ for ProtoDUNE-SP.

¹¹ 1.3.2 Physics

¹² The separation of physics vs engr goals may not be quite right yet

¹³ The use of a well defined test beam of charged particles of known type and incident energy will
¹⁴ significantly enhance the understanding of the ultimate performance of the LArTPC technology
¹⁵ and boost the optimization of event reconstruction, particle identification (PID) algorithms and
¹⁶ calorimetric energy measurements. The beam measurements will serve both as a calibration data
¹⁷ set to tune the Monte Carlo simulations and as a reference data set for the DUNE experiment.

¹⁸ Pion and proton beams in an energy range from about one to a few GeV will be used primarily
¹⁹ to study hadronic interaction mechanisms and secondary particle production. At higher energies,
²⁰ these beams will be used to study shower reconstruction and energy calibration. Electrons will
²¹ be used to benchmark and tune electron/photon separation algorithms, to study electromagnetic
²² cascade processes and to calibrate electromagnetic showers at higher energies. Charged kaons pro-
²³ duced in the tertiary beamline are rare but are copiously produced by the pion beam interactions
²⁴ inside the detector. These will be extremely useful for characterizing kaon identification efficiency
²⁵ for proton decay sensitivity studies. Samples of stopping muons with Michel electrons from muon
²⁶ decay (or without them, in the case of negative muon capture) will be used for energy calibra-
²⁷ tions in the low-energy range of the SN neutrino events and for the development of charge-sign
²⁸ determination methods.

²⁹ A cumulative ProtoDUNE-SP test-beam run period of eight weeks is assumed, but it depends on
³⁰ the extent of beamline sharing with other users at EHN1. The run will take place prior to the
³¹ long shutdown of the LHC in late 2018 (LS2).

³² check 8 weeks

³³ ProtoDUNE-SP will acquire cosmic data during periods with no beam. A dedicated external
³⁴ trigger system consisting of arrays of scintillator paddles, suitably positioned and arranged in
³⁵ *coincidence* trigger logic, will select specific classes of cosmic muon events. Dedicated runs, e.g.,
³⁶ runs looking for long muon tracks crossing the entire detector at large zenith angles, allow for an

1 overall test of the detector performance and the DAQ. Runs looking for muons stopping inside the
2 LAr volume and the accumulation of accurate Michel electron spectra may be useful for energy
3 calibration purposes in the low-energy range.

4 It is important to note that ProtoDUNE-SP offers much beyond calibration and detector perfor-
5 mance characterization. The LArTPC simultaneously features precise 3D tracking and accurate
6 measurement of energy deposited. Its large active volume allows for good containment of the
7 hadronic and electromagnetic interaction products in the few GeV range. These capabilities have
8 never before been combined in one detector. The unprecedented event reconstruction capability
9 combined with the exposure of the detector’s large active volume to the CERN charged-particle
10 beams open the way to a truly rich program of new physics investigations into particle interaction
11 processes.

12 Hadronic (π , K and p) interactions on an Ar target around one GeV produce low-multiplicity final
13 states rather than “hadron showers,” and 1-GeV electrons (with critical energy $\simeq 30$ MeV in Ar)
14 produce low-populated cascades, with only a few tens of secondary energetic electrons (positrons).

15

16 I don’t see relationship between this sentence and next. Maybe need a “therefore” in next sen-
tence?

17 Exploitation of “TPC/imaging-aided calorimetric measurements” in this energy range may al-
18 low investigation of energy deposition mechanisms and reconstruction methods where the usual
19 hadronic and electromagnetic shower concepts and features are either not well defined or cannot
20 be applied. Calorimetric measurements of the energy deposited can be accomplished, whenever
21 possible, for each individual secondary particle/track thanks to the imaging capabilities of this
22 type of detector.

23 the ‘wherever possible’ makes the sentence meaningless; please clarify

24 In particular, the determination of the electromagnetic content in hadron-initiated cascades, π^0
25 multiplicity, and the energy fraction carried as a function of primary hadron incident energy will
26 be of interest.

27 This whole last paragraph is somehow not gripping me; could it be clarified and then maybe
put above the previous paragraph (which would make a better conclusion).

28 1.4 Run plan

29 May need some intro/transition content here since this section was just moved in from a differ-
ent part of the document

1 Beam simulations show that the hadron rates at energies below 1 GeV/c are low. Moreover, low-
 2 energy beams are more subject to degradation by materials in the beamline. The optimization
 3 of the run plan factors in the beam composition and particle rates of the H4 beamline, and also
 4 particle interaction topologies in the ProtoDUNE-SP detector. Full FLUKA

5 cite fluka05,Fluka15

6 simulations of particle transport in the ProtoDUNE-SP detector, including the beam window, have
 7 been performed.

8 At a beam momentum of 1 GeV/c, 35% of protons are stopped before reaching the active TPC
 9 region, while the percentage reduces to 0.5% at 2 GeV/c. The kinetic energy distributions of
 10 protons and pions at the entrance point of the TPC for different beam momenta are shown in
 11 Figure 1.2. The fraction of stopping π 's for one π produced at the secondary target is 3% at
 12 $p = 0.4$ GeV/c and decreases to 1.3% at $p = 0.7$ GeV/c. The long distance (37 m) between the
 13 secondary target and the front of the LAr cryostat has a significant impact on the pion and kaon
 14 rates in the TPC. Due to pion lifetime, many of the low-energy pions produced at the secondary
 15 target decay in the beam pipe before reaching the cryostat. The situation is even more significant
 16 for kaons; most kaons below 2 GeV/c do not make it to the cryostat. Consequently the H4 beamline
 17 will not be operated much below 1 GeV/c in the hadron mode. For electrons, the beam momentum
 18 should go as low as possible to study the topology of very low-energy electron-initiated showers.

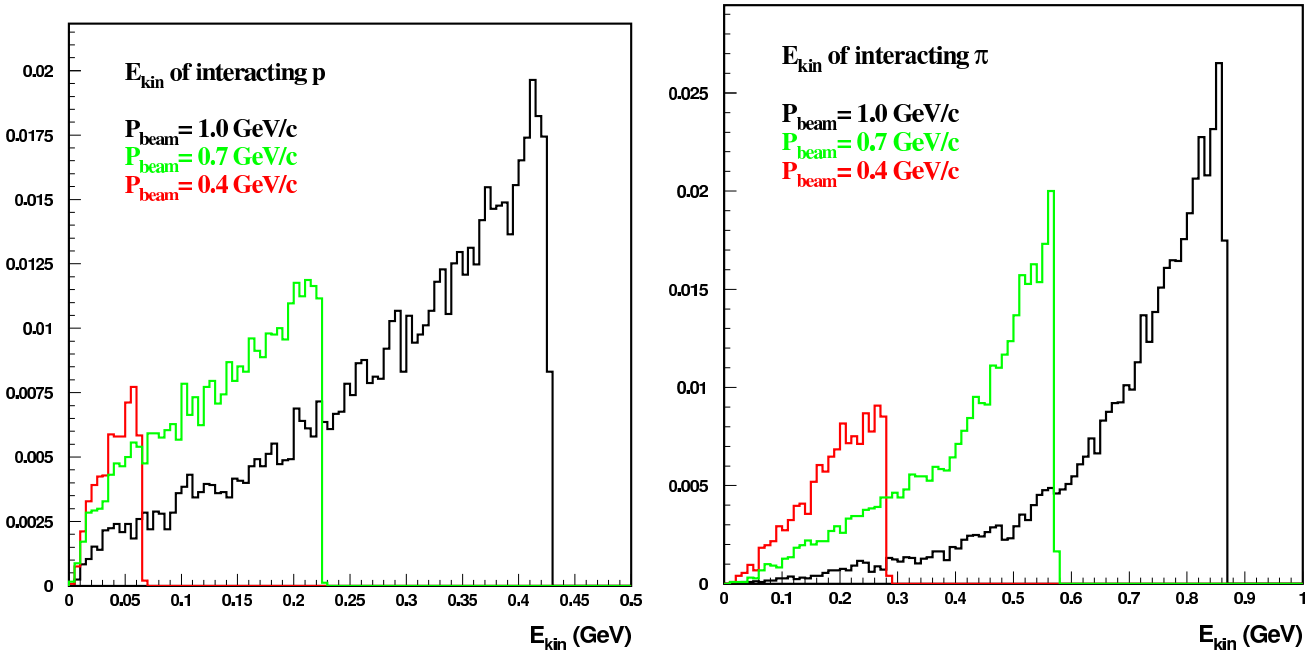


Figure 1.2: Kinetic energy of particles at the point of interaction in the ProtoDUNE-SP active volume, for different beam momenta. Histograms are normalized to one particle injected in the beamline acceptance. FLUKA simulations include the beam window materials, beams are considered as monochromatic and parallel. Left: protons, Right: pions.

19 To formulate a preliminary run plan, the hadron beam spectrum and rates are assumed as given in
 20 Tables 5.2 and 5.3. For the purpose of estimating the sample composition and beam time request,
 tab:beamonthematerials

- ¹ the following assumptions are used:
- ² • Trigger rate = 25 Hz
- ³ • Two 4.8 sec spills per SPS Super Cycle
- ⁴ • SPS Super Cycle = 48 sec
- ⁵ • 10^6 (10^4) secondary particles on target per spill for hadron (electron) beam
- ⁶ • Particle ID trigger for electrons from 0.5 to 7 GeV/c
- ⁷ • Trigger rate for electron in hadron beam is prescaled to 0.5 Hz
- ⁸ • Data collection efficiency = 50%

⁹ It is planned to run the H4 beamline in two modes: the first configuration is optimized for the
¹⁰ production of hadrons and the second configuration is optimized for the production of high-purity
¹¹ electrons. Even in the hadron mode, the beam is still dominated by electrons, especially for low
¹² beam momenta. However, the electrons in the hadron beam are not particularly “clean” due to
¹³ the amount of materials in the beamline from the particle identification (PID) instrumentations.
¹⁴ The proposal is to heavily prescale the electron events using PID (e.g., Threshold Cherenkov
¹⁵ counters) trigger while running in hadron mode. The PID systems that contribute significantly to
¹⁶ the material budget will be removed when the beamline is reconfigured for electron beam. Various
¹⁷ run plan scenarios are under investigation. One of the scenarios is shown in Tables 1.1 and 1.2.
¹⁸ Similar values are expected for the negative beam sample.

Table 1.1: A preliminary run plan for ProtoDUNE-S P hadron beam. The expected sample (positive beam) as a function of momentum is shown.

P (GeV/c)	# of Spills	# of e^+	# of K^+	# of μ^+	# of p	# of π^+	Total # of Events	Beam Time (days)
1	70K	84K	≈ 0	70K	689K	625K	1.5M	19.4 days
2	16K	19K	9K	36K	336K	572K	1.0M	4.4 days
3	13K	16K	26K	17K	181K	540K	780K	3.6 days
4	11K	13K	19K	16K	107K	510K	660K	3.1 days
5	11K	13K	29K	13K	96K	510K	660K	3.1 days
6	11K	13K	36K	12K	94K	510K	660K	3.1 days
7	11K	13K	42K	8K	87K	510K	660K	3.1 days
Total	143K	171K	161K	172K	1.6M	3.8M	5.9M	39.7 days

¹⁹ Based on the information available, the total estimated beam time needed to carry out the physics
²⁰ program in this proposal, with the assumptions stated earlier, is on the order of 16 weeks.

Table 1.2: A preliminary run plan for ProtoDUNE-SP electron beam. The expected sample for positive beam configuration is shown.

Momentum Bins (GeV/c)	# of Spills per Bin	# e^+ per Bin	Beam Time per Bin (days)
0.5, 06, 0.7, 0.8, 0.9, 1, 2, 3, 4, 5, 6, 7	5000	300K	1.4

cRunPlan

¹ Chapter 2

² Detector components

³ 2.1 Overview of detector components

⁴ The elements composing the detector, listed in Section 1.2, include the time projection chamber
⁵ (TPC), the cold electronics (CE), and the photon detection system (PDS). The TPC components,
⁶ e.g., anode planes, a cathode plane and a field cage, are designed in a modular way. The six APAs
⁷ are arranged into two APA planes, each consisting of three side-by-side APAs. Between them, a
⁸ central cathode plane, composed of 18 CPA modules, splits the TPC volume into two electron-drift
⁹ regions, one on each side of the cathode plane. A field cage (FC) completely surrounds the four
¹⁰ open sides of the two drift regions to ensure that the electric field within is uniform and unaffected
¹¹ by the presence of the cryostat walls and other nearby conductive structures. The sections in this
¹² chapter describe the components individually.

¹³ Figure 1.1 illustrates how these components fit together. The FC is shown in Figure 2.2.

Figure 2.1: NEED A FIGURE

¹⁴ Table 2.1 lists the principal detection elements of ProtoDUNE-SP along with their approximate
¹⁵ dimensions and their quantities.

¹⁶ 2.2 Anode Plane Assemblies (APA)

¹⁷ 2.2.1 Scope and requirements

¹⁸ Anode Plane Assemblies (APAs) are the detector elements utilized to sense ionization created by
¹⁹ charged particles traversing the liquid argon volume inside the single-phase TPC. The scope of the
²⁰ APAs includes:

Table 2.1: TPC detection components, dimensions and quantities

Detection Element	Approx Dimensions	Quantity
APA	6 m H by 2.4 m W	3 per anode plane, 6 total
CPA module	2 m H by 1.2 m W	3 per CPA column, 18 total in cathode plane
Top FC module	2.4 m W by 3.6 m along drift	3 per top FC assembly, 6 total
Bottom FC module	2.4 m W by 3.6 m along drift	3 per bottom FC assembly, 6 total
End-wall FC module	1.5 m H by 3.6 m along drift	4 per end-wall assembly (vertical drift volume edge), 16 total
PD module	2.2 m \times 86 mm \times 6 mm	10 per APA, 60 total

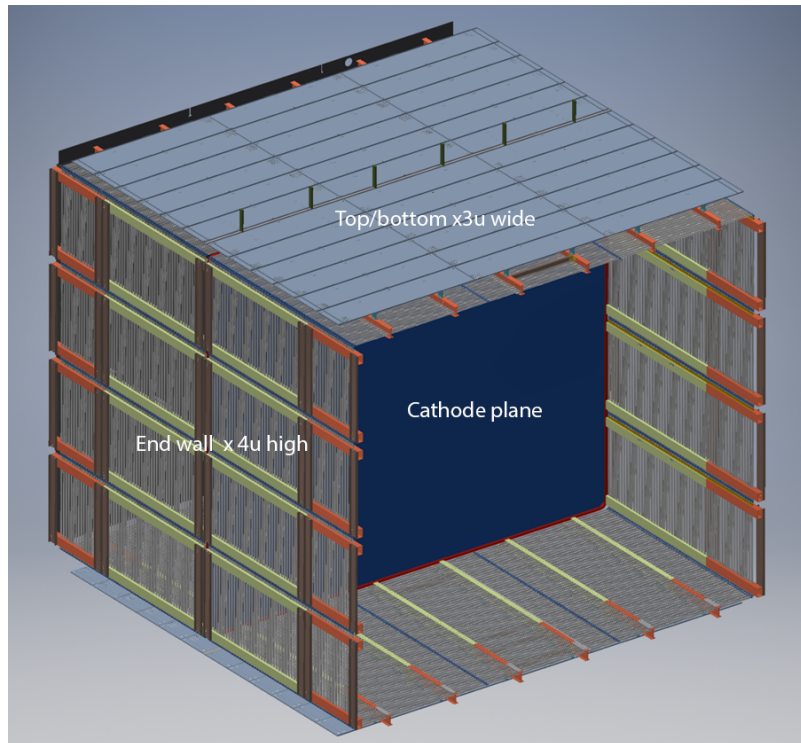


Figure 2.2: A view of the TPC field cage and the central cathode plane (CPA). The APA that would be positioned at the open end of the FC, and thus obscure the CPA, is not shown.

fig:fc-cpa

- 1 • framework of lightweight, rectangular stainless steel tubing;
- 2 • a mesh layer attached directly to both sides of the APA frame;
- 3 • layers of sense and shielding wires wrapped at varying angles relative to each other;
- 4 • stacked head electronics boards, which are wire boards for anchoring the wires at the top
5 (head) of the APA;
- 6 • capacitive-resistive (CR) boards that link the wire boards to the CE;
- 7 • side and foot boards along the other three edges of the APA with notches and pins to hold
8 the wires in place;
- 9 • modular boxes to hold the CE;
- 10 • comb wire supports, mounted on cross braces distributed along the length of the APA, to
11 prevent wire deflection; and
- 12 • pin/slot pairs on the side edges of adjacent APAs to maintain coplanarity.

13 The initial physics performance requirements that drive the design of the APA are listed in Ta-
14 ble 2.2. These are chosen to enable high-efficiency reconstruction throughout the entire active
15 volume of the LArTPC.

Table 2.2: Preliminary physics requirements that motivate APA design parameters.

Requirement	Value
MIP Identification	100% efficiency
High efficiency for charge reconstruction	>90% for >100 MeV
Vertex Resolution (x,y,z)	(1.5 cm, 1.5 cm, 1.5 cm)
Particle Identification	
Muon Momentum Resolution	<18% for non-contained <5% for contained
Muon Angular Resolution	<1°
Stopping Hadrons Energy Resolution	1-5%
Hadron Angular Resolution	<10°
Shower identification	
Electron efficiency	>90%
Photon mis-identification	<1%
Electron Angular Resolution	<1°
Electron Energy Scale Uncertainty	<5%

16 The ability to identify minimum-ionizing particles (MIPs) is a function of several detector param-
17 eters, including argon purity, drift distance, diffusion, wire pitch, and Equivalent Noise Charge
18 (ENC). It is required that MIPs originating anywhere inside the active volume of the detector be
19 reconstructed with 100% efficiency. The choice of wire pitch (i.e., ~5 mm), combined with the

¹ design values of the other high-level parameters, listed in Table 2.3, is expected to enable this
² efficiency.

³ The fine wire spacing of the APA enables excellent precision in identifying the location of any
⁴ vertices in an event (e.g., the primary vertex in a neutrino interaction, or gamma conversion
⁵ points in a π^0 decay), which has a direct impact on reconstruction efficiency. It is required to
⁶ reach a vertex resolution of ~ 1.5 cm along each coordinate direction. In practice, the resolution
⁷ on the drift-coordinate (x) of a vertex or hit will be better than that on its location in the y - z
⁸ plane, due to the combination of drift-velocity and electronics sampling-rate uncertainties.

⁹ we haven't define the coordinate system; is x along the drift direction?

2.2.2 APA design overview

¹⁰ overview
¹¹ An APA is constructed from a framework of lightweight, rectangular stainless steel tubing, with
¹² a fine mesh covering the rectangular area within the frame, on both sides, that defines a uniform
¹³ ground across the frame. Along the length of the frame and around it, over the mesh layer, layers
¹⁴ of sense and shielding wires are strung or wrapped at varying angles relative to each other, as
¹⁵ illustrated in Figure 2.3. The wires are terminated on boards that anchor them and also provide
¹⁶ the connections to the cold electronics. The APAs are 2.3 m wide, 6.3 m high, and 12 cm thick. The
¹⁷ size of the APAs is chosen for fabrication purposes, compatibility with over-the-road shipping, and
¹⁸ for eventual transport to the 4850 level at SURF and installation into the membrane cryostat of a
¹⁹ detector module. Sufficient shock absorption and clearances are taken into account at each stage.
²⁰ The dimensions are also chosen such that an integral number of electronic readout channels and
²¹ boards fill in the full area of the APA. The modularity of the APAs allows them to be built and
²² tested at off-site production facilities, decoupling their manufacturing time from the construction
²³ of the membrane cryostat. As mentioned above, the principal design parameters are listed in
²⁴ Table 2.3.

²⁵ Starting from the outermost wire layer, there is first a shielding (grid) plane, followed by two
²⁶ induction planes, and finally the collection plane. All wire layers span the entire height of the
²⁷ APA frame. The layout of the wire layers is illustrated in Figure 2.3.

²⁸ The angle of the induction planes in the APA ($\pm 35.7^\circ$) is chosen such that each induction wire
²⁹ only crosses a given collection wire one time, reducing the ambiguities that the reconstruction
³⁰ must address. The design angle of the induction wires, coupled with their pitch, was also chosen
³¹ such that an integer multiple of electronics boards reads out one APA.

³² The wires of the grid (shielding) layer, G, are not connected to the electronic readout; the wires
³³ run parallel to the long edge of the APA frame; there are separate sets of G wires on the two sides
³⁴ of the APA. The two planes of induction wires (U and V) wrap in a helical fashion around the
³⁵ long edge of the APA, continuously around both sides of the APA. The collection plane wires (X)
³⁶ run vertically, parallel to G. The ordering of the layers, from the outside in, is G-U-V-X, followed
³⁷ by the mesh.

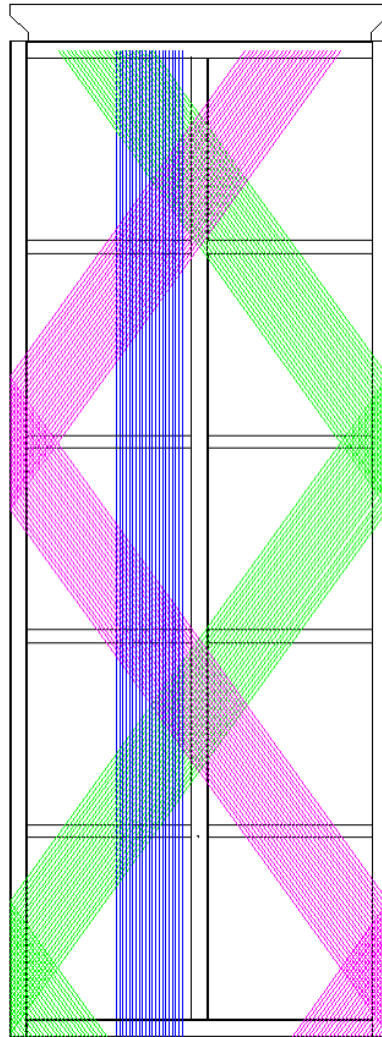


Figure 2.3: Sketch of a ProtoDUNE-SP APA. This shows only portions of each of the three wire layers, U (green), V (magenta), the induction layers; and X (blue), the collection layer, to accentuate their angular relationships to the frame and to each other. The induction layers are connected electrically across both sides of the APA. The grid layer (G) wires (not shown), run vertically, parallel to the X layer wires; separate sets of G and X wires are strung on the two sides of the APA. The mesh is not shown.

fig:tpc_

Table 2.3: APA Design Parameters.

Parameter	Value
Active Height	5.920 m
Active Width	2.295 m
Wire Pitch (U,V)	4.67 mm
Wire Pitch (X,G)	4.79 mm
Wire Position Tolerance	0.5 mm
Wire Plane Spacing	5 mm
Wire Angle (w.r.t. vertical) (U,V)	35.7°
Wire Angle (w.r.t. vertical) (X,G)	0°
Number Wires / APA	960 (X), 960 (G), 800 (U), 800 (V)
Number Electronic Channels / APA	2560
Wire Tension	5.0 N
Wire Material	Beryllium Copper
Wire Diameter	150 μm
Wire Resistivity	7.68 $\mu\Omega\cdot\text{cm}$ @ 20° C
Wire Resistance/m	4.4 Ω/m @ 20° C
Frame Planarity	5 mm
Photon Detector Slots	10

- ¹ The operating voltages of the APA layers are listed in Table 2.4. When operated at these voltages,
² the drifting ionization follows trajectories around the grid and induction wires, ultimately termi-
³ nating on a collection plane wire; i.e., the grid and induction layers are completely transparent
⁴ to drifting ionization, and the collection plane is completely opaque. The grid layer is present for
⁵ pulse-shaping purposes, effectively shielding the first induction plane from the drifting charge and
⁶ removing the long leading edge from the signals on that layer; again, it is not connected to the
⁷ electronics readout. The mesh layer serves to shield the sense planes from pickup from the Photon
⁸ Detection System and from “ghost” tracks that would otherwise be visible when ionizing particles
⁹ have a trajectory that passes through the collection plane.

Table 2.4: Baseline bias voltages for APA wire layers

Anode Plane	Bias Voltage
Grid (G)	-665 V
Induction (U)	-370 V
Induction (V)	0 V
Collection (X)	820 V
Mesh (M)	0 V

- ¹⁰ The wrapped style allows the APA plane to fully cover the active area of the LArTPC, minimizing
¹¹ the amount of dead space between the APAs that would otherwise be occupied by electronics and
¹² associated cabling.
¹³ In the current design of the DUNE-SP far detector module, a central row of APAs is flanked by

1 drift-fields, requiring sensitivity on both sides. The wrapped APAs allow the induction plane wires
 2 to sense drifting ionization originating from either side of the APA. This double-sided feature is
 3 not strictly necessary for the ProtoDUNE-SP arrangement, which has APAs located against the
 4 cryostat walls and a drift field on one side only, but it is compatible with this setup as the grid
 5 layer facing the wall effectively blocks any ionization generated outside the TPC from drifting in
 6 to the wires on that side of the APA.

7 The choices of wire tension and wire placement accuracy are made to ensure proper operation of
 8 the LArTPC at voltage, and to provide the precision necessary for reconstruction. The tension of
 9 5 N, when combined with the intermediate support combs (described in Section 2.2.5) ensure that
 10 the wires are held taught in place with no sag. Wire sag can impact the precision of reconstruction,
 11 as well as the transparency of the TPC. The tension of 5 N is low enough that when the wires are
 12 cooled, which increases their tension due to thermal contraction, they will stay safely below the
 13 break load of the beryllium copper wire, as described in Section 2.2.3. To further mitigate wire
 14 breakage and its impact on detector performance, each wire in the APA is anchored twice on both
 15 ends, with both solder and epoxy.

16 2.2.3 Wire properties

17 Beryllium copper (CuBe) wire is known for its high durability and yield strength. It is composed
 18 of \sim 98% copper, 1.9% beryllium, and a negligible amount of other elements. The APA wire has
 19 a diameter of $150\mu\text{m}$ (.006 in), and is strung in varying lengths across the APA frame. Three
 20 key properties for its usage in the APA are: low resistivity, high tensile or yield strength, and
 21 coefficient of thermal expansion suitable for use with the APA’s stainless steel frame.

22 Tensile strength of the wire describes the wire-breaking stress (see Table 2.5). The yield strength
 23 is the stress at which the wire starts to take a permanent (inelastic) deformation, and is the
 24 important limit stress for this case, though most specifications give tensile strength. Fortunately,
 25 for the CuBe alloys of interest, the two are fairly close to each other. Based on the tensile strength
 26 of wire purchased from Little Falls Alloy (over 1,380 MPa or 200,000 psi), the yield strength is
 27 greater than 1,100 MPa. Given that the stress while in use is around 280 MPa, this leaves a
 28 comfortable margin.

29 The coefficient of thermal expansion (CTE) describes how material expands and contracts with
 30 changes in temperature. The CTEs of CuBe alloy and 304 stainless steel are very similar. Inte-
 31 grated down to 87 K, they are 2.7e-3 for stainless and 2.9e-3 for CuBe [1]. Since the wire contracts
 32 slightly more than the frame during cool-down the wire tension increases. If it starts at 5 N, the
 33 tension rises to about 5.5 N when everything is cool.

34 The change in wire tension during cool-down could also be a concern. In the worst case, the wire
 35 cools quickly to 87 K before any significant cooling of the frame – a realistic case because of the
 36 differing thicknesses. In the limiting case, with complete contraction of the wire and none in the
 37 frame, the tension would be expected to reach \sim 11.7 N. This is still well under the \sim 20 N yield
 38 tension. In practice, the cooling will be done gradually to avoid this tension spike as well as other
 39 thermal shock to the APA.

Table 2.5: Tensile strength and coefficient of thermal expansion (CTE) of beryllium copper (CuBe) wire.

Parameter	Value
Tensile Strength (from property sheets) (psi)	208,274
Tensile Strength (from actual wire) (psi)	212,530
CTE of CuBe, integrated to 87 K (m/m)	2.9e-3
CTE of 304 stainless steel, integrated to 87 K (m/m)	2.7e-3

2.2.4 APA frame and mesh

- The stainless steel frame of the APA (Figure 2.4) is 6.06 m long, not counting electronics and mounting hardware, and 2.30 m wide. It is 76.2 mm thick, made from imperial size 3-in \times 4-in \times 0.120-in wall rectangular tubing. The cross pieces have a cross-sectional area of 2 in \times 3 in, and are connected to edge pieces using joints, as in Figure 2.5. It is mounted in the cryostat with its long axis vertical; multiple APAs are mounted edge-to-edge to form a continuous plane. An electron deflection technique is used to ensure that electrons drawn towards a joint between two APAs will be deflected to one or the other, and not lost.

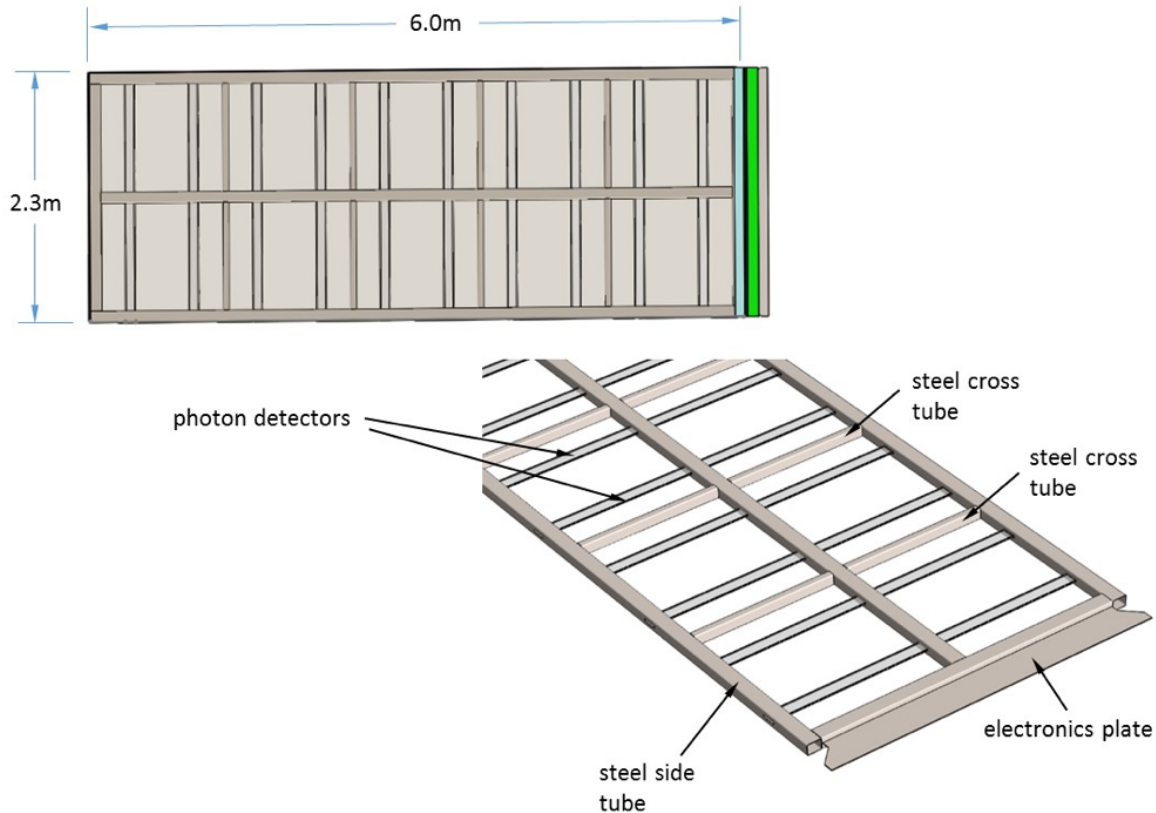


Figure 2.4: An APA showing overall dimensions and main components.

- A fine mesh screen is glued directly to the steel frame surface, over the frame on both sides. It creates a uniform ground layer beneath the wire planes.

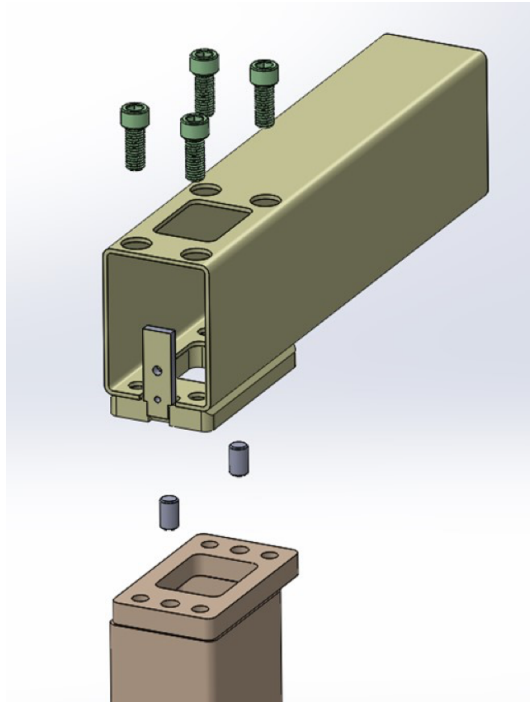


Figure 2.5: A model of the bolted joint. The holes on the top of the tube are for access to tighten the screws. The heads actually tighten against the lower hole, inside the tube.

[fig:tpc](#)

- 1 The mesh is clamped around the perimeter of the opening and then pulled tight (by opening and
- 2 closing clamps as needed during the process). When the mesh is taut, a 25-mm-wide strip is
- 3 masked off around the opening and glue is applied through the mesh to attach it to the steel.
- 4 Although measurements have shown that this gives good electrical contact between the mesh and
- 5 the frame, a deliberate electrical connection is also made. Figure 2.6 depicts the mesh application
- 6 setup for a full-size ProtoDUNE-SP APA.

[fig:tpc_apache_fullsize_mesh](#)
[drawing](#)

[e_anchor](#)⁷ 2.2.5 Anchoring elements and wire boards

[8](#) Head electronics boards

- 9 At the head end of the APA, stacks of electronics boards (referred to as “wire boards”) are arrayed
- 10 to anchor the wires. They also provide the connection between the wires and the cold electronics.

- 11 All APA wires are terminated on the wire boards, which are stacked along the electronics end of the
- 12 APA frame; see Figure 2.7. Attachment of the wire boards begins with the X plane (innermost).
- 13 After the X-plane wires are strung top to bottom along each side of the APA frame, they are
- 14 soldered and epoxied to their wire boards and trimmed. The remaining wire board layers are
- 15 attached as each layer is wound. The main CR boards (capacitive-resistive), which provide DC
- 16 bias and AC coupling to the wires, are attached to the bottom of the wire board stack. They are
- 17 described in Section 2.2.5.

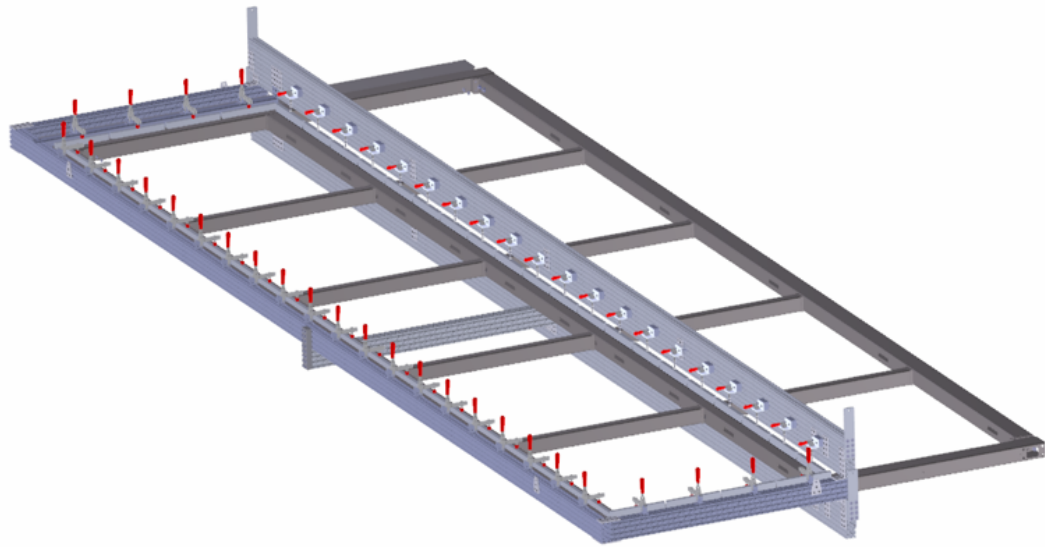


Figure 2.6: The mesh clamping jig for the full size APA.

fig:tpc_jig

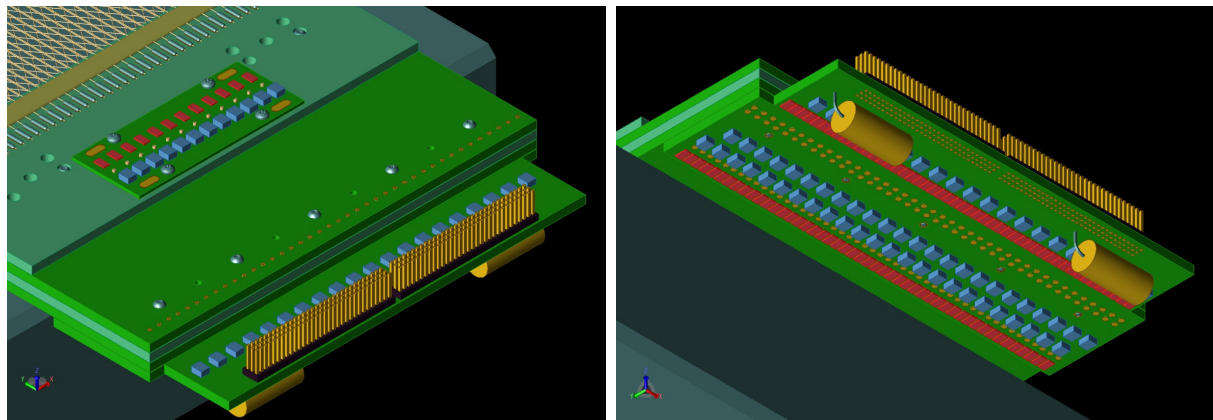


Figure 2.7: Left: View of the APA wire board stack, as seen from the top/side. The wire board layers can be seen at the bottom-left of the illustration, X on the bottom (it doesn't go all the way back, but extends farther forward and has the main CR board attached), followed by U, V, then G (which doesn't go all the way forward, and has its own CR board attached). Right: the same stack viewed from below.

fig:tpc_wires

fig:tpc_apa_boardstack
figure 2.7 needs labeling

1 2 The outermost G-plane wire boards connect adjacent groups of four wires together, and bias each
 3 group through an R-C filter whose components are placed on special CR boards that are attached
 4 after the wire plane is strung. The X, U and V layers of wires are connected to the CE (housed
 5 in boxes mounted on the APA) either directly or through DC-blocking capacitors. The X and U
 6 planes have wires individually biased through $50\text{-M}\Omega$ resistors. Electronic components for the X-
 7 and U-plane wires are located on a common CR board.

8 9 checking: X and U, not U and V?

10 11 Mill-Max pins and sockets provide electrical connections between circuit boards within a stack.
 12 They are pressed into the circuit boards and are not repairable if damaged. To minimize the
 13 possibility of damaged pins, the boards are designed so that the first wire board attached to the
 14 frame has only sockets. All boards attached subsequently contain pins that plug into previously
 mounted boards. This process eliminates exposure of any pins to possible damage during winding,
 soldering, or trimming processes.

15 16 Ten stacks of wire boards are installed across the width of each side along the head of the APA.
 17 The X-layer board in each stack has room for 48 wires, the V layer has 40 wires, the U layer 40
 18 wires and the G layer 48 wires. Each board stack, therefore, has 176 wires but only only 128 signal
 19 channels since the G wires are not read out. With a total of 20 stacks per APA, this results in
 20 2,560 signal channels per APA and a total of 3520 wires starting at the top of the APA and ending
 21 at the bottom. There is a total of ~ 23.4 km of wire on the two surfaces of each APA. Many of the
 22 capacitors and resistors that in principle could be on these wire boards are instead placed on the
 23 attached CR boards to improve their accessibility in case of component failure. Figure 2.8 depicts
 the connections between the different elements of the APA electrical circuit.

24 25 this figure could use some labelling

26 27 At the head end of the APA, the wire-plane spacing is set by the thickness of these wire boards.
 28 The first layer's wires solder to the surface of the first board, the second layer's wires to the surface
 29 of the second board, and so on. For installation, temporary toothed-edge boards beyond these wire
 boards align and hold the wires until they are soldered to pads on the wire boards. After soldering,
 the extra wire is snipped off.

30 CR boards

31 32 The CR boards carry a bias resistor and a DC-blocking capacitor for each wire in the X and U
 planes.

33 34 checking: X and U, not U and V?

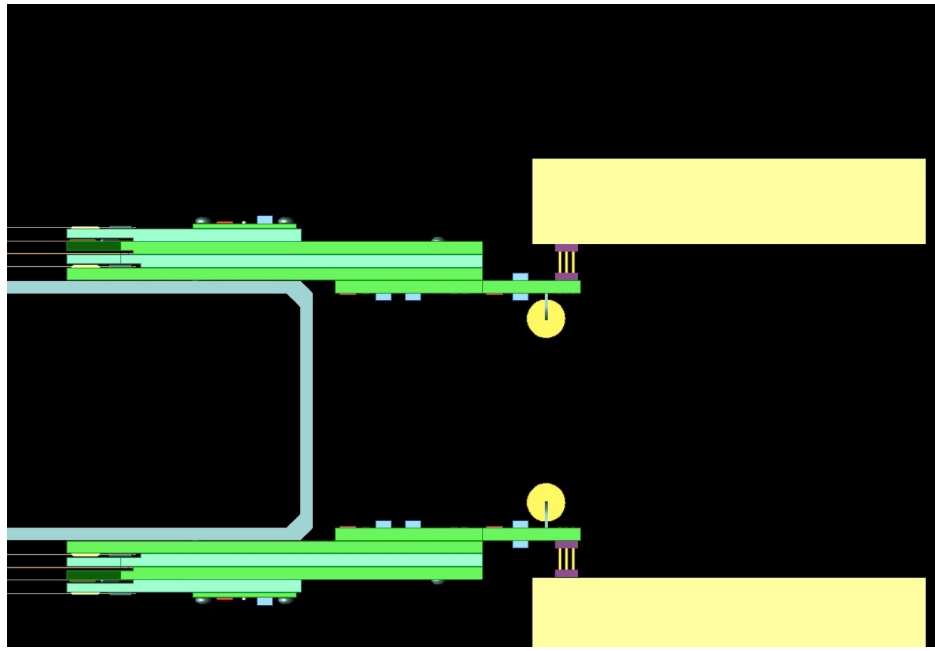


Figure 2.8: Diagram of the connection between the APA wires, viewed from the APA edge. The set of wire boards within a stack can be seen on both sides of the APA, with the CR board extending further to the right, providing a connection to the cold electronics, which are housed in the boxes at the far right of the figure

fig:tpc_

- ¹ These boards are attached to the board stacks after fabrication of all wire planes. Electrical
- ² connections to the board stack are made through Mil-Max pins that plug into the wire boards.
- ³ Connections from the CR boards to the CE are made through a pair of 96-pin Samtec connectors.

- ⁴ Surface-mount bias resistors on the CR boards have resistance of $50\text{ M}\Omega$ are constructed with
- ⁵ a thick film on a ceramic substrate. Rated for 2.0-kV operation, the resistors measure $0.12 \times$
- ⁶ 0.24 inches. Other ratings include operation from -55 to $+155$ C, 5% tolerance, and 100-ppm/C
- ⁷ temperature coefficient.

- ⁸ The selected DC-blocking capacitors have capacitance of 3.9 nF and are rated for 2.0-kV operation.
- ⁹ Measuring 0.22×0.25 inches across and 0.10 inches high, the capacitors feature flexible terminals to
- ¹⁰ comply with PC board expansion and contraction. They are designed to withstand 1,000 thermal
- ¹¹ cycles between the extremes of the operating temperature range. Tolerance is also 5%.

¹² Eric has question mark on the temp range

- ¹³ In addition to the bias and DC-blocking capacitors for all X- and V-plane wires, the CR board
- ¹⁴ includes two R-C filters for the bias voltages. The resistors are of the same type used for wire
- ¹⁵ biasing except with a resistance of $2\text{ M}\Omega$. Capacitors are 47 nF at 2 kV. Very few choices exist for
- ¹⁶ surface-mount capacitors of this type, and they are exceptionally large. Polyester or Polypropylene
- ¹⁷ film capacitors that are known to perform well at cryogenic temperatures are used.

1 Side and foot boards

- 2 The boards along the sides and foot of the APA have notches, pins and other location features to
 3 hold the wires in the correct position as they wrap around the edge from one side of the APA to
 4 the other.
- 5 G10 circuit board material is ideal for these side and foot boards due to its physical properties
 6 alone, but it has an additional advantage: a number of hole or slot features in the edge boards
 7 provide access to the underlying frame. In order that these openings are not covered by wires,
 8 the sections of wire that would go over the openings are replaced by traces on the boards. After
 9 the wires are wrapped, the wires over the opening are soldered to pads at the ends of the traces,
 10 and the section of wire between the pads is snipped out (Figure 2.9). These traces are easily and
 11 economically added to the boards by the many commercial fabricators who make circuit boards.

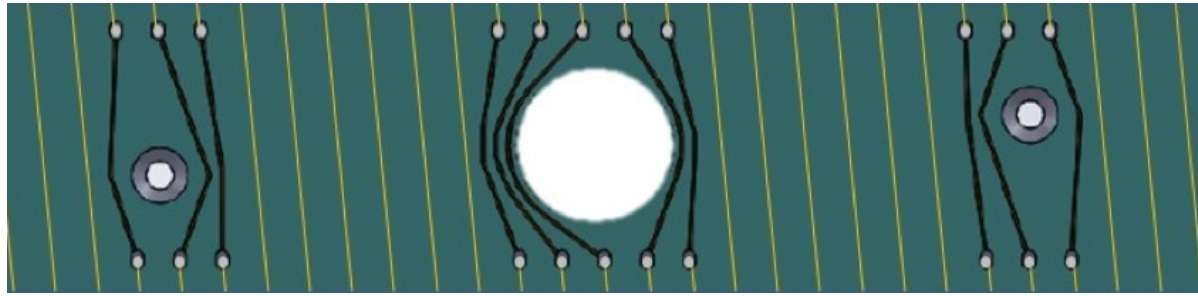


Figure 2.9: Model of board with wires showing how traces connect wires around openings in the side boards. The wires are wound straight over the openings, then soldered to pads at the ends of the traces. After soldering the sections between the pads are trimmed away.

fig:tpc_apa_sideboardmodel



Figure 2.10: Boards with injection molded tooth strips glued on. The left shows an end board with teeth for fixing the position of the longitudinal wires. The teeth there form small notches. The right is a side board for fixing the position of the angled wires where the wires are angled around a pin.

fig:tpc_apa_sideboardphoto

- 12 The placement of the angled wires are fixed by pins as shown in the right-hand picture of Fig-
 13 ure 2.10. The wires make a partial wrap around the pin as they change direction from the face
 14 of the APA to the edge. The longitudinal wires aren't pulled to the side so they can't be pulled

- 1 against a pin. Their positions are fixed by teeth with slots, as shown in the left-hand picture in
2 Figure 2.10.
fig:tpc_apa_sideboardphoto

3 Eric has question on ‘longitudinal’ is it vertical X and G plane?

- 4 The polymer used for the strips is Vectra e130i (a trade name for 30% glass filled liquid crystal
5 polymer or LCP). It retains its strength at cryogenic temperature and has a CTE similar enough
6 to G10 that differential expansion/contraction is not a problem.

7 Glue and solder

- 8 The ends of the wires are soldered to pads on the edge of the wire boards. Solder provides both an
9 electrical connection and a physical anchor to the wires. As an additional physical anchor, roughly
10 mm of the wires are glued near the solder pads. For example, in Figure 2.10, in addition to
11 soldering the wires on the pads shown in the left-hand photograph, an epoxy bead is applied on
12 the wires in the area between the solder pads and the injection-molded tooth strips.
fig:tpc_apa_sideboardphoto

- 13 Gray epoxy 2216 by 3M is used for the glue. It is strong, widely used (therefore much data is
14 available), and it retains good properties at cryogenic temperatures. A 62% tin, 36% lead and 2%
15 silver solder was chosen. A eutectic mix (63/37) is the best of the straight tin/lead solders but the
16 2% added silver gives better creep resistance.

17 Comb wire supports on inner frame members

- 18 Some wire segments are quite long; for instance, the longitudinal wires

19 Eric has question on ‘longitudinal’ is it vertical X and G plane?

- 20 extend from one end of the APA to the other without going around a side – a length of 6 m. Even
21 the diagonal wires across the middle of the APA are 3.9 m long. To prevent deflection from gravity,
22 electrostatic forces, or liquid drag from moving argon, the wires are supported at regular locations
23 along the length of the APA. This is done with *combs* mounted on each of the four cross braces
24 that are regularly spaced along the length of the APA. This keeps the longest unsupported wire
25 length under 1.6 m.

- 26 The nominal wire tension is 5 N but even the 1.6-m-long wires could fall to 3 N of tension before
27 the wire, held horizontally, would deviate 150 microns – one wire diameter. During operation the
28 wires are either vertical or 35.7° from vertical, so the actual deviation would be less.

- 29 The combs are made from 0.5-mm-thick G10 with slots cut into it. The comb for the lowest layer
30 is glued to a base strip that is glued to the frame. After each layer is wound, another comb strip
31 is glued to the tips of the teeth of the previous one to position the wires in the next layer. Each

- fig:tpc_apa_supportcombmodel
- 1 successive comb holds the previous layer of wires in the bottom of its slots (Figure 2.11).

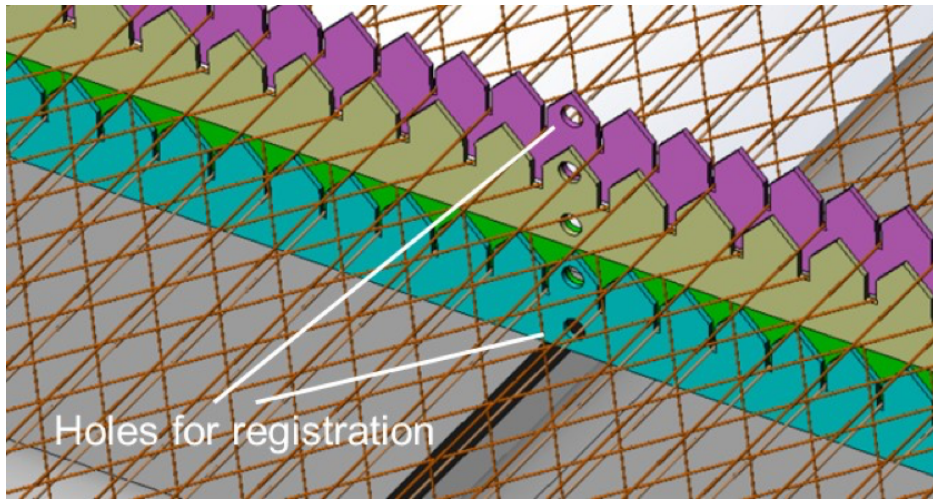


Figure 2.11: A model of the combs showing how they stack. After winding a layer, the comb for the next layer is put in place. Each comb hold the wires from the previous layer in its slots.

- 2 Periodic holes along the length of the strip allow the use of pins to accurately position each successive strip with respect to the previous one. A series of jigs is used to create and install these combs. One jig aligns the first strip to the base strip during gluing. Another jig locates this assembly on the frame as it is glued in place. A third jig locates each successive comb using these holes (labeled registration holes in Figure 2.11). fig:tpc_apa_supportcombmodel
- 7 The wire openings in the comb stack are small enough that the wires are accurately positioned at the combs, and therefore the gluing of wires into the combs is not required.

9 2.2.6 Interconnection features

10 CE boxes

11 Pins extending outward from the CR boards provide connections from the APA to the modularly
12 designed CE, and the CE modules are housed in small boxes that provide shielding. The CE boxes
13 are illustrated in Figure 2.12. Each board stack has one CE box installed near it that holds the
14 CE module for the stack. fig:tpc_apa_electronicsmountingdiagram

15 Putting the electronics in small boxes simplifies installation and replacement, and also helps with
16 the collection

17 dissipation?

18 of argon gas generated by the warm electronic components. The CE modules are mounted in such
19 a way that any of them can be removed from a single side of the APA after APA installation.

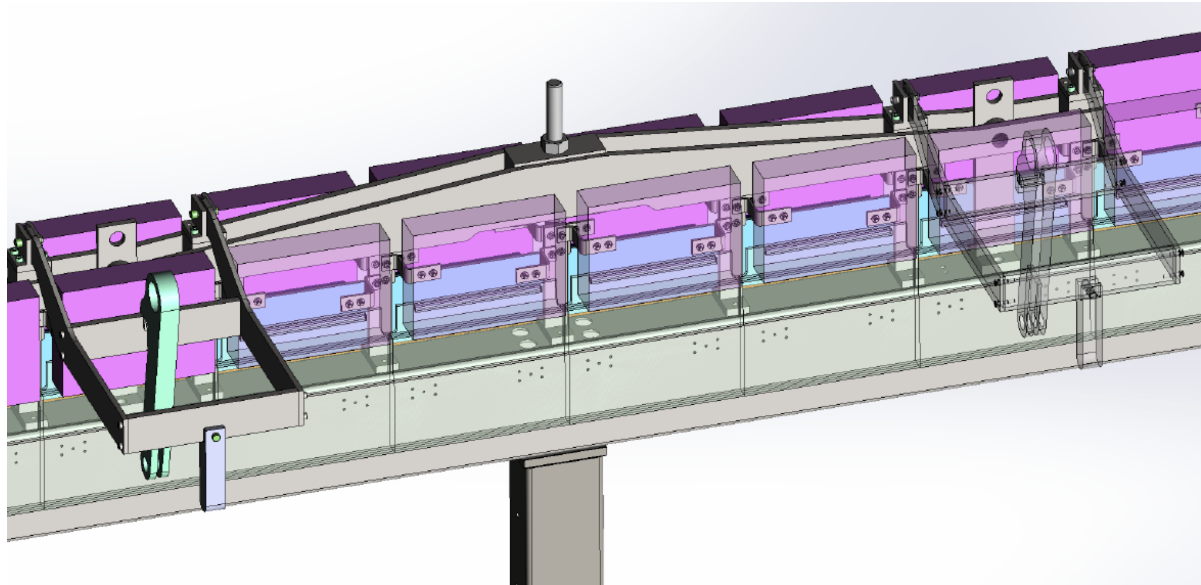


Figure 2.12: Solid model of modular CE boxes.

`fig:tpc_ce`

1 **Adjacent APAs**

- 2 A constraint is needed between adjacent APAs to keep them co-planar. It is also important that
- 3 this constraint not apply a vertical load to adjacent APAs. The constraint takes the form of a pair
- 4 of protruding pins on one edge of the APA (one high and one low) and a pair of matching slots
- 5 on the edge of the adjacent APA to engage the pins (Figure 2.13). The pins have steel cores for
- 6 strength.
- 7 Electronics noise concerns have made it desirable to isolate APAs from each other. Therefore, the
- 8 alignment pins have G10 sleeves covering their steel cores at places where they come into contact
- 9 with the frame of the adjacent APA.

10 **2.3 Cathode Plane Assembly (CPA)**

`sec:cpa`

11 **2.3.1 Scope and requirements**

- 12 The cathode plane, also called the cathode plane assembly, or CPA, is located in the middle of the
- 13 TPC, dividing the detector into two equal-distance drift volumes. The cathode plane's $7\text{ m} \times 6\text{ m}$
- 14 area is made up of six *CPA columns*, each of which is constructed of three vertically stacked *CPA*
- 15 *modules*. The CPA therefore consists of 18 CPA modules.

- 16 The scope of the CPA includes:

- 17 • 18 CPA modules, each with a frame and resistive cathode panel,

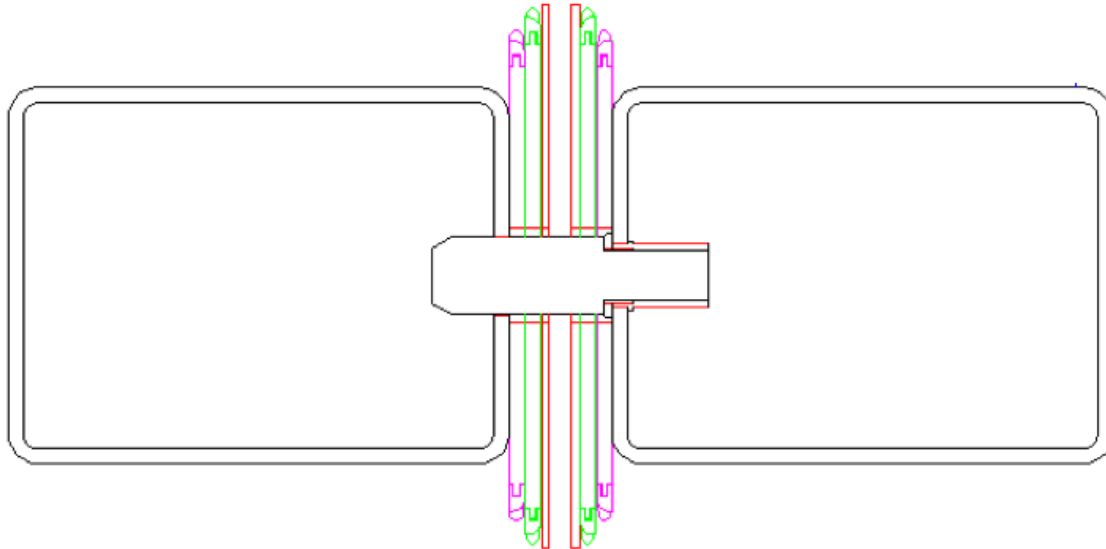


Figure 2.13: The pin/slot constraint. The pin screws into an insert in the outside frame member of one APA and engages a slot in the outside frame member of the adjacent APA.

`fig:tpc_`

- ¹ • HV bus connecting the CPA columns and modules, and
- ² • HV cup for receiving input from the power supply.
- ³ The CPA plane is required to:
- ⁴ • provide equipotential surfaces at -180kV nominal bias voltage,
- ⁵ • maintain a flatness better than 1 cm when submerged in the liquid argon,
- ⁶ • be constructed of materials with comparable CTEs to that of stainless steel,
- ⁷ • limit the electric field exposed to LAr to under 30 kV/cm
- ⁸ • prevent damage to the TPC, including its readout electronics, in case of a HV discharge anywhere on the cathode,
- ⁹ • provide constant bias voltage and current to all attached field cage (FC) resistor divider chains,
- ¹⁰ • support the full weight of the four connected top/bottom FC modules plus a person on the bottom FC during installation,
- ¹¹ • accommodate cryostat roof movement between warm and LAr-filled states,
- ¹² • be constructed in a modular form that can be easily installed in the cryostat,

- 1 • accommodate Photon Detection System (PDS) calibration features, and
- 2 • avoid any trapped volume of LAr.

3 **2.3.2 Design considerations**

- 4 For the DUNE-SP far detector, the cathode planes are planned to be 12 m tall by nearly 60 m
5 long. When biased to the nominal voltage of -180 kV , each of these cathode planes stores more
6 than 100 J of energy. If this energy were to be released suddenly and completely in a high-voltage
7 discharge event, it could greatly affect the ~~cathode-hv-1320~~ integrity of the detector elements, including the sensitive
8 front-end electronics. Study has shown [2] that a cathode plane made of interconnected metallic
9 electrodes would present significant risk to the front-end ASICs based on the potential charge
10 injection through the capacitive coupling between the cathode and the anode wires originating
11 from such an event.
- 12 To address this issue, the entire cathode plane is made out of highly resistive material such that
13 it has a very long discharge time constant. In the event of HV breakdown at a given location on
14 the cathode plane, the sudden change in voltage is restricted to a relatively localized area on the
15 CPA module in question. The rest of the CPA maintains its original bias voltage, and gradually
16 discharges to ground through the large resistivity of the cathode material. This greatly reduces
17 the instantaneous charge injection to the front-end electronics.

18 **2.3.3 CPA design**

19 **CPA modules**

- 20 The cathode plane design chosen for the ProtoDUNE-SP TPC is an array of 18 moderately sized
21 modules constructed from strong 6-cm-thick FR4 (the fire-retardant version of G10) frames. The
22 frames hold 3-mm-thick FR4 panels laminated on both sides with a commercial resistive Kapton
23 film. Each CPA module is 1.16 m wide and 2 m high, and they stack to form six CPA columns of
24 height 6 m. The six-column-wide CPA has the same dimensions as each of the two APA planes,
25 with a width of about 7 m.
- 26 The surface of the frame facing the APAs is covered by a set of resistive FR4 strips with a different
27 bias voltage, set such that the frame itself causes no distortion in the drift field beyond the resistive
28 surfaces.
- 29 Each CPA column is suspended under the cathode support rail by a single insulating FR4 bar. On
30 the top and bottom edges of a CPA, two hinges support the partial weight of the top and bottom
31 field cage modules. Adjacent CPAs are aligned through pin-and-slot connections to maintain
32 co-planarity while allowing minor relative vertical shift due to cryostat roof movement.

1 The electrical connectivity of the resistive panels vertically along each CPA column is maintained
 2 by several tabs through the edge frames. There is no direct electrical connection across the CPA
 3 columns. The HV bus is a loop of a HV cable placed along the outer edges of the entire cathode
 4 plane and horizontally between the CPA modules across the columns. Along the perimeter it is
 5 hidden between the field-shaping strip overhang and the main cathode resistive sheet. This cable
 6 must be capable of withstanding the full cathode bias voltage to prevent direct arcing to (and as
 7 a result, the recharging of) a CPA panel that discharges to ground. The HV bus makes redundant
 8 connections to the resistive panels across CPA columns. It also provides a low-resistance path for
 9 the FC resistive divider chains around the cathode edges.

10 check prev pgraph

11 The outer edges of the cathode plane facing the cryostat wall are populated with the same metal
 12 profiles, with insulating polyethylene caps, as used in the field cage. This eliminates the need for a
 13 special design of the most crucial regions of the cathode plane: the edges of the CPA now look just
 14 like a continuation of the FC. Since these profiles are the only objects facing grounded surfaces,
 15 they are the most likely candidates to have HV discharges to ground. To limit peak current flow,
 16 these edge profiles are resistively connected to the main cathode panels through their laminated
 17 resistive surfaces. The resistive surface concept is illustrated in Figure 2.14. Fig:cpa-concept

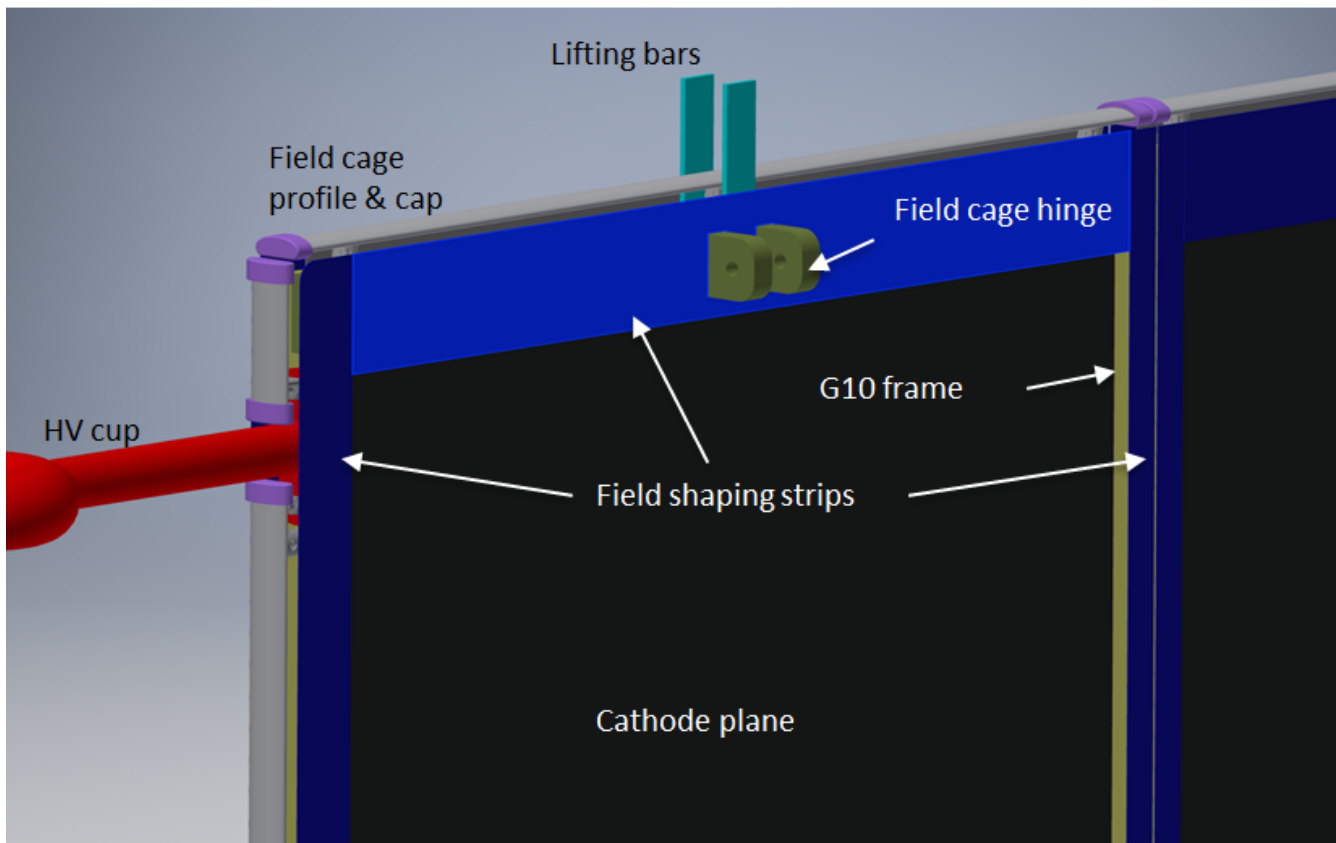


Figure 2.14: The resistive surface CPA concept showing a 3D model of a corner of the cathode with major components.

fig:cpa-

1 The CPA is connected to the HV feedthrough through a receptacle, called the *HV cup*, at the
 2 back end of the cryostat (with respect to the beam entrance) and biased at -180 kV . It provides
 3 this voltage and the required current to all the FC modules (top, bottom and end walls) through
 4 electrical interconnects (Section 2.4). The CPA is suspended by insulating bars from the CPA
 5 installation rail. It also mechanically supports six pairs of top/bottom FC modules.

6 The main criteria for the selection of Kapton as the resistive material to be used to coat the CPA
 7 module panels are:

- 8 • surface resistivity range,
- 9 • compatibility with cryogenic temperatures,
- 10 • robustness to HV discharges,
- 11 • material ageing,
- 12 • radio-purity,
- 13 • ability to coat a large surface area, and
- 14 • flatness, per the cathode flatness requirement.

15 Figures 2.15 and 2.16 show the basic geometry of the cathode plane. Figure 2.16a shows the block
 16 at the top of a CPA that is secured to the top cross bar and extends to the top supporting I-beam.
 17 This block must support the weight of four half FCs ($4 \times 220\text{ lbs}$) and the weight of the CPA
 18 itself (160 lbs) for a total weight of $1,041\text{ lbs}$. Figure 2.17 shows how the FC is attached to the
 19 assembled cathode plane.

20 *Deformation and stress due to pressure from circulating LAr*

21 Calculations indicate that a uniform 2-Pa pressure applied to the resistive panels during cooldown
 22 will result in 0.090 inch deflections of the panel at its center. The entire TPC (i.e., the CPA/FC/APA
 23 assembly) will displace 8.8 mm laterally as a result of the net force from this pressure.

24 *Thermal considerations*

25 When the CPA modules are cooled, their width will shrink by 0.9 mm. The supporting stainless
 26 steel beam will shrink by 1.6 mm over the width of the CPA. If the CPA supports are rigidly
 27 attached to the supporting stainless steel beam, then an interference of 0.7 mm (the difference)
 28 will occur. To prevent this interference and ensure contact between CPAs after cooldown, an initial
 29 gap of 0.7 mm between CPAs is required.

30 The steel beam between the CPA and APA will shrink by 5.2 mm relative to the field cage
 31 length when cooled to LAr temperature. The joint between the FC and the CPA is designed to
 32 accommodate this shrinkage.

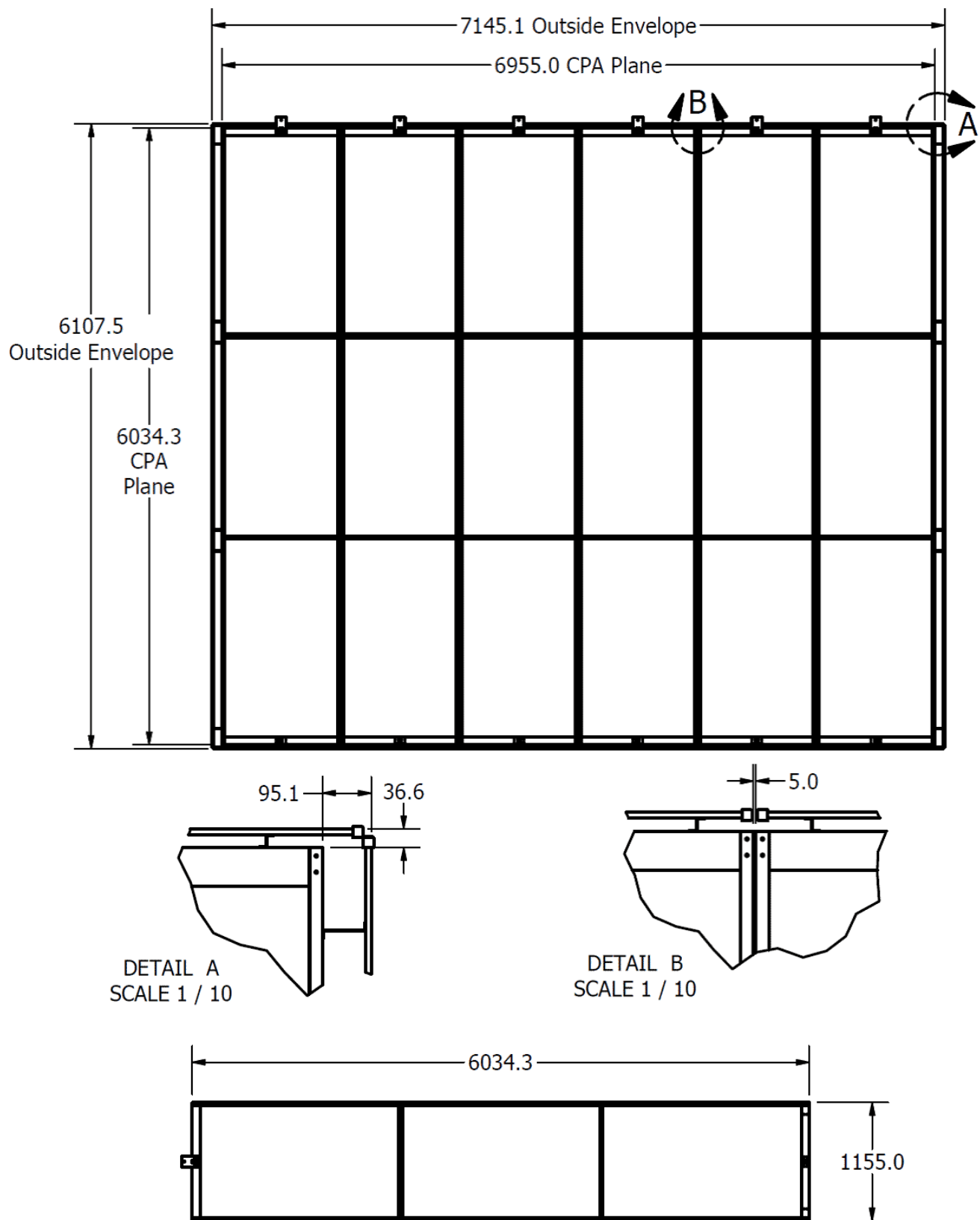


Figure 2.15: Basic geometry of the CPA array, close ups and a CPA column (on its side)

fig:cpa-

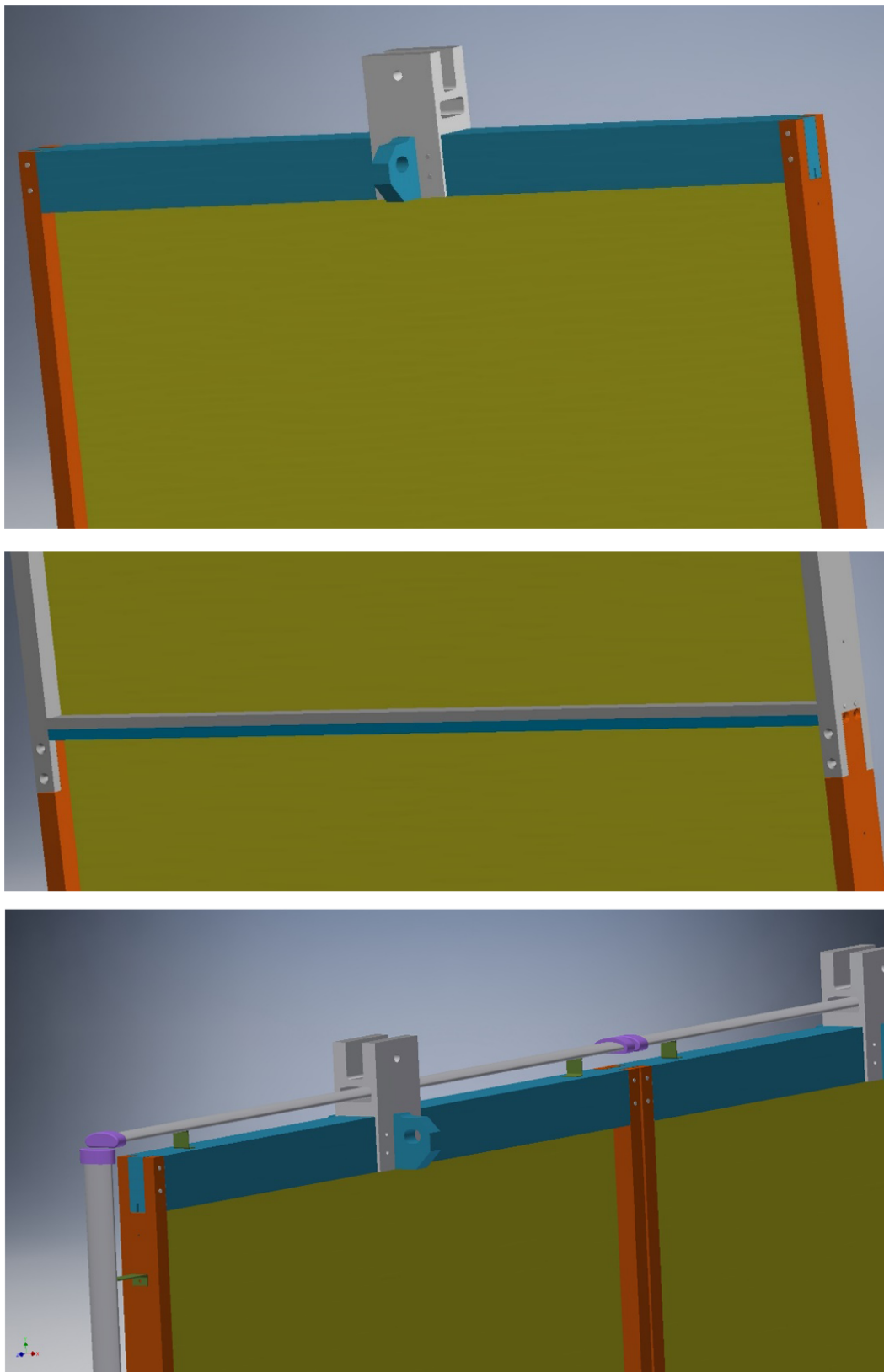


Figure 2.16: Views of various parts of a CPA. Top: the block at the top of a CPA. Middle: hardware connecting two vertically stacked CPA modules. Bottom: connection between two adjacent CPA columns.

fig:cpa-

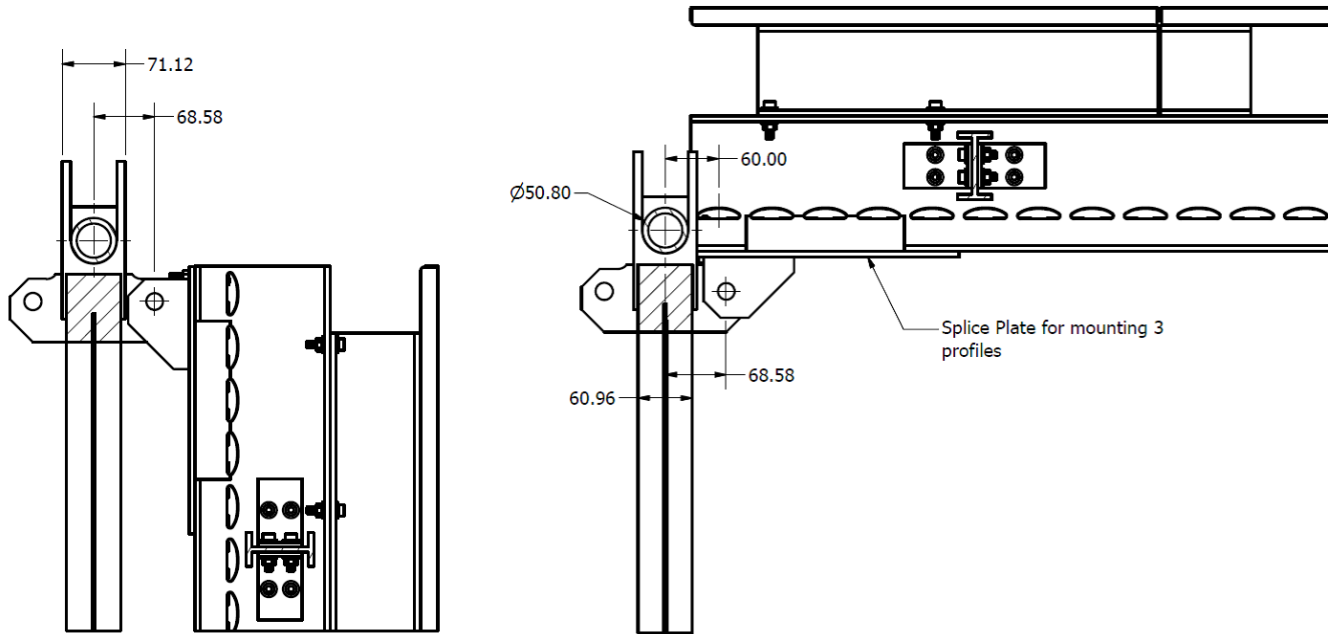


Figure 2.17: The top field cage modules are hung vertically with the CPAs when moved into the cryostat, then rotated to horizontal to attach to the APA.

fig:cpa-

2.3.4 Mechanical and electrical interconnections between modules

- 1 Three modules are stacked vertically to form the 6-m height of a CPA. The frames of these modules are bolted together using tongue-and-groove connections at the ends. The resistive cathode sheets and the field-shaping strips are connected using a few metallic buttons to ensure redundant electrical contact between the CPAs.

6 are the “buttons” called something else in the figures?

- 7 Each CPA is suspended from the cathode rail using a central lifting bar. Due to the roof movement between the warm and cold phases of the cryostat as it is cooled, each CPA is expected to move ~ 2 mm relative to its neighbors. Several pin-and-slot connections are implemented at the long edges of the CPA columns to ensure the co-planarity of the modules while allowing for a small vertical displacement.

- 12 The HV bus provides the high voltage to the FC circuits and CPA modules with a voltage drop much less than 0.1% of the default voltage. The location of the bus with respect to the CPA frame is shown in Figure 2.18. The field-shaping electrodes on the faces of the CPA module frames are part of the FC circuit, described in Section 2.4. FC electrodes on the outer edges of the CPA are held at the cathode potential to provide field uniformity and to protect the HV bus from discharge.

Fig:HVbusmodel
detcompsec-ic

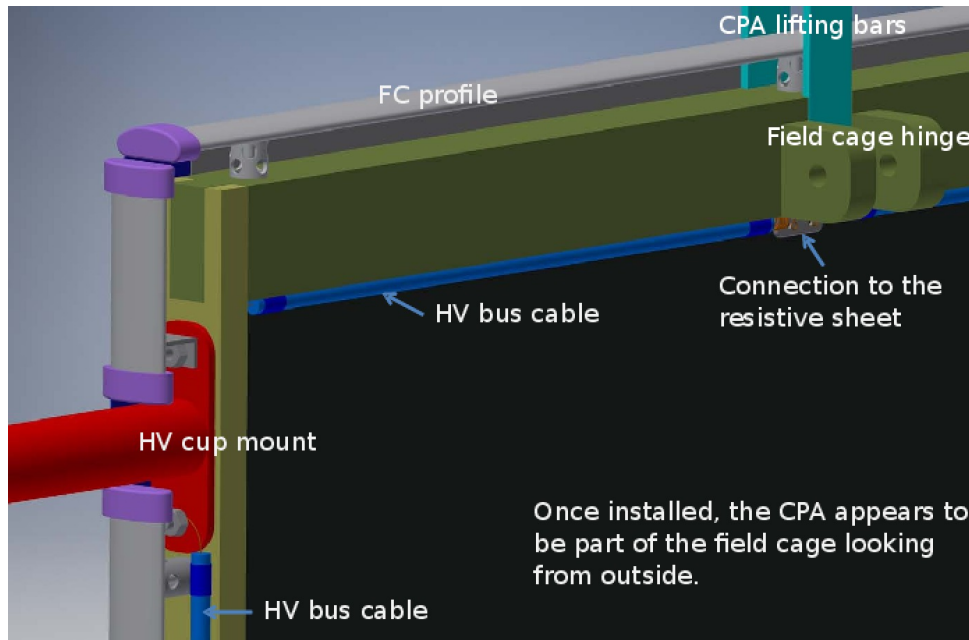


Figure 2.18: A perspective view of CPA frame showing the location of the HV bus cable and attachments to the HV cup and resistive cathode, with CPA frame electrodes omitted to make HV bus visible.

fig:HVbu

2.4 Field Cage (FC)

mpsec-fc

2.4.1 Scope and requirements

In the TPC, each pair of facing cathode and anode planes form an electron-drift region. A field cage (FC) must completely surround the four open sides of this region to provide the necessary boundary conditions to ensure a uniform electric field within, unaffected by the presence of the cryostat walls. The scope of the FC includes:

- six top FC assemblies;
 - six bottom FC assemblies; and
 - four end-wall panels, each of which consists of four (side) assemblies.
- Each assembly is made up of
- parallel metallic profiles;
 - a resistive divider chain that interconnects the parallel metal profiles to provide voltage step-down;
 - FR4 I-beams that form a support structure for the top and bottom assemblies; and

- ground planes (GP) for the top and bottom assemblies, six GP panels per FC module.
- In addition, the FC assemblies include FR4 pieces to make the mechanical connections to the CPA and APAs. One end-wall assembly is specially configured to accommodate the cylindrical beam plug, which displaces the LAr in the region where the beam enters the cryostat.
- The FC is required to:
- provide the nominal drift field of 500 V/cm;
 - withstand -180 kV near the cathode;
 - define the drift distance between the APAs and CPAs to $<1\text{ cm}$;
 - limit the electric field in the LAr volume to under 30 kV/cm;
 - minimize the peak energy transfer in case of a HV discharge anywhere on the field cage or cathode;
 - provide redundancy in the resistor divider chain;
 - maintain the divider current much greater than the ionization current in the TPC drift cell, yet less than the power supply current limit when all dividers are connected in parallel;
 - be modular in form such that they can be easily installed in the cryostat;
 - provide support for the beam plug;
 - support a 200-lb. person standing on the support beam of the bottom FC module; and
 - prevent any trapped volume of liquid.

2.4.2 Mechanical design

- The FC has six top and six bottom FC assemblies, arranged in sets of three along each horizontal boundary of the two drift regions. It has four end-wall panels (each made up of four end-wall assemblies), one covering each vertical boundary of the two drift regions, shown in Figures 2.2 and 2.19. Each endwall panel consists of four assemblies in “landscape” orientation, stacked vertically. FC assemblies are constructed from pultruded G10 I-beams and box beams that support extruded field-shaping aluminum profiles. The support structure for each of the top and bottom FC assemblies consists of two main I-beams that are 3.6 m long, and three cross I-beams that brace the main I-beams for structural stability. The main I-beams have cutouts to hold the field-shaping profiles.
- Aside from the profiles themselves, the nuts and bolts holding them, and the ground plane panels,

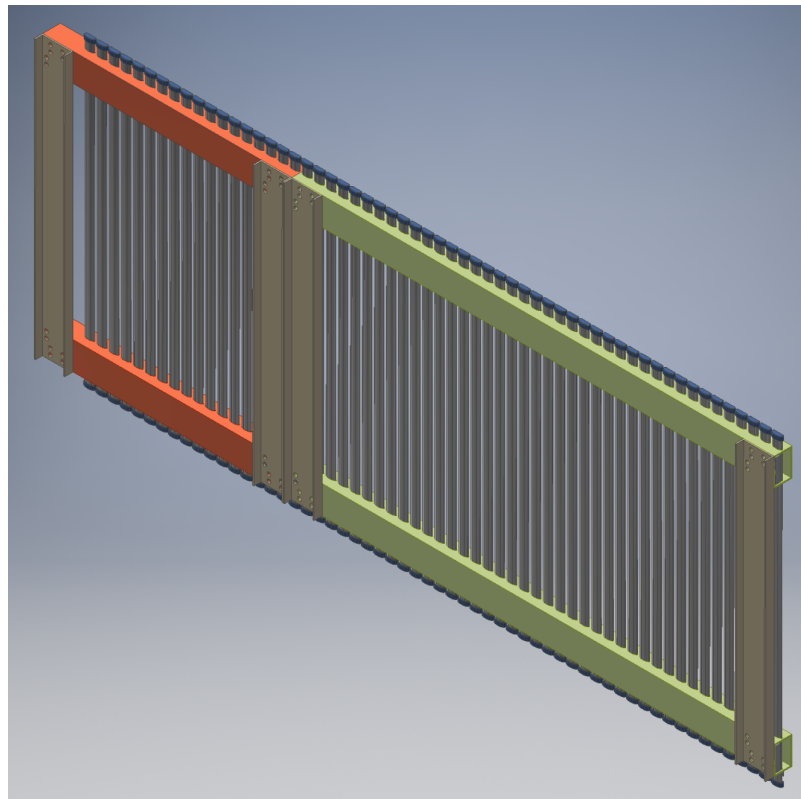


Figure 2.19: A view of an end-wall field cage assembly. An end-wall panel consists of a stack of four of these assemblies (each in landscape orientation).

fig:fc-e

- 1 all FC components are made of insulating material. The material selected for these structural
 2 components is fiberglass-reinforced plastic (FRP), which prevents binding when the structure is at
 3 cryogenic temperatures. The ground plane panels are made of stainless steel.
- 4 The inward-facing side of the ground planes are approximately 20 cm away from the top of the [fig:fc-with-ground-planes](#)
 5 field-shaping profiles, mounted at this fixed distance by standoffs. Figure 2.20 shows a set of
 6 ground planes situated over the I-beams and cross beams attached to a FC assembly.

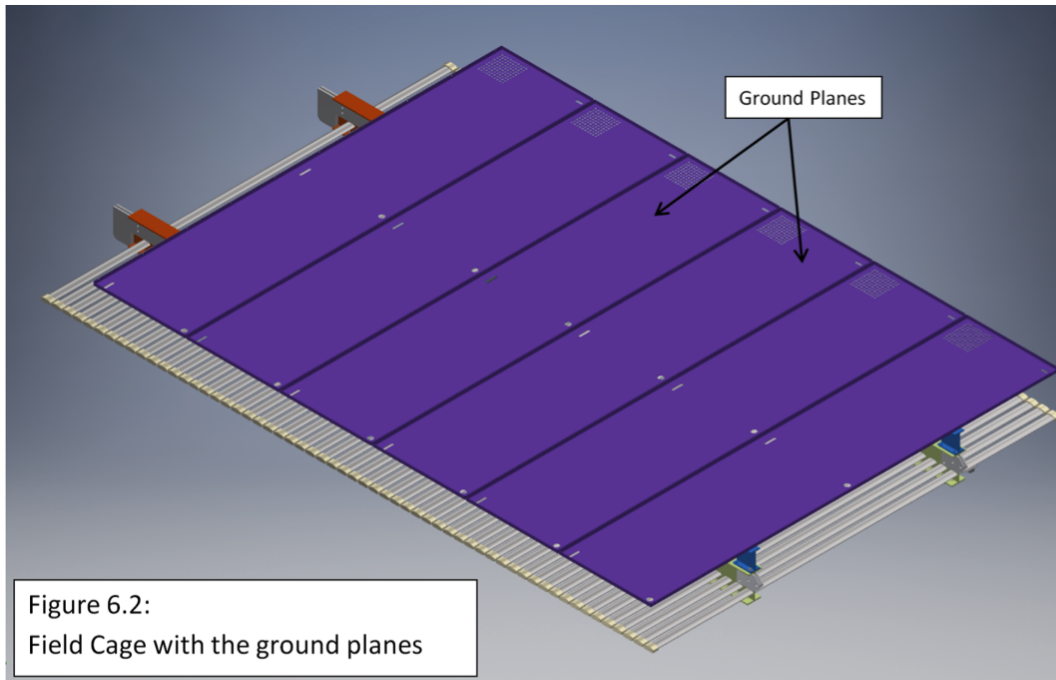


Figure 2.20: The field cage with ground planes

- 7 The parallel metal profiles in each FC assembly are interconnected by a resistive divider chain, and
 8 supported by the FRP beams that span the drift distance. Between adjacent field cage assemblies,
 9 however, the metal profiles are neither mechanically nor electrically connected. Gaps between
 10 assemblies that range from a few millimeters to a few centimeters are designed into the TPC
 11 assembly to ensure sufficient clearance for the installation. The electrical isolation between the
 12 field cage modules minimizes the peak energy dump in case of a HV discharge.

13 2.4.3 Electrical design

- 14 Given a large standoff distance between the FC and the grounded cryostat wall, it is relatively
 15 easy to design a FC that meets the 30-kV/cm electric field limit with 180-kV bias. However, as this
 16 distance is reduced to increase the active detector volume, the design becomes more challenging.
 17 Optimizing the active detector volume requires the use of electrodes with low profiles, rounded
 18 edges, no trapped volumes, and low cost. Fortunately, several commercially available roll-formed
 19 metal profiles were studied and appear to meet these requirements.

- 20 Figure 2.21 is a schematic of the electrical design of the CPA and a top/bottom field cage module

¹ pair.

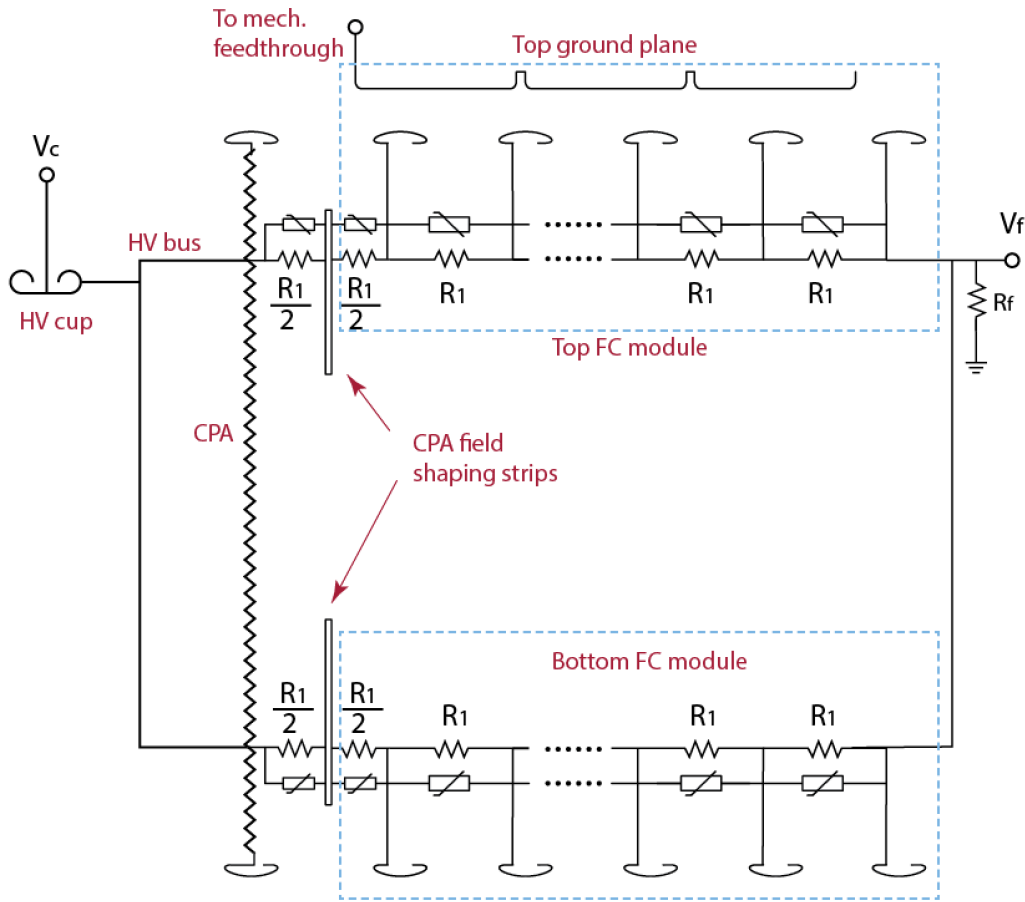


Figure 2.21: A schematic diagram of the CPA and a top/bottom field cage module pair

fig:fc-s

² 2.4.4 Top/bottom FC assemblies and GP modules

³ In order to confine the electric field in the active LAr region, a grounded metallic plane is installed
⁴ between the upper FC assemblies and the liquid-gas interface, and also between the lower FC
⁵ assemblies and the bottom of the cryostat. Each of the six top FC assemblies has six ground plane
⁶ (GP) panels attached to it, aligned along their long (2.3-m) dimension. The GPs are connected
⁷ to the FC I-beam with additional G10 support pieces that are also used to connect adjoining GP
⁸ panels. Figure 2.22 shows the frame of a top/bottom FC assembly and Figure 2.23 shows a 3D
⁹ model of a fully assembled FC module with attached GP panels.

¹⁰ The electrical connections between consecutive panels are to be made with either metallic screws
¹¹ (using holes on the planes edges) or looser connections, e.g., copper strips, that better adapt to the
¹² shrinking of the structure during cooldown. The GP panels are connected directly to the detector
¹³ ground, referenced from the top of the cryostat.

¹⁴ In addition to the six primary GP panels attached to the top FC modules,

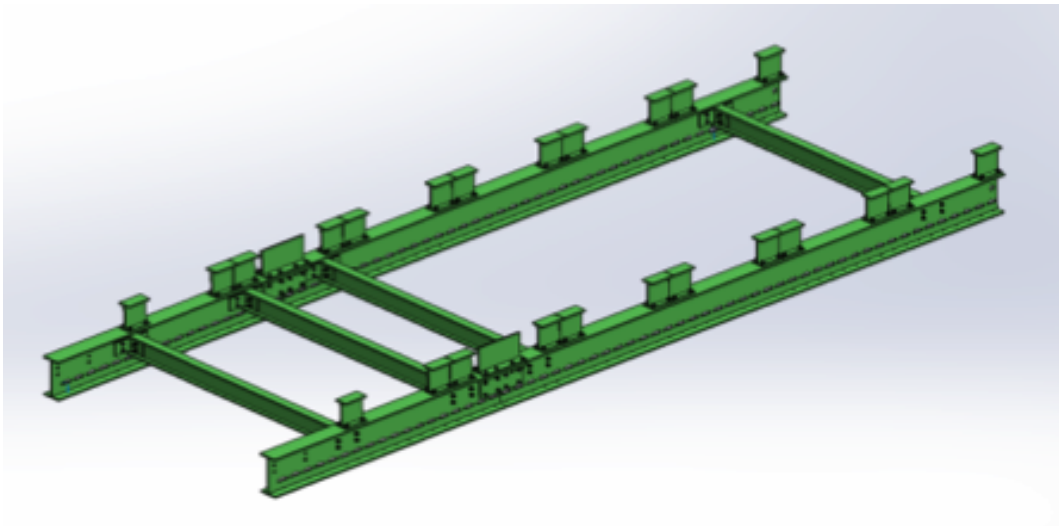


Figure 2.22: A top/bottom FC assembly with the frame

fig:fc-p

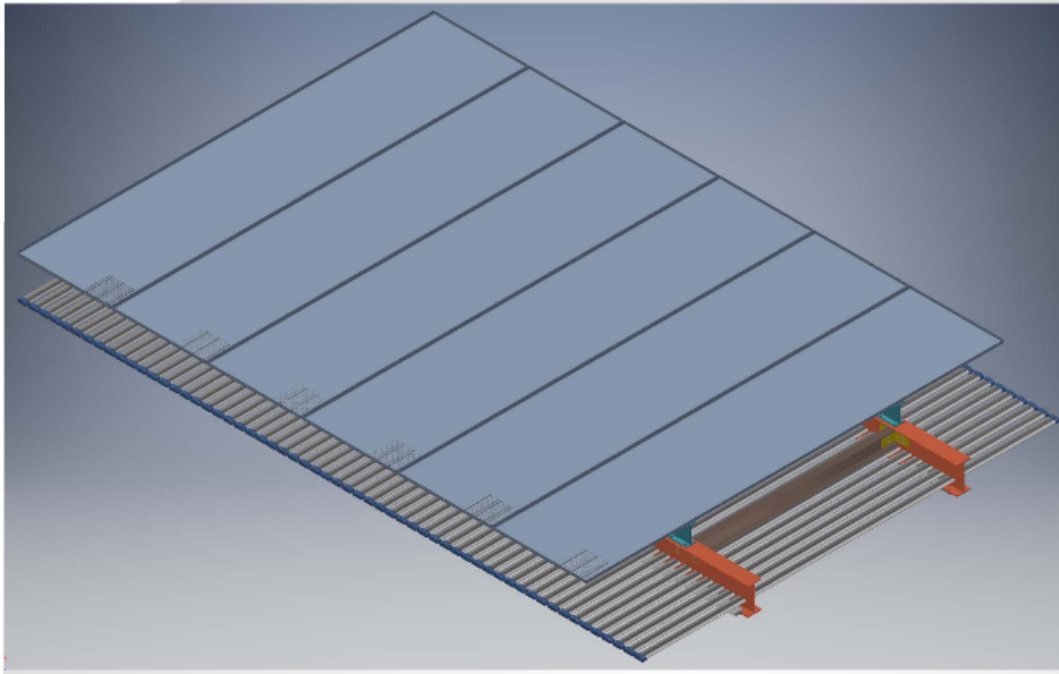


Figure 2.23: 3D model of one fully assembled FC+GP module

fig:fc_f

- Smaller panels are to be connected to the modules on one side of the CPA so that, once in position, they cover the CPA frame. Their dimensions are still to be defined, depending on the final design of the CPA hanging scheme. These pieces will also connect to the top FC modules covering the opposite drift region, once in their final position.
- An additional set of small panels is installed on the outer top FC modules of the FC to extend the GP coverage over the end-wall FC assemblies to further constrain the electric field in these regions. A FEA shows that the optimized overhang distance is 20 cm, provided that the surface of the LAr is 40 mm above the GP. In this configuration, the maximal residual field is of the order of 13 kV/cm, with no greater than 1 kV/cm fields in the gass ullage at the top of the cryostat.

2.4.5 Interfaces to other TPC components

FC to CPA

- On the top and bottom of the TPC, hinges connect each FC module to two CPA columns. These hinges allow the FC modules to be pre-attached to the CPAs during installation, preventing accidental damage to the APA wire planes when FC modules are raised and connected to the APAs.
- The end-wall FC assemblies are hung from the CPA and APA support rails. There is no strong mechanical coupling between the end-wall FC assemblies and the CPAs or APAs. However, the end-wall FC module resistive divider chains do have an electrical connection to the HV bus on the CPA plane.

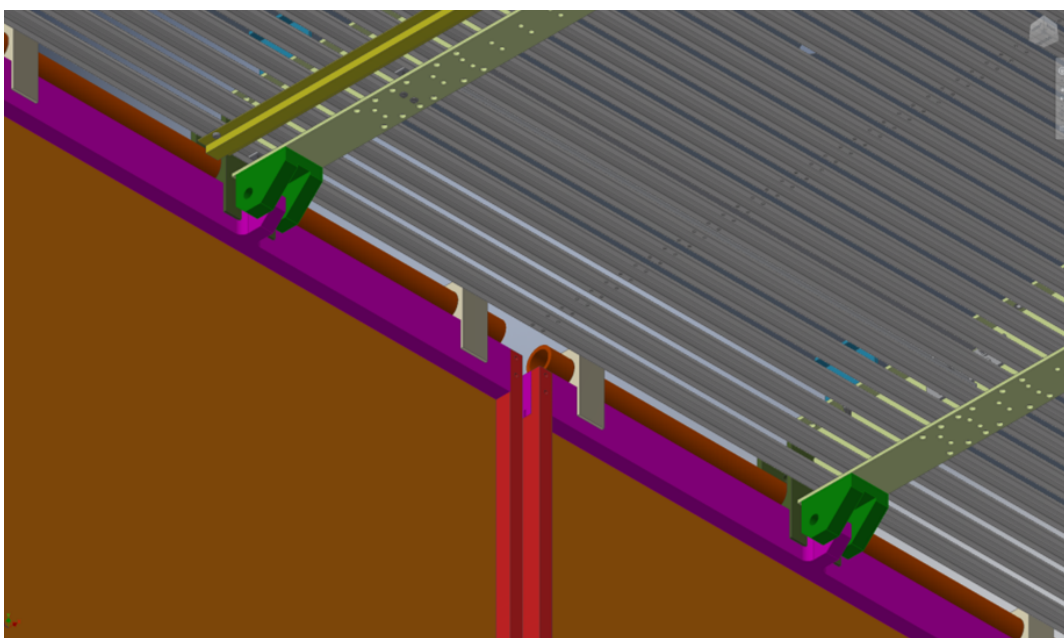


Figure 2.24: A top field cage module (grey) connected to two CPA modules (brown)

fig:cpa-

1 FC to APA

2 The I-beams of the top/bottom FC modules are designed to be latched onto mating brackets on
 3 the APAs. In addition to the mechanical connection, the ground side of the divider chain must
 4 be connected to the APA's frame ground. There is also an electrical connection between the FC
 5 module resistor divider chains, and ground is referenced from the APA frame.

6 FC to beam plug

7 The LAr-displacement beam plug, a cylindrical glass-fiber composite pressure vessel, about 50 cm
 8 in length and 22 cm in diameter, is filled with nitrogen gas via a stainless steel line that extends
 9 to the top of the cryostat. It is illustrated in Figure 2.25. A pressure relief valve (or burst disk)
 10 is installed on the nitrogen fill line on the top of the cryostat (externally) to ensure the pressure
 11 inside the beam plug does not exceed the safety level of 25 psi. A component-level view of the
 12 beam plug is shown in Figure 2.26. The beam plug is secured to the FC support structure as
 13 described in Section 2.4.5. The front portion of the beam plug extends 5 cm into the active region
 14 of the TPC through an opening in the FC. The FC support is designed with sufficient strength and
 15 stiffness to support the weight of the beam plug before filling, while it is suspended in air. When
 16 the cryostat is filled with LAr, the beam plug is roughly neutrally buoyant. The total internal
 17 volume of the beam plug is about 16 liters.

18 The requirements on the acceptable leak rate is between 7.8×10^{-5} scc/s and 15.6×10^{-5} scc/s.
 19 This is very conservative and is roughly equivalent to leaking 15% of the nitrogen in the beam
 20 plug over the course of a year. In the worst-case scenario in which all the nitrogen in the beam
 21 plug leaks into the LAr cryostat, the increase in concentration is about 0.1 ppm, which is still a
 22 factor of 10 below the maximum acceptable level, as specified by light detection requirements.

23 need some reference with details for this requirement

24 At nominal operation, the voltage difference across the beam plug (between the first and the last
 25 grading ring) is 165 kV.

26 To minimize risk of electrical discharges, the beam plug is divided into sections, each of which is
 27 bonded to stainless steel conductive grading rings. The seven grading rings are connected in series
 28 with two parallel paths of resistor chains. The ring closest to the FC is electrically connected to one
 29 of the FC profiles. The ring nearest the cryostat wall is grounded to the cryostat inner membrane
 30 via a short grounding cable. The type and value of the resistor is still under evaluation.

31 still?

32 A likely candidate is the high-voltage Super Mox 15-GΩ resistor by OHMITE. The maximum total
 33 power dissipated by the resistor chain is about 0.6 W.

34 The metal electrode rings are spaced at regular intervals and interspersed with composite tube



Figure 2.25: The beam plug is a composite pressure vessel filled with dry nitrogen gas. The vessel is about 50 cm in length and about 22 cm in diameter. The pressure vessel is divided into sections with each section bonded to a stainless steel grading ring. The grading rings are connected by two parallel paths of resistor chain.

fig:beam



Figure 2.26: Component-level view of the beam plug showing alternating electrode and composite ring structure.

fig:beam

sections. The shape of the rings has been designed to minimize high electric field corners. The results of the field calculations are shown in Figures 2.27 and 2.28. The average field in the vicinity of the beam plug is about 4.4 kV/cm. The maximum field of 15.7 kV/cm is on the electrode ring surface. In all regions the field is well below the 30-kV/cm limit.

5 citation to doc describing limit would be good

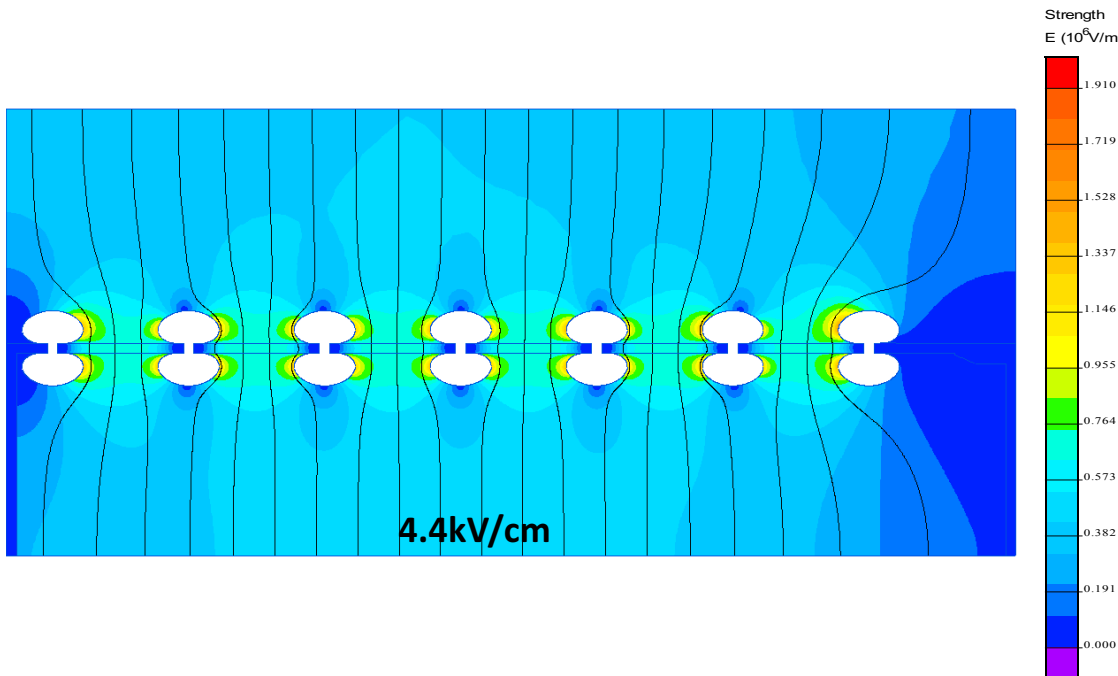


Figure 2.27: Electric field calculation of the electrode ring design. The average field in the beam plug region is about 4.4 kV/cm. The maximum field of 15.7 kV/cm is on the electrode ring surface.

6 The beam plug is mounted onto one of the field cage support structures as shown in Figures 2.29
 7 and 2.30.

8 2.5 TPC high-voltage (HV) components

9 2.5.1 Scope and requirements

10 The TPC high voltage (HV) components include the HV power supply, cables, filter circuit, HV
 11 feedthrough, and monitoring for currents and voltages (both steady state and transient).

12 A schematic of the complete TPC HV circuit is shown in Figure 2.31.

13 The cathode plane is biased at -180 kV to provide the required 500 V/cm drift field. It is powered
 14 by a dedicated HV power supply through an RC filter and HV feedthrough. The power supply for

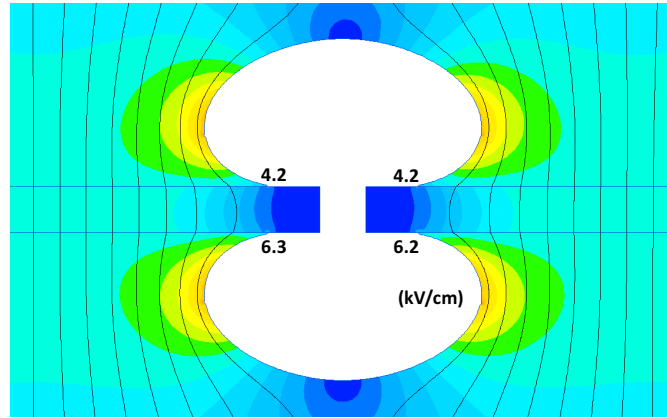


Figure 2.28: Electric field calculation near the vicinity of the electrode. The shape of the ring minimizes the high field region near the joints between the electrode, LAr, and composite shell. The field is well below the 30-kV/cm limit in all regions.

fig:beam

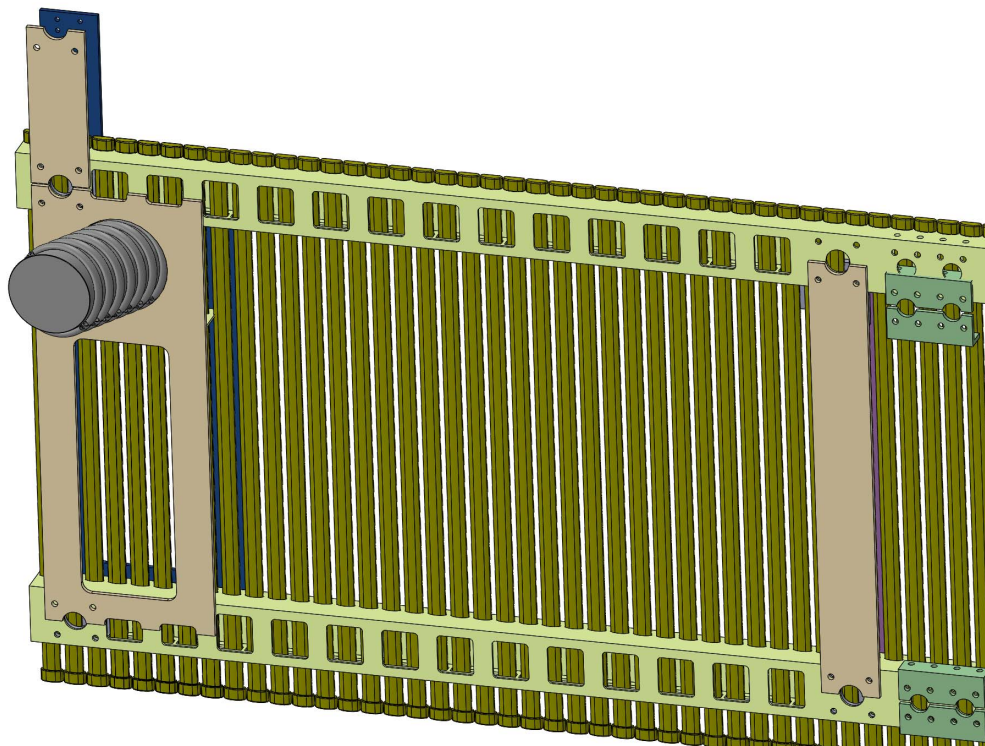


Figure 2.29: Beam plug to field cage interface.

fig:beam

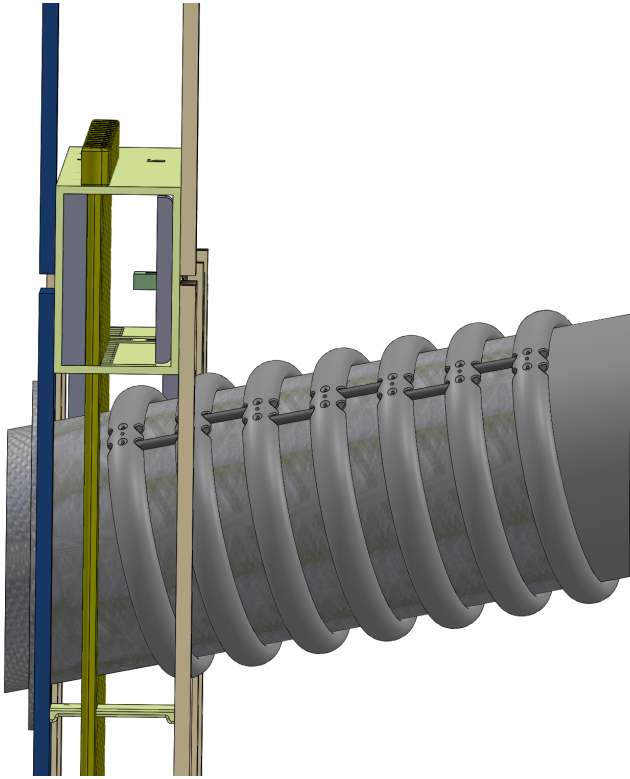


Figure 2.30: Cutaway sideview of the beam plug to field cage interface.

fig:beam

- 1 the cathode plane must be able to provide -200 kV . The output voltage ripple must not introduce
- 2 more than 10% of the equivalent thermal noise from the front-end electronics. The power supply
- 3 must be programmable to shut down its output at a certain current limit. During power cycling,
- 4 both controlled and uncontrolled, the voltage ramp rate at the feedthrough must be limited to
- 5 prevent damage to the in-vessel electronics from excess charge injection. The HV feedthrough
- 6 must be able to withstand -250 kV in its center conductors in a 1 atm argon gas environment
- 7 when terminated in liquid argon.

8 2.5.2 HV feedthrough design, power supply and cabling

- 9 The design of the HV feedthrough as well as the procurement of the HV power supply, cables, and
- 10 possibly filter circuits, are activities being jointly pursued by the ProtoDUNE-SP and ProtoDUNE-
- 11 DP efforts. In particular:

- 12 • The Heinzinger 300-kV power supply (residual ripple less than 10^{-5}) and cable specified for
- 13 ProtoDUNE-DP are well suited for ProtoDUNE-SP, which operates at a lower HV setting.
- 14 • The present ProtoDUNE-DP HV feedthrough design is adaptable to ProtoDUNE-SP without
- 15 any major modification in its dimensions or mechanical features.
- 16 • The filtering scheme and the monitoring system required for ProtoDUNE-SP is more de-

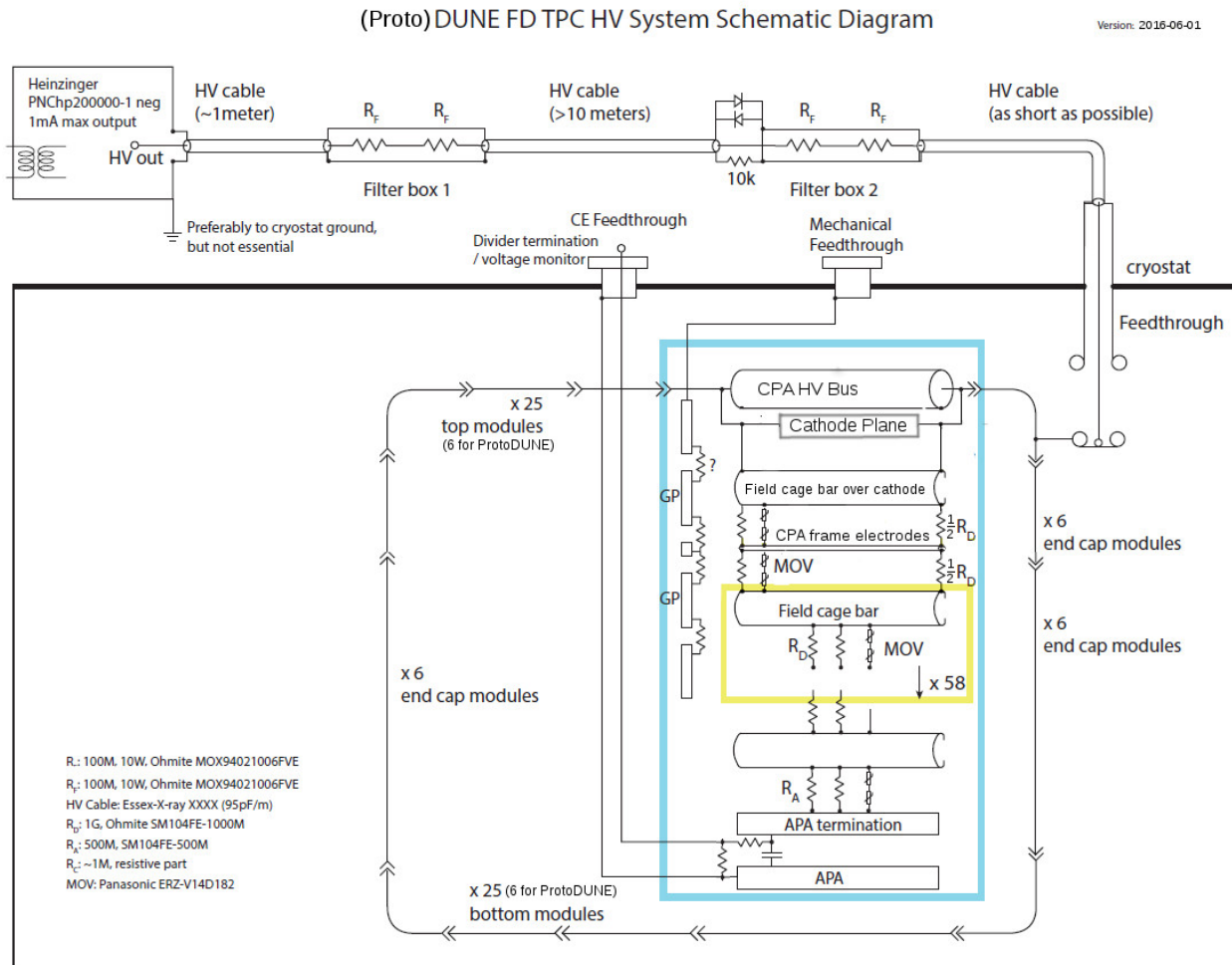


Figure 2.31: A schematic of the TPC high voltage circuit.

fig:TPCHV

1 manding than that for ProtoDUNE-DP, due to its more sensitive front-end electronics, and
 2 can be used for both detectors.

- 3 • Common spare components are also being utilized.

4 The design of the 300-kV feedthrough is based on the very successful construction technique
 5 adopted for the ICARUS HV feedthrough, which was operated at 75 kV without interruption
 6 for more than three years without any failure. The feedthrough was also successfully operated for
 7 several days as a test after the run at 150 kV. The design is based on a coaxial geometry, with an
 8 inner conductor (HV) and an outer conductor (ground) insulated by ultra-high-molecular-weight
 9 polyethylene (UHMW PE) as shown in Figure 2.32.


10 The outer conductor, made of a stainless-steel tube, surrounds the insulator, extending down
 11 through the cryostat into the LAr. In this geometry, the electric field is confined within regions
 12 occupied by high-dielectric-strength media (UHMW PE and LAr). The inner conductor is made
 13 of a thin-walled stainless steel tube to minimize the heat input and to avoid the creation of argon
 14 gas bubbles around the lower end of the feedthrough. A contact, welded at the upper end for
 15 the connection to the HV cable, and a round-shaped elastic contact for the connection to the
 16 cathode, screwed at the lower end, completes the inner electrode. Special care has been taken in
 17 the assembly to ensure complete filling of the space between the inner and outer conductors with
 18 the PE dielectric, and to guarantee leak-tightness at ultra-high vacuum levels.

19 
 Figure 2.32 is for DP not SP!

20 2.5.3 HV monitoring

21 HV-circuit monitoring devices include a toroid transformer to detect spikes and noise in the current
 22 draw, and a monitoring point at the end of the field cage resistor chain, which also provides a means
 23 to control field-shaping around the edge of the APA.

24 2.6 TPC Front-end Electronics

25 2.6.1 Scope and requirements

26 The DUNE single-phase TPC read-out electronics are referred to as the “Cold Electronics” (CE)
 27 because they reside in LAr, mounted directly on the APA, as shown in Figure 2.33, thus reducing
 28 channel capacitance and noise by minimizing the length of the connection between an anode wire
 29 and its corresponding electronics input.


30 
 Figure 2.33: APA fin is not defined

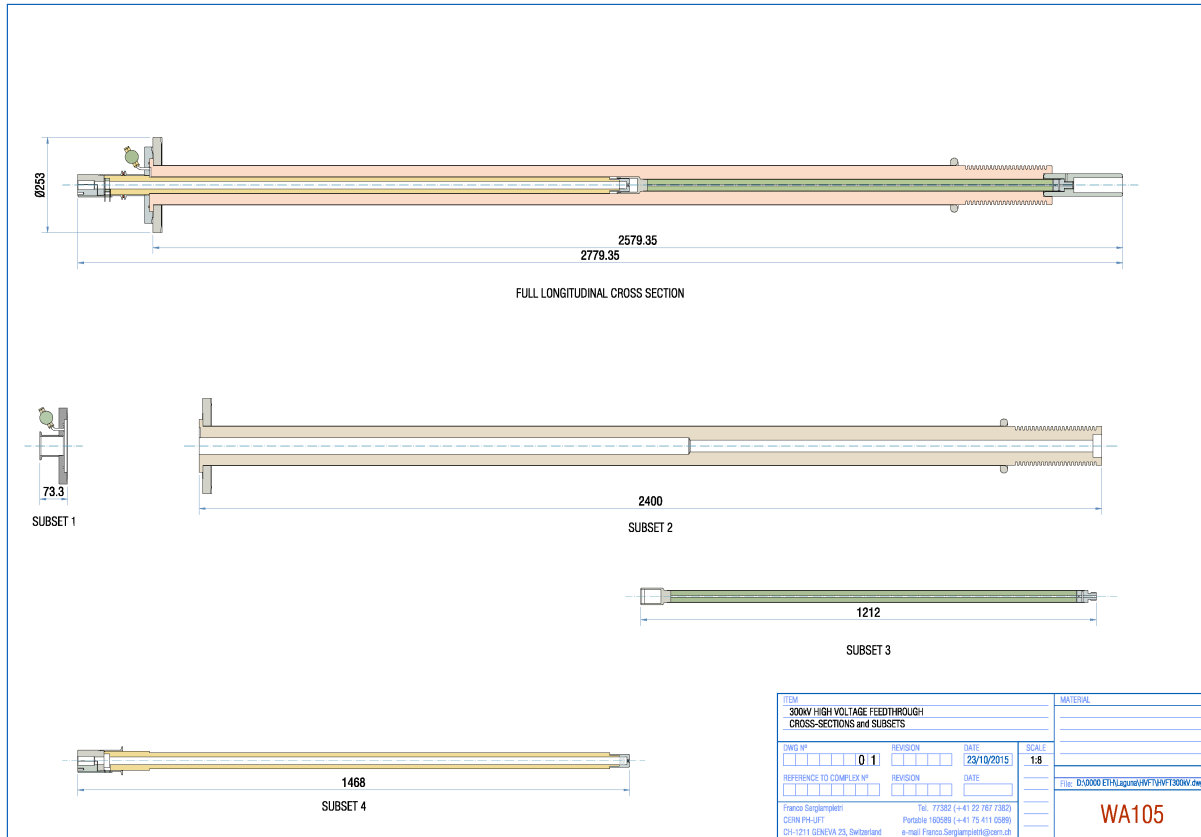


Figure 2.32: Preliminary design of the DP HV feedthrough.

fig: hv-f

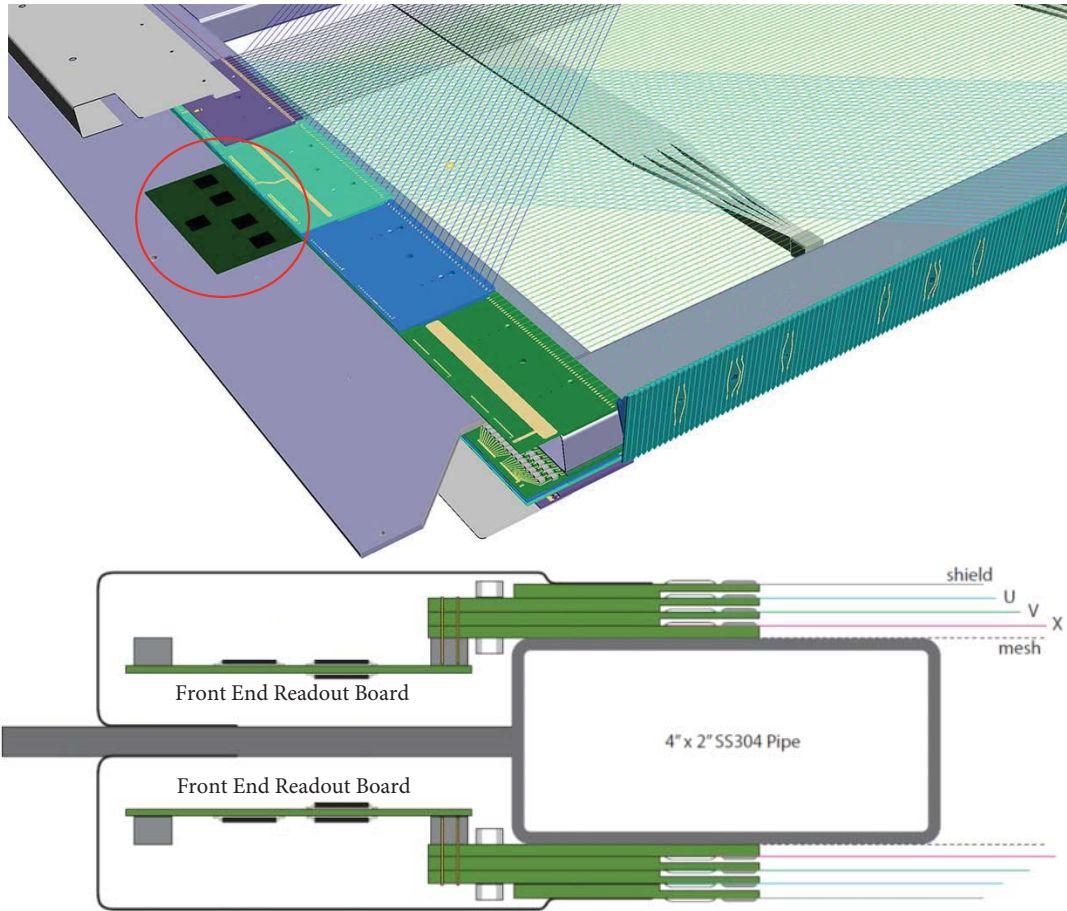


Figure 2.33: The front-end electronics as mounted on an APA. Top: The front-end electronics is shown in the red circle. Bottom: Cross section view showing the layered wire boards. Mounting hardware between the front-end electronics and the APA fin is not shown.

fig:tpcc

- 1 The CE signal processing is implemented in ASIC chips using CMOS technology, which has been
 2 demonstrated to perform well at cryogenic temperatures, and includes amplification, shaping,
 3 digitization, buffering, and multiplexing (MUX) of the signals. The CE is continuously read out,
 4 resulting in a digitized ADC sample from each APA channel (wire) up to every 500 ns (2-MHz
 5 maximum sampling rate).
- 6 The 2,560 channels from each APA are read out by 20 Front-End Motherboards (FEMBs), each
 7 providing digitized wire read-out from 128 channels. One cable bundle connects each FEMB to
 8 the outside of the cryostat via a feedthrough (a *CE feedthrough*) in the signal cable flange at the
 9 top of the cryostat, where a single flange services each APA, as shown in Figure 2.34. Each cable
 10 bundle contains wires for low-voltage (LV) power, high-speed data readout, and clock/digital-
 11 control signal distribution. Eight separate cables carry the TPC wire-bias voltages from the signal
 12 flange to the APA wire-bias boards, as shown schematically in Figure 2.35.
fig:tpcce_apa_flange
fig:tpcce_cr_board

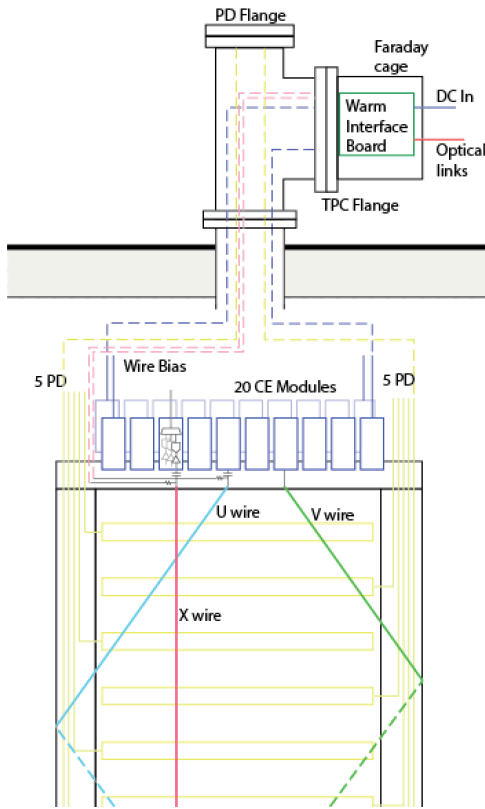


Figure 2.34: Connections between the signal flange and APA.

fig:tpcc

- 13 The components of the CE system are the
- 14 • Front-end mother boards (FEMBs), which house the cold ASICs and are installed on the
 15 APAs;
- 16 • Cables for the data, clock/control signals, LV power, and wire-bias voltages between the
 17 APA and the signal flanges (cold cables);
- 18 • Signal flanges with a CE feedthrough to pass the data, clock/control signals, LV power, and

1 APA wire-bias voltages between the inside and outside of the cryostat;

- 2 • Warm electronics crates (WECs) that are mounted on the signal flanges and contain the
3 warm interface boards (WIBs) and Power and timing cards (PTCs) for further processing
4 and distribution of the signals entering/exiting the cryostat;
- 5 • Fiber cables for transmitting data and clock/control signals between the WECs and the data
6 acquisition (DAQ) and slow control systems;
- 7 • Cables for LV power and wire-bias voltages between the signal flange and external power
8 supplies (warm cables); and
- 9 • LV power supplies for the CE and bias-voltage power supplies for the APAs.

10 The electrical cables for each APA enter the cryostat through a single signal flange, creating
11 an integrated unit that provides local diagnostics for noise and validation testing, and follows
12 the grounding guidelines in Section 2.6.2. The components, the quantity of each required for
13 ProtoDUNE-SP, and the number of channels that each component has, are listed in Table 2.6. tab:ce-components

Table 2.6: Electronics components and quantities

Element	Quantity	Channels per element
TPC	1	15,360
APA	6	2,560
Front-End Mother Board (FEMB)	120, 20 per APA	128
FE ASIC chip	120 × 8, 8 per FEMB	16
ADC ASIC chip	120 × 8, 8 per FEMB	16
FEMB FPGA	120, 1 per FEMB	128
Cold cable bundles	120, 1 per FEMB	128
Signal flange	6, 1 per APA	128 × 20 (i.e., 2,560)
CE feedthrough	6, 1 per APA	128 × 20
Warm interface boards (WIB)	30, 5 per APA	(128 × 20) /5 (i.e., 512)
Warm electronics crates (WEC)	6, 1 per APA	128 × 20
Power and timing cards (PTC)	6, 1 per APA	128 × 20
Passive backplane (PTB)	2	??
MPOD power supplies (chassis???)	2, 1 per 3 APAs	15,360 /2

14 tab:ce-components
check Table 2.6 ; there are some missing numbers

15 The most significant requirements for the CE are listed here. The CE shall:

- 16 • Provide the means to read out the TPC wires and transmit their data in a useful format to
17 the DAQ.
- 18 • Operate for the life of the facility without significant loss of function.

- 1 • Record the channel waveforms continuously without dead time.
- 2 • Be constructed only from materials that are compatible with high-purity LAr.
- 3 • Provide sufficient precision and range in the digitization to:
 - 4 – Discriminate electrons from photon conversions;
 - 5 – Optimize the reconstruction of high- and low-energy tracks from accelerator-neutrino interactions;
 - 6 – Distinguish a Minimum Ionizing Particle (MIP) from noise with a signal-to-noise ratio > 9:1;
 - 7 – Measure ionization up to 15 times that of a MIP particle, so that stopping kaons from proton decay can be identified.
- 8 • Ensure that all power supplies have:
 - 9 – Local monitoring and control;
 - 10 – Remote monitoring and control through DAQ; and
 - 11 – Over-current and over-voltage protection circuits.
- 12 • Ensure that the CE feedthroughs are able to withstand twice their nominal operating voltages with a maximum specified leakage current in 1-atm argon gas.

2.6.2 Grounding and shielding

- 17
- 18 To avoid structural ground loops, the APA frames described in Section 2.2.4 are insulated from
 19 each other. Each frame is electrically connected to the cryostat at a single point on the CE
 20 feedthrough board in the signal flange where the cables exit the cryostat. Mechanical suspension
 21 of the APAs is accomplished using insulated supports.
- subsec:apa_frame
- 22 The analog portion of the FEMB contains eight front-end (FE) ASICs configured as 16-channel
 23 digitizing charge amplifiers. Input amplifiers on the ASICs have their Common terminals connected
 24 to the APA frame. All power-return leads and cable shields are connected to both the Common
 25 plane of the FEMB and to the signal flange.
- 26 Filtering circuits for the APA wire-bias voltages are locally referenced to the Common plane of
 27 the FEMBs through low-impedance electrical connections. This approach ensures a ground-return
 28 path in close proximity to the bias-voltage and signal paths. The close proximity of the current
 29 paths minimizes the size of potential loops to further suppress noise pickup.

1 what's the Common plane? not defined. And why is "Common" capitalized (twice)?

2 Photon detector signals, described in Section 2.7, are carried directly on shielded, twisted-pair
 3 cables to the signal flange. The cable shields are connected to the cryostat at a second feedthrough,
 4 the PDS feedthrough, and to the PCB shield layer on the photon detectors. There is no electrical
 5 connection between the cable shields and the APA frame except at the signal flange.

6 **2.6.3 Distribution of APA wire-bias voltages**

7 Each side of an APA includes four wire layers as described in Section 2.2.2. The innermost X-plane
 8 layer of wires is nominally biased at +820 Volts, with each wire AC coupled to one of the 128 charge
 9 amplifier circuits on the FEMB. The V-plane wire layer is effectively biased at zero volts, with each
 10 wire directly connected to one of the charge amplifier circuits. The U-plane wire layer is nominally
 11 biased at -370 Volts with each wire AC-coupled to one of the 128 charge amplifier circuits. The
 12 outermost G-plane wire layer, which has no connection to the charge amplifier circuits, is biased
 13 at -665 Volts.

14 Electrons passing through the wire grid must drift unimpeded until they reach the X-plane col-
 15 lection layer. The nominal bias voltages are predicted to result in this electrically transparent
 16 configuration.

17 As described in Section 2.2.5 the filtering of wire-bias voltages and AC coupling of wire signals
 18 passing onto the charge amplifier circuits is done on Capacitance-Resistance (CR) boards that plug
 19 inbetween the APA wire-board stacks and FEMBs. Each CR board includes single R-C filters for
 20 the X- and U-plane wire-bias voltages. In addition, each board has 48 pairs of bias resistors and AC
 21 coupling capacitors for X-plane wires, and 40 pairs for the U-plane wires. The coupling capacitors
 22 block DC while passing AC signals to the CE motherboards.

23 Separate CR boards include a single R-C filter for the G-plane wires and 12 pairs of bias resistors
 24 and coupling capacitors. Groups of four wires are tied together to share single bias resistors and
 25 filter capacitors. These CR boards do not connect to the charge amplifier circuits on the FEMB.

26 The amplifier circuits have input impedance of 50Ω using 22-nF coupling capacitors. Clamping
 27 diodes limit the input voltage received at the amplifier circuits to between zero and +1.8 Volts.

28 Coupling capacitors for the X-plane and U-plane wires are required to block DC bias voltages.
 29 However they also impact the efficiency of the detector circuits. The sense wires are expected to
 30 have 200 pF of capacitance to the APA frame. Induced or collected charges are effectively divided
 31 between the wire capacitance and the coupling capacitor. To achieve a charge-calibration accuracy
 32 of 0.5 percent or better, the coupling capacitors must be 4.7 nF at ten percent tolerance, or 2.2 nF
 33 at five percent tolerance. Voltage ratings should be at least 1.5 times the expected operating
 34 voltages.

35 Bias resistance values should be at least $20\text{ M}\Omega$ to maintain negligible noise contributions. A

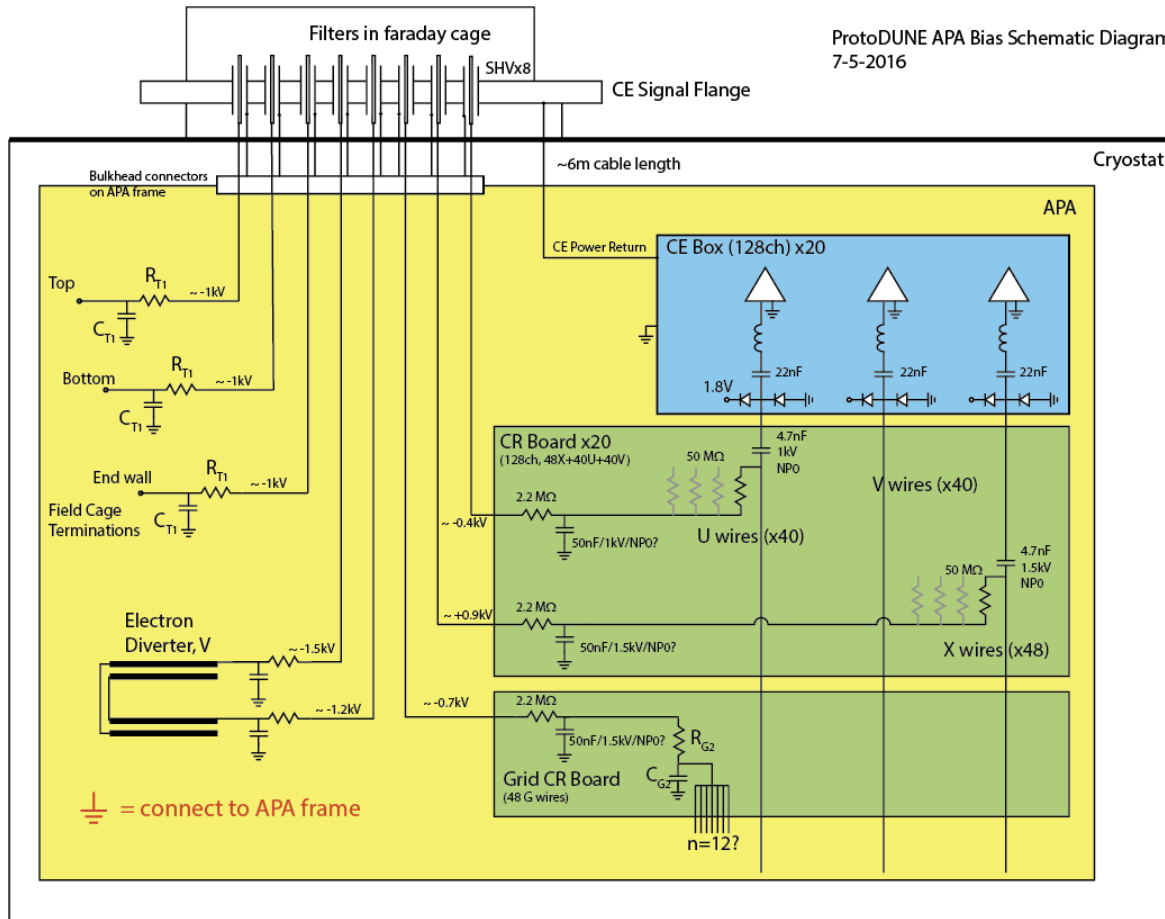


Figure 2.35: APA wire bias schematic diagram, including the Capacitance-Resistance (CR) board.

fig:tpcc

¹ target value of $50\text{ M}\Omega$ is desired. The higher value helps to achieve a longer time constant for the
² high-pass coupling networks. Time constants should be at least 25 times the electron drift time so
³ that the undershoot in the digitized waveform is small and easily correctable. However, leakage
⁴ currents can develop on PC boards that are exposed to high voltages over extended periods. If the
⁵ bias resistors are much greater than $50\text{ M}\Omega$, leakage currents may affect the bias voltages applied
⁶ to the wires.

⁷ The bias-voltage filters are R-C low-pass networks. Resistance values should be much smaller than
⁸ the bias resistances to control crosstalk between wires and limit the voltage drop if any of the wires
⁹ becomes shorted to the APA frame. A value around $2.2\text{ M}\Omega$ is desired. Smaller values may be
¹⁰ considered although a larger filter capacitor would be required to maintain a given level of noise
¹¹ reduction. A target value of 47 nF has been established for the filter capacitors.

¹² For the grid-plane bias filters, component values are less critical. If possible they will be identical
¹³ to those used for the bias resistors and coupling capacitors ($50\text{ M}\Omega$ and 2.2 to 4.7 nF).

¹⁴ 2.6.4 Front-End Mother Board

¹⁵ The main component of the CE architecture, illustrated in Figure 2.39, is the 128-channel FEMB,
¹⁶ which itself consists of an analog motherboard and an attached FPGA mezzanine card for processing
¹⁷ the digital outputs. Each APA is instrumented with 20 FEMBs, for a total of 2,560 channels
¹⁸ per APA. The FEMBs plug directly into the APA CR boards, making the connections from the U-
¹⁹ and V-plane induction wires and X-plane collection wires to the charge amplifier circuits as short
²⁰ as possible.

²¹ The analog mother board is instrumented with eight 16-channel FE ASICs, eight 16-channel ADC
²² ASICs, LV power regulators, and input-signal protection circuits. The 16-channel FE ASIC provides
²³ amplification and pulse shaping. The 16-channel ADC ASIC comprises 12-bit digitizers
²⁴ performant at speeds up to 2 MS/s, local buffering, and an 8:1 MUX stage with two pairs of serial
²⁵ readout lines in parallel.

²⁶ (Figure 2.40). Each FE ASIC channel has a charge amplifier circuit with a gain selectable from
²⁷ one of 4.7, 7.8, 14 and 25 mV/fC (full scale charge of 55, 100, 180 and 300 fC), a high-order
²⁸ anti-aliasing filter with adjustable time constant (peaking time 0.5, 1, 2, and 3 μs), an option to
²⁹ enable AC coupling, and a baseline adjustment for operation with either the collecting (200 mV)
³⁰ or the non-collecting (900 mV) wires. Shared among the 16 channels in the FE ASIC are the bias
³¹ circuits, programming registers, a temperature monitor, an analog buffer for signal monitoring,
³² and the digital interface. The estimated power dissipation of FE ASIC is about 6 mW per channel
³³ at 1.8 V supply.

³⁴ The FE ASIC layout is shown in Figure 2.38. The ASIC was implemented using the commercial
³⁵ CMOS process ($0.18\text{ }\mu\text{m}$ and 1.8 V), which is expected to be available for at least another
³⁶ 10 years. The charge amplifier input MOSFET is a p-channel biased at 2 mA with a L/W (channel
³⁷ length/width) ratio of $0.27\text{ }\mu\text{m} / 10\text{ }\mu\text{m}$, followed by dual cascade stages. The charge amplification
³⁸ and shaping filter have digitally programmable gain and peaking time (as specified in Section 2.6.4).

^{subsec:fe_arch}

- 1 Each channel also implements a high-performance output driver, which can be used to drive a long
 2 cable, but is disabled when interfaced to an ADC ASIC to reduce the power consumption. The
 3 ASIC integrates a band-gap reference (BGR) to generate all the internal bias voltages and cur-
 4 rents. This guarantees a high stability of the operating point over a wide range of temperatures,
 5 including cryogenic. The ASIC is packaged in a commercial, fully encapsulated plastic QFP 80
 6 package.
- 7 Prototypes have been evaluated and characterized at RT (300 K) and LN2 (77 K) temperature.
 8 During testing the circuits have been cycled multiple times between the two temperatures and
 9 operated without any change in performance. Figure 2.36 shows the measured pulse response,
 10 both as a function of temperature and the programmable settings of the chip. These results are
 11 in close agreement with simulations and indicate that both the analog and the digital circuits and
 12 interface operate as expected in a cryogenic environment.

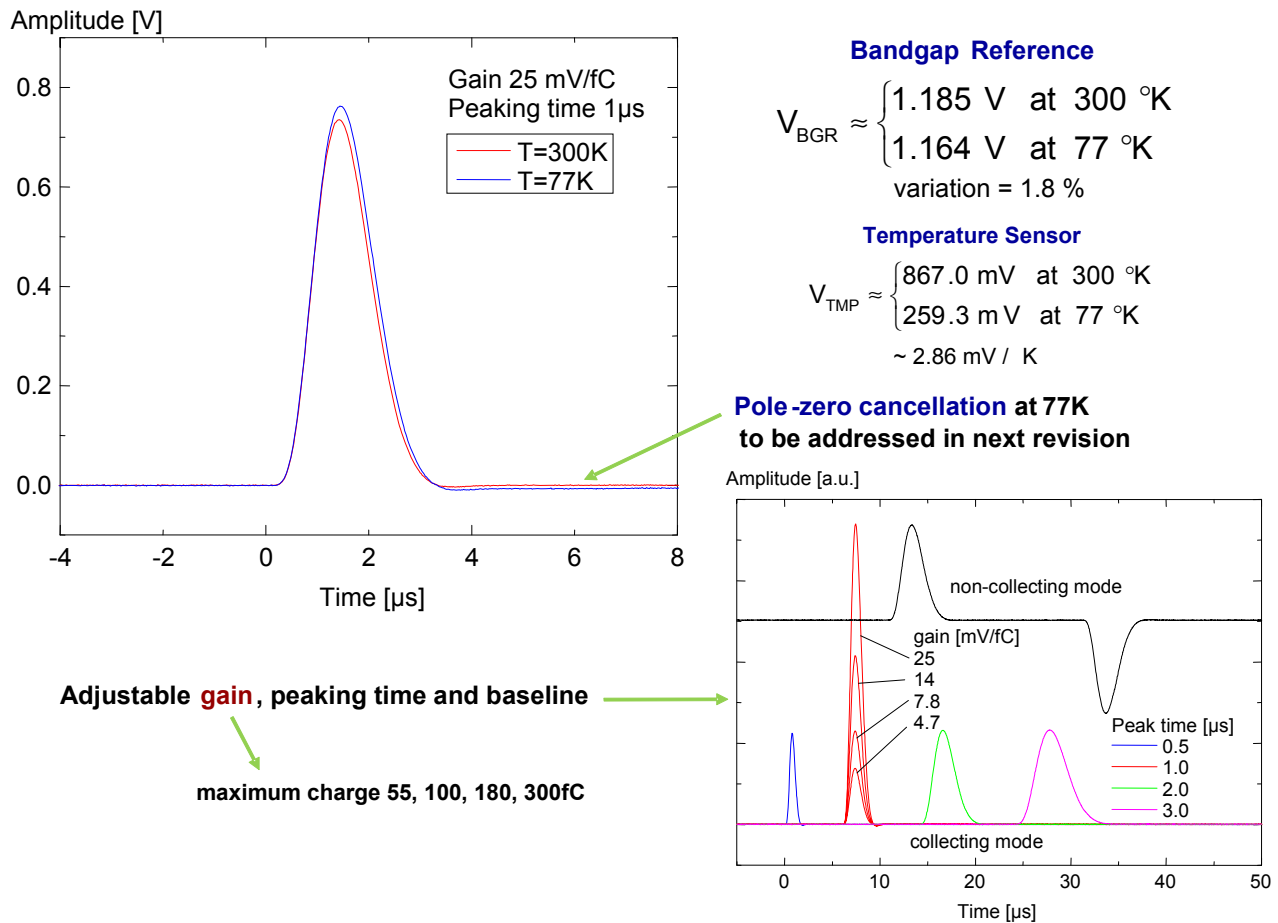


Figure 2.36: Measured pulse response with details on gain, peaking time and baseline adjustments

- 13 Figure 2.37 shows the measured Equivalent Noise Charge (ENC) versus filter-time constant (peak-
 14 ing time) for two different gains, where ENC is the value of charge (in electrons) injected across
 15 the detector capacitance that would produce at the output of the shaping amplifier a signal whose
 16 amplitude equals the output R.M.S. noise. These measurements were made with prototype FEMBs

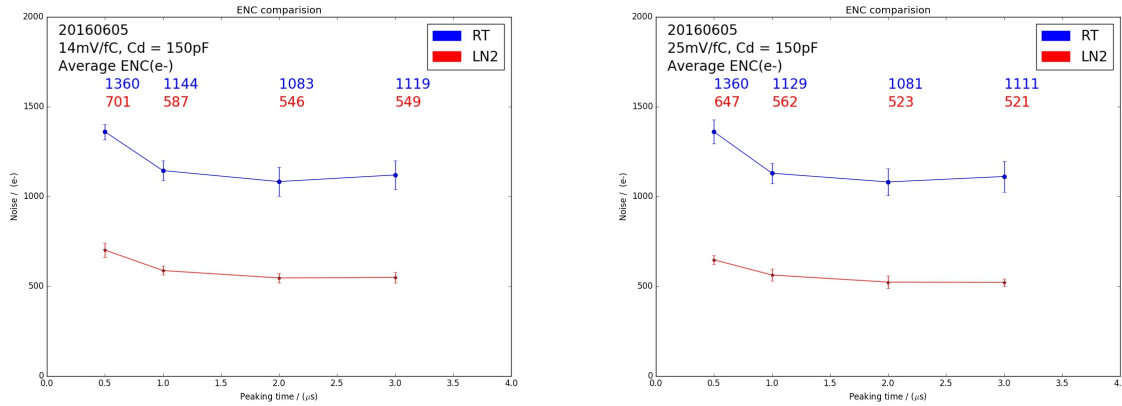


Figure 2.37: Measured ENC vs filter time constant from the latest prototype version of the FEMB for two different gains, 14 mV/fC and 25 mV/fC. RT = room temperature and LN2 = liquid nitrogen

fig:tpcc

1 at both RT and submerged in LN2 with a wire-simulating input capacitance of $C_f = 150 \text{ pF}$. In
 2 LN2, for peaking times $> 1 \mu\text{s}$, less than 600 e^- was measured. For comparison, a MIP travelling
 3 perpendicularly to the wire plane in the direction of wire spacing is expected to deposit $\sim 10,000 \text{ e}^-$
 4 on the collection wires, for a worst-case S:N $\sim 16:1$.

5 Each channel is equipped with an injection capacitor which can be used for test and calibration
 6 and can be enabled or disabled through a dedicated register. The injection capacitance has been
 7 measured using a calibrated external capacitor. The measurements show that the calibration
 8 capacitance is extremely stable, changing from 184 fF at RT to 183 fF at 77 K. This result and the
 9 measured stability of the peaking time demonstrate the high stability of the passive components
 10 as a function of temperature. Channel-to-channel and chip-to-chip variation in the calibration
 11 capacitor are typically less than 1%.

12 The ADC ASIC design is also implemented using the CMOS process ($0.18 \mu\text{m}$ and 1.8V). The
 13 layout of the ADC ASIC is shown in Figure 2.38. The ADC ASIC is a complex design with
 14 320,000 transistors, while the FE ASIC has 16,000. The transistor design work has been done
 15 following the rules for long cryo-lifetime. Shared among the 16 channels in the ADC ASIC are the
 16 bias circuits, programming registers, an 8:1 MUX, and the digital interface. The estimated power
 17 dissipation of FE ASIC is below 5 mW per channel at 1.8 V supply.

18 The ADC ASIC has an input buffer with offset compensation to match the output of the FE ASIC.
 19 The input buffer first samples the input signal (with a range of 0.2 V to 1.6 V), then provides a
 20 current output after compensating for offset voltage error. This current output is then supplied
 21 to the ADC which converts the input to digital in two phases. The MSB (Most Significant Bit)
 22 6 bits are first determined followed by the LSB (Least Significant Bit) 6 bits. After the conversion
 23 the thermometer code is converted to binary and latched. The output of ADC channel 16 can be
 24 monitored externally. The data from the 16 ADCs are transferred in parallel to the FIFO block.
 25 The built-in FIFO is 32 bits wide and 192 bits long, and has full and empty indicator flags, needed
 26 for interfacing to the FPGA. The ADC along with the input buffers are biased internally using a
 27 bias generator and a bandgap voltage reference. The bandgap voltage (VBGR) can be monitored
 28 and/or controlled externally. It can be put in the low-power sleep mode, and woken up in less

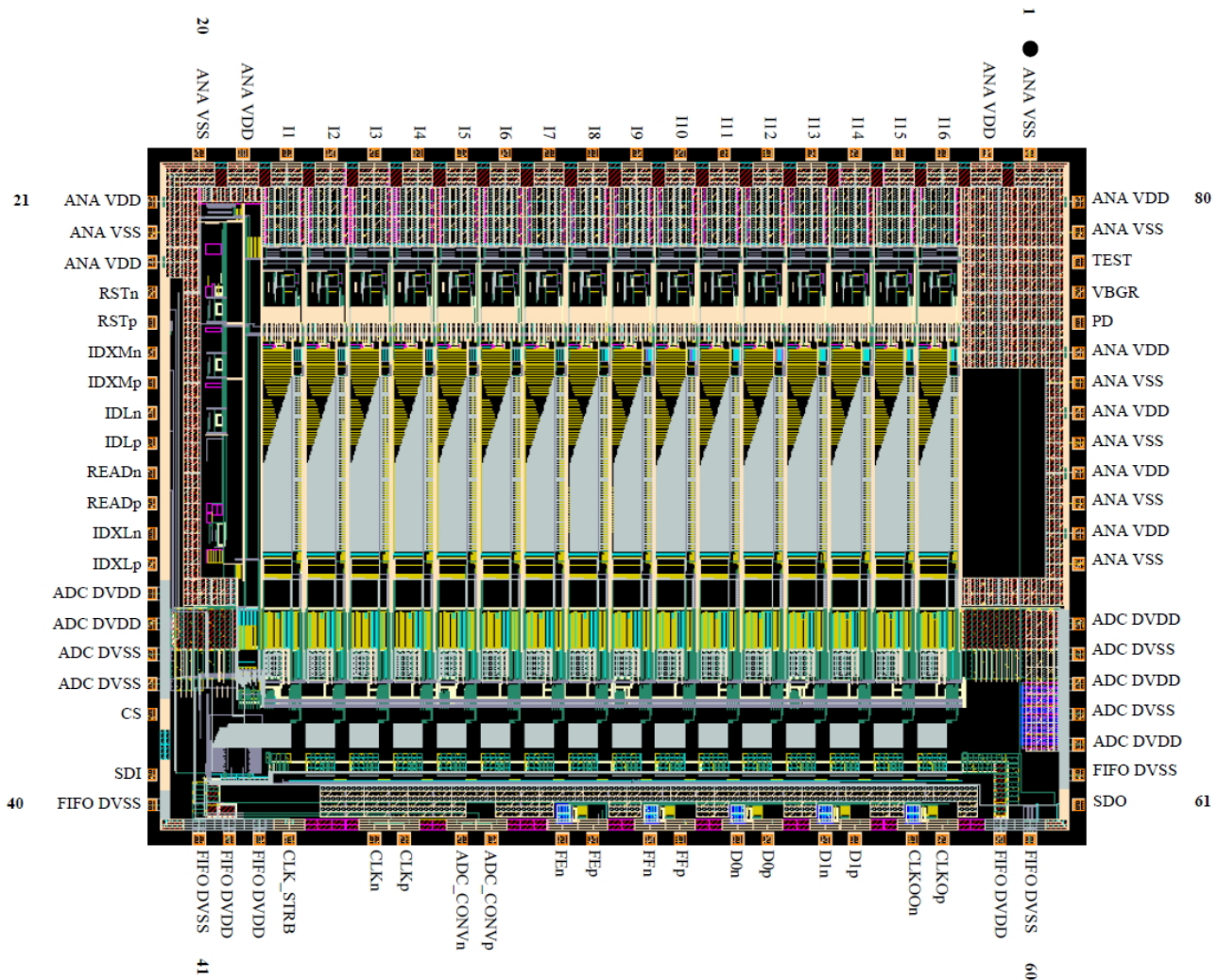


Figure 2.38: The layout of the 16-channel ADC ASIC

fig:tpc

¹ than 1 μ s.

² Prototypes have been evaluated and characterized at RT (300 K) and LN2 (77 K) temperature.
³ During these tests the circuits have been temperature-cycled multiple times. The effective resolution
⁴ with reference to the input referred noise is \sim 11.6 bits at both 300 K and 77 K. The differential
⁵ non-linearity (DNL) is less than 4 LSBs for 99% of ADC bins at both 300 K and 77 K.

⁶ The ADC outputs are passed to the FPGA mezzanine board for transmission to the warm elec-
⁷ tronics located on the outside of the signal flange. The FPGA has four 4:1 MUX circuits that
⁸ combine the 16 serial lines from the eight ADC channels into four serial lines of 32 channels each,
⁹ and four \sim 1.2 Gigabit-per-second (Gbps) serial drivers that drive the data in each line over cold
¹⁰ cables to the WIBs.

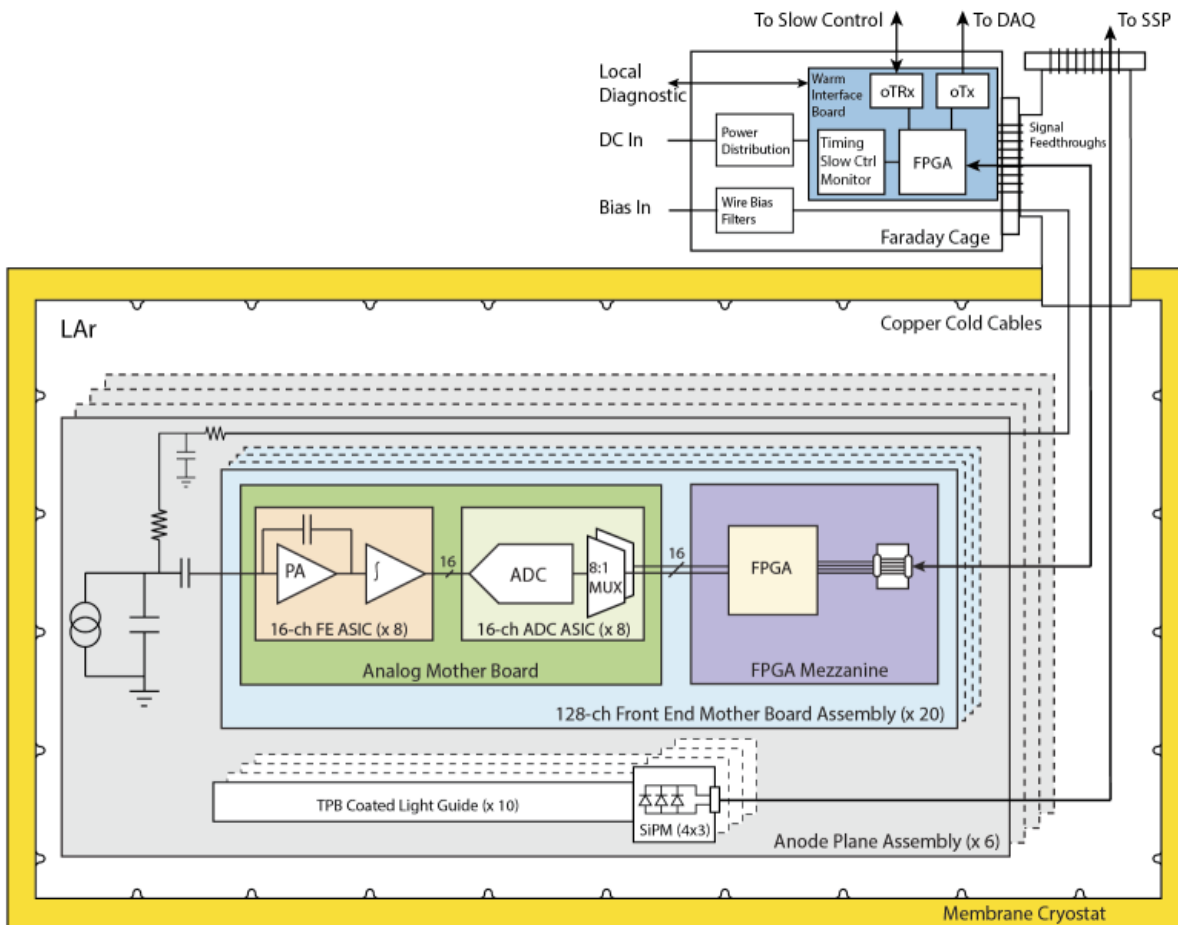


Figure 2.39: The CE Architecture. The basic unit is the 128-channel FEMB.

¹¹ The data are passed through the signal flange to the WIBs on copper cables utilizing LV differential
¹² signaling (LVDS). On the WIBs, the data is further MUXed by 4:1 and transmitted over optical
¹³ fibers to the DAQ system described in Section 2.9.9. sec:DAQ_online_interface

¹⁴ The FPGA on the mezzanine card is also responsible for communicating with the DAQ and timing
¹⁵ systems and providing the clock and control signals required by the FE and ADC ASICS.



Figure 2.40: The Front End Mother Board (FEMB), as used in the early set of tests. **Top:** The analog mother board, showing four ADC ASICs and four FE ASICs surface mounted. The other side of the board has another four ADC and FE ASICs. Except for anticipated small modifications, this board is essentially the final version. **Middle:** The FPGA mezzanine, used in place of the digital ASIC mezzanine for the early set of tests. **Bottom:** The complete FEMB assembly as used in the early set of tests. The cable shown in the high-speed data, clock, and control cable.

fig:tpcc

- 1 Each FEMB is enclosed in a Faraday box to provide shielding from noise. As shown in Figure 2.41,
 2 the Faraday box is designed to make the electrical connection between the FEMB and the APA
 3 frame. Mounting hardware inside the Faraday box connects the common plane of the FEMB to
 4 the box casing. The box casing is electrically connected to the APA frame via twisted conducting
 5 wire (not shown in Figure 2.41). This is the only point of contact between the FEMB and APA,
 6 except for the input amplifier circuits connected to the CR board, which also terminate to ground
 7 at the APA frame, as shown in Figure 2.35.

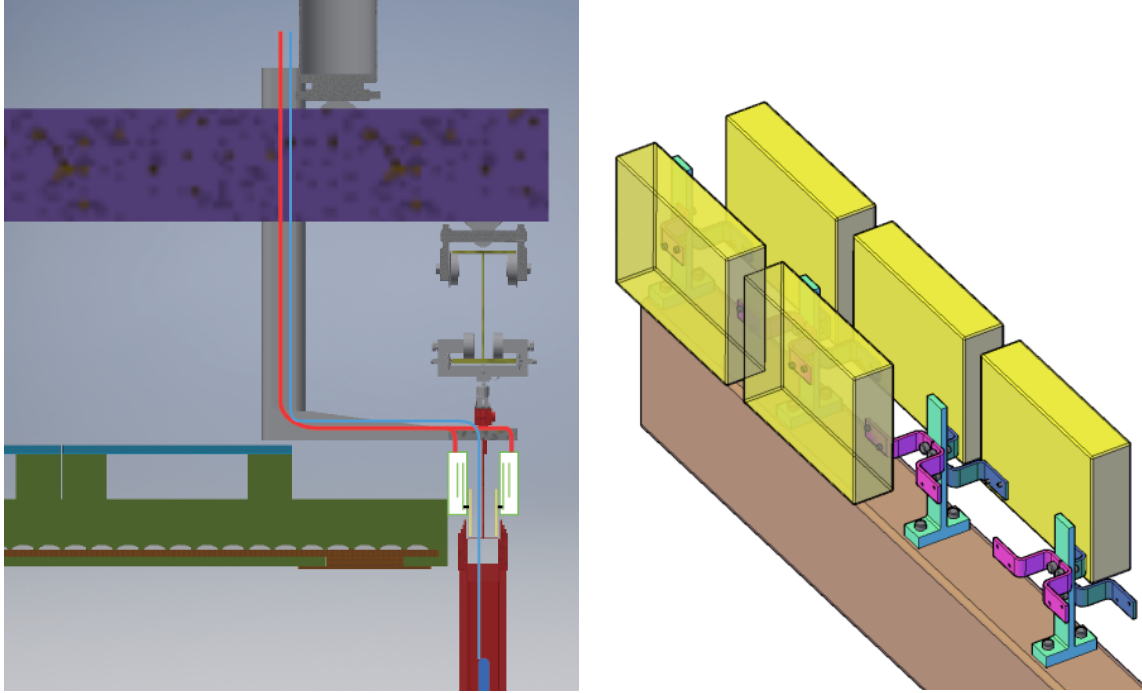


Figure 2.41: Faraday box for the FEMB.

fig:tpcce_box

2.6.5 CE feedthroughs and cold cables

- 8 **CE feedthroughs and cold cables**
- 9 All cold cables originating from inside the cryostat connect to the outside warm electronics through
 10 PCB board feedthroughs installed in the signal flanges that are distributed along the cryostat roof
 11 (Figure 2.42). The TPC data rate per APA, with an overall 32:1 MUX and 80 ~1 Gbps data
 12 channels per APA, is sufficiently low that the signals can be driven over copper LVDS transmission
 13 lines. Additional LVDS transmission lines are available for the distribution of clock signals and
 14 control information, which are transmitted at a lower bit rate. Optical fiber is employed externally
 15 from the WIBs on the signal flange to the DAQ and slow control systems.
- 16 The current design of the signal flange includes a T-shaped pipe, separate PCB feedthroughs
 17 for the CE and PDS cables, and an attached crate for the TPC warm electronics, as shown in
 18 Figure 2.43. The wire-bias voltage cables connect to standard SHV (safe high voltage) connectors
 19 machined directly into the CE feedthrough, ensuring no electrical connection between the wire-
 20 bias voltages and other signals passing through the signal flange. Each CE feedthrough serves the
 21 bias/power/digital IO needs of one APA, as shown in Figure 2.44.

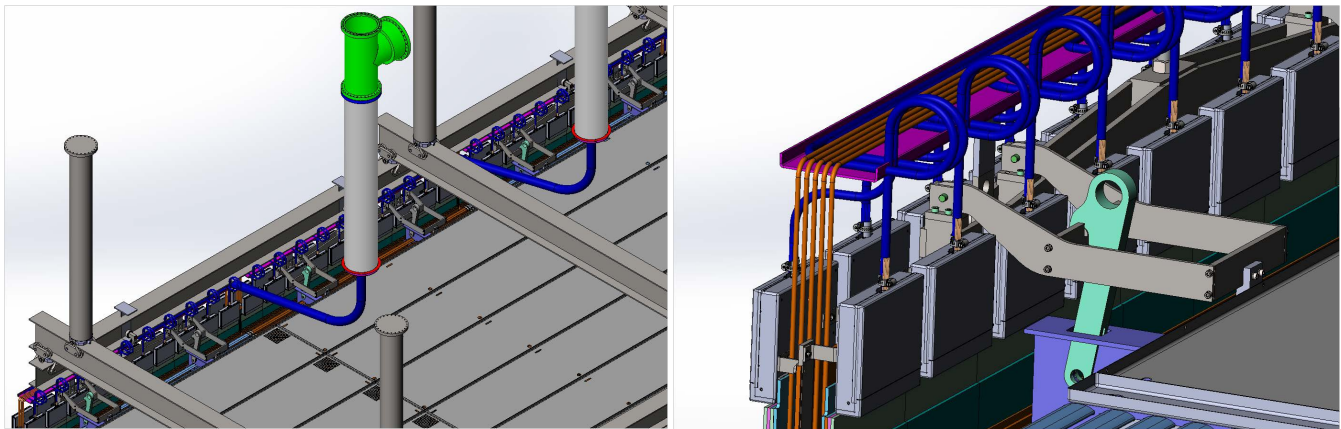


Figure 2.42: The CE feedthrough configuration and internal cable routing. The left panel shows a cutaway view of the cryostat. The right panel shows more detail at the Faraday boxes.

fig:tpcc

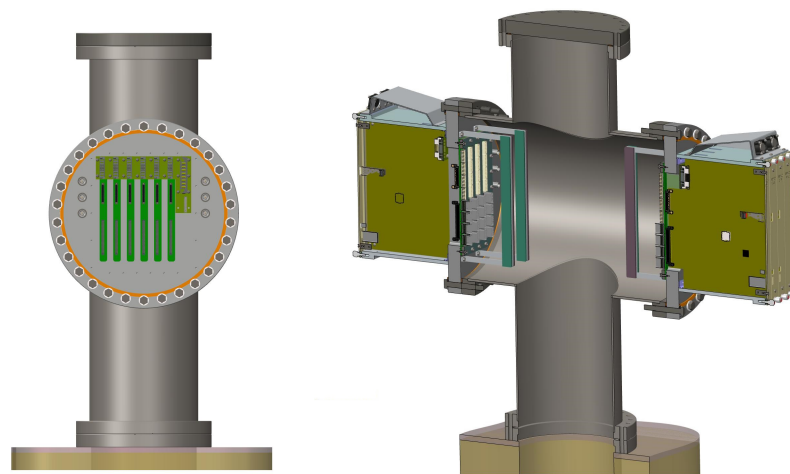


Figure 2.43: TPC CE feedthrough. The WIBs are seen edge-on in the left panel, and in an oblique side-view in the right panel, which also shows the warm crate for a DUNE module in a cutaway view (for ProtoDUNE-SP, there is a crate only on one side).

fig:tpcc

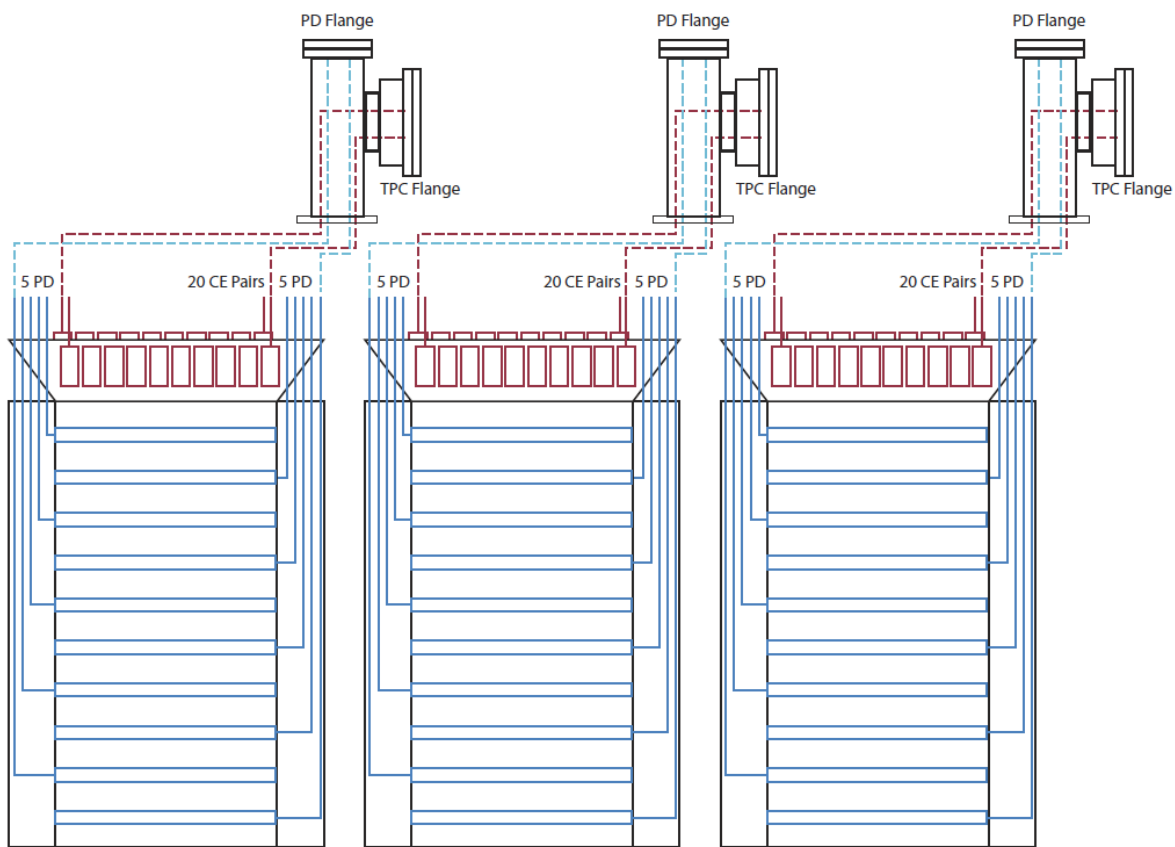


Figure 2.44: TPC cable routing scheme for three APA section.

fig:tpcc

¹ A program for minimizing potential contamination of the LAr from the cable plant contained
² within the ullage (the warmer gas phase at the top of the cryostat) is being carefully followed.

³ Data/control cable bundles are used to send system clock and control signals from the signal
⁴ flange to the FEMB, stream the ~ 1 Gbps high-speed data from the FEMB to the signal flange,
⁵ and provide backup JTAG programming to the cold FPGA, in case the power-up programming
⁶ from the onboard EEPROM fails. As described in Section ^{subsec:ce_intro} 2.6.1, each FEMB connects to a signal
⁷ flange via one data cable bundle, leading to 20 bundles between one APA and one flange. Each
⁸ data bundle contains 12 low-skew copper twin-axial cables with a drain wire, to transmit the
⁹ following differential signals:

- ¹⁰ • 4×1.2 Gbps high-speed data
- ¹¹ • One 50 MHz system clock
- ¹² • One 2 MHz CONVERT clock
- ¹³ • 2 I2C control and configure
- ¹⁴ • 4 single-ended JTAG programming for the FPGA

¹⁵ The selected cables are Samtec 26 AWG twin-axial bundles with Samtec HSEC08 connectors to
¹⁶ both the FEMB mezzanine board and the signal flange. The HSEC08 connectors lock into place
¹⁷ with tabs on each side of the connector. A sample of the Samtec cable with THV outer jacket has
¹⁸ passed outgassing tests in the LAr Materials Test Stand at Fermilab.

¹⁹ The Samtec 26 AWG cable has been tested and demonstrated to have low enough dispersion such
²⁰ that both the LVDS 50 MHz system clock and ~ 1 Gbps high-speed data can be recovered over
²¹ 25 meters of RT cable, significantly longer than the required seven meters needed to run cables
²² between the FEMBs and signal flanges.

²³ ^{fig:tpcce_samtec_results} Figure 2.45 shows results from the cable validation testing. The eye diagrams show the edges of
²⁴ the differential signals after LVDS transmission over the specified cable types and lengths. The
²⁵ height of eye diagram shows the size of the recovered signal in mV and the slope of the rising and
²⁶ falling edges are jitter in picoseconds (ps). An eye diagram is sufficient to show that the edges of
²⁷ the differential signals can be recovered, but not enough to demonstrate the bit error rate (BER).
²⁸ However, the Samtec 26 AWG cable has also passed a BER test, transmitting 10^{13} bits without
²⁹ error.

³⁰ LV power is passed from the signal flange to the FEMB by bundles of 16 Samtec 20 AWG twisted-
³¹ pair wires, as shown in Figure 2.44. ^{fig:tpcce_cable_routing} One IPD1 connector attaches all 16 wires at the signal flange,
³² and two IPD1 connectors are attached to the FEMB (one to the analog motherboard and one to
³³ the FPGA mezzanine). In total, 20 wire bundles bring LV power to the FEMBs associated with
³⁴ one APA.

³⁵ Eight of the 16 wires are power feeds, as described in Figure 2.46. ^{fig:tpcce_lv_req} The other eight wires are
³⁶ attached to the common of the input amplifier circuits, as described in Section 2.6.3. For a single
^{subsec:ce_wire_bias}

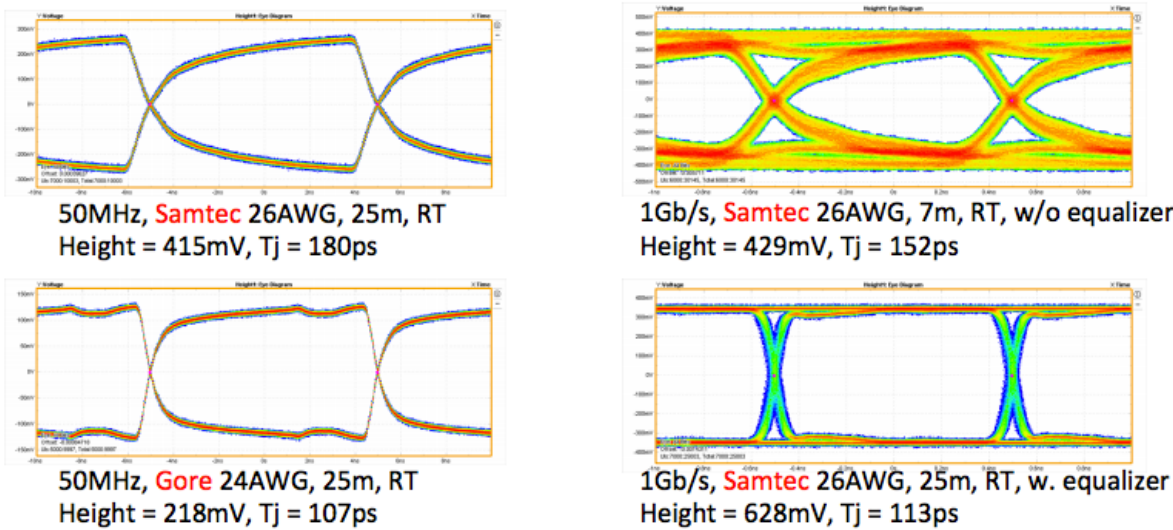


Figure 2.45: Eye diagrams from cable validation testing. **Top Left:** 50 MHz system clock over 25 m RT (RT) Samtec 26AWG cable. For comparison, **Bottom Left** shows the same clock over the heavier, prohibitively expensive Gore 24AWG cable. **Top Right:** 1 Gbps data over 7 m (ProtoDUNE length) RT Samtec 26AWG cable without active recovery by equalizers. **Bottom Right** 1 Gbps data over 25 m (DUNE length) RT Samtec 26AWG cable with active recovery.

fig:tpcc

- ¹ FEMB, the resistance is < 30 mΩ at RT or < 10 mΩ at LAr temperature. Each APA has a copper
- ² cross-section of approximately 80 mm², with a resistance < 1.5 mΩ at RT or < 0.5 mΩ at LAr
- ³ temperature.

FEMB 7m Cable	Net Name	# of Wires	R_RT [Ω]	R_LAr [Ω]	XSection [mm ²]
Analog Mother Board	FE-ANA-IN	3	0.078	0.025	1.554
	REGR_BIAS	1	0.233	0.074	0.518
FPGA Mezzanine	P1.5V	1	0.233	0.074	0.518
	P2.8V	1	0.233	0.074	0.518
	P3.6V	1	0.233	0.074	0.518
	BIAS	1	0.233	0.074	0.518
Summary		8	0.029	0.009	4.144

Figure 2.46: Samtec LV power feed wire specifications.

fig:tpcc

- ⁴ The wire-bias voltage cables are required to deliver voltages up to a few thousand Volts and currents up to a few milliAmps.
- ⁶ The bias voltages are applied to the X-, V-, and G-plane wire layers, three field cage terminations, and an electron diverter, as shown in Figure 2.35. The voltages are supplied through eight SHV connectors mounted on the signal flange. RG-316 coaxial cables carry the voltages from the signal flange to a patch panel PCB which includes noise filtering mounted on the top end of the APA.
- ¹⁰ From there, wire-bias voltages are carried by single wires to various points on the APA frame, including the CR boards, a small PCB mounted on or near the patch panel that houses a noise filter and termination circuits for the field cage voltages, and a small mounted board near the

- ¹ electron diverter that also houses wire-bias voltage filters.

2.6.6 Warm interface electronics

- ³ The warm interface electronics are housed in warm electronics crates (WECs) attached directly to
⁴ the signal flange. The WEC shown in Figure 2.47 contains one Power and Timing Card (PTC),
⁵ up to five Warm Interface Boards (WIBs) and a passive backplane (PTB), which fans out signals
⁶ and LV power from the PTC to the WIBs.

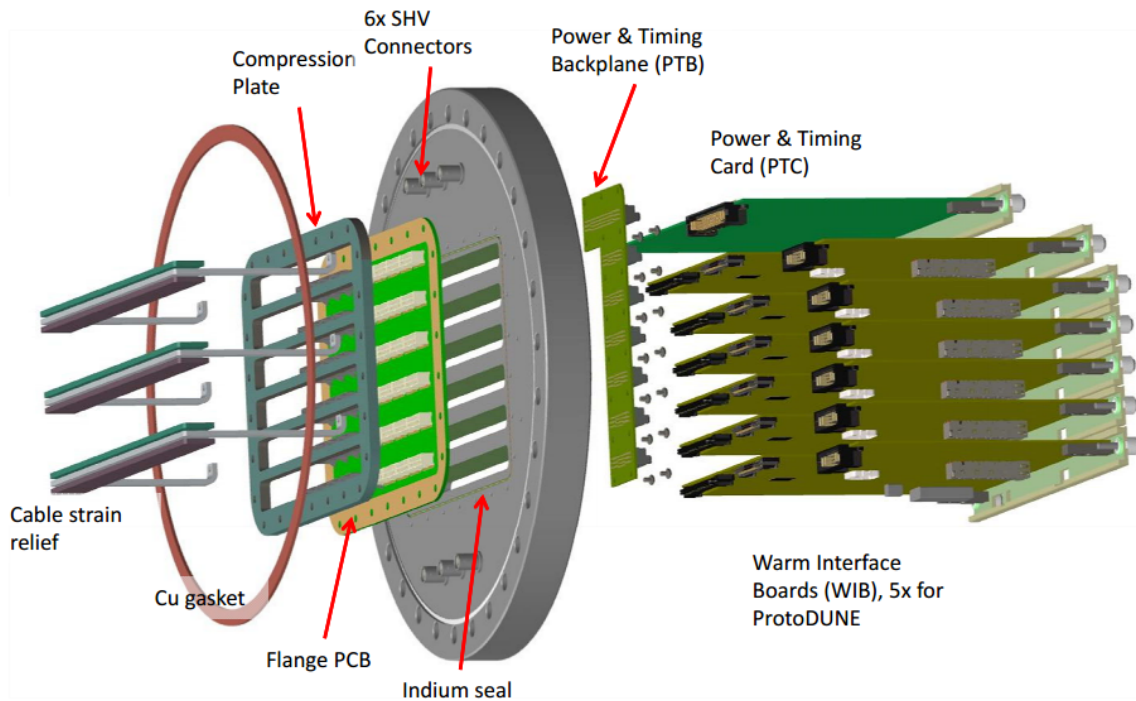


Figure 2.47: Exploded view of the signal flange for SBND (ProtoDUNE-SP has five WIBs).

- ⁷ The WIB is the interface between the DAQ system and up to four FEMBs. It receives the system
⁸ clock and control signals from the timing system and provides for processing and fan-out of those
⁹ signals to the four FEMBs. The WIB also receives the high-speed data signals from the four
¹⁰ FEMBs and transmits them to the DAQ system over optical fibers. The WIBs are attached
¹¹ directly to the TPC CE feedthrough on the signal flange. The feedthrough board is a PCB with
¹² connectors to the cold signal and LV power cables fitted between the compression plate on the cold
¹³ side, and sockets for the WIB on the warm side. Cable strain relief for the cold cables is supported
¹⁴ from the back end of the feedthrough.

- ¹⁵ The PTC provides a bidirectional fiber interface to the timing system. The received data is
¹⁶ separated into clock and data using a clock/data separator. The clock and data streams are
¹⁷ separately fanned-out to the five WIBs as shown in Figure 2.48. The PTC fans the clocks out to
¹⁸ the WIB over the PTB, which is a passive backplane attached directly to the PTC and WIBs.

- ¹⁹ The PTC also receives LV power for all cold electronics connected through the signal flange,

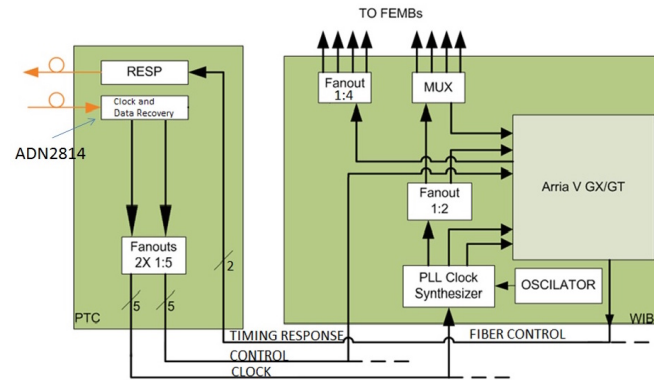


Figure 2.48: Power and Timing Card (PTC) and timing distribution to the WIB and FEMBs.

fig:tpc

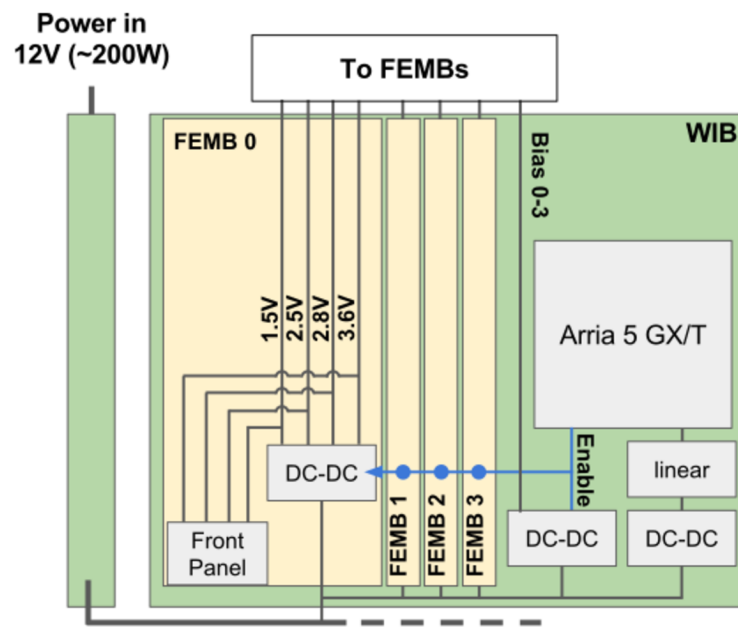


Figure 2.49: LV power distribution to the WIB and FEMBs. 200 W is for a fully-loaded crate with the majority of the power dissipated by the 20 cold FEMBs in the LAr.

fig:tpc

- 1 approximately 200 W at 12 V for a fully-loaded flange (five WIB + 20 FEMB). The LV power is
 2 then fanned out on the PTB to each WIB, which provides the necessary DC/DC conversions and
 3 fans the LV power out to each of the cold FEMBs supplied by that WIB, as shown in Figure 2.49.
 4 The majority of the 200W drawn by a full flange is dissipated in the LAr by the cold FEMB.

fig:tpcce_wib_p

- 5 Each WIB contains a unique IP address for its UDP slow control interface. The IP address for the
 6 WIB is derived from a crate and slot address: the crate address is generated on the PTC board via
 7 dipswitches and the slot address is generated by the PTB slot, numbered from one to five. Note
 8 that the WIBs also have front-panel connectors for receiving LV power; these can be used in place
 9 of the LV power inputs on the PTB generated by the PTC.

- 10 The WIB is also capable of receiving the encoded system timing signals over bi-directional optical
 11 fibers on the front panel, and processing these using either the on-board FPGA or clock synthesizer
 12 chip to provide the 50 MHz clock required by the cold electronics.

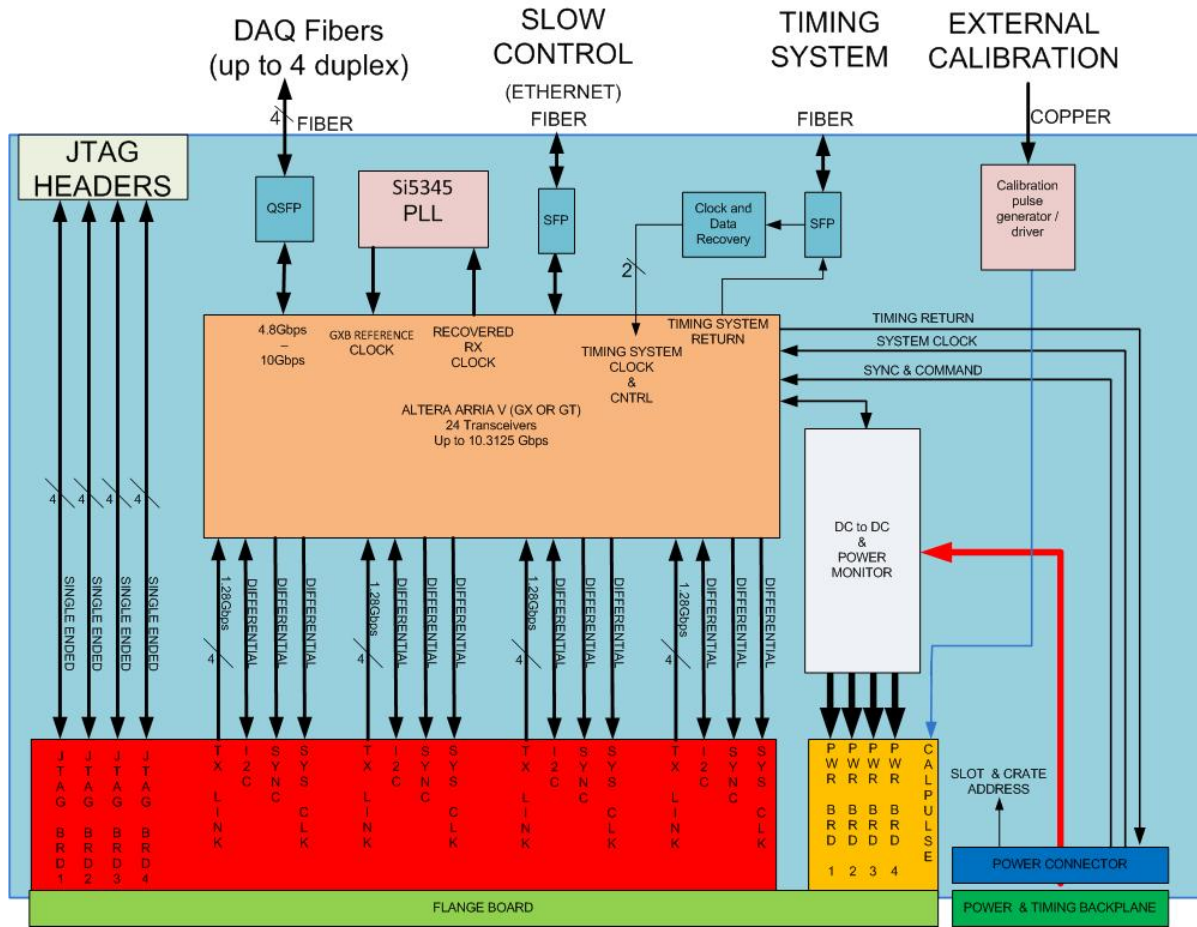


Figure 2.50: Warm interface board (WIB). Note that front panel inputs include a LEMO connector and alternate inputs for LV power.

fig:tpcce

- 13 The FPGA on the WIB is an Altera Arria V GT variant, which requires a 125 MHz clock for its
 14 state machine that is provided by an on-board crystal oscillator. The GT variant of the Arria V
 15 transceivers can drive the high-speed data to the DAQ system up to 10.3125 Gbps per link, implying
 16 that all data from two FEMB (2×5 Gbps) could be transmitted on a single link. However, it is

- ¹ planned to use a QSPF socket on the WIB to deliver \sim 5 Gbps on four optical fibers (one fiber per
² FEMB) to two RCEs.

³ write out

- ⁴ The FPGA has an additional Gbps Ethernet transceiver I/O based on the 125 MHz clock, which
⁵ provides real-time digital data readout to the slow control system.

⁶ 2.6.7 External Power and Cables

- ⁷ The LV power to the FEMB and WIB is supplied by Weiner MPOD power supplies.

⁸ define MPOD

- ⁹ The CE power-per-channel is about 25 mW in the LAr. Including power for the WIB, a fully loaded
¹⁰ WIB (one WIB plus four FEMBs) requires 12V and draws approximately 3.3 Amps. Therefore,
¹¹ the full electronics for one APA (five WIBs + 20 FEMBs) requires 12 V and draws approximately
¹² 16 Amps, for a total power of almost 200 W, as described in Section 2.6.6. subsec:warm_interface_elec

- ¹³ Each MPOD LV power unit has two DSUB37 connectors, each with four channels of LV output,
¹⁴ including negative and positive sense wires. Each channel has three pins of negative output and
¹⁵ three pins of positive output. Five of the eight channels provide the 12 V/3.3 A to each WIB via
¹⁶ the PTC, and one channel provides LV power to the PTC itself, with two of the eight channels
¹⁷ unused.

- ¹⁸ Each MPOD wire-bias voltage unit supplies the wire-bias voltages to eight SHV connectors at the
¹⁹ signal flange. One MPOD chassis contains three LV and three wire-bias units, and can supply all
²⁰ the LV and wire-bias power to three APAs worth of cold electronics. Therefore, a total of two
²¹ MPOD chassis are required for the detector.

- ²² The LV power cable uses DSUB37 connectors. The bottom of the fuse PCB at the MPOD end of
²³ the cable is shown in Figure 2.51. Each of the three output pins on each channel are tied together
²⁴ in parallel going to one wire large enough to carry the full supply voltage. Fuses can optionally be
²⁵ populated on each output pin as shown in Figure 2.51; however, if fusing is not selected, the pins
²⁶ will be connected with 0Ω resistors. This fusing would serve as a final protection. The primary
²⁷ protection would come from the Over Current protection on the MPOD, which is set above the
²⁸ 3.3 A required by each WIB, but below the combined fuse value. fig:tpcce_fused_cable

- ²⁹ The five separate 12 V/3.3 A channels to the WIBs are delivered to the PTC using two normal
³⁰ DSUB37 connectors to attach the LV power cable. The fusing for the sense wires is implemented
³¹ on the PTC.

- ³² Each APA requires three wire-bias voltage connections at $+820\text{V}$, -370V , and -665V , as described
³³ in Section 2.6.3. The current on each of these supplies is expected to be zero at normal operation. subsec:wire_bias

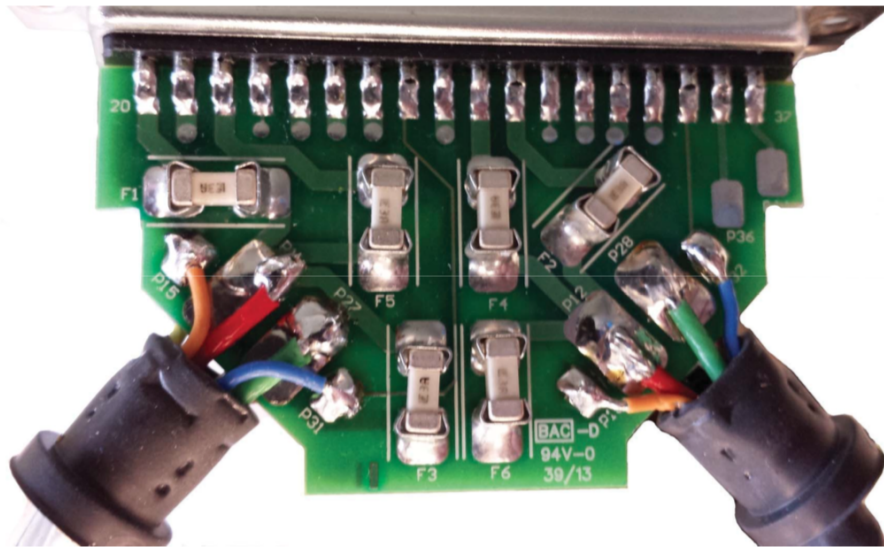


Figure 2.51: Bottom of the fuse PCB at the MPOD end of the cable.

fig:tpcc

- ¹ However the ripple voltage on the supply must be carefully controlled to avoid noise injection into
- ² the front-end electronics.

- ³ RG-58 coaxial cables connect the wire bias voltages from the MPOD to the standard SHV connec-
- ⁴ tors machined directly into the CE feedthrough, so there is no electrical connection between the
- ⁵ LV power and data connectors and wire-bias voltages. The length of the cables from the Weiner
- ⁶ MPODs to the signal flanges is estimated to be 18 meters.

- ⁷ Optical fibers provide the connections between the WECs, which act as Faraday-shielded boxes, to
- ⁸ the DAQ and slow control systems. Each WIB uses QSFP sockets for four pairs of fiber, implying
- ⁹ a total of 120 optical data fibers for the 30 WIB boards in the system. The optical fibers from the
- ¹⁰ signal flanges to the DAQ room are estimated to be 30–40 m in length.

- ¹¹ Duplex LC optical fiber is under consideration for transmitting the one GIG-E connection from
- ¹² each WIB to the slow control system. The WIB reports the current draw from each FEMB to the
- ¹³ slow control system, while the current draw for each WIB is monitored at the MPOD itself.

¹⁴ 2.7 Photon Detection System (PDS)

- ¹⁵ LAr is an excellent scintillating medium and the photon detection system (PDS) is used to obtain
- ¹⁶ additional event information from the photons produced by particles traversing the detector. With
- ¹⁷ an average energy of 19.5 eV needed to produce a photon (at zero field), a typical particle depositing
- ¹⁸ 1 MeV in LAr generates 40,000 photons with a wavelength of 128 nm. In higher electric fields this
- ¹⁹ number is reduced, but at 500 V/cm the yield is still \sim 20,000 photons per MeV. Roughly 1/4 of
- ²⁰ the photons are promptly emitted with a lifetime of about 6 ns, while the rest are produced with
- ²¹ a lifetime of 1100–1600 ns. Prompt and delayed photons are detected in precisely the same way
- ²² by the photon detection system. LAr is highly transparent to the 128-nm VUV photons with a

1 Rayleigh scattering length of (66 ± 3) cm ^{Rayleigh} [?]

2 Missing this citation in common/pdune-tdr-citedb.bib"

3 and absorption length of >200 cm; assuming a LN₂ content of less than 20 ppm. The relatively
4 large light output makes the scintillation process an excellent candidate for determining the t_0
5 for non-beam related events. Detection of the scintillation light can also be helpful in performing
6 background rejection and triggering on non-beam events.

7 2.7.1 Scope and requirements

8 The photon detector system (PDS) includes the following components:

9 • Light collection system including wavelength shifter and light guides

10 • Light sensors: Silicon photo-multipliers (SiPMs)

11 • Readout electronics

12 • Monitoring system

13 • Related infrastructure (frames, mounting boards, etc.).

14 The primary requirement is the detection of light from proton decay candidates (as well as beam
15 neutrino events) with high efficiency to enable 3D spatial localization of candidate events. The
16 assumed light yield necessary for meeting this requirement is 0.1 pe/MeV for a particle track near
17 the cathode plane (the farthest possible location from the PDS). In DUNE, the TPC provides
18 supernova neutrino detection, while the detection of light from supernova neutrino interactions
19 localize the events and disentangles them from background noise in the TPC. The photon system
20 provides the t_0 of events relative to TPC timing with a resolution better than 1 μ s (providing
21 position resolution along the drift direction on the order of a couple of mm). Measurements will
22 determine the absolute light yield by measuring light from beam particles and cosmic ray muons
23 tracked in the TPC or identified by external muon trigger counters.

24 ^{fig:PD overview} Figure 2.52 shows the layout for the photon detector system described in this section.

25 2.7.2 Photon detector modules

26 Two different styles of PDS modules are planned to be installed in the detector. The two de-
27 signs test similar light-collection strategies, which differ primarily in the number of times the LAr
28 scintillation light is shifted.

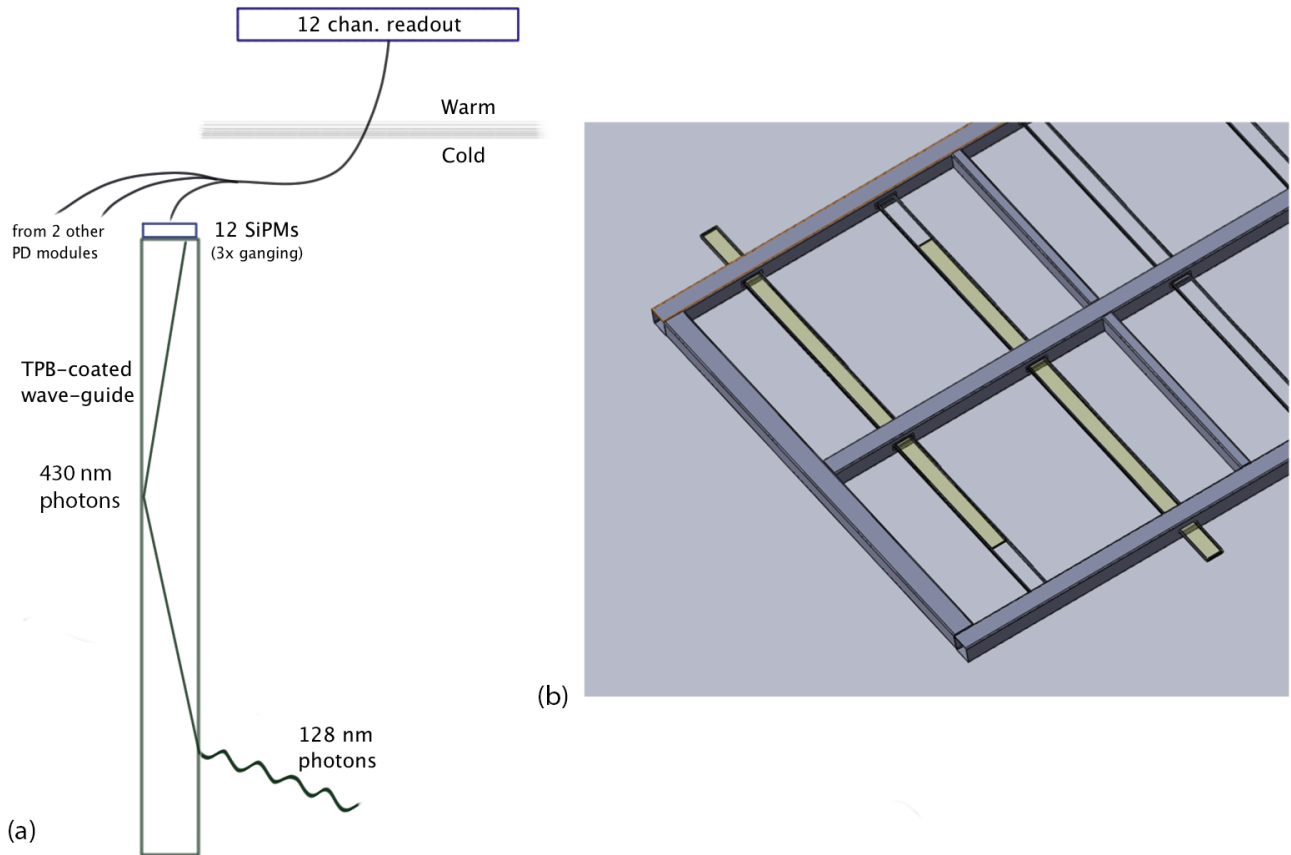


Figure 2.52: Overview of the PDS system showing a cartoon schematic (a) of a single PDS module in the LAr and the channel ganging scheme used to reduce the number of readout channels. Panel (b) shows how each PDS module is inserted into an APA frame. Ten photon detectors (PDs) are inserted into an APA frame.

fig:PD_c

¹ The first design, shown schematically in Figure 2.52. is based on wavelength-shifting radiator plates
² mounted to wavelength-shifting light guides. The plates are coated with tetraphenyl-butadiene
³ (TPB) to produce blue (430nm) light from the 128-nm VUV scintillation light. This blue light
⁴ is absorbed by the commercially produced wavelength shifting (WLS) polystyrene bar with Y-
⁵ 11 fluor, producing green light, which is transmitted through the light guide to the photosensor
⁶ mounted at its end. The radiator plates are held captive in mounting blocks that are glued to the
⁷ WLS bar at regular intervals as shown in Figure 2.53.

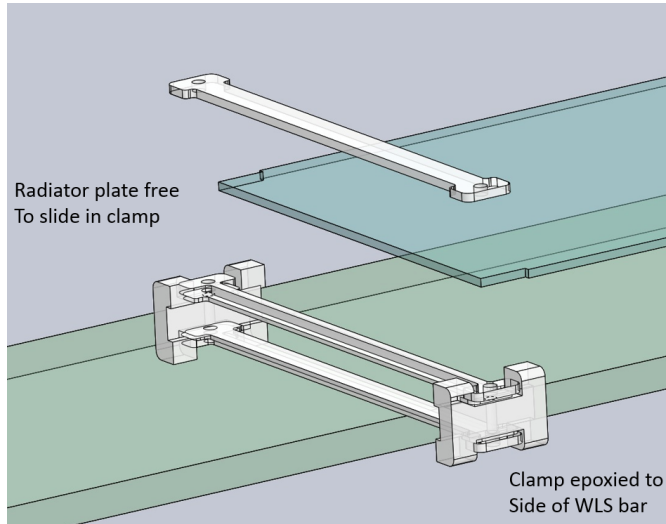


Figure 2.53: Mounting of the radiator plates to the WLS bar for the reference design scheme

⁸ The second design uses the same mounting, but with no radiator plates installed. Instead, an
⁹ acrylic light-guide bar is dip-coated with a solution of TPB, solvents, and a surfactant to produce
¹⁰ a wavelength-shifting layer on the outside surface of the bar. The 128-nm VUV scintillation light
¹¹ is shifted directly to

¹² ?

¹³ and transmitted through the lightguide to the photosensor. Because the design uses only one
¹⁴ wavelength shifting step, potential efficiency increases are possible.

¹⁵ 2.7.3 Sensors

¹⁶ The planned photodetector is a SiPM, model SensL C-Series 6 mm² (MicroFB-60035-SMT). This
¹⁷ model of SiPM has a detection efficiency of 41%; the quoted detection efficiency incorporates
¹⁸ Quantum Efficiency (QE) and the effective area coverage accounting for dead space between pixels.
¹⁹ At LAr temperature (89 K) the dark rate is of order 10 Hz (0.5 p.e. threshold), and after-pulsing
²⁰ has not been observed. An on-going testing program is in place to ensure that the SiPMs can
²¹ reliably survive the stresses associated with any thermal cycling in LAr and long-term operation
²² at LAr temperature.

²³ All photodetectors are subjected to testing to determine forward and reverse bias I-V curves,

- 1 breakdown voltage, dark current and dark count rate, photodetector gain, crosstalk estimation,
- 2 response, and bias dependence of parameters.

- 3 Each SiPM is tested before mounting on the readout boards to determine if the part meets the
- 4 specifications in a warm test. After mounting to the readout board all items are tested both warm
- 5 and cold (cryogenic temperature) to determine the operating characteristics.

- 6 In addition to these tests, the photodetectors are tested for their response to light signals from an
- 7 LED of appropriate wavelength. These tests will be sensitive enough to determine if one of the
- 8 three SiPM elements operating in parallel is not functioning.

9 2.7.4 Mechanical design and installation

- 10 The PDS is configured as a set of *modules* that are mounted on the APA frames. A PDS module
- 11 is the combination of one light guide (also called a “bar” due to its shape) and 12 SiPMs, as
- 12 shown in Figure 2.52 (a). The APA frames hold ten PDS modules, approximately 2.2-m long,
- 13 86-mm wide and 6-mm thick, equally spaced along the full length of the APA frame, as shown in
- 14 Figure 2.52 (b). The light guides are inserted into the APA frame on rails gliding on their radiator
- 15 plate mounting blocks, as shown in Figure 2.54 (right).

16 check if right figure ref

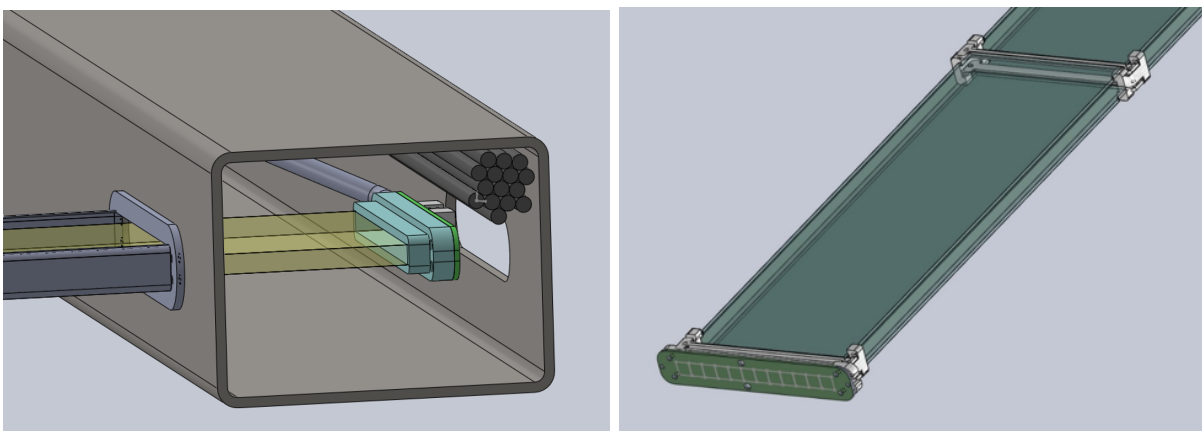


Figure 2.54: (left) Rendering of the installation of a PDS module into an APA frame, shown just before it comes to rest on the inside face of the APA tube. (right) Rendering of the the SiPM mounting board installed on the end of the PDS module before insertion.

- 17 The mounting system has been tested using a prototype PDS module as shown in Figure 2.55.

- 18 Each photon detector has a single SiPM mounting board with 12 surface-mount SiPMs mounted
- 19 on its face as shown in Figure 2.56 (left). Four groups of 3 SiPM elements go to single channels
- 20 of the readout electronics in order to reduce the overall system cost. The board is held close to
- 21 the bar, without touching, using four screws that go into tapped holes on the end mounting block

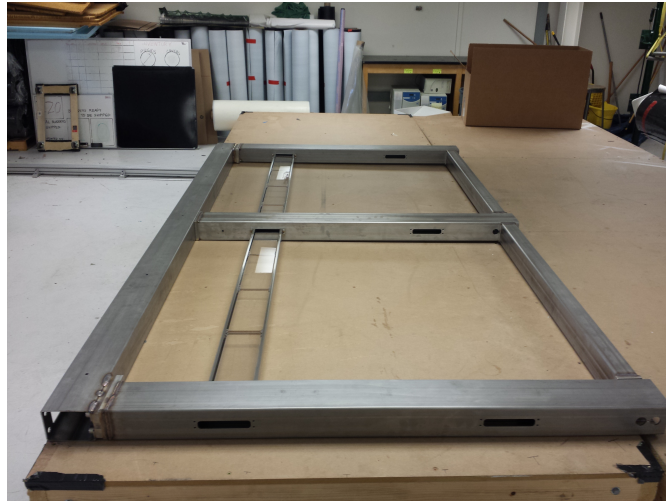


Figure 2.55: Photograph of the installation test of a mock PDS module in a 1/5 section of an APA frame.

`fig:PD_f`

- 1 that is glued to the bar. The mounting block assembly is shown in Figure 2.54 (right) The circuit
- 2 board also has holes at each end for mounting to the APA frame.

`fig:PD_mounting inslide`



Figure 2.56: Photograph of a SiPM mounting board with the full complement of 12 SiPMs installed on the board (left), and with the RJ-45 connector for the cable (right).

`fig:PD_S`

- 3 The cabling plan for the system has one cable with four shielded twisted pairs connected to each
- 4 SiPM mounting board via the surface mount RJ-45 connector shown mounted on the back of the
- 5 readout PCB in Figure 2.56 (right). The cables run through the APA tubing to the top of the
- 6 APA frame as seen in Figure 2.57. The cable bundles are installed and connected after the PD
- 7 has been installed into the slot.

`fig:PD_SiPM PCB front`

`fig:PD_cable intube`

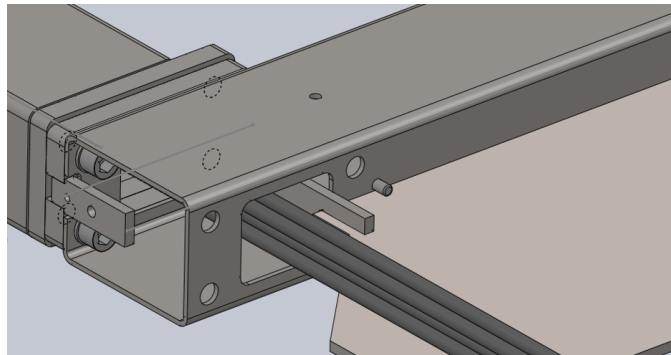


Figure 2.57: Diagram showing the routing of the PDS cables through the APA frame.

fig:PD_c

2.7.5 Alternative photo detector under development

While a sufficient number of the two types of PDS modules are being produced to fully outfit the detector, it is possible that a few of the 60 APA slots will be used to house experimental photon detectors. One type of detector that is being developed in an attempt to increase the light detection efficiency is referred to as the ARAPUCA design.

The ARAPUCA design is based on a new technology that allows for the collection of photons in a $5 \times 5\text{-cm}^2$ window with detection efficiencies at the level of several percent. The trapped light is detected by two SiPMs (SensL 60035 - $6 \times 6\text{ mm}^2$ active area each). The basic concept behind the ARAPUCA design is to trap photons inside a teflon box, of dimensions of $5 \times 5 \times 1\text{ cm}^3$, with highly reflective internal surfaces, such that the detection efficiency of the trapped photons remains high even with limited sensor coverage on these internal surfaces [3].

Photon trapping is achieved by using a wavelength-shifting technique coupled with the technology of the dichroic shortpass optical filters. The latter are multilayer acrylic films with the property of being highly transparent to photons with a wavelength below a tunable cut-off while being almost perfectly reflective to photons with wavelength above the cut-off. A dichroic shortpass filter deposited with two different wavelength shifters (one on each side) is the core of the device. In particular, it serves as the acceptance window for the ARAPUCA device. The rest of the device is a flattened box with highly reflective internal surfaces (PTFE, 3M-VIKUITI ESR, ...), closed on the top by the dichroic filter deposited with the two shifters. A fraction of the internal surface of the box is occupied by the active photo-sensors (Silicon Photomultipliers, or SiPMs) that detect the trapped photons.

It is envisioned that several of these devices could be installed on the detector to directly compare their performances with those of the other PDS modules. A mechanical solution has been developed such that 16 of the ARAPUCA devices can be installed on the same mounting structure used for the other PDS modules as shown in Figure 2.58.

The readout scheme foresees the ganging of the SiPMs from two ARAPUCA devices (four sensors total). The 16 devices on one mounting structure then have a total of four readout channels, which can take advantage of the same cabling and readout scheme used for the other PDS modules.

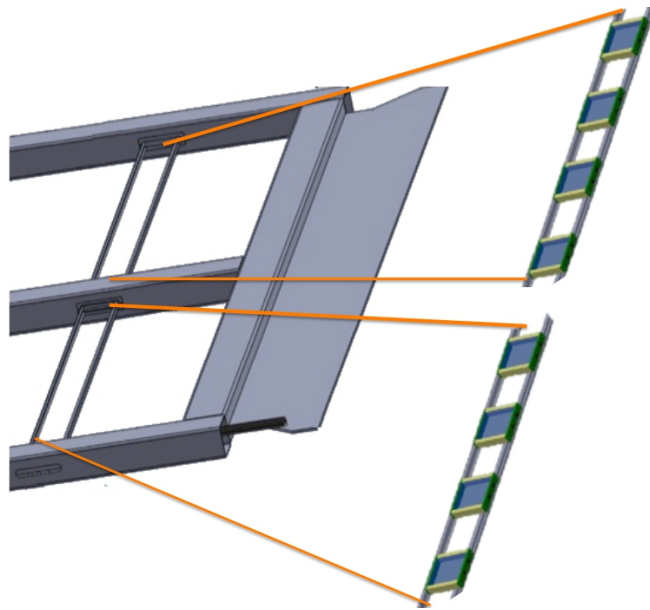


Figure 2.58: One ARAPUCA array of eight devices installed in a APA frame in place of a scintillating bar.

fig:arap

2.7.6 Photon detector UV-light monitoring system

A UV-light-based monitoring system is used to monitor the relative performance and time resolution of the system. The system uses external UV LEDs (245-280 nm) as light sources in the VUV wavelength range, which are coupled to quartz fibers to transmit light from outside the detector volume to desired locations on the CPA plane. Light diffusers located on the CPA surface uniformly illuminate the APA area containing the PDS. The UV light system is used in association with cosmic ray muon tracks and Michel electrons as means of calibration. The UV light essentially mimics physics, although at a different wavelength starting from the wavelength-shifter conversion, light guide propagation, photo-sensor detection and the front-end electronics readout.

The external UV-light monitoring system is designed with the following goals:

- No active components within PD/APA;
- Provide uniform illumination over the APA surfaces;

In terms of technical requirements the system needs to:

- provide light levels down to a single p.e. for individual photon-detector channels,
- provide higher light levels to test linearity of the PDS,
- provide variable pulse width to test the time resolution of the photon detector response, and

Figure 2.59 illustrates the system design schematically. The system consists of a 1U rack mount

- ¹ Light Calibration Module (LCM) sitting outside the cryostat. The LCM generates light pulses
² that propagate through a quartz fiber-optic cable to diffusers at the CPA to distribute the light
³ uniformly across the photon detectors mounted within the APA. Five light diffusers on the CPA
⁴ plane are used: one in the center and four diffusers close to the CPA corners.

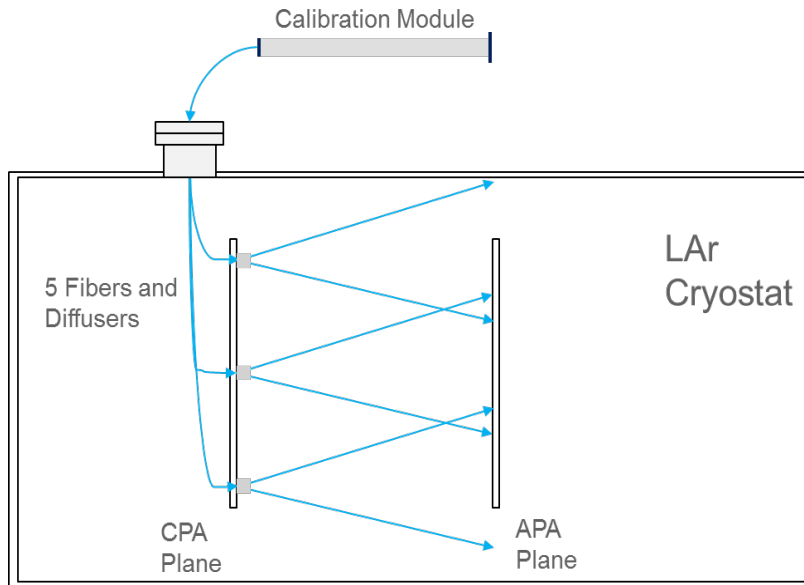


Figure 2.59: Concept of the UV-light monitoring system for the photon detector in liquid argon.

- ⁵ The LCM utilizes the logic and timing control of the photon-detector readout electronics (*SSP*)
⁶ unit, described in Section 2.8. A single SSP board was repackaged into a deeper rack mount
⁷ chassis that accommodates a new internal LED Pulser Module (LPM) and an additional bulk
⁸ power supply. The LPM utilizes five digital outputs from the SSP board to control the LPM pulse
⁹ and its duration. These outputs are derived from the charge injection control logic within the SSP's
¹⁰ FPGA. The even-channel SiPM bias Digital to Analog Converters (DACs) are used to control the
¹¹ LPM pulse amplitude. The adjacent odd channels are used to read out a reference photodiode
¹² used for pulse-by-pulse monitoring of the LED light output. The output of the monitoring diode
¹³ is available for normalizing the response of the SiPMs in the detector to the monitoring pulse.

¹⁴ A bunch of content removed from here; but then gap in (paper) pages received from Flavio
 (missing 4-147 to 4-180); not sure what to do with remainder of this file. Anne

¹⁵ How long do these monitoring run take ? When would they be taken (relative to beam and
 comics running) ? Some interference with light from comics is expected; how will this be ad-
 dressed ? Time of a flash will be known much better than 1us, so not much overlap with ran-
 dom cosmic events at 1ms

- ¹⁶ The controlled source of light in this monitoring system is used to perform time offset and time
¹⁷ resolution measurements. Many effects contribute to a finite time resolution, including the rela-

- ¹ tive time offset of photon-detector channels, scintillation time constants, photon conversion with
² wavelength shifter, photon propagation through photon-detector paddle, SiPM jitter, and FEE
³ resolution.

⁴ FEE = front end electronics?

- ⁵ Most of these effects are constant and can be individually measured on the bench. The UV light
⁶ monitoring system monitors overall stability of the photon detector in both time and amplitude.

⁷ 2.8 PDS electronics

- ⁸ Scintillation light from LAr comes from two different excited states with lifetimes of about 6 ns
⁹ and 1.6 μ s. Only a limited amount of light is collected, so the electronics are designed to collect the
¹⁰ light from both excited states. A summary of the general requirements for the system, including
¹¹ initial requirements from a physics performance perspective, are given in Table 2.7. ^{tab:fee_req}

Table 2.7: Physics requirements for the PDS electronics

Performance Parameter	Target
Time Resolution	Better than 30 ns wrt event time zero ("t0")
Charge Resolution	0.25% photo-electron equivalent
Dynamic Range	~ 10 better than detector (1000:1)
Linearity	Sufficient to resolve 1 photo-electron signals
Multi-Hit Capability	Sufficient to measure Triplet (late) Photons
Dead Time	Live up to 2 drift times either side of beam spill
Bias Control	0.1 V resolution up to 30 V per channel
Calibration	On-board Charge Injection
Timing	Events time-stamped using NO ν A Timing or equivalent syst.

- ¹² There are no PDS front-end electronics in the LAr cold volume. The un-amplified signals from the
¹³ SiPMs are transmitted directly to outside the cryostat for processing and digitization, with the
¹⁴ advantage that the infrastructure required for inside the cryostat is reduced (power, data cables,
¹⁵ precision clocks, data protocols, etc.). A custom module, called the SiPM Signal Processor (SSP),
¹⁶ receives the SiPM signals outside the cryostat.

- ¹⁷ An SSP consists of 12 readout channels packaged in a self-contained 1U module. Each channel
¹⁸ contains a fully-differential voltage amplifier and a 14-bit, 150 MSPS analog-to-digital converter
¹⁹ (ADC) that digitizes the waveforms received from the SiPMs. The front-end amplifier is config-
²⁰ ured as fully-differential with high common-mode rejection, and receives the SiPM signals into a
²¹ termination resistor that matches the characteristic impedance of the signal cable. Currently there
²² is no shaping of the signal, since the SiPM response is slow enough relative to the speed of the dig-
²³ itization to obtain several digitized samples of the leading edge of the pulse for the determination
²⁴ of signal timing.

- 1 The digitized data is stored in pipelines in the SSP, for up to $\sim 13 \mu\text{s}$. The processing is pipelined,
 2 and performed by a Xilinx Artix-7 Field-Programmable Gate Array (FPGA). The FPGA im-
 3 plements an independent Data Processor (DP) for each channel. The processing incorporates a
 4 leading edge discriminator for detecting events and a constant fraction discriminator (CFD) for
 5 sub clock timing resolution. Because the FPGA is programmable and accessible, it is possible to
 6 explore different data processing algorithms and techniques, and even customize the readout for
 7 a given type of event (supernova for example.) A picture of the module is shown in Fig. 2.60. A
 8 block diagram of the system is shown in Fig. 2.61.

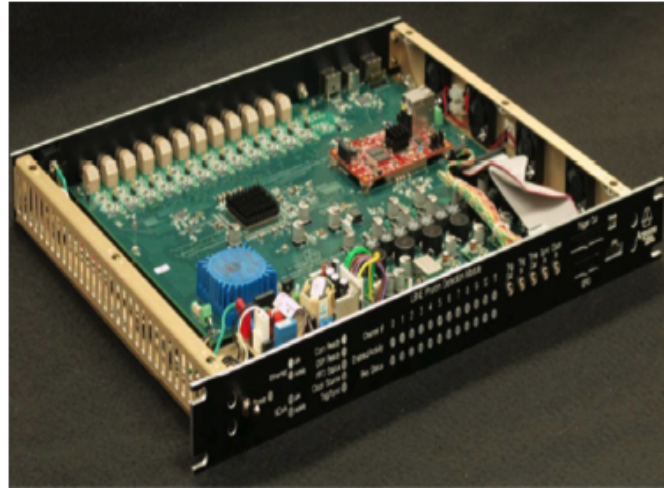


Figure 2.60: Picture of SSP module.

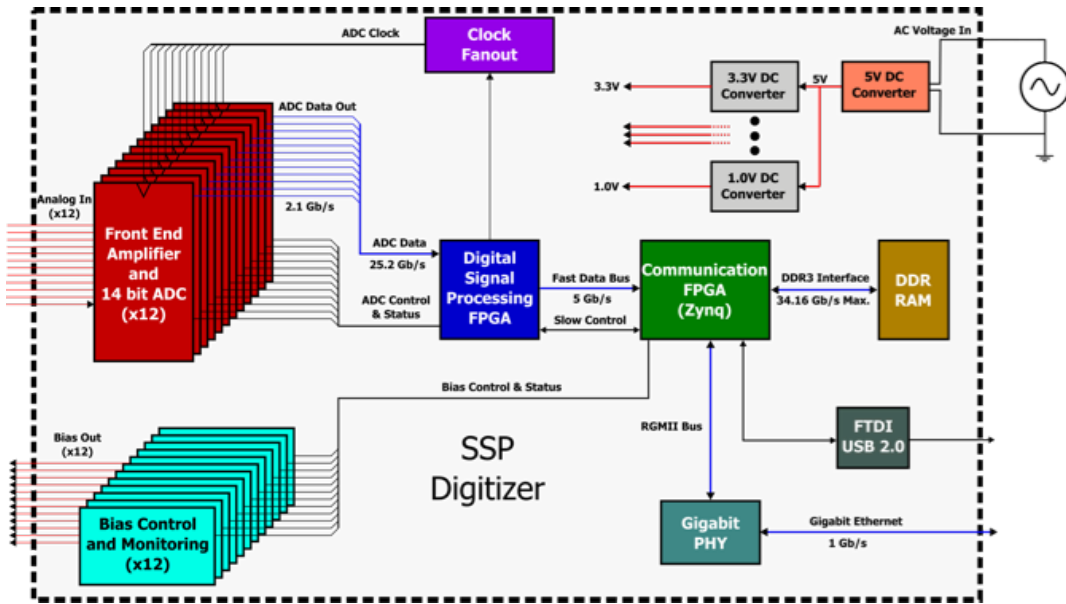


Figure 2.61: Block diagram of the SSP Module.

- 9 In the simplest mode of operation, the module performs waveform capture, using either an internal
 10 or external trigger. Up to 2046 waveform samples may be read out for each event. When wave-
 11 form readouts overlap the device can be configured to offset, truncate or completely suppress the
 12 overlapping waveform. Pile-up events can also be suppressed.

- 1 In order for the events measured in the photon detector to be matched up with the corresponding
 2 events in the TPC, the front-end electronics attaches a timestamp to the data as it is acquired.
 3 The timestamp is unique, and has a correspondence with the timestamps in the TPC electronics
 4 processing. The timestamp in the SSP is applied to the event data as it is digitized. In the case
 5 where zero-suppression and data sparsification are used, the timestamp on accepted data remains
 6 intact. To achieve this, the TPC and PD electronics must be synchronized, including timestamp
 7 counter resets, based on a known and stable calibration for the timing resolution of the ADC
 8 conversion between the two systems.
- 9 A Xilinx Zynq FPGA, onboard the MicroZed system-on-module, handles the slow control and
 10 event data transfer. The SSP has two parallel communication interfaces; USB 2.0 and 10/100/1000
 11 Ethernet. The 1 Gb/s Ethernet supports full TCP/IP protocol. The module includes a separate
 12 12-bit high-voltage DAC for each channel to provide up to 30 V of bias to each SiPM. The module
 13 also feature charge injection for performing diagnostics and linearity monitoring, and also voltage
 14 monitoring.
- 15 In tests to date, the SSP is capable of measuring single photo-electron signals coming from the
 16 SiPMs over a cable length of 30 meters when the SiPMs are operated at LAr temperatures. The
 17 timing resolution of the signals has been measured to be better than 3 ns. The full-differential
 18 signal processing in the front-end circuitry is important in achieving this result.
- 19 As noted previously, three PDS SiPM signals are ganged together into a single readout channel.
 20 A multi-conductor cable with four twisted pairs is used to read out PDS modules, each of which
 21 incorporates 12 SiPMs.

22 **2.9 Data Acquisition (DAQ)**

sec:daq

23 **2.9.1 Scope and requirements**

- 24 The data acquisition (DAQ) system is shown in Figure 2.62 along with its interfaces to the cold
 25 electronics, beam instrumentation, and online computing systems.

26  Figure 2.62 requires significant zooming to read. Need a simpler diagram initially to show the
 major pieces, and only the DAQ pieces. Also some descriptive text; relate the physical compo-
 nents to data rates and such.

27 List components: timing, trigger, throttle systems, FPGA-based master, etc.

- 28 The physics requirements of ProtoDUNE-SP are the primary drivers of the DAQ system require-
 29 ments. The front-end electronics and assumed bandwidth and storage requirements from the online
 30 and offline computing systems impose additional constraints.

- 31 The run plan (see Section 1.4) calls for about 25 M analyzable beam events to be collected in the

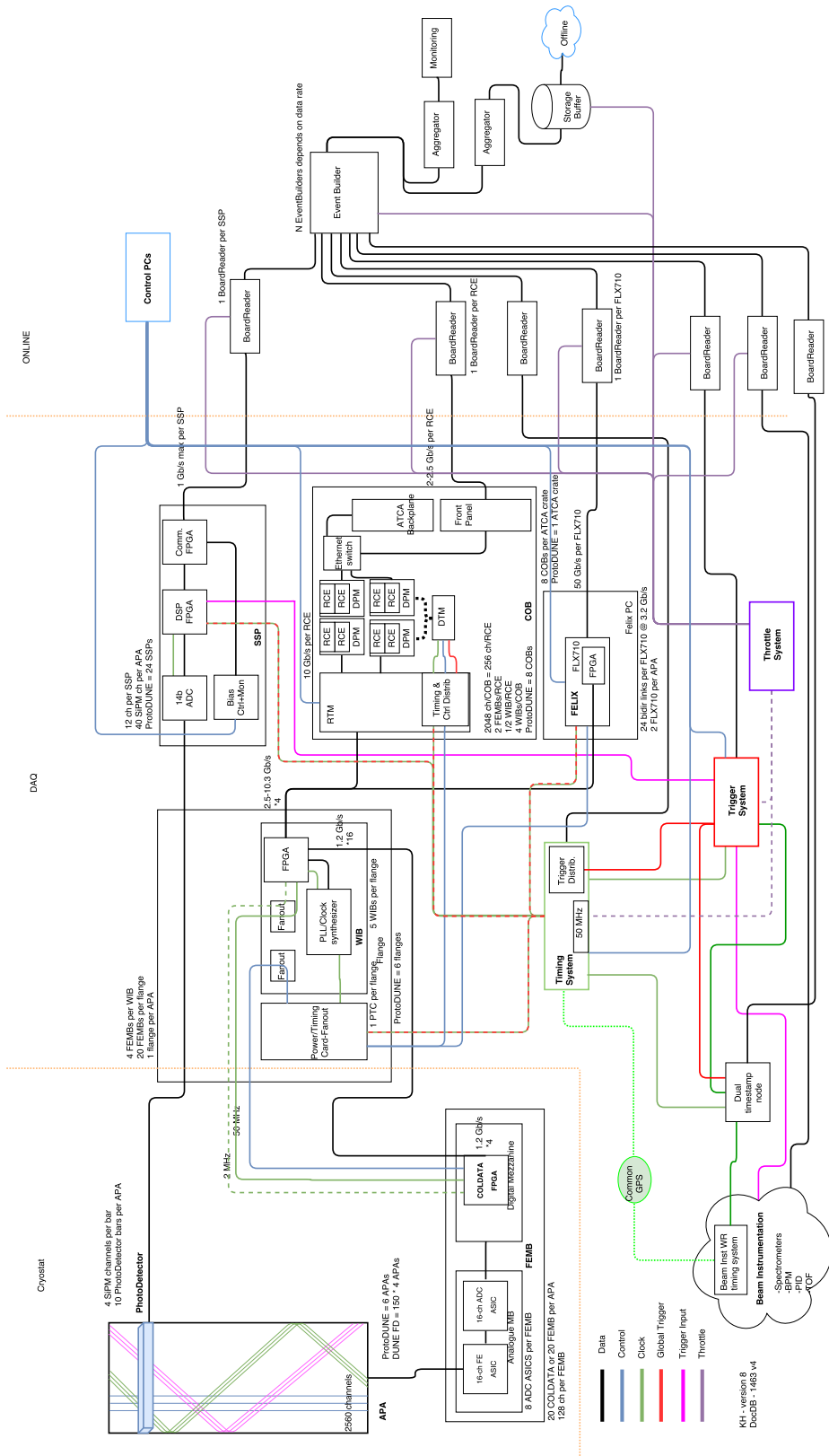


Figure 2.62: Detailed overview of the DAQ system, its interconnections, data flow, timing and control signals, and the interfaces to the electronics and online computing systems

fig:daq-

¹ first run of ProtoDUNE-SP. Data sets may be enhanced in desirable particle types and energies
² with dedicated triggers (such as PID) from the beam instrumentation. The latter is described in
³ Section 5.3.

⁴ Parameters of the data collection plan are listed in Table 2.8. The lossless compression factor cited
⁵ in the table is based on the assumption that the signal-to-noise level is similar to or better than
⁶ that achieved by MicroBooNE.

⁷ needs citation

Table 2.8: Parameters defining data rate and volume in the “most likely” scenario v5 [4]. The buffer depth includes both the in-spill and out-of-spill data. data spreadsheet

Parameter	Value
Trigger rate	25 Hz
Spill duration	4.8 s
SPS Cycle	22.5 s
Readout time window	5 ms
# of APAs to be read out	6
Single readout size (per trigger)	230.4 MB
Lossless compression factor	4
Instantaneous data rate (in-spill)	1440 MB s^{-1}
Average data rate	576 MB s^{-1}
3-Day buffer depth	300 TB

⁸ The baseline trigger rate during the SPS spill is taken to be 25 Hz. Cosmic data are also acquired at
⁹ an appropriate rate such that bandwidth and processing priority are given to beam data. The data
¹⁰ rate from the electronics is dominated by the TPC data. However, the photon detection system
¹¹ (PDS) can produce a significant amount of calibration data (where full waveforms are extracted),
¹² during commissioning and special runs (up to 24 Gb/s maximum).

¹³ The TPC data are sent via the Warm Interface Boards (WIB) on the cryostat flanges for the six
¹⁴ APAs, un-triggered at a total rate of 480 Gb/s. The PDS is estimated to send data at a total rate
¹⁵ of 1.2 Gb/s from the 24 SSPs (detailed further in Section 2.9.6). The maximum bandwidth from
¹⁶ the ProtoDUNE-SP online system to CERN IT (and hence, the offline world), is 20 Gb/s at a
¹⁷ maximum. Therefore, the DAQ system must reduce the data by a significant fraction before they
¹⁸ are sent offline. This is achieved by a combination of data compression and triggering.

¹⁹ 2.9.2 Timing, trigger and beam interface

²⁰ The timing and trigger are two distinct subsystems. The timing system provides the distribution
²¹ for the trigger signals over the same fabric as the clock and calibration signals.

1 Timing

2 The timing system is required to provide a stable and phase-aligned master clock to all DAQ
 3 components; synchronize external signals into the ProtoDUNE-SP clock domain and time-stamp
 4 them; distribute synchronization, trigger and calibration commands to the DAQ system; and
 5 conduct continuous checks of its own function. In addition, the timing system acts as a data
 6 source, providing a record of triggers received, distributed, or throttled. The system is designed
 7 to meet the full eventual requirements of the DUNE experiment, but needs only a subset of that
 8 functionality for ProtoDUNE-SP. For instance, absolute time-stamping with respect to an external
 9 GPS reference is not required.

10 An FPGA-based master unit

11 is this part of the DAQ?

12 receives a high-quality clock signal (from a quartz crystal oscillator or external source) and external
 13 signals from the trigger system and SPS accelerator. It interfaces to the ProtoDUNE-SP control
 14 and DAQ via a gigabit Ethernet interface. The master unit multiplexes synchronization and trigger
 15 commands, along with arbitrary command sequences requested by software, into a single encoded
 16 data stream, which is broadcast to all timing endpoints, and decoded into separate clock and data
 17 signals. A uniform phase-aligned cycle counter, updating at the ProtoDUNE-SP system frequency
 18 of 50 MHz, is maintained at all endpoints, allowing commands to take effect simultaneously at all
 19 endpoints regardless of cable lengths or other phase delays.

20 The timing signal is broadcast via multi-mode optical fiber (for medium-distance connection to the
 21 WIB crates on the detector) and LVDS signals are sent over twisted-pair cable (for short-distance
 22 connection to RCEs, SSPs and FELIX modules). Optical signals are fanned out and recombined
 23 using commercial 32:1 passive splitters, and active optical-LVDS converter boards further split
 24 the signals for local distribution to endpoints.

25 Endpoints decode the timing signal into separate clock and data signals using a commercial clock-
 26 data recovery ASIC ^{siliconlabs:S1534} [5], which in turn feeds a low-bandwidth PLL

27 define

28 in order to remove any remaining jitter in the clock and provide phase adjustment. The data stream
 29 employs 8b/10b encoding, ensuring sufficient transitions in the timing signal for clock recovery and
 30 correct operation of optical links, and uses scrambling of idle patterns to minimize electromagnetic
 31 interference (EMI). A common firmware block is used to decode the timing protocol, which is
 32 incorporated into the overall firmware design for the receiving FPGA in each DAQ component.
 33 This block provides a cycle counter, several independent trigger, calibration and synchronization
 34 signals, and a general-purpose packet data output

35 packet of data output?

- ¹ to each endpoint. The cycle counter is used to generate low-frequency timing signals for further
² propagation, e.g., the 2-MHz sampling signal for the cold ADCs.

³ Trigger

⁴ The baseline trigger solution for ProtoDUNE-SP is the Central Trigger Board (CTB). The CTB is
⁵ designed to receive triggers from various subsystems (Photon Detection System, Beam Instrumen-
⁶ tation, SPS spill signal, veto signals, etc.). Up to 100 input channels are provided. It combines
⁷ these into a global trigger based on a configurable input mask (or more sophisticated algorithm, if
⁸ desired). It provides functionality to globally time-stamp triggers, keep event counts, and provide
⁹ artDAQ-compatible (see Section 2.9.7) header information with trigger type and error conditions.
¹⁰ Internally generated triggers and calibration pulses allow for testing the board itself and the end-
¹¹ points receiving the trigger signals.

¹² The CTB is based on the MicroZed development board [6], which comprises a Xilinx Zynq-
¹³ 7000 System-on-Chip (SoC), 1-GB DDR3 RAM, Gigabit Ethernet, and 115 I/O ports. The
¹⁴ Programmable Logic of the Zynq-7000 is used to perform fast triggering operations, whilst the
¹⁵ Processing System is used to interface to the readout and controls systems.

¹⁶ Configuration and operation is performed using an XML file which is sent to the CTB. This allows
¹⁷ for fast reconfiguration of the CTB without the need for new firmwares. The file is used to both
¹⁸ configure the board and send start/stop/reset, etc., commands from the run control. The trigger
¹⁹ output format consists of a trigger type (physics/calibration/random), a time-stamp, the trigger
²⁰ word, counter information and the values of the inputs causing the triggers. The trigger system
²¹ uses the timing system clock and global triggers are distributed via the timing system.

²² Beam Interface

²³ The beam instrumentation is described in Section 5.3. The beam instrumentation DAQ and the
²⁴ DAQ for ProtoDUNE-SP have separate timing systems. A common GPS clock is used to keep both
²⁵ systems synchronized relative to each other. A common endpoint receives time stamps from both
²⁶ WhiteRabbit (for the beam instrumentation) and the ProtoDUNE-SP timing system are used to
²⁷ create a matching table from the two systems.

²⁸ what does the ‘both’ refer to?

²⁹ Data from the beam instrumentation are acquired continuously via a separate DAQ path.

³⁰ separate from the actual data?

³¹ Triggered data for ProtoDUNE-SP have both the TPC, PDS, and beam instrumentation data and
³² the timestamps and trigger information of both.

¹ here ‘both’ seems to refer to 3 things

² 2.9.3 TPC data readout

³ The readout of the TPC wires, prior to being received by PCs in the back-end DAQ, consists of CE
⁴ on the APAs inside the cryostat and electronics outside the cryostat, both directly on the cryostat
⁵ flange and in a rack (the warm electronics). This section addresses the warm part of the TPC
⁶ readout and describes how it receives data from the CE (the Front-End Boards), manipulates the
⁷ data, and delivers them to the back-end DAQ.

⁸ From an electronics point-of-view, the flange (one per APA) consists of a 5-slot “crate,” where the
⁹ connectors on the warm side of the feedthrough form the “back-plane” into which the boards plug
¹⁰ when inserted into the crate assembly.

¹¹ crate vs crate assembly?

¹² These connectors and the boards that plug into them (warm interface boards, WIBs) serve to send
¹³ the power, timing, and configuration down to the FEBs

¹⁴ define

¹⁵ and receive the high-speed signals from the FEBs. From a data standpoint, each WIB receives the
¹⁶ data from four FEBs over sixteen 1.25-Gbps data lines, and multiplexes these data to four 5-Gbps
¹⁷ (or two 10 Gbps) lines that are sent over optical fiber to the DAQ.

¹⁸ Two systems are used to receive data from the WIBs. The baseline solution is based on Reconfigurable Computing Elements (RCE) and read out data from five APAs. An alternative exploratory
¹⁹ prototype based on the Front-End-Link-EXchange (FELIX) system is used to readout the sixth
²⁰ APA.

²² 2.9.4 RCE-based readout

²³ The data from the WIB are received by processing units called RCEs (Reconfigurable Cluster
²⁴ Element), [7] which are housed in industry-standard ATCA shelves on COB (cluster-on-board)
²⁵ motherboards that are designed at SLAC for a wide range of applications. The RCE is a SoC
²⁶ from the Xilinx Zynq family and contains a full Linux processor system on the chip accompanied
²⁷ by 1 GByte of DRAM. The primary processing functions of the RCEs are compression (and/or
²⁸ zero-suppression) and buffering of the raw data and then sending data to the back-end upon the
²⁹ receipt of an external trigger. Each COB carries eight RCEs, all connected to each other via an
³⁰ on-board 10-Gbps Ethernet switch, which also sends data out of the COB to the back-end DAQ
³¹ PCs.

- ¹ The interface with the WIB is provided via the ATCA compliant rear-board, the RTM (Rear
² Transition Module). This application-specific board uses a set of QSFP transceivers to receive the
³ data from the WIB and an SFP+ (small form-factor pluggable) optical interface for communication
⁴ with the timing and trigger distribution system.
- ⁵ As the multiplexed data from the WIB come into the RCE FPGA fabric, it is de-multiplexed
⁶ and buffered into per-channel, fixed-time-length chunks (for instance 512- or 1024-ticks). These
⁷ chunks are compressed and written to the DRAM where the RCE processor waits for a trigger
⁸ (also handled by the FPGA) to arrive. Upon a trigger, the processor sends data for a fixed window
⁹ in time, including pre- and post-trigger time chunks for all channels, to the back-end PCs.
- ¹⁰ For ProtoDUNE-SP, 256 wires worth of data (2 FEBs) are sent to each RCE. Given that there
¹¹ are 120 FEBs in ProtoDUNE-SP, 60 RCEs are needed to readout the full detector. These fit into
¹² eight COBs which in turn reside in a single 14-slot ATCA shelf.

¹³ 2.9.5 FELIX-based readout

¹⁴ The FELIX is a PCIe card receiving data on point-to-point links from the detector electronics and
¹⁵ routing those through a switched network to computers. The aim is to reduce to a minimum any
¹⁶ specific hardware developments and to fully rely on commercial networks and servers to perform
¹⁷ the DAQ tasks. For ProtoDUNE-SP, data from five WIBs (20 FEBs) are read out over ten 9.6-
¹⁸ Gbps links into two FELIX cards. Grouping time slices around a trigger signal, as well as data
¹⁹ compression, is dealt with in software. Similar to the RCE-based readout, the FELIX generates
²⁰ artDAQ fragments to be sent to the event builder.

²¹ 2.9.6 PDS and beam instrumentation data readout

²² A combination of externally triggered events and self-triggered events make up the PDS data.
²³ The external triggers come from the beam instrumentation via the trigger system at 25 Hz. This
²⁴ amounts to 118 Mb/s. The self-triggered data are induced by cosmic rays. A cosmic rate of
²⁵ 10 kHz is assumed, totalling 1106 Mb/s. The combined rate comes to \approx 1.2 Gb/s. An alternative
²⁶ scheme with just self-triggered header-only data with a resultant rate of \approx 1.1 Gb/s is considered
²⁷ for implementation if the former proves difficult.

²⁸ 2.9.7 Event-building software

²⁹ Developed within the Fermilab Scientific Computing Division and already used for the 35-t proto-
³⁰ type, *artDAQ* provides data transfer, event building, and event analysis functionality. This latter
³¹ feature includes built-in support for the *art* event analysis framework, also developed at Fermi-
³² lab [8], allowing experiments to run *art* modules for real-time filtering, compression, disk-writing

1 and online monitoring. As art is also used for offline analysis, a major advantage of artDAQ is
2 that it allows developers to easily switch between developing online and offline software.

3 ArtDAQ provides three types of processes, each of which fulfills a specific role. In the order of
4 upstream-to-downstream, these are boardreader processes, eventbuilder processes, and aggregator
5 processes. A given boardreader process is intended to be associated with a particular geographical
6 region of the detector, and provides hooks (in the form of C++ base classes) for an experiment’s
7 developers to embed experiment-specific code (called “fragment generators”), designed both to
8 upload configuration values to hardware and to read out the hardware. For ProtoDUNE-SP, the
9 full DAQ consists of 87+ boardreaders, in charge of the 60 RCEs, 24 SSPs, the timing system,
10 the Penn Trigger Board, and at least one for the beam instrumentation. For testing purposes,
11 fragment generators can perform useful functions such as providing a “playback” mechanism,” and
12 modeling sudden or unexpected data flow events.

13 Downstream of the boardreader processes are the eventbuilder processes. An eventbuilder receives
14 data from every boardreader (a chunk of data from one boardreader corresponding to an event is
15 referred to as a “fragment”), and assembles the fragments for a given event into a raw, complete
16 data event. Optionally, filtering via art modules can be performed at this stage.

17 The most downstream process type is the aggregator. Traditionally in artDAQ-based DAQ sys-
18 tems, there are two aggregators, one in charge of writing data to disk and reporting aggregate
19 statistics (e.g., MB/sec), and one in which experiments can run art analysis modules for real-time
20 online monitoring. For ProtoDUNE-SP this model will change as artDAQ becomes more flexible
21 and throughput capability increases. The functionality of aggregators may be replicated in event-
22 builders. While this solution reduces the number of interprocess connections in the DAQ software,
23 the number of processes assembling raw events is the same as the number of processes writing to
24 disk.

25 For the 35-t prototype, artDAQ processes were controlled by a program called *DAQInterface*.
26 DAQInterface takes charge of launching the artDAQ processes, checking for error states, and shut-
27 ting down processes in an orderly fashion as needed, to avoid improperly closed output files, zom-
28 bie processes, etc. For ProtoDUNE-SP, some of the functionality of DAQInterface (e.g., querying
29 status) is shifting to JCOP (Joint Controls Project); DAQInterface code is reused as appropri-
30 ate/possible, to minimize duplication of effort.

31 **2.9.8 Control, configuration and operational monitoring**

32 The artDAQ software used for all applications dealing with the movement, processing and storage
33 of data is interfaced with software of the Joint Controls Project (JCOP) for the purpose of control,
34 configuration and operational monitoring. JCOP provides a toolkit to implement run control
35 (finite state machine (FSM), distribution of commands, error propagation and handling) as well
36 as graphics tools that allow for the implementation of user interfaces and monitoring dashboards.

37 In order to minimize the software development needs, the same FSM as defined by artDAQ is
38 implemented and commands are sent to the applications using the already supported XML-RPC

1 protocol. Monitoring data are pushed into the JCOP framework by implementing the appropriate
 2 artDAQ monitoring plugin. Log and error messages will be most probably collected and processed
 3 using an implementation of the ELK (elastic search, logstash, kibana [9]) stack. The internal
 4 configuration of DAQ applications are carried out using the mechanisms provided by artDAQ.
 5 The overall system is modeled and configured using the JCOP paradigm (data points).

6 **2.9.9 Interface of the DAQ to the online storage**

7 This could use a bit of introduction, so I'm moving things around a bit, e.g., start with

8 The software framework for interfacing with the electronics, building events, writing data files, and
 9 providing an interface to online monitoring of data as they are acquired is *artdaq* [10].

10 Computers running BoardReader processes read out the RCEs and SSPs and transmit data to a
 11 set of computers running EventBuilder processes. These computers and a pair of 10 Gbit/sec NIC
 12 provide the CPU and networking needed to build events, collect basic metadata, and send the data
 13 to storage and online monitoring. The Event Builders assemble data fragments into self-consistent
 14 events and perform basic data integrity checks before writing records out.

15 end Anne's intro

16 Table 2.8 indicates a nominal trigger rate of 25 Hz for the mid-range scenario. Data are assumed to
 17 be collected based on prompt trigger signals generated by the beamline instrumentation in order
 18 to purify samples of desired particles.

19 Current estimates put the PDS data at approximately 10% of the TPC data rate. Beam instru-
 20 mentation data are expected to be lower still. Although adding to the total data rate only slightly,
 21 adequate resources must be provisioned in order to acquire and store the data from these systems.

22 The network speed of all computers in the DAQ chain is anticipated to be 20 Gbits/sec. Comput-
 23 ers running nearline processing of subsets of the data, which are generally CPU-bound, may be
 24 connected with 1 GBit/sec links.

25 Given that each RCE reads out 256 channels of the TPC, 60 RCEs need to be active. For the
 26 PDS, 24 SSPs are used. At least two computers running BoardReader processes are therefore used
 27 to read out the RCEs and transmit the data to the EventBuilder processes.

28 The online buffer layer consists of \sim 300 TB of storage, which is connected directly to the Event
 29 Builders. The baseline storage option consists of two SAS arrays DAS with > 40 Gbit/s bandwidth,
 30 redundant paths, controllers, and power supplies. A backup option for storage is an XRootD
 31 cluster [11] taking data directly from the Event Builders over the network.

32 After the data are written to disk by artDAQ, the data handling system creates metadata files,
 33 optionally runs nearline monitoring jobs, and transfers the data from EHN1 to the CERN Com-

- ¹ putting Center [12]. The *Fermi File Transfer Service* (F-FTS) software developed and maintained
² at Fermilab is the central element of the data flow management at this level.

³ 2.9.10 Data-quality monitoring

- ⁴ In addition to the monitoring of the operations of the DAQ system, the quality of the data taken
⁵ by the detectors has to be constantly monitored. This assurance is provided by the online and
⁶ nearline monitoring systems. This subsection describes the baseline monitoring frameworks for
⁷ ProtoDUNE-SP. The final implementation is subject to change, but will likely be similarly linked
⁸ to artDAQ and LArSoft as described here.

⁹ Online monitoring

¹⁰ The online monitoring framework runs as a DAQ process and therefore is able to provide data
¹¹ quality assurance in real-time. ArtDAQ splits the data into distinct physics and monitoring streams
¹² via its aggregator processes. The data rate to the monitoring is tunable such that the monitoring
¹³ can digest the data in a timely fashion. The software framework used for online monitoring consists
¹⁴ of an `art::Analyzer` module which interfaces with the artDAQ framework and owns instances of
¹⁵ further classes, each designed to handle different aspects of the monitoring.

¹⁶ The DataReformatters restructure the data to allow for efficient subsequent analysis and provide
¹⁷ a standard interface to the methods, which look through the events. These reformatted objects
¹⁸ are passed to MonitoringData, which owns all of the data products (`TTrees`, `TH1s`, `TGraphs`, etc.)
¹⁹ output from the monitoring software and provides methods for filling them when required. Finally,
²⁰ the online event displays are written as part of the monitoring framework, so the `EventDisplay`
²¹ class was responsible for this.

²² prev sentence is awkward

²³ The output is then saved in a common area for offline access and for syncing with a web server.
²⁴ This is hosted at CERN and allows for remote monitoring of the experiment.

²⁵ Nearline monitoring

²⁶ The nearline monitoring is designed to provide complimentary information to that given by the
²⁷ online system. It runs separately as a series of automated shell scripts and provides feedback on
²⁸ a slower timescale than the online monitoring, thus allowing for a broader view of the quality of
²⁹ data over time. It also utilizes offline software (LArSoft) to provide, for example, reconstruction,
³⁰ facilitating a more complete monitoring of much more complex information.

³¹ Once an output data file has been closed by the DAQ, it can be processed by the nearline system.

- 1 A LArSoft job is initially run over the events to perform reconstruction and extract information
- 2 from the data. The output of this, along with the output of other runs, is then analyzed by a
- 3 separate automated job, to form the high-level view of the data for monitoring.
- 4 Similarly to the online framework, an interface for this system with the web allows for remote
- 5 access of the information.

6 **2.10 Cryostat and feedthroughs**

7 **2.10.1 Scope and requirements**

8 This may need some massaging to put ‘scope and req’ at the beginning of this section

- 9 The cryostat consists of a steel warm outer structure, layers of insulation and an inner cold mem-
10 brane. The outer structure (shown in Figure 2.63), which provides the mechanical support for the
11 membrane and its insulation, consists of vertical beams that alternate with a web of metal frames.
12 It is constructed to withstand the hydrostatic pressure of the liquid argon, the pressure of the gas
13 volumes and satisfies the external constraints. In particular, this structure is to be constructed in
14 EHN1 without any mechanical attachment to the floor or the building side walls.

15 what are the ext constraints? Also, the text on the figure is too small; is it intended to indicate what each color is? Can you clarify and make sure each part/color is labeled?

- 16 Inside the steel structure, a 10-mm thick skin of stainless steel plates are welded to provide a
17 gas barrier to the outside. The top of the cryostat is accessible for installation of the detector
18 elements, the electrical/signal feedthrough, the detector supports and other cryogenics services.
19 The dimensions are dictated by the required active volume of LAr, constraints on the distances from
20 the active volume to the cryostat inner walls and cryostat material thicknesses. The inner cryostat
21 dimensions are: width = 8.548 m, length = 8.548 mm and height = 7.900 m. The dimensions
22 ensure that all crossing penetrations are arranged as requested and that there is enough space for
23 maintenance.

- 24 A secondary membrane is located within the insulation layer. The cold vessel is based on the GTT
25 membrane technology [13]. Thermal requirements call for a thickness of 800 mm, including the
26 insulation, and the primary and secondary membranes. These two membranes provide a first and
27 second level of containment. There is no requirement at this point for additional containment at
28 the level of the warm steel structure. The SS skin of 10-mm thickness between the warm structure
29 and the insulation provides an effective gas enclosure, which allows control of the argon atmosphere
30 inside the insulation volume. All necessary information can be found in [14]. The 3D detailed CAD
31 model is visible in [15].

- 32 Prior to installation of the GTT insulation and inner membranes, the gas tightness of the SS 10-mm
33 membrane will be measured and verified by CERN using dye penetrant analysis, local vacuum-

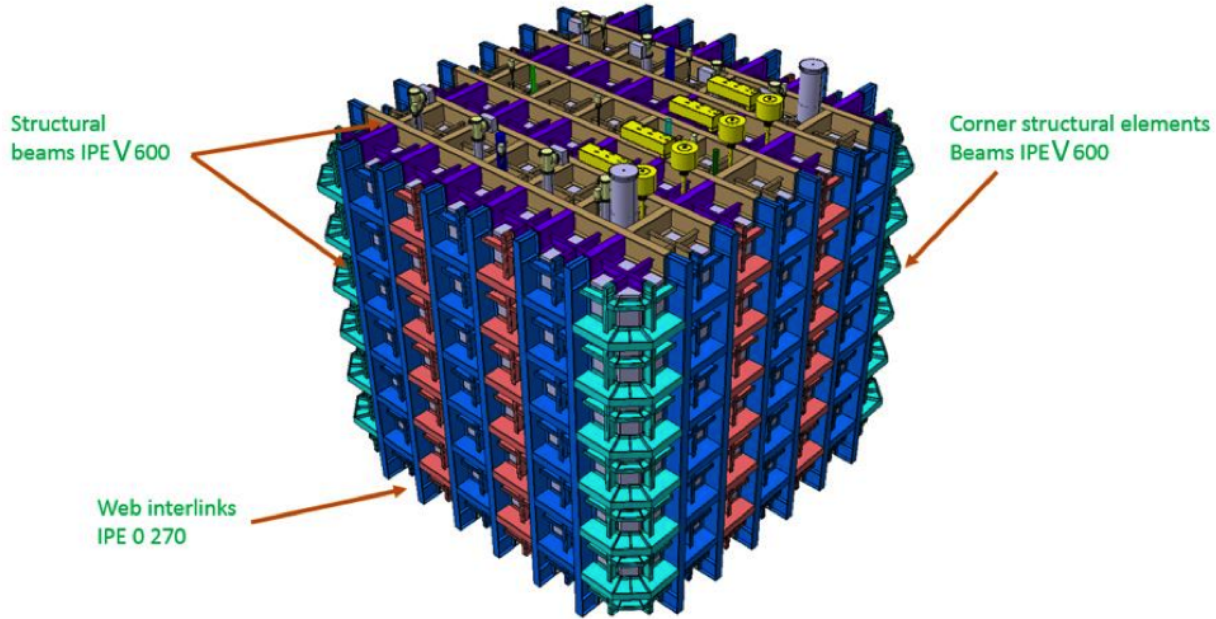


Figure 2.63: Warm vessel layout showing the various major components

fig:warm

- ¹ bag techniques, and He leak detection at the level of the natural He present in the atmosphere
- ² ($\sim 2 - 3 \times 10^{-6} \text{ mbar/l/sec}$). A report will be presented to GTT.

³ 2.10.2 Storage characteristics

- ⁴ The cryostat is required to store LAr at a temperature between 86.7 K and 87.7 K with a pressure
- ⁵ inside the tank of $950 < P < 1100 \text{ mbar}$. The thermal fluxes must be tightly controlled, i.e., they
- ⁶ will be kept under 5 W/m^2 on the inner membrane that is in contact with liquid, in order to
- ⁷ prevent boiling of the LAr.

- ⁸ The storage parameters of the cryostat are as follows:

- ⁹ • The inner dimensions are 7900 mm high \times 8548 mm length \times 8548 mm wide. This corre-
- ¹⁰ sponds to a total volume of $\sim 580 \text{ m}^3$.
- ¹¹ • Tank liquid capacity (assuming a $\sim 4\%$ ullage): $\sim 557 \text{ m}^3$
- ¹² • Residual Heat Input (RHI): $5-6 \text{ W/m}^2$
- ¹³ • Insulation weight: 90 kg/m^3
- ¹⁴ • Insulation thickness (all included): 0.8 m

- Design pressure: Max 1350 mBar / Min 950 mBar. The 1350 mBar is for an accident condition during the cryogenics operation.
- Operating temperature: 86K-89 K

[fig:cryo-overall-dim](#)
Figure 2.64 shows a side cross section of the cryostat with the inner dimensions of the cryostat, the thickness of the insulation and the overall outer dimensions of the warm structure.

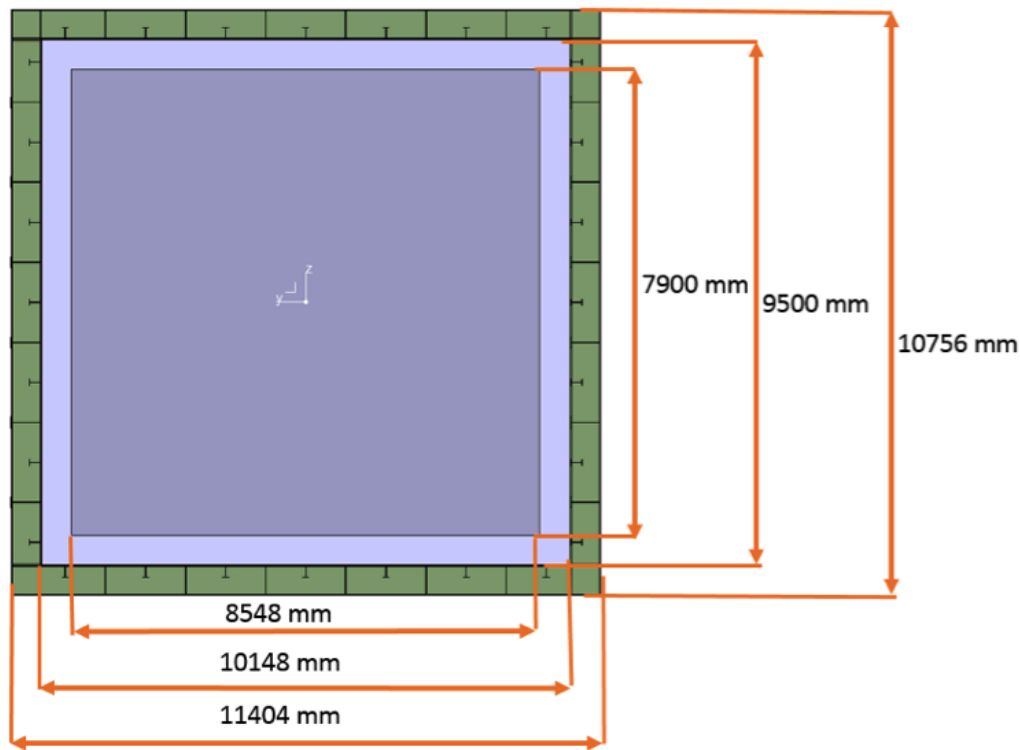


Figure 2.64: Cryostat overall dimensions

[fig:cryo](#)

2.10.3 Cold GTT vessel

The GTT cold vessel is installed inside the warm support structure, which includes the stainless steel gas enclosure membrane. The cold vessel consists of a thermal insulation, a primary corrugated stainless steel membrane, as well as a secondary thin membrane, to provide primary and secondary liquid containment. A cross sectional view of the insulation and membrane layers is shown in Figure 2.65.

The primary membrane is made of corrugated stainless steel 304 L and is 1.2 mm in thickness. The standard size of the sheets is 3m × 1m. The secondary membrane is made of Triplex. This is a composite laminated material of a thin sheet of aluminium between two layers of glass cloth and resin. It is positioned inside the prefabricated insulation panels between two of the insulation layers. The insulation is made from reinforced polyurethane foam. The insulation panels are

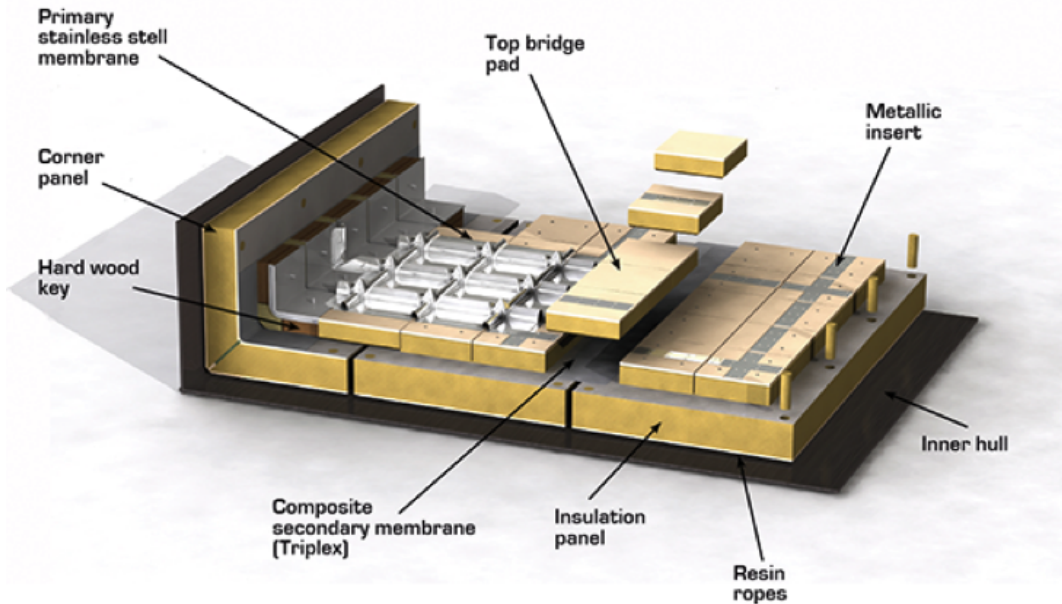


Figure 2.65: Cross section of insulation layers on membranes

`fig:xsec`

- 1 bonded to the inner 10 mm skin using resin ropes. The insulation layers are instrumented with
- 2 gas inlets, outlets, temperature and pressure sensors.

3 2.10.4 Temporary Construction Opening (TCO)

- 4 A dedicated access window is necessary to install the ProtoDUNE-SP detector. This is referred
Fig:front-tco-np04
- 5 to as the temporary construction opening (TCO) and shown in Figure 2.66. This means that
- 6 no insulation of membrane can be installed at the beginning in this location. Once the detector
- 7 installation has progressed as far as possible and all of the large TPC components are inside the
- 8 cryostat, the TCO will be closed. The 10-mm SS skin, insulation and cold membranes are installed
- 9 and welded in place.

10 2.10.5 LAr pump penetration

- 11 To keep the high level of purity required, LAr is extracted from a point as low as possible in the
- 12 cryostat and pushed by cryo-pumps to the external filtering system through the liquid recirculation
- 13 circuit. A special penetration is thus required on one side wall of the cryostat to connect through
- 14 a dedicated system of safety valves to the liquid argon pumps. This penetration requires a local
- 15 modification of the insulation panels and the SS primary membrane, and consists of a crossing
- 16 tube with a diameter of 168 mm for the insulation and the membrane, and a larger-diameter hole
- 17 at the stainless steel plate.

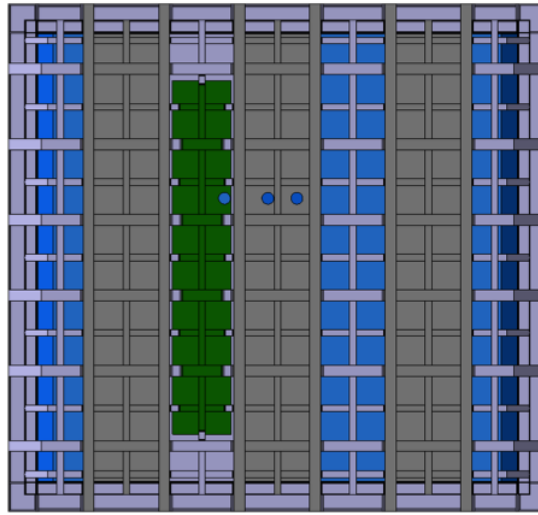


Figure 2.66: Front view of the cryostat with the TCO for the NP04 cryostat shown in green.

fig:front

2.10.6 Beam window penetration

- ¹ amwindow
- ² Once constructed, the ProtoDUNE-SP detector will be exposed to the charged particle beam from
 - ³ the SPS accelerator. To minimize energy loss and multiple scattering of the beam particles in the
 - ⁴ dead material of the cryostat and its insulation, a beam window is inserted at the primary beam
 - ⁵ position as defined in Section 5.1. [sec:beamrequirements](#)

 - ⁶ The vacuum pipe of the beamline has an external diameter of 219 mm. The beam window is
 - ⁷ being designed with a dimension of 250 mm in diameter to allow for alignment tolerances. The
 - ⁸ direction of the beam window follows the one of the beam. The outer portion of the beam window
 - ⁹ penetration is a vacuum pipe that extends from the H4 beamline (see Section 5.2) through the
 - ¹⁰ outer insulation layer and ends at the secondary membrane. A safety valve at the cryostat entrance
 - ¹¹ ensures fast segmentation of the vacuum in case of accident. The portion of the foam insulation
 - ¹² between the secondary and the primary membrane is replaced with a lower density foam (9 kg/m^3). [sec:h4beamline](#)
 - ¹³ To maintain structural integrity, the plywood supporting the primary membrane in the vicinity
 - ¹⁴ of the beam window penetration is replaced with a Nomex honeycomb plate sandwiched between
 - ¹⁵ thin G10 or Carbon layers. Nomex is a polymer material with high thermal resistance and Nomex
 - ¹⁶ sandwiches are well known for their structural resistance, and have already been used at cryogenic
 - ¹⁷ temperatures in the ATLAS detector. In this design, both the primary and secondary stainless steel
 - ¹⁸ membranes remain intact. Care has been taken to position the beam window exit on the interior of
 - ¹⁹ the cryostat to match a flat section of the corrugated primary SS membrane. Thermal and stress
 - ²⁰ analyses are being conducted in collaboration with GTT. These will influence the detailed design
 - ²¹ of the first segment of the beam window. The total amount of material in this design, including the
 - ²² primary membrane, and assuming a 0.3 mm G10 thickness on both sides of the Nomex sandwich
 - ²³ and a 0.3-mm-thick steel beam window, is equivalent to 10% of a radiation length.

¹ 2.10.7 Roof signal, services and supports penetrations

² The penetrations through the cryostat have been arranged by position and diameter. Most of
³ the penetrations are placed on the ceiling of the cryostat. They have been differentiated into two
⁴ main groups according to their function and the thermal stresses they will be submitted to. The
⁵ classification determines whether penetrations can be used to support the weight of the detector
⁶ or not. The penetrations on the roof of the NP04 cryostat are detailed in Table ^{tab:roofpenetrations} 2.9. A 3D CAD
⁷ model to identify all positions can be found at [16] and in an associated drawing [17]. ^{edms4} ^{edms5}

Table 2.9: Cryostat penetrations in roof and on side.

Component	Quantity	Value
West TPC translation suspension:	crossing tube diameter	200 mm
Center TPC translation suspension:	crossing tube diameter	200 mm
East TPC translation suspension:	crossing tube diameter	200 mm
Signal cable chimney FTs:	crossing tube diameter	250 mm
Spare on Signal cable row FTs:	crossing tube diameter	250 mm
Laser FTs:	crossing tube diameter	160 mm
Calibration Fiber CPA FT:	crossing tube diameter	250 mm
Spare on CPA line FTs:	crossing tube diameter	150 mm
HV FT:	crossing tube diameter	250 mm
Manhole:	crossing tube diameter	710 mm
Angled beam windows – west side:	crossing tube diameter	250 mm
	Vertical:	11.342°
	Horizontal:	11.844°
TCO - side:	1200mm × 7300mm	
Cryogenic pipes - roof:	crossing tube diameter	250 mm
	crossing tube diameter	304 mm
	crossing tube diameter	152 mm
	crossing tube diameter	125 mm
	crossing tube diameter	250 mm
Cryogenic pipes – north side:	crossing tube diameter	168 mm

⁸ 2.10.8 Detector Support Structure (DSS)

⁹ Prior to the installation of the TPC, the detector support structure DSS is installed inside the
¹⁰ cryostat. The DSS is shown in Figure ^{fig:dss-install} 2.67. It is positioned near the ceiling and is supported
¹¹ by nine penetrations through the cold side of the membrane extending up to the warm structure
¹² of the cryostat. The warm structure of the cryostat supports all of the loads from the detector.
¹³ The DSS consists of two layers of I beams. The top (yellow) layer is oriented in the y direction
¹⁴ and designated as the Y beams and the bottom (purple) layer is oriented in the x direction and

- ¹ designated as the X beams.
- ² The Y beams are fixed in the y direction at the center support point, but free to move during
³ the cool down at the two outer points. The ends of the Y beams are expected to shrink \sim 10 mm
⁴ towards the center during cooldown to LAr temperature.
- ⁵ The X beams are used for the direct support and positioning of the TPC components. Only three
⁶ X beams are shown in Figure 2.67, but there are two additional inbetween the ones shown. The
⁷ full set of beams is shown in Figure 2.68 along with the naming convention for the X beams. X
⁸ beam A supports the row of APAs near the Saleve side of the cryostat. X beam B is used for the
⁹ installation and support of the end wall FC in the Saleve drift of the cryostat. X beam C supports
¹⁰ the row of CPAs. X beam D is used for the installation and support of the end wall FC in the
¹¹ Jura drift. X beam E supports the row of APAs near the Jura side of the cryostat.
- ¹² The X beams have the ability to translate on rolling trolleys in the Y direction in order to move
¹³ the TPC components from the TCO entrance to their correct position in Y inside the cryostat.
¹⁴ They are fixed in the X direction to the Y beams at the beam side of the cryostat. The reason
¹⁵ to fix the X beams on the beam side is to limit the movement of the beam side of the TPC with
¹⁶ respect to the membrane wall since the beam plug is mounted at this side of the TPC.



Figure 2.67: Detector support system

fig:dss-

¹⁷ 2.11 Installation

¹⁸ 2.11.1 Anode Plane Assemblies (APAs)

- ¹⁹ The APAs will be delivered to EHN1 in containers as shipped from the production sites. These
²⁰ containers will be opened inside EHN1 and special lifting fixtures will be attached to each end of
²¹ the APA. The APA will be positioned and attached to two conveyances installed in EHN1. Both

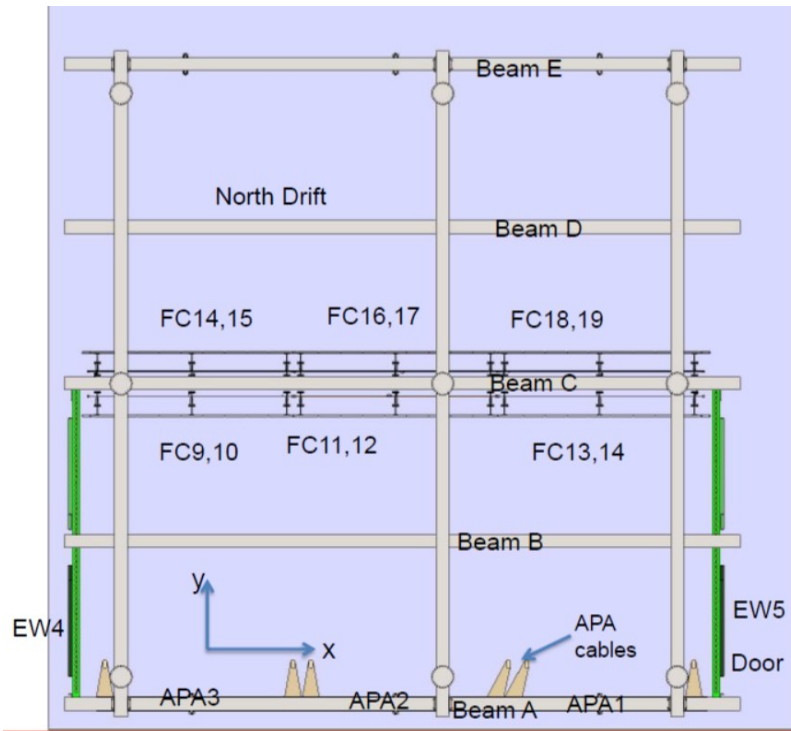


Figure 2.68: DSS showing full set of beams

fig:dss-

- 1 conveyances will be used to lift the APA from the container, oriented as shown in Figure 2.69
- 2 (right), and then rotate it 90° from that orientation, as in the left portion of the figure.

- 3 Once the APA is removed from the container and properly oriented, the lifting strap and fixtures
- 4 will be removed for the lower edge of the APA, the roof hatch on the material SAS for

next to?

- 5 the clean room will be opened, and the APA will be lowered through the hatch. The APA will
- 6 then be transferred to a rolling trolley attached to a series of rails, and moved into the clean room
- 7 via these rails. These spaces and rails are described in more detail in Chapter 4.
- 8 ch:spacereq

- 9 Once in the clean room, the APA will go through a series of acceptance tests for both electrical
- 10 integrity and wire tension. It will also be inspected for broken wires or any other damage that
- 11 could have resulted from shipment.

12 2.11.2 Photon Detection System (PDS)

- 13 After this testing is complete, the APA is integrated with the PDS. There are ten PDs per APA,
- 14 inserted into alternating sides of the APA frame, five from each direction. This is shown in
- 15 Figure 2.70. Once a PD is inserted, it is attached mechanically to the APA frame with fasteners,
- 16 a single electronics cable is attached, and strain is relieved. Each PD is tested immediately after

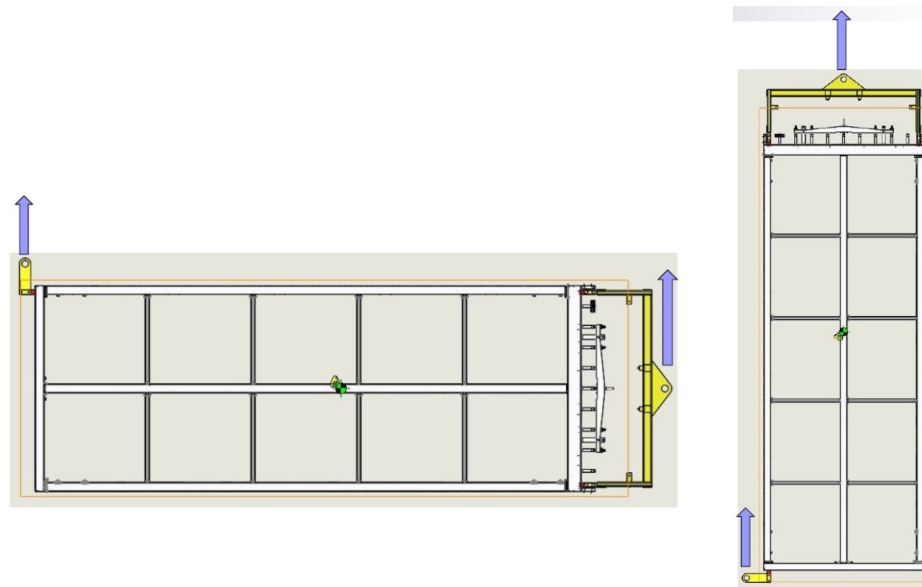


Figure 2.69: The APA with the lifting tooling attached. The right image shows the orientation of the APA as delivered, the left shows the orientation when it is lowered into the material SAS.

fig:apa-

- ¹ installation to ensure proper operation and to verify the cable readout.

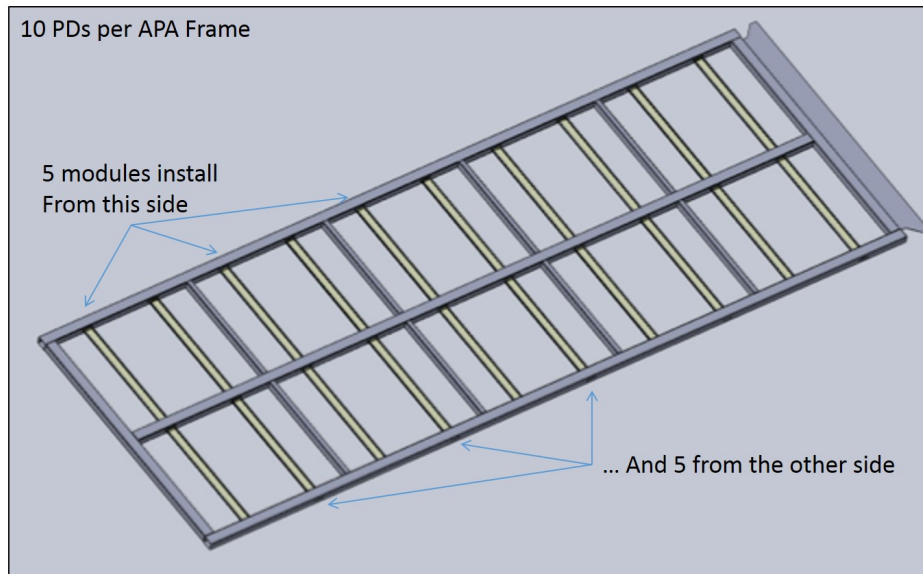


Figure 2.70: PDS installation

fig:pds-

² 2.11.3 Cold Electronics (CE)

- ³ Once the PD installation is complete 20 CE units are installed at the top of the APA frame. Each
- ⁴ CE unit consists of an electronics enclosure that contains the TPC read-out electronics inside. Each
- ⁵ unit also includes a bundle of cables that connect the electronics to the outside of the cryostat
- ⁶ via the flange on the feedthrough port. The location of the CE units on the APA is shown in

- [fig:ce-install](#)
- 1 Figure 2.71. These units will be connected via matching electrical connectors on the FEMB and
 - 2 the CR board mounted on the APA. There will also be mechanical fasteners to hold the enclosure
 - 3 to brackets supported by the APA frame.

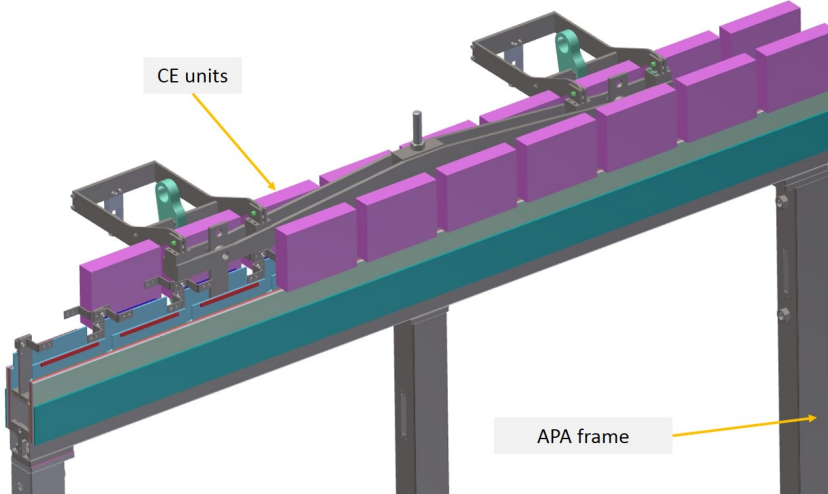


Figure 2.71: CE installation

- [fig:cold-test-stand-open](#)
- 4 After the APA has been fully integrated with the PDS and CE, it will be moved via the rails in
 - 5 the clean room to the integrated cold test stand. This test stand, shown in Figure 2.72, is a large
 - 6 insulated box that is light-tight for PD testing and has a Faraday shield for CE testing. At the top
 - 7 of the box is a crossing tube, similar to those in the cryostat, with a ConFlat fitting that accepts
 - 8 the warm-cold interface flange for the PD and CE cable connections. To prepare for the series of
 - 9 warm electronics tests, the PD and CE cables will be routed and connected to their flanges, the
 - 10 APA will be moved inside the test stand box, and the end cap that completes the Faraday cage
 - 11 will be installed closing the box.
-
- 12 A first set of tests at room temperature will be performed. Once the warm tests are complete,
 - 13 the inner volume of the box will be purged with dry gas and the volume will be slowly cooled,
 - 14 using cold nitrogen gas, to a temperature of approximately 100 °K. The rate of cooldown must
 - 15 be less than 10 °K/hr, the same foreseen for the cryostat cooldown. The cooldown system is
 - 16 designed to maintain the inner volume near 100 °K for approximately 48 hours. A full set of tests
 - 17 at a temperature close to operation LAr temperature will be performed for detectors functionality
 - 18 (APA and PD) and electronic noise assessment. After the cold test procedure is complete and the
 - 19 detector slowly warmed up back to room temperature, the box is opened, cables are disconnected
 - 20 and secured and the APA is extracted from the box on the rail system in the clean room.
-
- 21 The APA is now ready to be moved into the cryostat through the TCO and transferred onto the
 - 22 appropriate rail in the detector support system. The two anode planes of the TPC (Saleve side
 - 23 and Jura side) will then be assembled inside the cryostat, each one out three fully tested APAs
 - 24 mechanically linked together. Signal cables from the TPC read-out electronics boards and from
 - 25 the PD modules are routed up to the feedthrough flanges on the cryostat top side. The cables
 - 26 from each of the CE and PDs on the APA are then routed and connected to the final flanges on
 - 27 the cryostat.

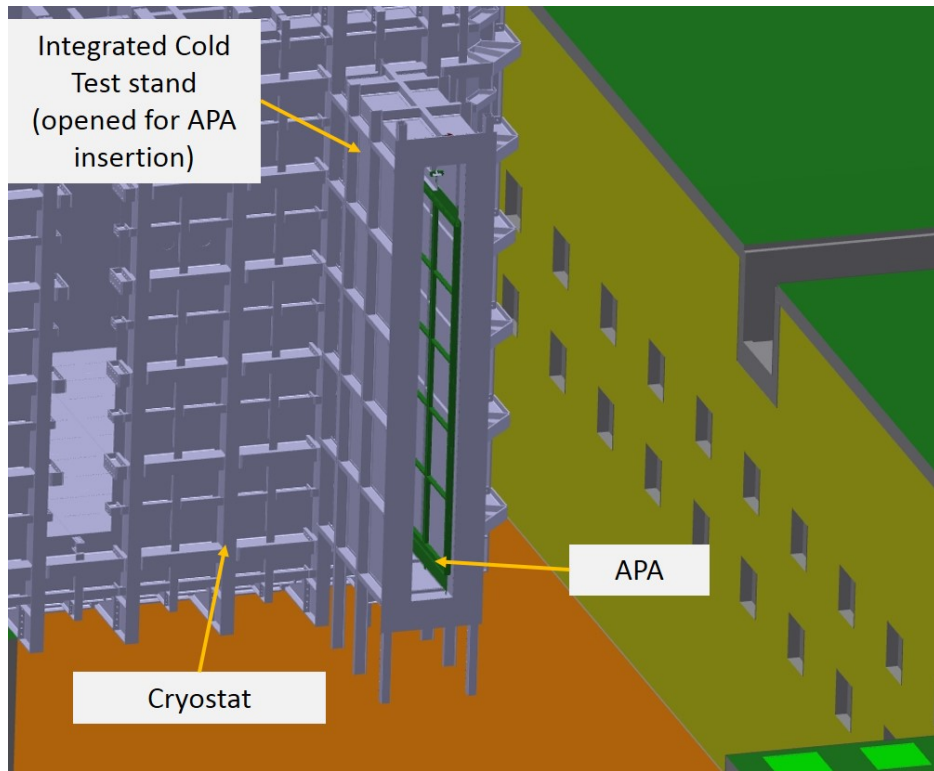


Figure 2.72: A model of the integrated cold test stand in the ProtoDUNE-SP clean room in EHN1.

fig:cold

¹ 2.11.4 Cathode Plane Assemblies (CPAs)

² Individual CPA modules will be delivered to EHN1 in containers as shipped from the production
³ sites. Each CPA module weights roughly 24 kg and will be lifted out of the shipping crate by
⁴ hand. Three CPA modules will be placed on a flat surface and screwed/pinned together to form a
⁵ CPA column. The crane then will be attached at the top end of the CPA column with appropriate
⁶ lifting straps and shackles. The assembled CPA column will be lifted to the vertical position.
⁷ Once the successive CPA column is formed, it is brought together with the previous one within
⁸ 1 mm along their (vertical) length. This alignment is provided by two pins located on the side of
⁹ the CPA that will fit into a vertical slot on the side of the next CPA. Six CPAs columns locked
¹⁰ together will eventually form the cathode plane and moved inside the cryostat through the TCO
¹¹ and positioned parallel to the APA plane at the design drift distance.

¹² FLC: it would be desirable to have a picture of the CPA here

¹³ 2.11.5 Field Cage (FC)

¹⁴ Three basic elements comprise the FC: the top, bottom and end-wall FC assemblies. The top and
¹⁵ bottom FC assemblies are basically mirror assemblies that are hinged from the top and bottom
¹⁶ of the CPAs. Figure 2.73 (left) shows a top/bottom FC assembly. The ground plane covers one
¹⁷ side of the field shaping profiles. The right-hand image in the figure shows a top and bottom FC

- ¹ attached only to one side of the CPA. These will be attached to both sides for the ProtoDUNE-SP
² installation.

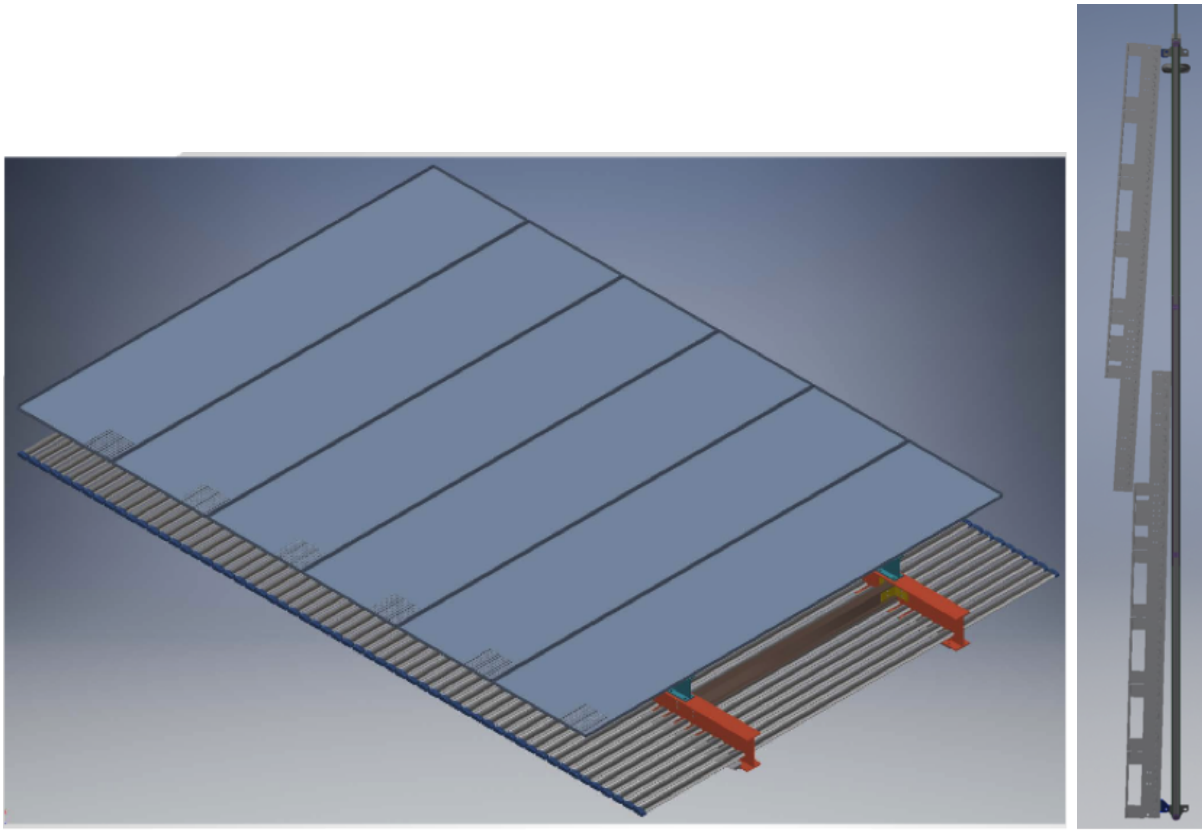


Figure 2.73: Top/bottom FC assembly

- ³ The end-wall FC assembly is constructed from four stacked end-wall FC modules. Figure 2.74
⁴ shows one of the end-wall FC modules. Four of these modules will be stacked and connected
⁵ together to build the end-wall. The stacking will be done by the overhead hoist near the TCO in
⁶ the clean room. Once the end wall is complete, it will be moved into the cryostat on the rails in
⁷ the clean room and positioned on the appropriate beam in the DSS. The end-wall is supported
⁸ by a spreader bar that is in turn supported from the beam. The spreader can swivel about the
⁹ support point; this is necessary for positioning the end-wall with respect to the APA and CPA.

Figure 2.74: FC end wall panel

¹⁰ Jack needs to remake the fc end wall panel picture

- ¹¹ The sequence of installation for the FC components is as follows:

- ¹² • After the first row of APAs is installed and translated to the Salève side of the cryostat, the
¹³ two end-walls for the Salève drift will be constructed and moved inside the cryostat supported
¹⁴ by X beam B.

¹⁵ shown in some figure?

- 1 ● As the CPAs are constructed outside the cryostat, both the top and bottom FC assemblies
2 are attached on both sides, top and bottom. This combination of FC and CPA is then moved
3 into the cryostat and supported by X beam C.

4 shown in some figure?

5 This is done three times to get all into position.

- 6 ● After the second row of APAs is installed and translated to the Jura side of the cryostat, the
7 two end-walls for the Jura drift are constructed and moved inside the cryostat supported by
8 X beam D.

9 again, figure?

10 **2.12 Cryogenics and LAr purification systems**

11 **2.12.1 Overview, Overall planning and ES&H**

12 The scope of the ProtoDUNE Cryogenics includes the design, procurement, fabrication, testing,
13 delivery, installation oversight and acceptance tests of a comprehensive cryogenic system that
14 meets the performance requirements for purging, cooling down and filling the cryostat, acquiring
15 and maintaining the LAr temperature within ± 1 K around nominal temperature (88.3 K), purifying
16 the Liquid Argon (LAr) outside the cryostats, and re-condensing and purifying the boil-off Gaseous
17 Argon (GAr).

18 The reference-design for the ProtoDUNE cryogenics infrastructure includes the External, Proximity
19 and Internal Cryogenics.

20 The *External Cryogenics* includes the systems used for the storage and eventual production of the
21 cryogens needed for the operation of the cryogenic system (liquid nitrogen, LN₂, for cooling; LAr for
22 the cryostat) and GAr generated from the cryogenic storage tanks. In particular, it encompasses:

- 23 ● The receiving facilities for LAr and LN₂ tanker trucks;
- 24 ● The cryogenics transfer lines to deliver LAr and LN₂ to the Proximity Cryogenics (in the
25 vicinity of the cryostat);
- 26 ● The ambient vaporizer and transfer lines to deliver GAr to the cryostat for the piston purge
27 and the GAr make-up; and
- 28 ● The regeneration system for the LAr purification (with GAr and GAr/H₂ cylinders).

¹ The *Proximity Cryogenics* takes the cryogens from the External Cryogenics and delivers them to
² the Internal Cryogenics under the required pressure, temperature, purity and mass flow rate. It
³ encompasses:

- ⁴ • The condenser (with heat exchanger) to re-condense the boil-off GAr;
- ⁵ • The LAr purification system with inline purity monitor;
- ⁶ • The LAr recirculation pumps;
- ⁷ • The LAr Phase separator to feed the cryostat;
- ⁸ • The LN₂ Phase separator to feed the condenser;
- ⁹ • The GAr purification system;
- ¹⁰ • The cryostat-purge equipment; and
- ¹¹ • The condenser LAr pump.

¹² The *Internal Cryogenics* includes all the cryogenic equipment located inside the cryostat. It en-
¹³ compasses:

- ¹⁴ • The cryostat/detector cool down manifolds
- ¹⁵ • The LAr distribution manifold
- ¹⁶ • The GAr purge distribution manifold.

¹⁷ The equipment described in this chapter will be used for the cool-down, filling, operation, purifi-
¹⁸ cation, emptying and warm-up of the ProtoDUNE Single Phase cryostat. These operations are
¹⁹ described in greater detail in Section 2.12.3. ^{1sec:cryo-op-modes}

²⁰ The development of the ProtoDUNE cryogenics is part of a common effort between CERN and
²¹ Fermilab which includes the cryogenics for the ProtoDUNE Single Phase and Dual Phase detectors
²² at CERN, and the Short Baseline Neutrino Near Detector (SBND) and Far Detector (SBN-FD)
²³ at Fermilab.

²⁴ The cryogenic systems for all four projects are developed jointly with a standard approach to min-
²⁵ imize the duplication of work, benefit of existing knowledge (at Fermilab and CERN), and also
²⁶ prototype for the Long Baseline Neutrino Facility (LBNF)/Deep Underground Neutrino Experi-
²⁷ ment (DUNE) project. The systems build on the successful experience of the Liquid Argon Purity
²⁸ Demonstrator (LAPD), 35-t prototype, and MicroBooNE at Fermilab, and the development of
²⁹ the WA105 1×1×3 Dual Phase prototype at CERN and CERN’s experience in the design and
³⁰ operation of large-volume noble liquid detectors.

³¹ During all phases, CERN codes and standards will guide the design, procurement and installation

1 phases of the ProtoDUNE Single Phase cryogenics. The planned work process will provide for
2 reviews throughout all phases of the project to guarantee stringent adherence to the safety and
3 scientific requirements.

4 The project requirements for the ProtoDUNE cryogenics system are identical to those of the DUNE
5 Far Detector cryogenics. The current list of requirements is available at [18].
DUNE FD cryogenics req

6 A selection of the most relevant requirements is presented here:

- 7 • Cryo-se-4: The system shall allow recirculation and purification of the liquid argon inventory
8 to achieve the needed LAr purity to meet the scientific requirement (less than 10 day/volume
9 change based on ICARUS experience).
- 10 • Cryo-se-6: The purification system shall be capable of removing contaminants from the LAr
11 prior to filling and shall maintain purity during operation.
- 12 • LArFD-L2-se-44: Electron lifetime greater than 3 ms (maximum drift time at nominal field
13 is 2.25 ms).
- 14 • Cryo-se-5: The system shall provide an argon gas boil off and reliquefaction system.
- 15 • Cryo-se-16: The cryogenics system shall not allow sources of argon gas reliquefaction inside
16 the cryostat, e.g. uninsulated pipes carrying liquid argon.
- 17 • Cryo-se-25: The cryostat and cryogenic systems shall be designed for using the piston-purge
18 technique (introducing heavy gas at the bottom and taking out exhaust from the top) for
19 removing initial electronegative impurities.
- 20 • Cryo-se-8: The cryogenics system shall not introduce unwanted noise into the electronics.
- 21 • Cryo-se-10: The cryogenics system shall provide a stable environment in the cryostat for the
22 detector.
- 23 • Cryo-se-28: The cryogenics system shall be designed in accordance with the cryostat to main-
24 tain a single phase in the entire liquid argon volume at a stable temperature. The chosen
25 temperature is $88.3\text{ K} \pm 1\text{ K}$.

26 2.12.2 Cryogenics Layout

27 The Process Flow Diagram (PFD) of the ProtoDUNE cryogenic system is shown in Figure 2.75.
28 The External Cryogenics located outside of the EHN1 building, is shared with the Dual Phase
29 prototype, which is located in the same experimental hall, few tens of meters away.
fig:cryo-process

30 The system has the following functions:

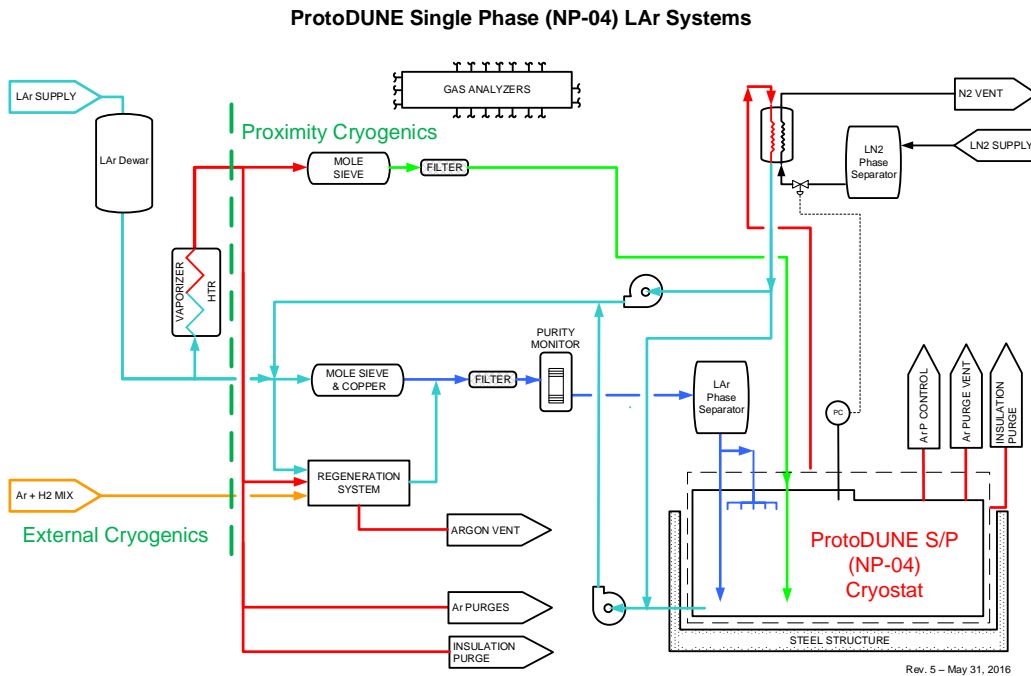


Figure 2.75: Process Flow Diagram

fig:cryo

- 1 • It provides the GAr for the piston purge phase and the GAr make-up.
- 2 • It provides the LAr to the cryostat.
- 3 • It provides the LN2 to the condenser.
- 4 • It provides the cooling power by means of evaporation of liquid nitrogen and condensation of GAr, to the liquid argon cryostat, for its cool-down, normal operation and warm-up phases.
- 5
- 6 • It provides the capability to purify the cryostat liquid argon volume to a level of parts per trillion (ppt) Oxygen equivalent contamination; the purification process uses mole-sieve and active copper.
- 7
- 8
- 9 • It provides the capability to purify the re-condensed boil off before reintroducing it inside the cryostat.
- 10
- 11 • It provides means to cool down the cryostat and the detector following the requirements.
- 12 • It distributes the LAr and GAr inside the cryostat to meet the requirements.

fig:3d-view-cryo-installation

Figure 2.76 shows a 3D view of the cryogenic installation as currently designed. The red and green lines entering from the bottom of the figure are the LN2 and LAr supply lines, respectively, from the external cryogenics.

fig:int-cryogenics-detail

Figure 2.77 shows a 3D view of a detail of the internal cryogenics: the cryostat and detector cool down manifolds at the top of the cryostat.

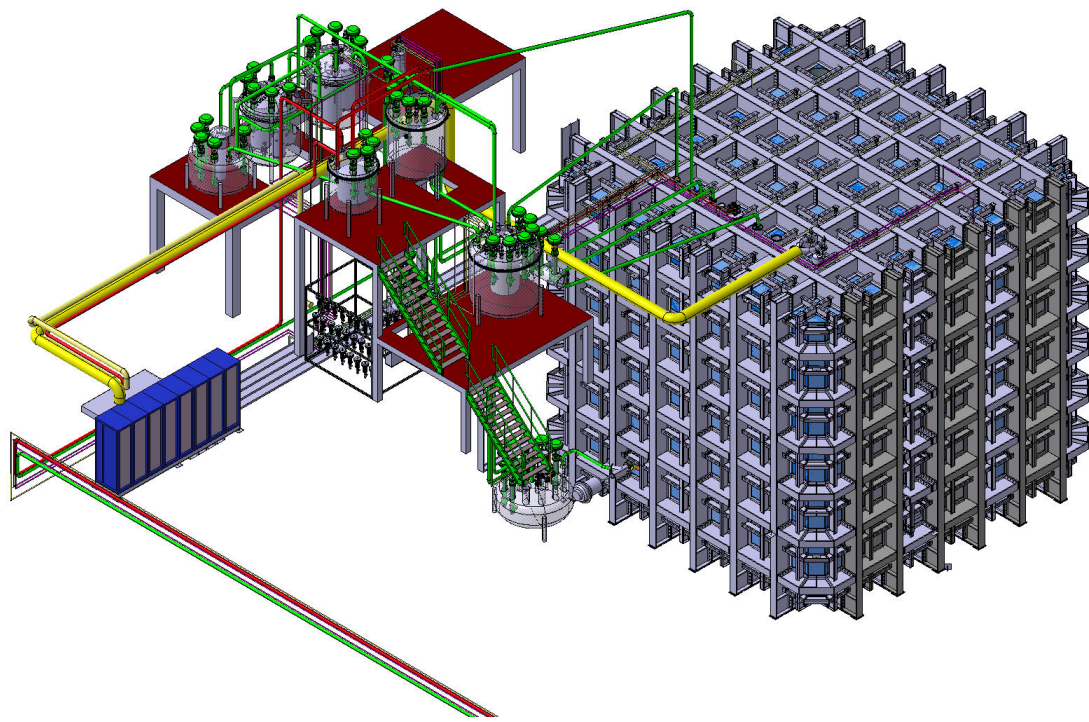


Figure 2.76: 3D model of the installation

fig:3d-v

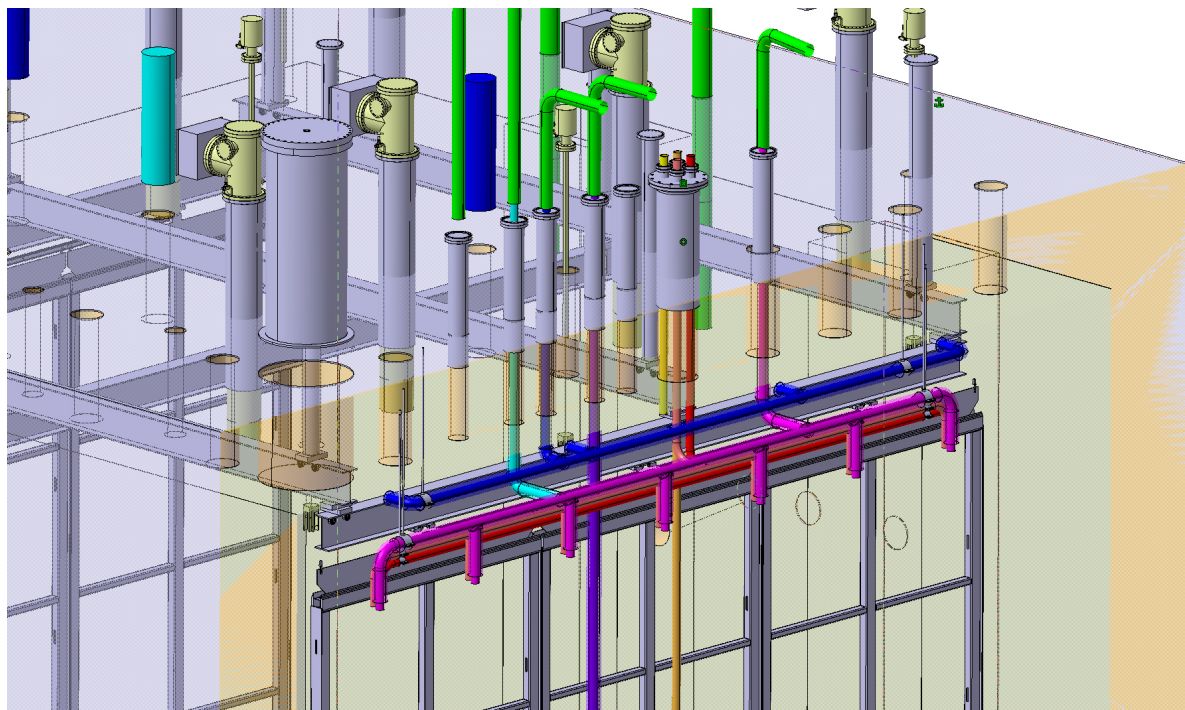


Figure 2.77: Detail of the internal cryogenics

fig:int-

- 1 There is a common receiving facility for NP-02 and NP-04 located outside the building, from which
- 2 Argon and Nitrogen lines take LAr, GAr, and LN₂ to the respective installations.
- 3 A 50 m³ (69 tons of LAr capacity) vertical dewar will allow for receipt of LAr deliveries for the
4 initial filling period. This liquid argon dewar serves also as a buffer volume to accept liquid argon
5 during the fill period. An analyzer rack with instruments to check water, nitrogen, and oxygen
6 content of the delivered LAr batches will also be located in the vicinity. A 55-kW vaporizer is used
7 to vaporize the liquid argon from the storage dewar prior to delivery to the GAr pipes.
- 8 The cryostat will have its own argon condenser (16 kW of cooling power), argon-purifying equip-
9 ment and overpressure protection system. The full power of the argon condenser is used during
10 the initial cool down phase only, which is expected to take two to three weeks.
- 11 A 50 m³ vertical dewar (40-t LN₂ capacity) will allow for receipt of LN₂ deliveries and storage of
12 LN₂ for cool down and normal operations. LN₂ is flown into the heat exchanger of a condenser
13 located in close proximity of the cryostat to recondense the boil-off GAr coming from the cryostat
14 itself.
- 15 Two LAr recirculation pumps are placed outside of the membrane cryostat to circulate liquid from
16 the bottom of the tank through the purifier and then back to the tank to ensure the needed LAr
17 purity. The purification filters are located in the vicinity of the cryostat. The filters contain dual
18 media, a molecular sieve for removal of water and a copper coated catalyst media for oxygen
19 removal. There is one gas filter that is used during the purge in closed loop phase and two liquid
20 filters used during the filling and normal operations to continuously purify the bulk of the LAr
21 inside the cryostat. Associated with the filters, there will be regeneration equipment such as heaters
22 and a Ar/H₂ mix. Before the Ar is returned to the cryostat, the LAr flows into a phase separator:
23 the liquid is taken from the bottom and delivered to the cryostat, while the gas is returned to the
24 condenser.

25 2.12.3 Modes of operation

- op-modes
- 26 The major functions of the cryogenics system servicing the cryostat are to supply cryogens for
27 cool down and fill, and to provide gas argon filtration and condensing, liquid argon filtration and
28 circulation. The methods presented in this section are motivated by experience from the cryogenic
29 systems of other LAr Time Projection Chamber (TPC) experiments, such as ICARUS, LAPD, the
30 35 ton detector and MicroBooNE.

- 31 **Cryostat piston purge** After the cryostat construction and following the installation of all sci-
32 entific equipment, the cryostat will be cleaned and purged in preparation for cool down and filling.
33 Construction procedures leading up to this point will ensure that the completed cryostat does not
34 contain debris and is free of all loose material that may contaminate the LAr.

Purge in open loop Argon piping will be isolated, evacuated to less than 0.1 mbar absolute pressure and backfilled with high-purity argon gas. This cycle will be repeated several times to reduce contamination levels in the piping to the ppm level. The reference-design choice for removing air from the membrane cryostat will be to flow/piston-purge argon, introducing the heavier argon gas at the bottom of the tank and removing the exhaust at the top. The exhaust will be taken from the main GAr outlet, but also from all the side ports located on each penetration through the roof to ensure that all volumes (especially trapped volumes) are properly purged.

The flow velocity of the advancing GAr will be set to 1.2 m/hour. This is twice the diffusion rate of the air downward into the advancing argon so that the advancing pure argon-gas wave front will displace the air rather than just dilute it. A 2D ANSYS model of the purge process shows that after about 13 hours of purge time and 2 volume changes, the air concentration will be reduced to less than 1%. At 44 hours of elapsed time and seven volume changes, the purge process is complete with residual air reduced to a few ppm. This simulation includes a representation of the perforated field cage at the top and bottom of the detector and heat sources due to the readout electronics.

The Computational Fluid Dynamics (CFD) model of the purge process has been verified in multiple arrangements: (1) in an instrumented 1 m-diameter by 2 m-tall cylinder, (2) in LAPD, a 3 m-diameter by 3 m-tall cylindrical tank where gas-sampling measurements were at varying heights and times during the purge process, and (3) within the 35 ton membrane cryostat, the prototype vessel built at FNAL in 2013. The results of these tests are available in [19] and [20]. Once the residual air inside the tank is at the the ppm level, the process continues in the closed loop configuration.

Purge in closed loop Water and oxygen will continue to be removed from the system for several days following the initial purge. During this step the GAr is no longer exhausted but recirculated through the GAr purifier and sent back to the bottom of the cryostat. The cryostat contains a relatively large amount of FR4 circuit-board material and a smaller inventory of plastic-jacketed power and signal cables. These somewhat porous materials may contain as much as 0.5% water by weight. Water-vapor outgassing from these materials will be entrained in the gas flow exiting the top of the cryostat and will be removed from the gas stream by filters. Adsorbed water will also be removed from the metallic inner surfaces of the cryostat and piping system. Water deep within porous materials will remain; this is not a problem since the water diffusion rate in FR4 at room temperature is already quite low ($0.3 \text{ } (\mu\text{m})^2/\text{s}$) and the FR4 assemblies are relatively thick (1 cm).

This process reduces the oxygen and water contamination inside the cryostat to sub-ppm levels, at which point the cool down may commence.

Cool-down Purified LAr will be mixed with GAr and distributed by a set of dedicated sprayers near the top of the cryostat and on the side of the TPC to cool down the cryostat and the detector in a controlled way. The sprayers deliver a mix of LAr and GAr in atomized form that is moved inside the cryostat by another set of sprayers flowing GAr only. Part of the boil-off gas is re-condensed inside the condenser and it then flows back as liquid to feed the LAr sprayers. The balance is vented during the process. Simulations have shown that this cool-down method can

¹ maintain the cool down requirements of the detector, as listed in Table 2.10¹, and those of the
² cryostat, which are less stringent. The required cooling rate is determined by the maximum stress
³ that detector components can tolerate. For example, the 150 μm APA wires will cool much more
⁴ rapidly than the APA frames. A temperature-monitoring system (provided by the detector) will
⁵ be used to control the temperature difference across the cryostat and the detector.

⁶ **Filling** Once the cryostat and the TPC are cold, LAr is introduced in the cryostat through the
⁷ cryostat filling pipework. Argon is transferred directly from the LAr storage tank after passing
⁸ thorough the LAr filtration system for purification. The filling process will take place over three
⁹ to four weeks if two trucks per day are delivered; if only one truck per day is delivered, it will take
¹⁰ twice as long.

¹¹ **Steady state operations** During steady state operations :

- ¹² • LAr is continuously circulated and purified by means of an external LAr pump (two are
¹³ installed for redundancy, but only one is in use at a time).
- ¹⁴ • Boil-off GAr is re-condensed in a condenser situated outside the cryostat and purified before
¹⁵ being reintroduced as LAr. The re-condensed LAr is sent to the LAr filtration system by
¹⁶ means of a dedicated LAr pump and mixed in line with the bulk of the liquid coming from
¹⁷ the cryostat. Alternatively, it is possible to send it to the inlet of the main LAr circulation
¹⁸ pumps and from there as a single LAr stream to the filtration system.

¹⁹ **Emptying** At the end of operations (or if/when maintenance on the tank is needed) the tank is
²⁰ emptied and the LAr removed. The LAr is returned to the storage tank outside the building and
²¹ from there unloaded back to LAr tankers.

²² **Parameters** Table 2.10 presents a list of relevant parameters for the installation. The filling flow
²³ rate of 18 l/min (0.42 kg/s) is an estimate. The actual value might be limited by the pressure
²⁴ inside the LAr storage dewar. We are also assuming that we are able to receive 2 trucks/day of
²⁵ LAr, which will need to be confirmed by the suppliers.

²⁶ 2.12.4 Features

²⁷ This section briefly describes the main features of the various parts of the cryogenic system.

²⁸ **External Cryogenics** The external cryogenics comprises the Liquid Argon and Liquid Nitrogen
²⁹ receiving facilities, the LAr/GAr and LN2 distribution systems, the Argon/Hydrogen mixture to
³⁰ regenerate the LAr/GAr purification filters and the mechanical filters on the LAr filling line.

Table 2.10: List of engineering parameters for cryogenics installation

Mode	Parameter	Value	Notes
Piston purge	GAr flow rate	88 m ³ /hr	From 1.2 m/hr
Cooldown	Maximum cool-down rate TPC	40 K/hr	T sensors on the detector responsibility of detector
Cooldown	Maximum delta T between any two points in the detector	50K	T sensors on the detector responsibility of detector
Filling (*)	LAr filling flow rate	18 l/min (0.42 kg/s)	Assuming 2 trucks/day
Normal ops	Cryostat static heat leak	3.0 kW	GAr boil-off (18 g/s)
Normal ops	Other heat loads (estimate)	5.0 kW	Total estimate is ~8 kW
Normal ops	LAr circulation (5 days turnover)	72 l/min (1.67 kg/s)	72 l/min (1.67 kg/s)
Emptying	Nominal flow rate emptying	72 l/min (1.67 kg/s)	
All	Condenser size	16 kW	

¹ The cryostat will hold an inventory of 760 ton of liquid argon. The standard grade specification for argon is a minimum purity of 99.995%, allowing a maximum concentration of 5.0 ppm for O₂ and 10.5 ppm for H₂O.

⁴ This implies that N₂ is at the level of 30-35 ppm - way too bad for the Scintillation Light .. practically unacceptable, as it would imply a loss of 70% of the light due to N₂ quenching.

⁵ This is designated as Grade 4.5 in the gas-supply industry. Requiring higher-purity product might increase the cost and push out the schedule. Suppliers may also decide not to quote for such an amount of a higher purity fluid. Therefore, standard product will be procured.

⁸ Facilities are required for the offloading of LN₂ and LAr road tankers. Vehicle access and hard-surfaced driving areas are being constructed adjacent to the LN₂/LAr dewars and the LAr/LN₂-supply pipes. A LAr storage dewar will hold the contents of a road tanker in order to minimize off-loading time. Road tankers will connect to a manifold and will use their on-board pumps to transfer the LAr to the storage dewar. The LAr will be stored and transported as a liquid inside the cryostat during the filling process. A battery of fourteen (14) 12-bottle racks containing 1.5% Hydrogen (by volume) and a balance of Argon will be stored outside the building as well. They will be used to regenerate the LAr and GAr purification filters as needed. One 1-micron mechanical filter is located on the LAr feed line. It prevents dirt and impurities from the LAr supply to enter the purification system and the cryostat.

¹⁸ **Proximity Cryogenics** The Proximity Cryogenics comprises the argon condenser, the purification system for the LAr and GAr, the LAr circulation pumps, and the LAr/LN₂ phase separators:

²⁰ **Argon reliquefaction and pressure control** The high-purity liquid argon stored in the cryostat will continuously evaporate due to the unavoidable heat ingress. The argon vapor (boil-off gas) will

- 1 be recovered, chilled against a stream of liquid nitrogen, condensed and returned to the cryostat.
 2 A closed system is required in order to prevent the loss of the high-purity argon. The re-condensed
 3 boil-off can be returned to the cryostat in three ways:
- 4 1. With a small LAr pump that sends it into the main LAr circulation stream (normal mode).
 5 2. Directly to the condenser (emergency mode, when we cannot go through the purification
 6 system).
 7 3. To the inlet of the main LAr circulation pumps (when the small LAr pump needs mainte-
 8 nance, to guarantee a continuous purification of the boil-off GAr).
- 9 During normal operation the expected heat ingress of approximately 8 kW to the argon system
 10 will result in an evaporation rate of 30 g/s and expanding in volume by a factor of 200 when it
 11 changes from the liquid to vapor phase. This increase in volume within a closed system will, in
 12 the absence of a pressure-control system, raise the internal pressure.
- 13 Argon vapor will also be removed from the top of the cryostat through the chimneys that contain
 14 the cryogenic feedthroughs. As the vapor rises, it cools the cables and feedthrough, thereby
 15 minimizing the outgassing. The exiting gaseous argon will be directed to the same condenser as
 16 above, in which it is chilled against a stream of liquid nitrogen and condensed back to a liquid. As
 17 the argon vapor cools, its volume reduces and, in the absence of pressure control, further gas would
 18 be drawn into the heat exchanger, developing a thermal siphon. Therefore, a pressure-control valve
 19 on the boil-off gas lines will control the flow to the condenser to maintain the pressure within the
 20 cryostat at $0.113 \text{ MPa} \pm 0.003 \text{ MPa}$. The liquid nitrogen stream (that provides the coolant for the
 21 condenser) will be supplied from the LN2 phase separator, which is fed by the LN2 storage dewar
 22 located outside of the building. After the heat exchanger the returning N2 vapor is exhausted
 23 outside the building. The estimated heat loads to the argon system are listed in Table 2.11. [tab:cryostat-est-heat](#)

Table 2.11: Estimated heat loads within the cryostat

Item	Heat Load (kW)
Insulation Heat Loss	3.0
All other contributions (Recirculation pumps, pipes, filters, electronics, etc.)	5.0
Total	8.0

- heatload
- 24 **Argon purification** The cryostat is designed with one penetration below the liquid level for
 25 external pumps used to transfer LAr from it to the purification system. The pumps are inserted
 26 into a valve box that is an integral part of the proximity cryogenics. The pump suction must be
 27 located at a minimum distance (normally about 1.5 to 2.0 m) below the lowest liquid level at which
 28 they are to pump in order to prevent cavitation and vapor-entrainment. There are two pumps for
 29 continuous operation during maintenance, but only one is expected to be in service at any moment
 30 in time.

- 31 The liquid-argon volume will turn over every 5.5 days, which corresponds to 1.67 kg/s (72 l/min)

1 of flow rate. As a point of comparison, ICARUS T600 has a maximum turn-over rate of eight to
2 ten days.

3 The multiple-pump arrangement provides a high level of redundancy, which will extend the
4 maintenance-free operating period of the cryostat.

5 The liquid purification system, located nearby the cryostat, consists of two sets of three filter
6 vessels containing molecular-sieve (1) and copper media (2) filters. They have been arranged in
7 this configuration to reduce the size of the valve box containing them. Each molecular-sieve filter
8 is 0.4 m in diameter by 0.9 m tall and contains 80 kg of media. Each copper filter is 0.6 m in
9 diameter by 1.3 m tall and contains 298 kg of media. The filters are sized to provide effective
10 media usage at low pressure drop over the expected range of flow rates. They are used during the
11 filling and normal operations.

12 The gas purification system, located nearby the cryostat as well, is used to purify the GAr for the
13 purge in close loop process. It consists of one filter vessel containing molecular-sieve and copper
14 media filters in the same vessel. The mol sieve part measures 0.3 m in diameter by 0.1 m tall and
15 contains 5 kg of media. The copper part measures 0.3 m in diameter by 0.6 m tall and contains
16 34 kg of media.

17 During the filling the LAr will flow through the liquid filtration, then the LAr phase separator and
18 into the cryostat.

19 After the filling is completed, the cryostat liquid argon inventory is continuously circulated through
20 one set of liquid purification filters for oxygen and water in order to quickly reduce and maintain the
21 impurity concentration at the level of < 100 ppt oxygen equivalent, matching the required electron
22 lifetime of the TPC detector. A dedicated special device, originally developed by ICARUS (usually
23 indicated as "Purity Monitor"), for the measurement of the impurity concentration in liquid argon
24 will be located immediately downstream the filtration system, providing information about the
25 quality of the liquid and correspondingly about the actual level of impurity removal efficiency
26 of the filter. After the filter the ultrapure argon is returned back to the cryostat via the LAr
27 phase separator. Purity monitors will also be resident inside the cryostat, measuring the electron
28 lifetime at different depths of the LAr volume. The purity monitors (provided by the ProtoDUNE-
29 SP collaboration) are described in greater detail in Section 2.13.1. section-dev-sensors

30 The filter material, composed by molecular sieve pellets to remove water and by alumina porous
31 granules covered by highly active metallic copper for catalytic removal of O₂ by Cu oxidization,
32 is subject to saturation when the trapped/reacted impurity budget exceeds the removal capacity
33 of the filter material. When this occurs (signaled by the fast drop of LAr purity level detected by
34 the external purity monitor) the liquid argon flow is switched to the back-up, ready-for-use filter
35 and the saturated one is regenerated in-situ.

36 The filter regeneration process is done in subsequent steps. The saturated filter is first warmed up
37 with heated argon gas to an elevated temperature driving into the gas the water captured by the
38 molecular sieve media. A gas mixture of 1.5% hydrogen (reducing agent) with a balance of argon
39 (inert carrier) at high temperature (500 K) is then used for the reduction of the copper oxide back
40 to metallic copper. Water produced by the reduction process is vented out with the gas flow. The

¹ regenerated filter is finally cooled down and ready to be switched into service.

² **Internal Cryogenics** Internal piping is positioned inside the cryostat to support the air purge and
³ cool-down processes, but also the LAr distribution during filling and normal operations. During
⁴ air purge argon gas is injected at the bottom of the cryostat and distributed through a set of pipes
⁵ that pushes the air up and forces it out from the roof. The flow nozzles will be directed
⁶ downward and to the side so that the injection velocity will not cause local vertical gas plumes
⁷ or turbulent mixing but rather will spread across the bottom of the tank and produce a stable,
⁸ upwardly advancing argon wave front. The vertical velocity of 1.2 m/hr for the gas purge includes
⁹ a contingency for some level of turbulent mixing. In addition to the main vent, all nozzles and
¹⁰ dead-end (stagnant) volumes located at the top of the cryostat will have gas-exhaust lines for
¹¹ the initial purge and for continuous sweep-purge of those volumes during normal operations. The
¹² sweep-purge during the initial stage of purging will be vented outside of the building, whereas the
¹³ sweep-purge during normal operations will be re-condensed and recirculated as liquid.

¹⁴ The cool-down of the cryostat and detector is performed through a set of manifolds flowing LAr
¹⁵ (one) and GAr (two). The LAr manifold and a GAr manifold are joined together and terminate
¹⁶ with a set of sprayers that deliver a mist of LAr and GAr. This mist is circulated within the
¹⁷ cryostat by a jet of GAr coming from the other manifold, which also terminates with sprayers.
¹⁸ These manifolds are located on the Jura side and are off to the side of the TPC so as not to flow
¹⁹ LAr and GAr directly over the detector itself. The chosen sprayers guarantee a flat profile of the
²⁰ fluid (LAr and GAr) coming out.

²¹ During filling and normal operations, the LAr-supply pipework distributes the LAr at the bottom
²² of the cryostat. The outlets are at the end of the pipes, as far away as possible from the side
²³ penetration from which the LAr is sent to the purification system.

²⁴ 2.12.5 Cryostat pressure control

²⁵ The pressure inside the cryostat is maintained within a very narrow range by a set of active
²⁶ controls. There are pressure control valves that can increase or decrease the cooling power in the
²⁷ condenser by controlling the amount of LN₂ flowing to the heat exchanger and being vented. Other
²⁸ pressure control valves can be used to vent GAr to atmosphere and/or introduce clean GAr from
²⁹ the storage, as needed. The system is always in place, from the initial purge to the emptying of
³⁰ the cryostat at the end of operations.

³¹ **Normal Operations** The pressure-control valves are sized and set to control the internal cryo-
³² stat pressure under normal operating conditions to the nominal design pressure of 0.113 MPa.
³³ Fluctuations within the range 0.105 MPa (80 mBarg) to 0.120 MPa (230 mBarg) will be allowed.
³⁴ Excursions of a few percent (exact values to be determined) above or below these levels will set off
³⁵ warnings to alert the operator to intervene. Further excursion may result in automatic (executive)
³⁶ actions. These actions may include stopping the LAr circulation pumps (to reduce the heat ingress
³⁷ to the cryostat), increasing the argon flow rate through the condenser, increasing the LN₂ flow

1 through the heat exchanger inside the condenser, powering down heat sources within the cryostat
 2 (e.g., detector electronics), venting some of the GAr to reduce the pressure in a controlled way.
 3 Eventually, if the pressure continues to rise, it will trigger the Pressure Safety Valves (PSVs) to
 4 operate.

5 If the pressure decreases, we can introduce fresh GAr in the cryostat through the GAr make-up
 6 line, a dedicated GAr feed line that takes argon directly from the outside supply. If the pressure
 7 continues to decline, it will trigger the Vacuum Safety Valves (VSVs) to operate. Table 2.12
 8 summarizes the cryostat pressures during normal operation.

Table 2.12: Cryostat pressures during normal operations

Cryostat part	Pressure
Vessel ullage pressurization	0.100 MPa (30 mBarg)
Pressure regulation	0.110 MPa (140 mBarg)
Vessel ullage depressurization	0.125 MPa (280 mBarg)
Relief valve set pressure	0.135 MPa (380 mBarg)
Warm structure design working pressure	0.135 MPa (380 mBarg)

9 The ability of the control system to maintain a set pressure is dependent on the size of pressure
 10 upsets (due to changes in flow, heat load, temperature, atmospheric pressure, etc.) and the volume
 11 of gas in the system. The reference design has 0.4 m of gas at the top of the cryostat. This is
 12 5% of the total argon volume and is the typical vapor fraction used for cryogenic storage vessels.
 13 Reaction times to changes in the heat load are slow and are typically on the order of an hour.

14 **Overpressure control** In addition to the normal-operation pressure-control system, it is planned
 15 to provide a cryostat overpressure-protection system. This must be a high-integrity, automatic,
 16 failsafe system capable of preventing catastrophic structural failure of the cryostat in the case of
 17 excessive internal pressure.

18 The key active components of the planned system are Pressure Safety Valves (PSVs) located on
 19 the roof of the cryostat that will monitor the differential pressure between the inside and the
 20 outside of the cryostat and open rapidly when the differential pressure exceeds a preset value. A
 21 pressure-sensing line is used to trigger a pilot valve which in turn opens the PSV. The PSVs are
 22 self-contained devices provided specially for tank protection; they are not normally part of the
 23 control system.

24 The installation of the PSVs will ensure that each valve can periodically be isolated and tested
 25 for correct operation. The valves must be removable from service for maintenance or replacement
 26 without impacting the overall containment envelope of the cryostat or the integrity of the over-
 27 pressure protection system. This normally requires the inclusion of isolation valves upstream and
 28 downstream of the pressure-relief valves and at least one spare installed relief valve ($n+1$ provision)
 29 or the use of a diverter valve that allows one valve to be always connected to the cryostat.
 30 When the valves open, argon is released, the pressure within the cryostat falls and argon gas
 31 discharges into the argon vent riser. The valves are designed to close when the pressure returns
 32 below the preset level.

¹ **Vacuum-relief system** The cryostat vacuum-relief system is a high-integrity, automatic, failsafe system designed to prevent catastrophic structural failure of the cryostat due to low internal pressure. The vacuum-relief system protects the primary membrane tank. Activation of this system is a non-routine operation and is not anticipated to occur during the life of the cryostat.

⁵ Potential causes of reduced pressure in the cryostat include operation of discharge pumps while the liquid-return inlet valves are shut, gaseous argon condensing in the condenser (a thermo-siphon effect) or a failure of the vent system when draining the cryostat. Vacuum-relief valves are provided on LNG storage tanks to protect the structure from these types of events.

⁹ The key active components of this additional protection system are Vacuum Safety Valves (VSVs) located on the roof of the cryostat that will monitor the differential pressure between the inside and the outside of the cryostat and open when the differential pressure exceeds a preset value, allowing air to enter the cryostat to restore a safe pressure. A combo PSV-VSV may be used instead of two separate devices, one for overpressure and one for vacuum.

¹⁴ 2.13 Detector monitoring and slow control

¹⁵ The scope of the ProtoDUNE-SP detector control system (DCS) includes the design, procurement, fabrication, testing, and delivery of a comprehensive detector monitoring, control and safety system.

¹⁸ The responsibility for the system is split between ProtoDUNE-SP and CERN:

- ¹⁹ • The ProtoDUNE-SP collaboration is responsible for all the devices that will be installed and cabled inside the cryostat, the sensors needed to monitor the cryostat and its content, and the specifications for the system.
- ²² • CERN is responsible for the implementation of the control system elements outside the cryostat (hardware, firmware and software), including the high-voltage and low-voltage power supplies necessary for the detector operation.

²⁵ This section describes the main requirements, constraints and assumptions of the control system, and its general structure and components.

²⁷ 2.13.1 Monitoring devices and sensors

²⁸ A number of devices and sensors will be located inside the cryostat for either periodic or continuous monitoring of the LAr as well as the GAr in the ullage, and for the monitoring of the detector functionality.

³¹ A short section on requirements here would be useful

1 Purity Monitors

2 Three purity monitors (PrM) with sensitivity in the ppt range will be used for the direct determina-
 3 tion of the impurity content of the LAr inside the ProtoDUNE-SP cryostat. These PrMs have
 4 been generously provided by ICARUS [?]

5 Can't find citation in bib file

6 after being decommissioned from the T600. The design has been replicated for MicroBooNE and
 7 other R&D test experiments at FNAL. Inside the ProtoDUNE-SP the monitors are arranged in
 8 a single vertical string located behind the APA planes on the Jura side (see Figure 4.2). The
 9 string hangs from the large blanking flange on the manhole, and ports with ConFlat sealing on
 10 the blanking flange will be made available for HV/Signal/OptFiber feedthroughs. The string is
 11 about 7 m long, with the three PrMs strung at different heights: one near the LAr surface, one at
 12 mid-height, and one at the very bottom near the LAr-return manifold, for monitoring the purity
 13 of the LAr entering the cryostat after the filtration process.

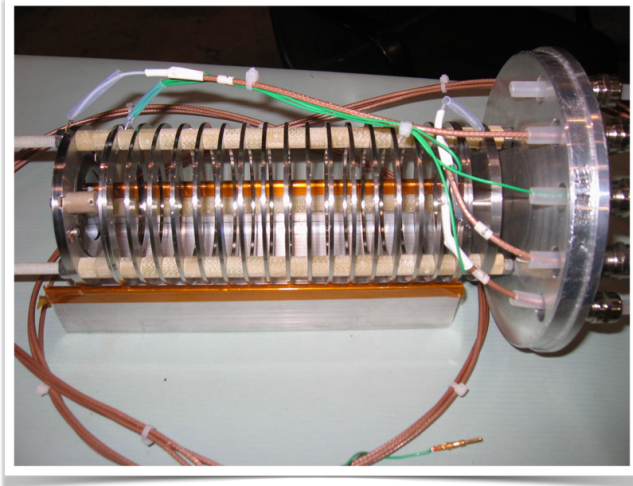


Figure 2.78: Picture of a purity monitor from the ICARUS T600, now available for installation in the ProtoDUNE-SP detector

¹⁴ ^{fig:IcaPrM} Figure 2.78 was not referenced; I added one. It's pretty, but not very informative. It could use more description like “the 16(?) divisions in the device are the whatever, and the connection on the right is ...” Or we could take it out.

¹⁵ The three PrMs, one of which is pictured in Figure 2.78, are currently being refurbished with new
 16 gold photocathode and new quartz fiber. The drift length (25 cm) is the same for all them. Using
 17 parts of another (available) PrM to extend the drift length of one of the three (e.g., to 40 cm)
 18 for more precise measurements of the longer e^- lifetimes is currently under consideration. The
 19 mechanical structure of the string, the anchorage to the manhole flange at the top end, and the
 20 fastening of the string at the bottom are still under study. An additional PrM at the bottom on
 21 the opposite side of the cryostat would be useful for monitoring variations in the quality of the

1 LAr at that level, and providing information for the fluid-dynamics computation inside the cryostat.
2

3 **Vertical Temperature Gradient Monitor**

4 Precise monitoring of the temperature gradient as a function of LAr depth is an important input
5 for fluid dynamics modeling and simulations. The installation of a set of devices with precision
6 better than 50 mK along the entire height of the LAr volume has recently been included in the
7 internal instrumentation plan for this purpose. Commercial calibrated resistance temperature
8 detectors (RTDs – Pt100 or Pt1000) with 15-mK precision at LAr temperature are well suited to
9 this application, however the temperature probe wiring and signal transport outside the cryostat
10 require extreme care in order to maintain the intrinsic precision of the probe.

11 The design for this device consists of a series of 25 Pt100 probes positioned at ~30 cm intervals
12 along a ~7.5-m-long rigid string hanging behind the APA plane from an available port at the
13 top of the cryostat. A special multi-pin FT is mounted on the flange for the signal extraction
14 and readout from a temperature controller. Again, the mechanical structure, including the cable
15 routing up to the multi-pin FT, is still subject to a detailed engineering study. A number of RTDs
16 will also be positioned on the APAs and on the cryostat walls at different heights to monitor the
17 temperature during the cooling process.

18 **Webcams**

19 Based on a system developed by ETH Zurich for WA105, six commercial webcams, sealed inside
20 a specially developed metal case with a ConFlat optical window to allow operation at cryogenic
21 temperatures, are located inside the cryostat. They are positioned at strategic points allowing
22 inspection of the interior during filling and commissioning, and detection (and recording) of possible
23 sparks in locations exposed to high electric field intensity.

24 **Level Meters**

25 Reliable LAr level determination is required in the ±20 cm around the nominal LAr surface
26 level. Commercially available liquid-level sensors provide high-reliability monitoring. These are
27 available in multiple technologies, including solid-state electro-optical, conductive, capacitive and
28 piezo-resonant. Although the technology choice has not been madedesigned ports on the top of
29 the cryostat are available for this instrumentation. The vertical temperature gradient device will
30 provide a coarse level reading during filling and a differential pressure transducer will also provide
31 additional indication about LAr level.

32 the temp gradient device provides “coarse” measurement, but this device provides “reliable”
measurement, not “precise” measurement. Pls clarify

1 Pressure Sensors

2 Precise measurement of pressure in the GAr ullage is necessary. A number of pressure sensors,
3 including a differential pressure transducer, are planned, and designated ports on the top of the
4 cryostat are available for this instrumentation.

5 2.13.2 Slow Control System

6 The design of the ProtoDUNE-SP safety and control system is largely based on the experience
7 gained in collaboration with ETH Zurich during the pilot WA105 project at CERN. The compo-
8 nents of this system and their functions are as follows:

- 9 • The Process Control System (PCS) reads temperature sensors including the Vertical T Gra-
10 dient monitor, pressure sensors and the purity monitors inside the cryostat and the trace
11 analyzers (O_2 , N_2 , H_2O) in the external recirculation line.
- 12 • The Detector Control System (DCS) monitors and controls the low voltage (LV) and high
13 voltage (HV) from the power supplies.
- 14 • The Detector Safety System (DSS) performs temperature surveys and monitors interlocks.

15 The system provides a graphical user interface to visualize the trends of monitored values, the
16 alarms, and to control the

17 operation of the?

18 experiment. A web interface allows remote monitoring of the behavior of the experiment.

19 relating ‘control the experiment’ and ‘monitor behavior of experiment,’ it seems out of order.
Can you start with monitor and then say control?

20 The physical interface of the control system is located at the level of the outer flanges on the
21 cryostat.

22 Where is this shown?

23 CERN EP/DT-DI will take care of connecting the control system to the flanges and interfacing
24 to the cryogenics control infrastructure for information and signal exchange. The ProtoDUNE-SP
25 experiment is responsible for all sensors, power distribution, etc., inside the cryostat, as well as for
26 defining the system specifications, I/O parameters and control & safety logics.

27 logic or logistics?

1 The supervisory control of the system and data acquisition (SCADA) will be developed, tested
2 and provided by CERN EP/DT-DI.

3 still ‘will be developed’?

4 Figure 2.79 shows the general architecture of the control and safety system for ProtoDUNE-SP,
5 including the PCS, the DCS and the DSS.

6 The control system is composed of:

- 7 • a chassis for electrical distribution (380 Vac, 220 Vac, 24 Vdc redundant);
- 8 • two chassis for the PCS, composed of an FPGA, signal conditioners, interface, and cabling;
- 9 • one chassis for the DCS, composed of an interface for LV/HV monitoring & control;
- 10 • a chassis for the DSS, composed of an FPGA and relays for the safety of the experiment;
- 11 • a chassis for a PC data acquisition & supervision (PVSS SCADA Supervisor), composed of
12 a computer with a display monitor, a switch and a server;
- 13 • four chassis for the remote I/O to capture signals close to the detector and to avoid multi-
14 cabling structure; and
- 15 • one chassis for the HV, controlled by the slow-control system.

16 All these elements will be mounted in 19-in. racks.

17 The supervisory software is based on the JCOP framework, an integrated set of software tools
18 originally developed for the control of the LHC experiments at CERN and now used in several
19 more experiments at CERN. Besides providing a supervisory control and data acquisition system,
20 the framework offers many tools for the implementation of finite state machines, archival of data,
21 as well as graphical interfaces as web dashboards.

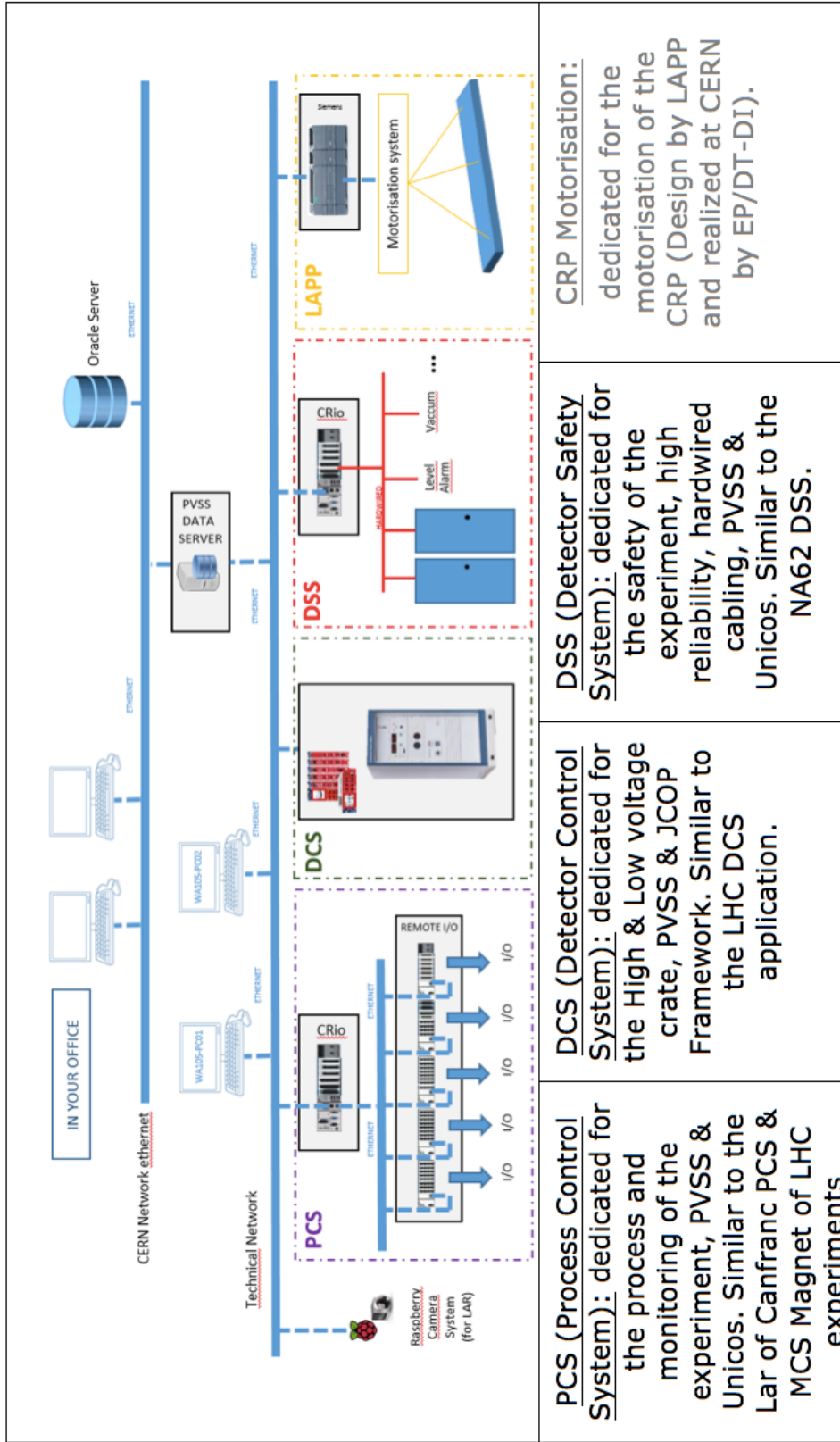


Figure 2.79: Proposed architecture and technical solution of the control and safety system.

fig:dcsd

¹ Chapter 3

² Software and Computing

³ 3.1 Overview

- ⁴ This chapter outlines the technical design of the offline computing system and introduces the
- ⁵ software that will be used to simulate and reconstruct ProtoDUNE-SP data.

- ⁶ The data rate and the total data volume are the main factors influencing the design choices
- ⁷ and scale of the offline computing system. The ^{data managm sys} system provides resources necessary for data
- ⁸ distribution, processing, and analysis on the grid[21].

- ⁹ The planned data processing steps include calibration, reconstruction, ntupleizing and user analysis.
- ¹⁰ Multiple passes through this chain will be required for final results, as calibrations, algorithms,
- ¹¹ and ntuple definitions are expected to evolve.

- ¹² A fraction of the data will be subject to *prompt processing*, which performs partial reconstruction
- ¹³ of the data for QA/QC purposes with a short turnaround time (see 3.3.2). A metadata and file
- ¹⁴ catalog system is necessary for managing the data.

¹⁵ 3.2 Data storage and management system

¹⁶ 3.2.1 Data characteristics

- ¹⁷ The characteristics of the raw ProtoDUNE-SP data are defined by the properties of the TPC:

- ¹⁸ • the multiple wire planes, the fine wire pitch, and the resulting high channel count;

- ¹⁹ • high digitization frequency (which is essential to ensure a precise position measurement along

1 the drift direction); and

- 2
- relatively slow drift velocity of electrons in LAr, which requires a readout window of the
3 order of milliseconds to collect the ionization in the LAr volume stemming from the event of
4 interest and overlapping cosmic rays.

5 Triggered readouts of the detector (events), contain a large amount of raw data, impacting the
6 bandwidth and storage requirements. The run plan, described in Section 1.4, determines the
7 total number of events, and thus helps define the design requirements for the data storage and
8 management system.

9 The “*ProtoDUNE-SP Data Scenarios*” spreadsheet [4] describes a few possible running conditions.
10 It includes estimates for their resulting data volumes and rates, and interpretations of these es-
11 timates in terms of network and disk bandwidth. The set of conditions labeled as “Central”

12 represents the most likely scenario and is matched to the run plan. Estimates are also provided
13 for data taken out of the spills in order to measure the contributions from cosmic rays. Table 2.8
14 summarizes these estimates.

15 Based on the estimated event size quoted in Table 2.8, the anticipated total raw data volume to
16 be taken during the planned SPS run is 3 PB.

3.2.2 Raw data flow

17 A conceptual diagram of the raw data flow is presented in Figure 3.1. It shows the general logic
18 of the data flow and does not rely on assumptions of specific technical implementations. It also
19 reflects the central role of CERN EOS in the raw data management scheme, which is motivated
20 by the experience and architecture of the LHC experiments.

22 what’s EOS?

23 EOS serves as the staging area from which the data are committed to CASTOR (a hierarchical
24 storage management system developed at CERN) and from which data are transmitted to a number
25 of endpoints including principal data centers such as Fermilab and others. It is also used to provide
26 input to QA and other express processing streams at CERN (Section 3.3.2).

3.3 Offline data processing

27 The data to be processed by the offline system can be classified as follows:

- 28
- A variety of calibration data derived from experimental data, including dedicated calibration
29 runs where necessary, and/or subsamples of data collected specifically for calibration purposes
30 during normal running conditions;

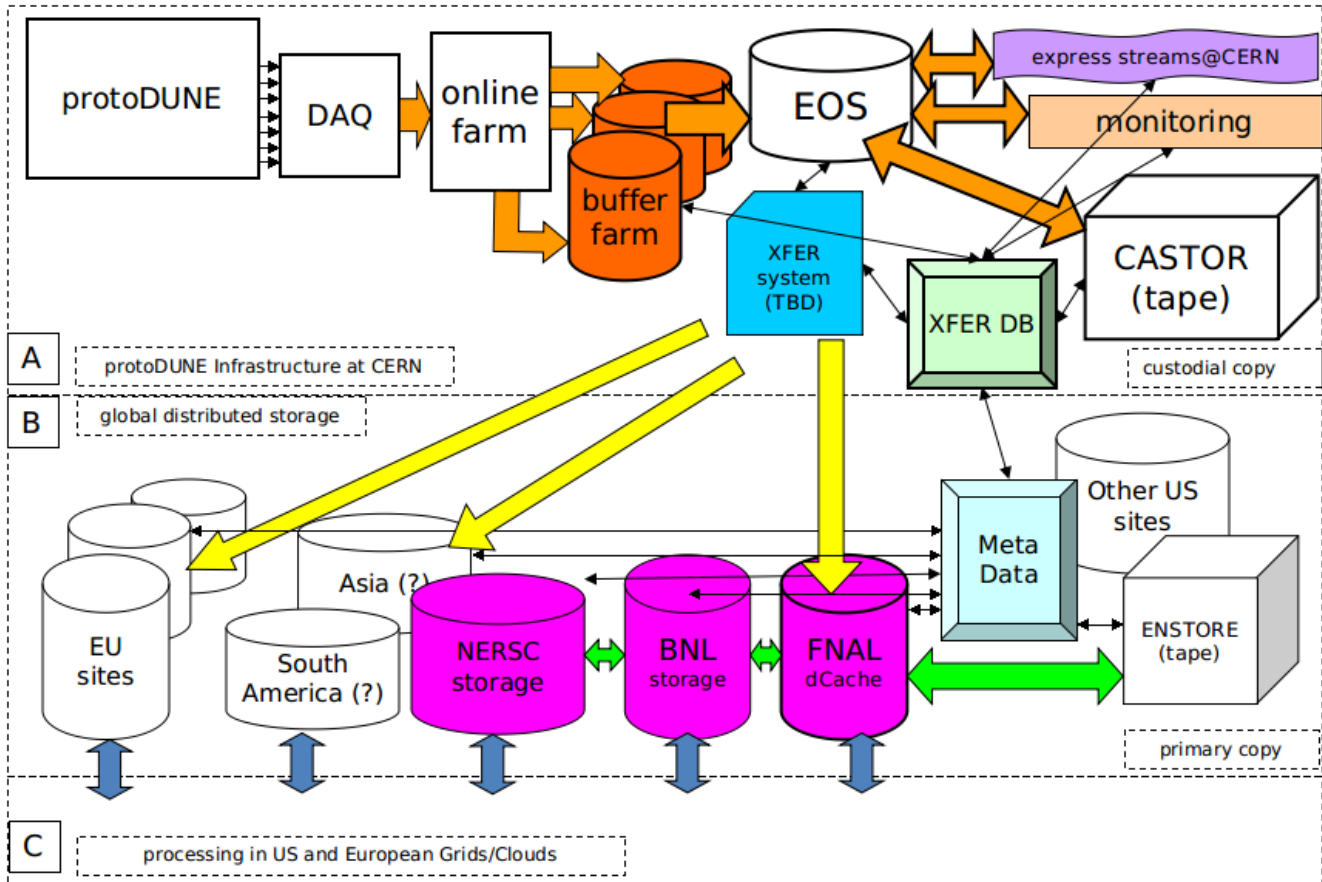


Figure 3.1: Conceptual diagram of the flow of raw data in ProtoDUNE-SP

- 1 Processed experimental data, which may exist in several parallel branches corresponding
2 to different reconstruction algorithms being applied, with the purpose of evaluating the
3 performance of the different algorithms;
- 4 • Monte Carlo (MC) data, which contain multiple event samples to cover various event types
5 and other conditions during data-taking; and
- 6 • Data derived from MC events, and produced with a variety of tracking and pattern recogni-
7 tion algorithms in order to create a basis for the detector characterization.

8 3.3.1 Production processing

9 The production processing will likely have

10 typically has?

11 more than one processing step, thus

1 creating derived data and

2 multiplying the data volume. The volume of the derived data is assumed to be smaller than that
3 for the raw data. Given the anticipated raw data volume, the plan is to provision \sim 10 PB of tape
4 storage to keep the raw and processed data. This includes two copies of the raw data at 3 pb each,
5 two passes of derived data at 1 PB each, and 2 PB of simulation samples. One copy of the raw
6 data may be included as part of the output of the reconstruction, for convenience in comparing
7 raw and reconstructed data objects while also serving the purpose of providing a backup copy of
8 the raw data.

9 For efficient processing, disk storage is necessary to provide access to the data stored on tape.
10 Extrapolating from experience running MC for previous DUNE MC campaigns, it is estimated that
11 a few hundred TB of continuously available disk space is needed for samples that are repeatedly
12 accessed, as well as ntuples for user analysis. The offline system takes advantage of the shared
13 dCache resource

14 dcache reference needed

15 at Fermilab in order to provide efficient access to the data stored on tape.

16 3.3.2 Prompt processing

17 In the present context, *prompt processing* refers to a number of fast signal-processing and recon-
18 struction processes (also called “express stream”) that process a fraction of the raw data. Its main
19 purpose is to aid in QA of the data and produce quick calibrations that may be necessary for
20 detailed monitoring of the detector. For example, calculating the frequency spectra of noise and
21 monitoring its level, evolution and other characteristics is an important aspect of ensuring the
22 stability of the readout chain.

23 A limited number of metrics are calculated in order to make the process as quick as possible,
24 enabling the operators to take action should the QA process indicate a potential problem in the
25 detector or the data.

26 Processing roughly 1% of the data stream collected by the detector is predicted to be enough to
27 meet the most important goals of prompt processing. The general strategy is to locate some of the
28 prompt processing capability at CERN, at a scale adequate for the mid-range data-taking scenario,
29 such as presented in Table 2.8. An estimated 300 cores are needed to cope with processing at that
30 rate.

3.4 The LArSoft framework for simulation and reconstruction

1 cross check with description in DAQ section; there is some tolerable (?) overlap

2 LArSoft [22] is a suite of tools for simulating and reconstructing data collected from LArTPC detectors. It is built on the *art* [23] event-processing framework. The main features of the *art* framework are its configurability by human-readable and editable control files (that use the Fermilab Hierarchical Control Language (*FHiCL*)), and the scheduling of program module execution. The modules are of five types: event sources, filters, data-product producers, analyzers, and output. Common utilities that can be accessed by any program module at any time are called *services*.

9 The *art* framework defines the input/output structure of ROOT-formatted files using TTrees to store the data, metadata, and provenance information. The provenance information consists of the contents of the FHiCL documents used to steer the processing of the job that created a file, and those of input files and parents.

13 give some adjective before ‘file’ e.g., ‘output’?

14 The *art* framework’s division of the simulation and reconstruction jobs into modular pieces allows multiple developers to contribute to an effort, and to test their ideas in isolation before integrating them into a larger system. Because the data read in from an event is placed in read-only memory, analyzers can program with confidence that upstream algorithms cannot alter the data, but must produce additional data products which can later be processed or written out.

19 The LArSoft suite provides the interface to the event generators and GEANT-4 [?]

20 need citation in bib file

21 for simulation of the passage of particles through the detector, the details of which are described in Section 3.5, and event reconstruction, the details of which are presented in Section 3.6.

23 The *art* framework and LArSoft source code are publicly available, and pre-built versions are provided [24] for supported versions of Linux and Mac OS X. Tools for compiling the framework and applications are also provided, along with all of the required dependencies, including the gnu C++ compiler. The versions of the software and its dependencies are managed by the UNIX Product Support (UPS) system, which allows easy version selection, setup and configuration of the LArSoft environment on computers with previous versions already installed, such as those at Fermilab.

30 LArSoft is under rapid development by both the core LArSoft team and by contributors from participating experiments: ArgoNeuT, LArIAT, MicroBooNE, SBND, and DUNE. Within DUNE, the LArTPC near-detector option, both ProtoDUNE detectors, and the Far Detector are clients and contributors of LArSoft.

1 3.5 Event simulation

2 Two kinds of events must be simulated in the ProtoDUNE-SP detector geometry: beam events
 3 and cosmic-ray events. Beam events are generated using a dedicated particle gun generator that
 4 has as input parameterizations of the flux and the beam profile parameters. The upstream beam
 5 instrumentation devices – wire chambers, Cherenkov counters, and time-of-flight-counters – are
 6 fully simulated as described in Section 5.3. Cosmic-ray events are simulated either with the
 7 CRY [25, 26] event generator or CORSIKA [27]. Neutrino scattering events are simulated using
 8 GENIE [28]. While neutrino scattering events will be very rare in the detector, the extrapolation
 9 of the performance of the detector to the FD will require simulating neutrino scattering events.
 10 A dedicated generator in LArSoft simulates radionuclide decay products which can be overlaid on
 11 other events.

12 The detector geometry is coded in GDML files [29] that are generated by the GeGeDe [30] geometry
 13 system. These files contain the locations, sizes, shapes, and material content of the detector
 14 components, the active liquid argon volume, and the surrounding materials, such as the field
 15 cage, the beam windows, the cryostat the supporting structure, and the experimental hall. These
 16 external features will impact the distributions of cosmic-ray particles impinging on the active
 17 detector. The channels and volumes are numbered and named in the GDML files, with conventions
 18 followed by the LArSoft simulation code.

19 The active volume of the detector is divided into cubes $300 \mu\text{m}$ on a side, called *voxels*. GEANT4
 20 tracks particles through the argon. Each step ends on a voxel boundary, allowing the simulation of
 21 small-scale physics processes such as delta-ray emission and showering at a level of detail smaller
 22 than the intrinsic resolution of the detector. While GEANT4 calculates the energy deposited
 23 by each particle for each step, the simulation of ionization and scintillation photon emission is
 24 performed using one of two algorithms in LArSoft: a dedicated parameterization that depends on
 25 the electric field in the liquid argon and the ionization density [31], or NEST [32], which is tuned to
 26 previous noble-liquid experimental results and introduces an anti-correlation between the photon
 27 yield and the ionization electron yield for each step.

28 An alternate simulation based on FLUKA [33, 34, 35] is being interfaced into LArSoft. FLUKA
 29 provides a MC simulation of neutrino-nucleus interactions as well as detailed modeling of particles
 30 traversing the detector, configurably replacing the functionality of both GENIE and GEANT in
 31 the simulation. The availability of alternatives allows for better flexibility in tuning the models to
 32 the data, as well as a basis of estimating systematic uncertainty.

33 The average specific energy loss for a minimum-ionizing particle (MIP) is approximately $2.12 \text{ MeV}/\text{cm}$.
 34 The W -value for ionization is 23.6 eV per electron-ion pair, and the W -value for scintillation is
 35 19.5 eV per photon, resulting in tens of thousands of drifting electrons and photons per cm of
 36 charged-particle track in the detector. It is impractical to simulate the paths of each of these
 37 electrons and photons using GEANT4, and

38 therefore?

- ¹ computational techniques are incorporated into LArSoft to achieve a high simulation speed while
² preserving accuracy. The electrons are propagated by LArSoft-specific tools, including a tool that
³ integrates over the distributions created by longitudinal and transverse diffusion, and a geometry
⁴ tool that indicates the wire locations that record charge, assuming uniform wire spacing.

⁵ The prev sentence replaces this: The electrons are propagated by LArSoft-specific tools includ-
 ing an integral over the distributions created by longitudinal and transverse diffusion, and the
 wire locations on which to record the charge passing or collecting are looked up from the ge-
 ometry assuming uniform spacing.

- ⁶ The effect of charge loss due to attachment of electrons to impurities (the effect of the electron
⁷ lifetime),

⁸ that affects the lifetime?

- ⁹ is implemented in this step. Effects due to space charge are simulated using a smoothly parame-
¹⁰ terized map of distortions in the apparent position components (x, y, z) of the charge deposits as
¹¹ functions of the true position. This map can be made using SPaCE [36], a program that traces
¹² particle trajectories in LAr based on the electric field calculated using Poisson’s equation, a given
¹³ space-charge density map, and the boundary conditions provided by the cathodes, anodes, and
¹⁴ field cages. It is anticipated that the space-charge distortions in ProtoDUNE-SP may be as large
¹⁵ as 20 cm [36].

¹⁶ I took this out because I don’t think it’s discussed in this document. Anne “Space charge ef-
 fects and resulting field distortions for protoDUNE are discussed in Section ??.”
 [sec:SCEintro]

- ¹⁷ Photon propagation is simulated using a library that contains the probabilities of observing a
¹⁸ photon emitted at a particular point in space by a particular photon detector. Here, the space is
¹⁹ divided into cubical voxels 6 cm on a side, and the library is indexed by photon detector element.

- ²⁰ The simulated arrival times and charge amounts on each wire, and of each set of photons arriving
²¹ at each photon detector, along with the identity of the particles generating them, are stored in the
²² simulation output file for use in determining the performance of the downstream reconstruction
²³ algorithms. These charge depositions and photons are inputs to the detector response functions –
²⁴ the field response and the electronics response are convoluted with the true arrival times to make
²⁵ simulated waveforms. The detector field response functions are simulated using GARFIELD [37],
²⁶ but they will be validated with real data, as the simulation contains oversimplifications, such as
²⁷ inadequate modeling of induction signals.

- ²⁸ The electronics gain is applied so that the simulated signals match the expected responses. Simu-
²⁹ lated noise is then added, and the result is quantized to reproduce the behavior of a 12-bit ADC,
³⁰ including realistic pedestals and saturation. A similar process is followed to simulate the response
³¹ of the photon detectors, given the arrival times of the photons. Functionality exists within LArSoft
³² to overlay MC-simulated particles with raw digits in the data in order to simulate pileup of cosmics
³³ and other beam interaction particles. The simulated raw digits are then written to compressed

¹ ROOT files for further analysis.

² 3.6 Event reconstruction algorithms and performance

³ 3.6.1 Reconstruction

⁴ The interpretation of the data from LArTPC detectors has proven challenging, largely due to the
⁵ wealth of information provided in each event by the detector, but also due to the high rate of
⁶ multiple scattering and particle interactions, as well as the projection of 3D information onto a
⁷ discretized 2D space of readout ADC counts on wires as functions of time. The flexibility of the
⁸ *art/LArSoft* framework allows for multiple approaches for reconstructing and analyzing the data,
⁹ and for the use of different approaches depending on the targeted physics deliverable.

¹⁰ For current large LArTPC detectors, noise filtering is applied to improve the signal-to-noise ratio.
¹¹ A large component of the noise in existing LArTPC experiments is from coherent sources – sources
¹² that affect many neighboring wires and/or neighboring readout channels. (Channels from different
¹³ planes may be interleaved in the front-end electronics).

¹⁴ prev sentence in parens sounds like it's for a particular expt

¹⁵ The contribution from coherent noise to a measured ADC value on a channel can be estimated
¹⁶ from the data on nearby channels at the same time, and subtracted out. However, this procedure
¹⁷ reduces the signal as well as the noise, in a manner that depends on the angle of the track or
¹⁸ shower with respect to the drift field.

¹⁹ prev sentence replaces: A drawback of this procedure is that signals also arrive on neighboring
²⁰ channels at the same time, and this procedure reduces the signal as well as the noise, in a
²¹ manner that depends on the angle of a track or shower with respect to the drift field.

²⁰ Procedures that first identify signal hits and protect them from distortion ^{microboone-noise} [38] are under study.
²¹ With software noise filtering, MicroBooNE ^{noise filter} [39] has achieved excellent noise levels, consistent with
²² expectations, based on the design specification of the cold electronics.

²³ THEIR cold electronics?

²⁴ In MicroBooNE, various sources of noise have been identified and hardware upgrades are ongoing
²⁵ to eliminate them. Once noise has been removed, signals will be processed to recover the ionization
²⁶ charge.

²⁷ No longer in doc? “as described in Section ^{sec:tpc-signal-calibration} ??”

- 1 Hits are identified by seeking deconvoluted signals exceeding thresholds that are adjusted to min-
2 imize the creation of false noise hits while preserving the true signal hits. The standard LArSoft
3 hit finder fits Gaussian functions to the deconvoluted signals, and saves the times, widths, and am-
4 plitudes of the Gaussians. In addition, it saves the sum of the ADC readings in the time windows
5 corresponding to the hits; since a Gaussian function is not always representative of the charge
6 arrival distribution, the resolution of the calorimetry is improved by summing the ADC counts.
- 7 The hits are associated with DAQ channels not wire segments, since, due to the wrapping of the
8 induction-plane wires in the APA's, the location of the charge deposition contributing to the hit
9 is ambiguous. Because the wire angle is chosen such that each induction wire intersects each
10 collection-plane wire at most one time, only two views are needed in order to identify hits and
11 resolve ambiguities. A separate LArSoft module compares the hits in the collection and induction
12 views and assigns choices to remove ambiguity.

13 choices?

- 14 Physics analyses are most sensitive with a full 3D reconstruction of the event – the primary vertex
15 (if there is one), the tracks and the showers. ProtoDUNE-SP is implementing several approaches
16 to achieve this. Once hits are identified on wire segments, 2D reconstruction identifies clusters and
17 tracks in each view separately, and 3D hypotheses for the event are constructed by comparing the
18 2D clusters in the separate planes. The 2D clustering algorithms currently in use are the Blurred
19 Clustering Algorithm [?], LineCluster [40], and TrajCluster [41].

20 3.6.2 Performance

- 21 The performance metrics are efficiency, purity, and completeness. The efficiency of the algorithm
22 is defined as the fraction of true particles that match reconstructed objects within the bounds of
23 pre-specified criteria, such as matching position and length and the type of object expected. The
24 purity of the reconstructed object is defined as the fraction of hits (or charge) included in that
25 object that truly came from the matched particle, divided by the total number of hits (or charge)
26 included in the reconstructed cluster. The completeness is defined as the number of true hits that
27 are found in a cluster, track or shower expressed as a fraction of total true hits in that object.
- 28 Particle-level and event-level performance metrics include particle identification and misidentifica-
29 tion rates, shower energy resolution, and energy scale offsets.

30 What is the type of performance discussed in the first paragraph? (as opposed to particle- and event-level)

1 EMShower

2 The EMShower package [42] takes the output of the Blurred Clustering Algorithm and produces
 3 energies, angles, and start positions for 3D showers, as well as the dE/dx in the initial part
 4 of the shower. Identifying events with two showers consistent with $\pi^0 \rightarrow \gamma\gamma$ decays allows for
 5 an *in situ* calibration of the electromagnetic energy scale as well as the performance of shower
 6 identification and reconstruction for photons that are produced inside the detector. A distribution
 7 of reconstructed π^0 masses in Monte Carlo is shown in Figure 3.2. fig:pizero mass

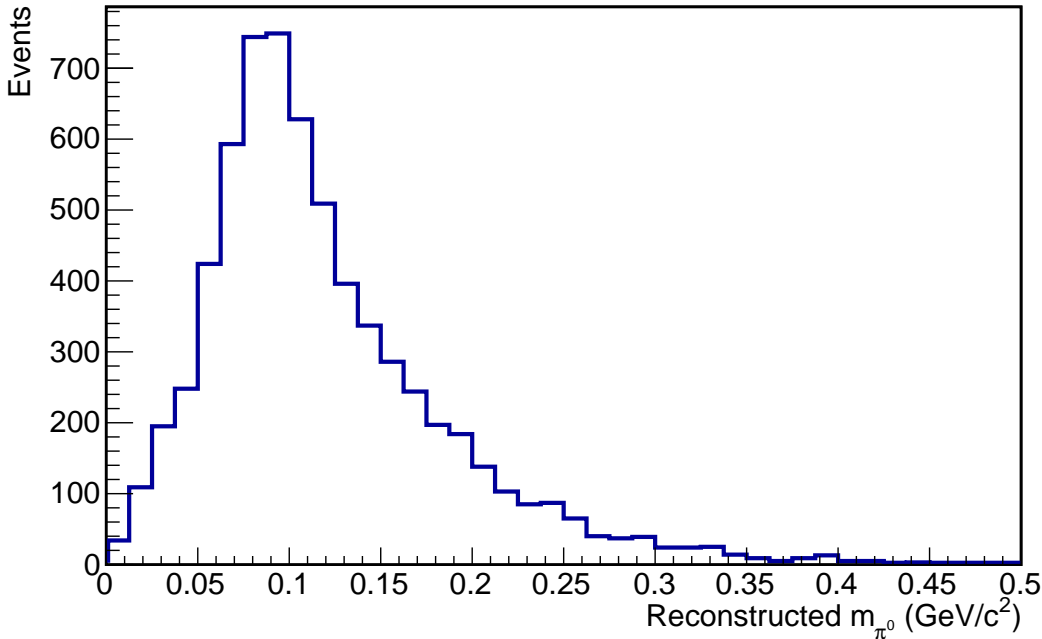


Figure 3.2: The reconstructed invariant masses of π^0 candidates in Monte Carlo using the BlurredCluster and EMShower algorithms.

8 PANDORA

9 The reconstruction framework PANDORA [43] also works by building up a 3D picture from 2D
 10 reconstructed objects. PANDORA is a flexible framework developed for ILC detector simulation,
 11 and provides a convenient way to develop algorithms for reconstructing particles. In all, more
 12 than 80 algorithms, each targeting a specific topology, have been incorporated into PANDORA to
 13 date. Multiple passes through reconstructing the data are possible. Different criteria for clustering
 14 hits into tracks and showers may be applied when seeking cosmic rays for removal rather than
 15 for identifying signal events. PANDORA follows a process that clusters hits in 2D, reconstructs
 16 vertices in 3D, reconstructs tracks in 3D, reconstructs showers in 3D, performs a “mop-up” step
 17 in 2D and 3D, and finally performs full event-building in 3D. Marshall:2015rfa

18 ILC - int'l linear collider?

19 Plots of the efficiency, the completeness, and the difference between the true and reconstructed

- 1 track lengths for single muons with momentum between 300 MeV and 5 GeV in the ProtoDUNE-SP
 2 geometry are shown in Figure 3.3. The PANDORA algorithm performs very well, although a small
 3 inefficiency occurs in the current algorithm’s ability to match track segments from one APA’s drift
 4 volume to another.

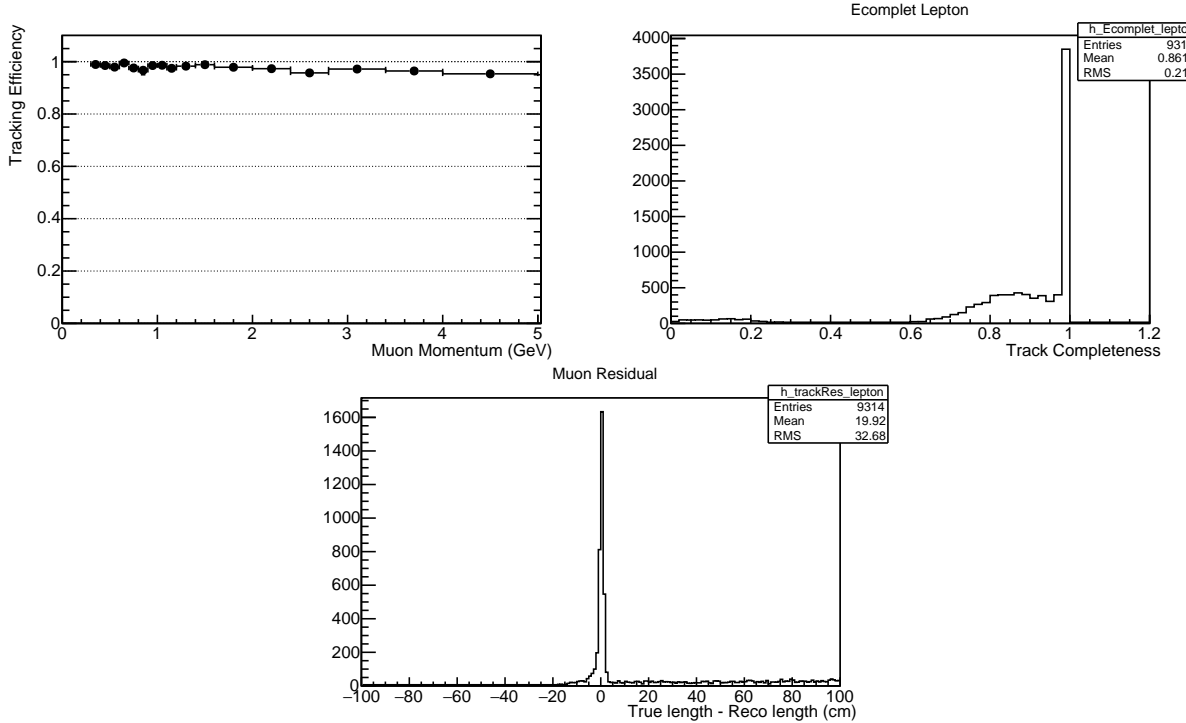


Figure 3.3: Performance of the PANDORA reconstruction algorithm for single muons with momentum between $300 \text{ MeV}/c$ and $5 \text{ GeV}/c$. The left-hand figure shows the tracking efficiency as a function of muon momentum, the middle figure shows the distribution of tracking completeness, and the right-hand figure shows the distribution of the difference between the reconstructed muon track length and the true track length.

fig:muonpandoraperf

5 PMA

- 6 Another approach to 3D reconstruction in LArTPC detectors is referred to as the *Projection*
 7 *Matching Algorithm (PMA)* [44]. PMA was primarily developed as a technique for 3D reconstruc-
 8 tion of individual particle trajectories (trajectory fits) [?]. Instead of building up a 3D hypothesis
 9 from 2D clusters, it starts with the 3D hypothesis and compares the 2D projection of the predicted
 10 trajectory of a particle with the observed data. Association of hits between the 2D planes is not
 11 needed in this approach, improving its performance in problematic cases, such as isochronous and
 12 short tracks.

- 13 PMA can take as input the output from different pattern recognition algorithms, from LineClus-
 14 ter [40] to WireCell (described below). Because these 2D algorithms are run on each 2D projection
 15 independently, and because of detector defects, clusters from particles may be broken into several
 16 smaller pieces, fractions of 2D clusters may be missing, and clusters obtained from complementary
 17 projections are not guaranteed to cover corresponding sections of trajectories. Such behavior is

- expected since ambiguous trajectories can be resolved only if the information from multiple 2D projections is used. PMA performs higher-level pattern recognition using as input clustering information from all projections in order to search for the best matching combinations of clusters. The algorithm also attempts to correct hit-to-cluster assignments using properties of 3D reconstructed objects.
- Plots of the efficiency, the completeness, and the difference between the true and reconstructed track lengths for single muons with momentum between 300 MeV and 5 GeV in the ProtoDUNE-SP geometry are shown in Figure 3.4.

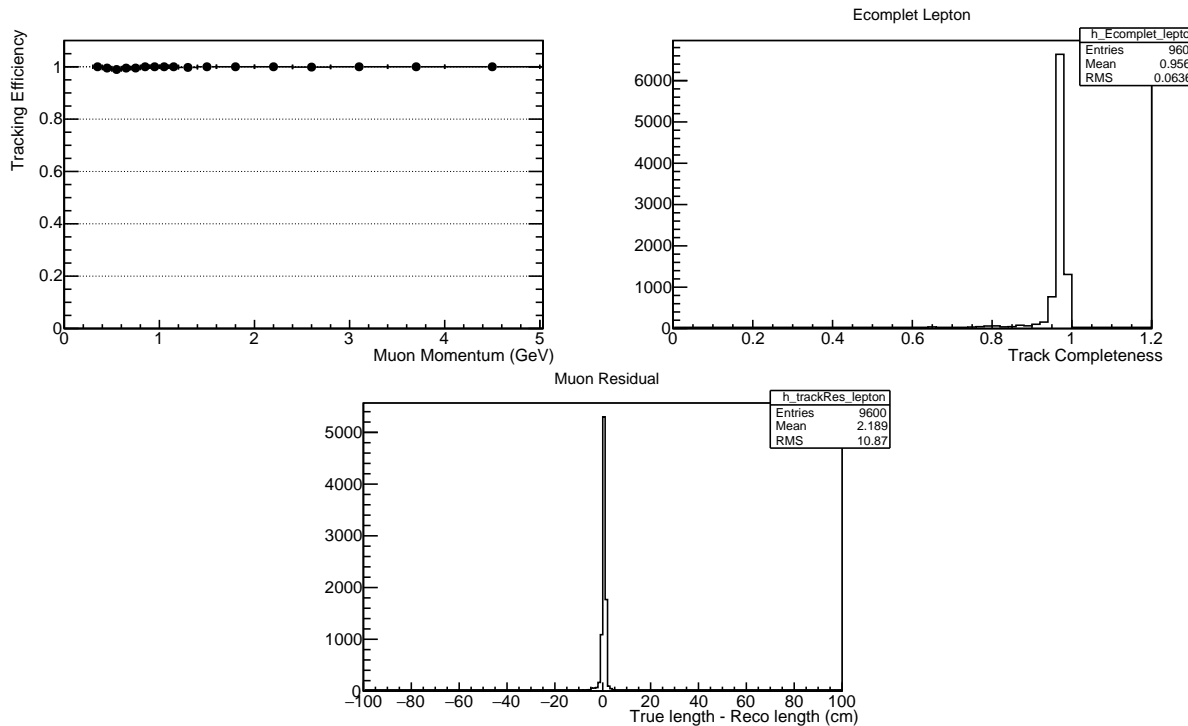


Figure 3.4: Performance of the PMA reconstruction algorithm for single muons with momentum between 300 MeV/c and 5 GeV/c. The left-hand figure shows the tracking efficiency as a function of muon momentum, the middle figure shows the distribution of tracking completeness, and the right-hand figure shows the distribution of the difference between the reconstructed muon track length and the true track length.

- PMA has been used successfully in ProtoDUNE-SP to reconstruct simulated beam particles. In order to illustrate the performance of the entire reconstruction chain, Figure 3.5 shows the spatial resolution of the interaction vertex with neutral pion production appearing in the 2-GeV/c π^+ sample. The resolution is found to be 0.6 cm in this study. A similar resolution is obtained for the reconstruction of inelastic interaction vertices in the 2-GeV/c proton sample.
- Figures 3.6 and 3.7 show examples of reconstruction of a 2-GeV/c proton in the test beam and cosmic-ray muons, respectively.

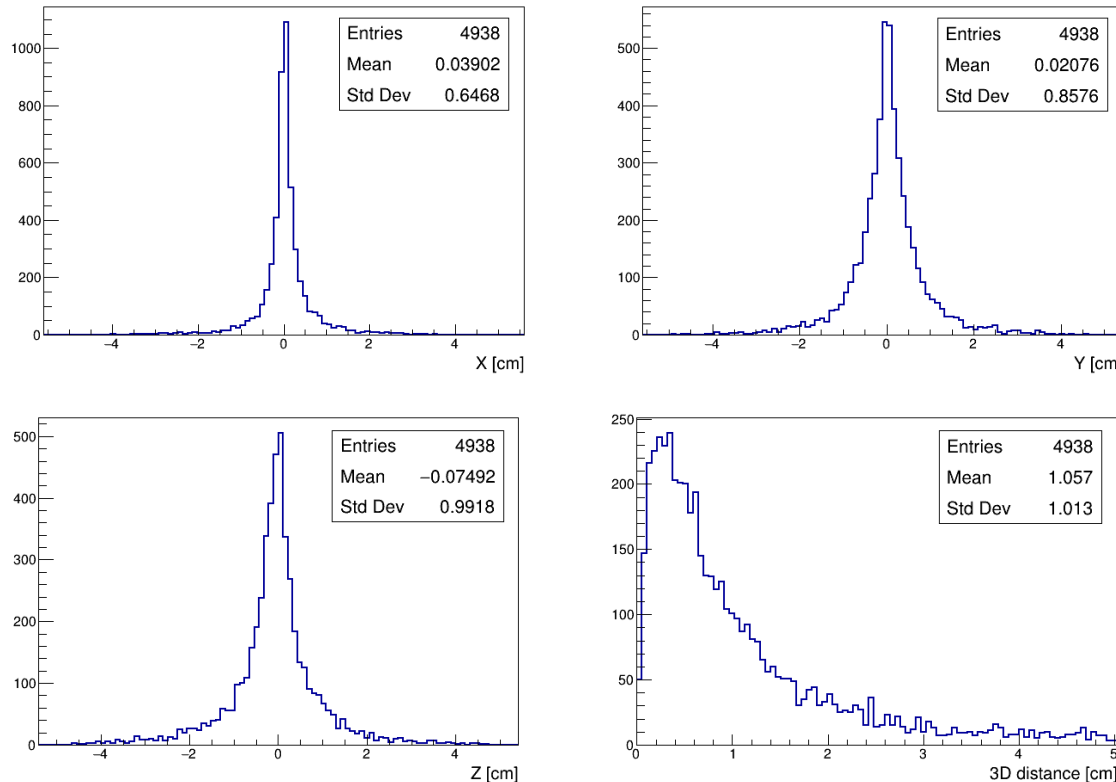


Figure 3.5: Vertex position resolution in cm in x , y , and z and 3D for the inelastic interaction of charged pions on liquid argon nuclei in events in which a π^0 is produced, in ProtoDUNE-SP, using the PMA algorithm.

increase size of stat box entries; if possible remove "temp" header

fig:PMAp

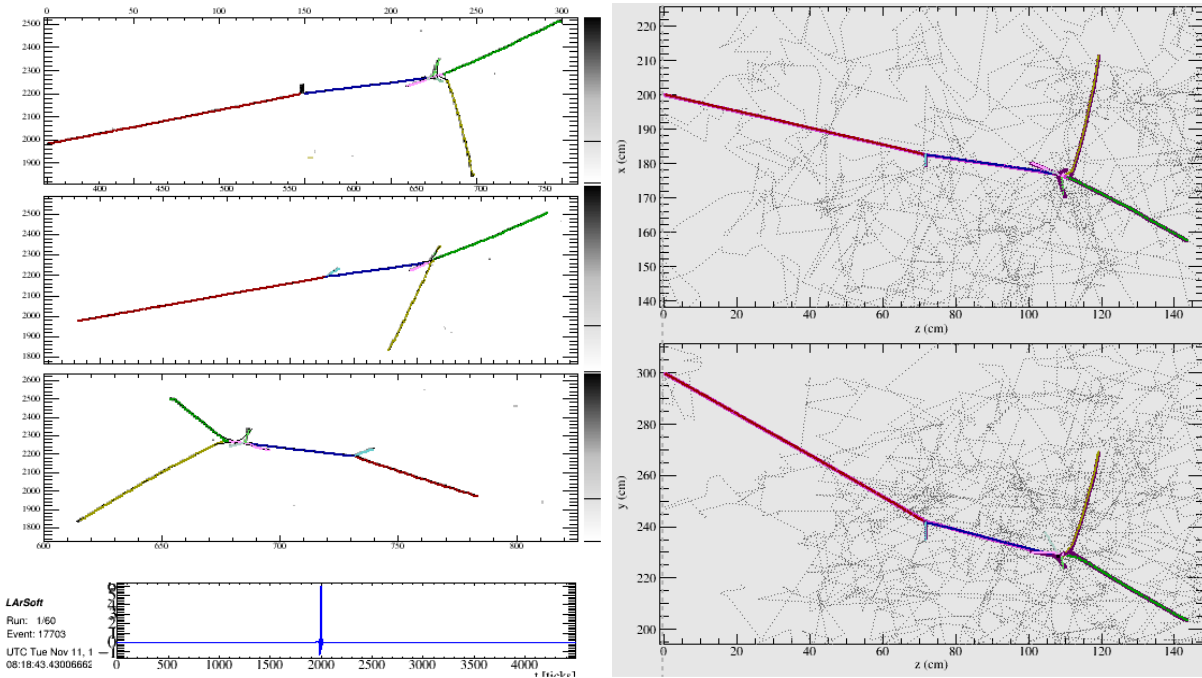


Figure 3.6: Example of reconstructed event of simulated proton with initial momentum 2 GeV/c (reconstruction algorithms: gaushtit, Line Cluster and PMA).

fig:PMApp

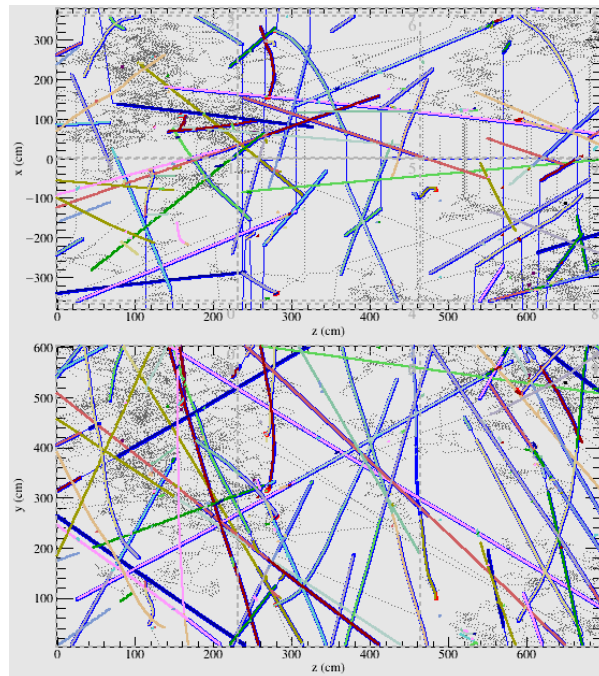


Figure 3.7: Example of reconstructed cosmic muons using gaushtit, Line Cluster and PMA.

fig:PMAMu

1 WireCell

2 WireCell [45] adopts a very different approach from the aforementioned algorithms and is a new
3 reconstruction method under development. Instead of directly doing pattern recognition on each
4 of the 2D views (drift time versus wire number), the first step of the WireCell reconstruction is to
5 perform 3D imaging with time, geometry, and charge information. The algorithm takes advantage
6 of this information in order to suppress the effects of electronic noise. Hits from different wire
7 planes arriving in different time slices cannot be associated with each other. (The definition of *hit*
8 is based on signal strength after charge extraction in a $2\text{-}\mu\text{s}$ time slice.) Hits from wires that do
9 not cross in a region consistent with the charge deposition cannot be associated with each other.
10 Hits from different wire planes with different signal strengths are unlikely to be associated with
11 each other. Use of the charge information takes advantage of the fact that in a LArTPC with
12 induction planes, each of the wire planes, in principle, detects the same ionization electrons as the
13 other planes. Figure 3.8 shows an example of the improvement of WireCell 3D imaging over the
14 more traditional approach.

15 The suppression of the electronic noise comes at the cost of more sensitivity to hit inefficiencies
16 from dead channels or the signal processing steps. Since the track and shower hypotheses are
17 not used, the 3D imaging works for any event topology. Pattern recognition is needed to identify
18 the content of these 3D images. Figure 3.9 shows the performance of the currently available 3D
19 pattern recognition in WireCell. For the long track going close to parallel to the wire plane, the
20 reconstructed track shows a zig-zag behavior. This is due to the current lack of a fine track-fitting
21 algorithm that is expected to be added in the near future. Further developments of the WireCell
22 pattern recognition algorithms are needed before meaningful physics quantities can be calculated.

23 Something like the following could go into a summary of the document; the other chapters
don't include a summary like this.

24 ProtoDUNE-SP run will collect a large amount of raw data that will provide a tremendous opportu-
25 nity to test the detector design, to test and optimize data processing and reconstruction techniques,
26 and to measure the properties of particle interactions in LAr. While the reconstruction algorithms
27 are still under development, the richness of the information provided by the detector promises new
28 opportunities to study the physics processes of charged particle and neutrino scatters.

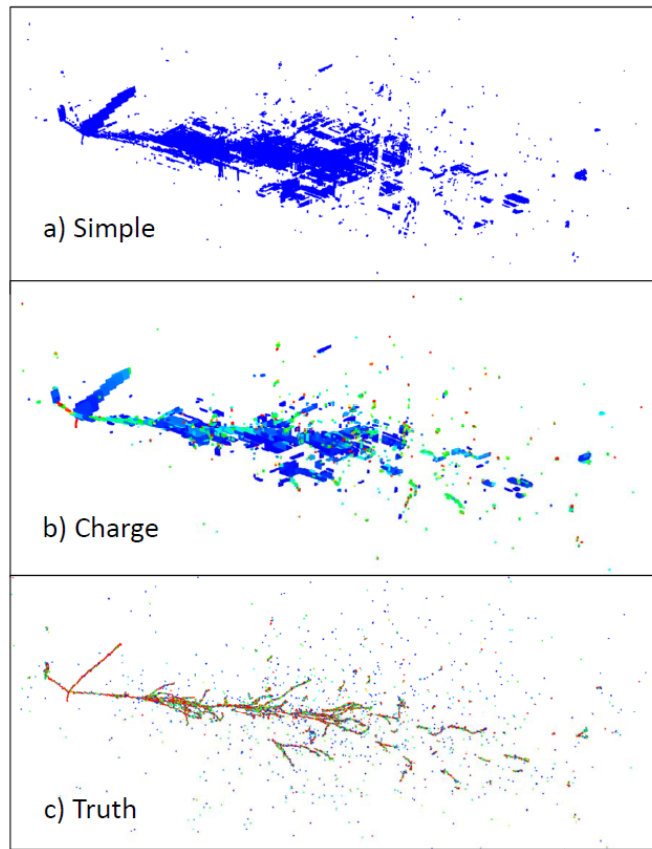


Figure 3.8: Comparison of imaging reconstruction qualities with and without the charge information.

`fig:qual`

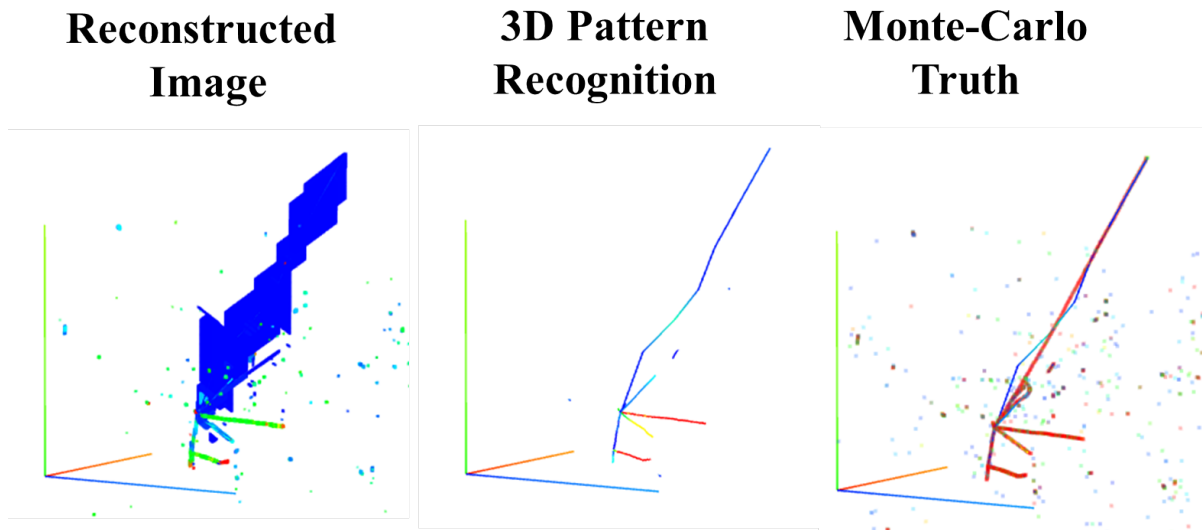


Figure 3.9: The reconstructed image is shown on the left panel for one neutrino interaction event. The image was passed through the 3D pattern recognition program with tracks identified (middle panel). The identified pattern is compared with Monte-Carlo truth in the right panel. The zig-zag line in the right panel is the identified track. More sophisticated track-fitting algorithms, to be added in the future, will improve the track reconstruction.

`fig:track`

¹ Chapter 4

² Space and infrastructure

spacereq

³ ProtoDUNE-SP is to be housed in an extension to the EHN1 hall in the North Area of the Prévessin
⁴ site at CERN. The cryostat is constructed in a pit inside the building, surrounded on three sides by
⁵ the pit walls. On the fourth side of the cryostat, an ISO 8 clean room provides a space to construct,
⁶ test and assemble the TPC. A material pass-through structure (material SAS) is adjacent to the
⁷ clean room. Figure 4.1 shows the layout of these structures in EHN1. A naming convention has
⁸ been established for the four sides of the cryostat, shown in Figure 4.2. The upper side is *Jura*,
⁹ the lower is *Salève*, the left is *Beam*, and right is *Downstream*.

¹⁰ define SAS

¹¹ As detector materials are brought into EHN1, they are passed into the SAS through its removable
¹² roof, then transported through a set of large doors from the SAS into the clean room, where they are
¹³ tested and assembled. When ready, each assembled TPC component passes through a temporary
¹⁴ construction opening (TCO) in the cryostat for installation. While material is lowered into the
¹⁵ SAS from the gallery floor, the doors to the clean room remain closed to reduce contamination of
¹⁶ the filtered air in the clean room. Once the roof of the SAS is closed, these doors can be opened
¹⁷ to move the material into the clean room.

¹⁸ The lighting inside the clean room and any temporary lighting inside the cryostat is filtered to
¹⁹ limit the exposure of the PDS components to UV light. Wavelengths below 450 nm are filtered
²⁰ out.

²¹ Figure 4.3 shows an elevation section view of the cryostat indicating the position of the TCO and
²² the location of the integrated cold testing stand (described in Section ??).

²³ Inside the clean room, a series of rails facilitate the movement of the TPC components during
²⁴ the test and installation processes. The conceptual layout of these rails is shown in Figure 4.4.
²⁵ The rails are positioned vertically at the same height as the detector support structure (DSS) rails
²⁶ inside the cryostat. A temporary rail is installed through the TCO to bridge the DSS rails and
²⁷ clean room rails. All the large components of the cryogenics piping and TPC are supported from
²⁸ these rails on movable trolleys as they are transported to the interior of the cryostat. Figure 4.4

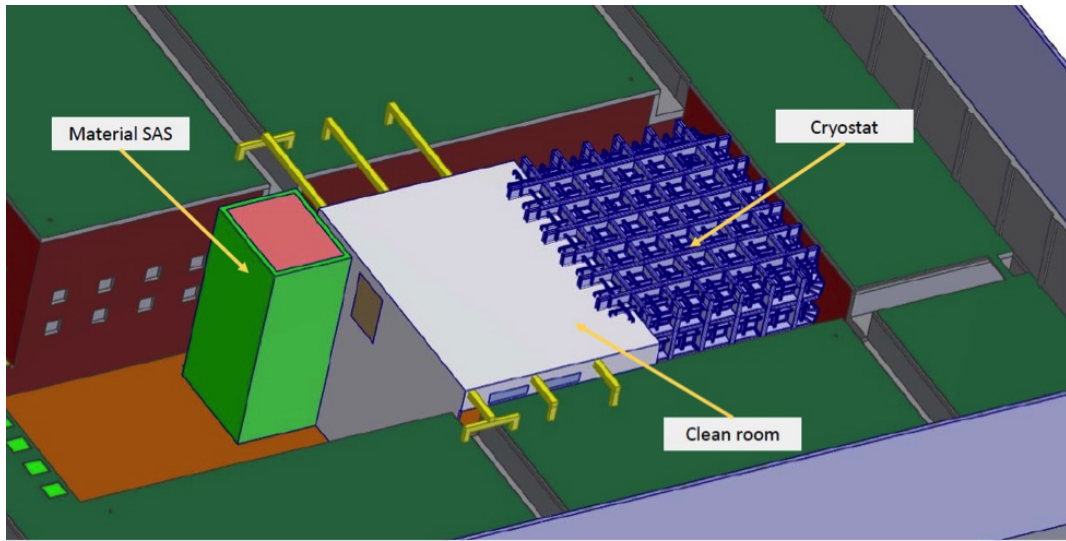


Figure 4.1: Layout of ProtoDUNE-SP cryostat, clean room and material SAS in EHN1

fig:cryo

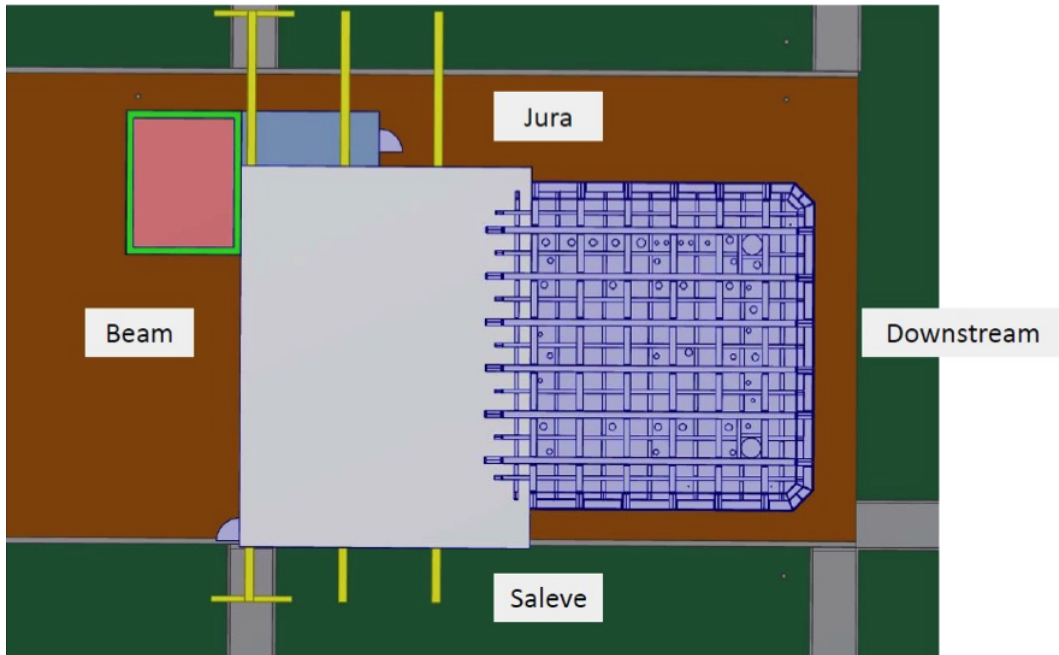


Figure 4.2: Conventions for labeling the four sides of the cryostat

fig:cryo

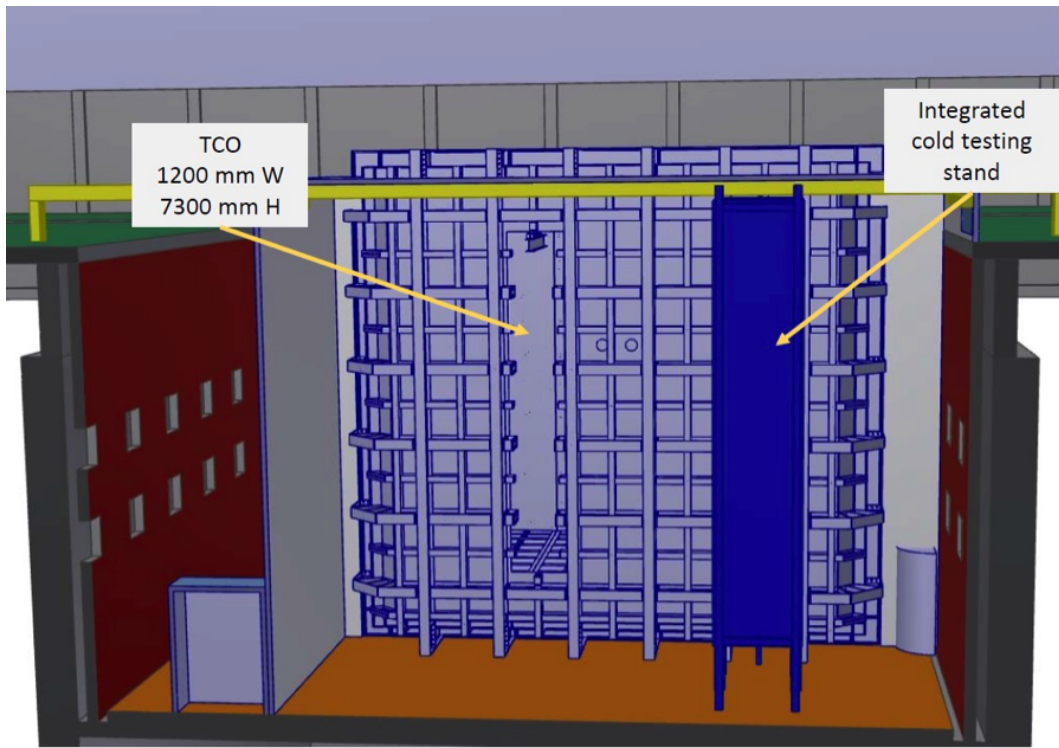


Figure 4.3: Elevation section view of the cryostat

fig:elev

¹ also shows the approximate dimensions for the SAS and the footprint of the clean room space.
² These spaces are limited by the pit walls on two sides (top and bottom of figure), and by the
³ supports for the beam and beam instrumentation on the other (see left side of figure). Figure 4.5
⁴ shows the planned locations for all of the activities that will be performed inside the clean room.

- ⁵ The activities that will take place in the clean room include:
- ⁶ • Assembly of the CPA panels into CPA modules (on a large horizontal surface);
⁷ • Rotation of CPA modules from horizontal to vertical, and placement on the clean room rails;
⁸ • Attachment of FC assemblies to CPA modules;
⁹ • Unpacking and testing of the PDS elements, and installation on the APA frames;
¹⁰ • Unpacking and testing of the CE elements, and mounting onto the APAs; and
¹¹ • Integrated testing of APA with PDS and CE.

[fig:sas-locati](#)

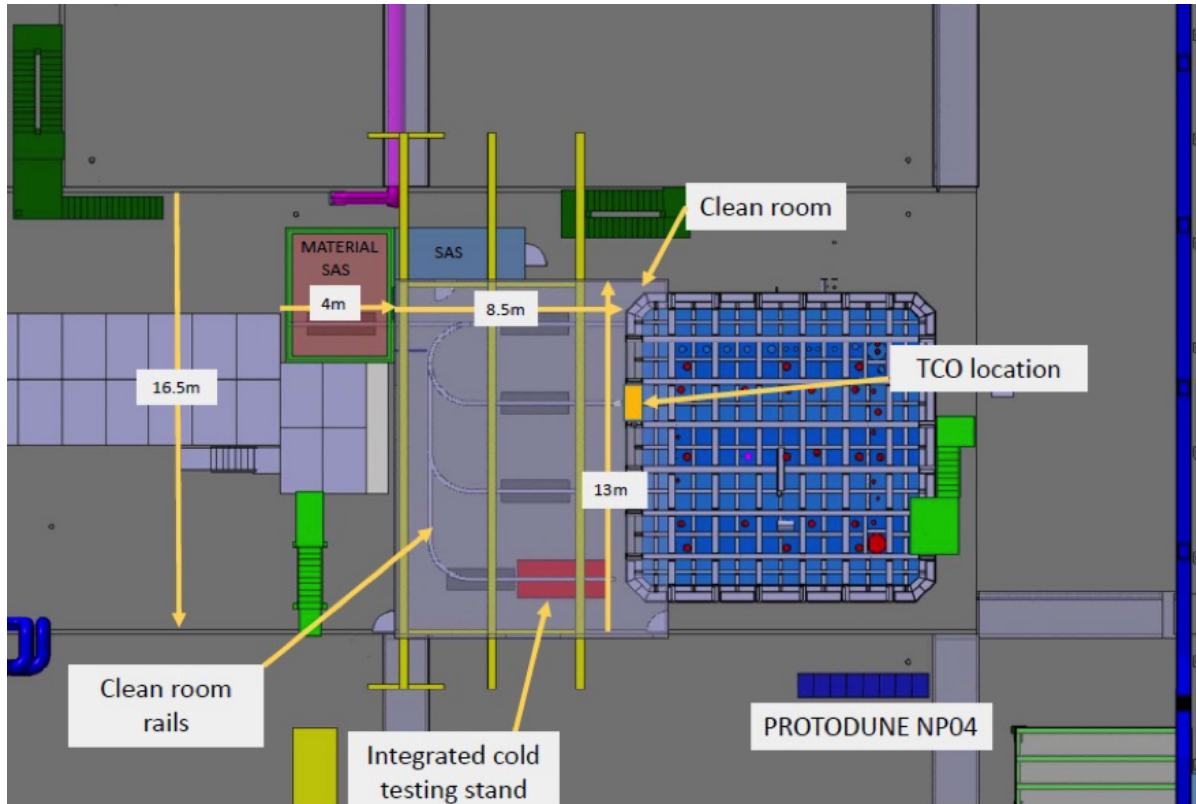


Figure 4.4: Conceptual layout of rails in clean room to facilitate movement of TPC components, approximate dimensions for the material SAS and the footprint of the clean room space are shown.

fig:rail

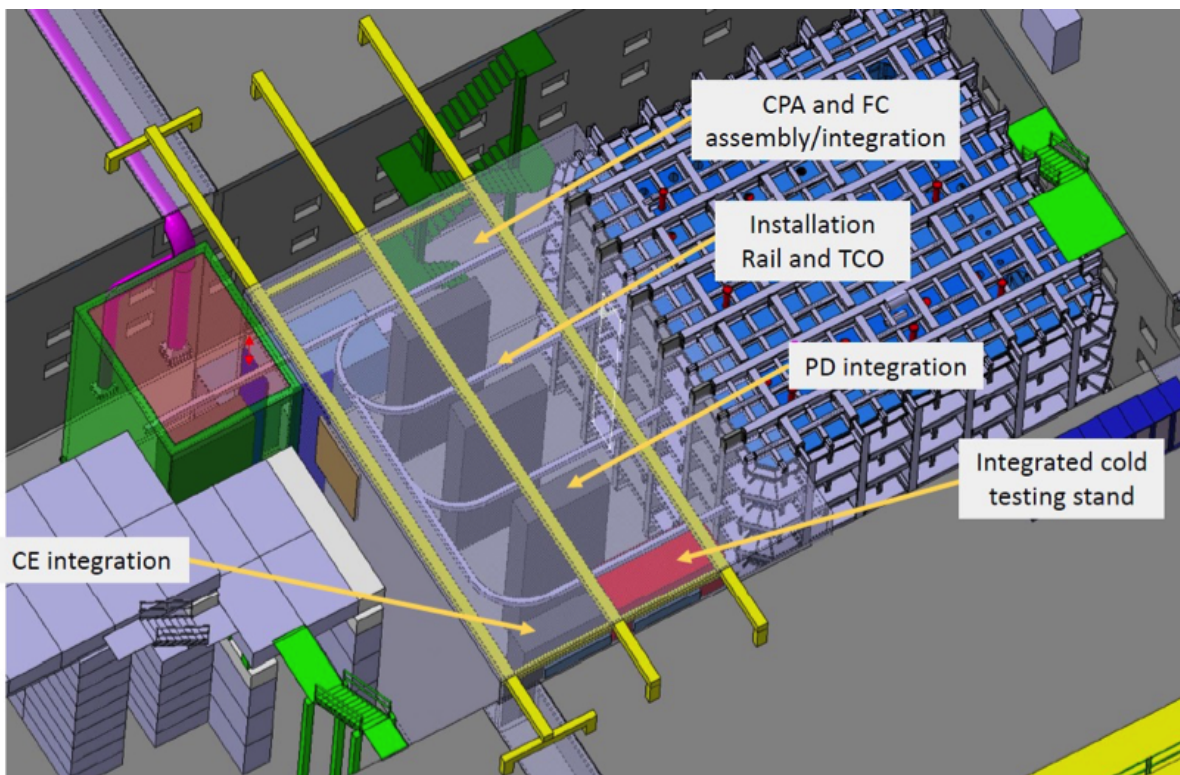


Figure 4.5: Locations of activities to be performed in the clean room

fig:sas

¹ Chapter 5

² Test beam specifications

³ The ProtoDUNE-SP (NP04) experiment will be housed in the EHN1 building at CERN. The
⁴ detector is situated at the end of the H4 beamline in the newly constructed extension of EHN1.
⁵ The H4 beamline is also extended and configured to deliver either a hadron or a pure electron beam
⁶ to the experiment. To produce particles in the momentum range of interest, the secondary beam
⁷ from the T2 primary target is sent onto a secondary target to generate a tertiary beam. Particles
⁸ in this tertiary beam are momentum- and charge-selected and transported down the H4 beamline
⁹ extension to the ProtoDUNE-SP detector. In this Chapter, we discuss the beam requirements, H4
¹⁰ tertiary beamline design and instrumentations, DAQ/trigger, and the physics run plans.

¹¹ 5.1 Beam requirements

¹² The CERN test beam results from ProtoDUNE-SP will be used to evaluate the detector perfor-
¹³ mance, understand the various physics systematic effects, and provide data for event reconstruction
¹⁴ studies that are representative of neutrino interactions. The parameters defining the test beam are
¹⁵ primarily driven by the requirement that these test beam results be directly applicable to DUNE’s
¹⁶ future large underground single-phase detector module(s) with minimal extrapolation. To match
¹⁷ the charged-particle spectrum and topologies that are expected in the DUNE far detector, the H4
¹⁸ tertiary beam must span a broad range of particle momenta, be composed of electrons, muons,
¹⁹ and hadrons, and charge-selectable. The expected momentum distributions for secondary particles
²⁰ from neutrino interactions in the far detector has a large spread that ranges from a few hundred
²¹ MeV/c to a few GeV/c. The desirable range for ProtoDUNE-SP is in the low-momentum region.
²² Based on the feedback and constraints from the CERN accelerator group, the design of the beam-
²³ line extension has been developed to allow the transport of beam particles from about 0.5 GeV/c
²⁴ up to 7 GeV/c.

²⁵ The maximum electron drift time in the ProtoDUNE-SP TPC is about 2.25 ms. In order to keep
²⁶ the pile-up in the TPC at the percent level, the planned beam particle rate should be below 100 Hz.
²⁷ The ProtoDUNE-SP TPC has two drift volumes separated by a cathode plane. It is desirable to

1 aim the particle beam such that a large fraction of the lower-energy hadronic showers are contained
 2 in one drift volume, thus minimizing the uncertainties from particles lost in the inactive detector
 3 materials. As shown in Figure 5.1, multiple beam injection points have been explored. Based on
 4 inputs from the physics group, the larger angle (beam # 3) w.r.t. the APA plane (Saleve side),
 5 which corresponds to about 13° , is preferred. Due to engineering and safety considerations, only
 6 beam #3 will be fully instrumented with the beam window system as described in Sections 2.4.5
 7 and 2.10.6. The remaining two beam positions will have partial installation of the beam window
 8 system. With this configuration, beam #3 is the primary beam with which most of the physics
 9 data will be taken.

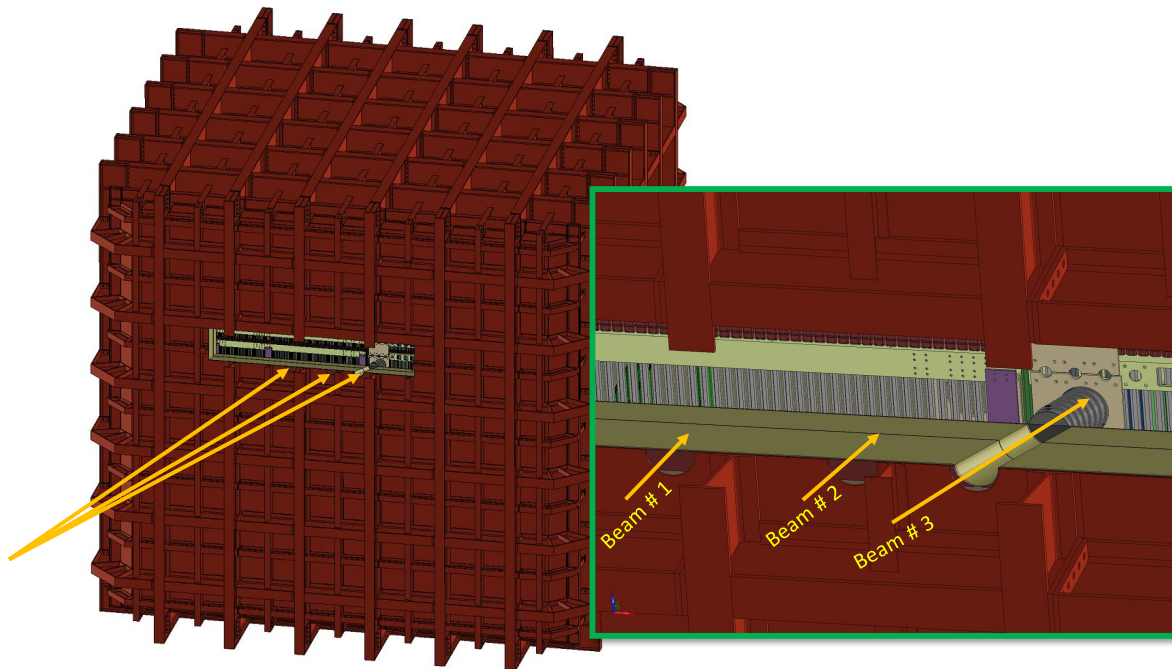


Figure 5.1: Three possible beam injection points. The cryostat support structures near the beam injection points are removed in the Figure to show the interior. Beam window and beam plug are installed only for beam # 3.

10 A summary of the beam requirements is shown in Table 5.1.

fig:beam

Table 5.1: Particle beam requirements. (Kaon rate is low for beam momentum below 2 GeV/c.)

Parameter	Requirements
Particle Types	$e^\pm, \mu^\pm, \pi^\pm, (K), p$
Momentum Range	0.5 - 7 GeV/c
Momentum Resolution	$\Delta p/p \leq 3\%$
Transverse Beam Size	RMS(x,y) ≈ 1 cm (At the entrance face of the LAr cryostat)
Beam Entrance Position	Beam # 3 (Figure 5.1) - Saleve side TPC
Rates	$\sim 25 - \sim 100$ Hz

beamspecs

1 5.2 Beamlne

beamline

- 2 The design of the H4 beamline extension mirrors that of the H2. In this section, we describe the
 3 beamline design and the expected beam properties.

4 **5.2.1 H4 beamline layout and optics**

- 5 The placement of the quadrupole and dipole magnets in the H4 beamline extension is illustrated
 6 in Figure 5.2. The distance from the secondary target to the front of the NP04 cryostat is about
 7 37 m. For the hadron beam, either a tungsten or a copper target will be used. For the electron
 8 beam, a Pb target of a few radiation lengths will be used. The first two dipole magnets (shown
 9 in red) after the secondary target are rotated by about 56° to steer the beam downward towards
 10 the cryostat. The third dipole magnet (shown in green) is used for steering the beam horizontally
 11 into one of the three beam windows.

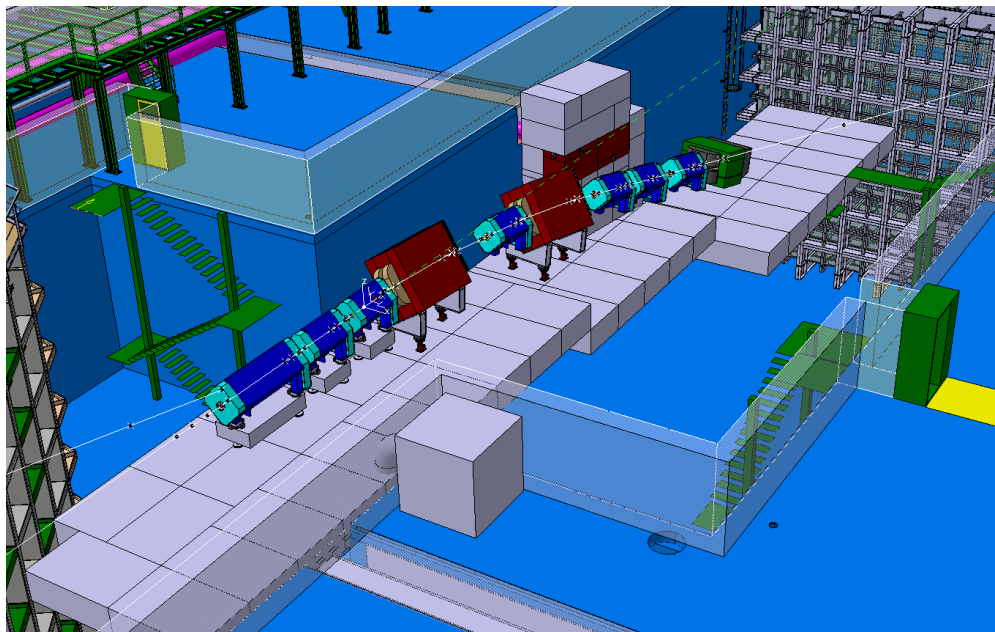


Figure 5.2: Layout of the quadrupole and dipole magnets in the H4 beamline extension. The secondary target (not shown) is upstream of the first quadrupole magnet on the left side of the Figure. Vacuum beam pipe and beam instruments are also not shown. (Courtesy of V. Clerc, CERN).

fig:H4la

- 12 The beamline optics from the target to the cryostat for the horizontal and vertical planes are
 13 shown in Figure 5.3. The Figures show the position of the quadrupole magnets (Q17-Q22), dipole
 14 magnet (B17 - B19), collimator (C12), Time-of-Flight detectors (TOF1-2), beam profile monitors
 15 (BPROF1-4), and the Threshold Cherenkov counters (XCET1-2) relative to the secondary target.
 16 For the nominal configuration, the beam is focused at the front of the cryostat to ensure maximum
 17 acceptance of beam particles through the beam window penetration and the beam plug inside the
 18 cryostat.

fig:beamoptics

- ¹ The beamline is in vacuum, with a beam pipe extending from the secondary target down to the
² beam window in the cryostat upstream face.

³ 5.2.2 Beam properties

- ⁴ A full GEANT4 simulation of the H4 beamline including its extension to the ProtoDUNE-SP de-
⁵ tector has been performed. The beamline model starts with the H4 secondary beamline and derives
⁶ the particle properties in the tertiary beamline. Target, magnets, collimators and a preliminary
⁷ assumption about beam instrumentation are included. The secondary target has been modeled
⁸ as a Tungsten cylinder ($R=30$ mm, $L=300$ mm) for beam momenta ≤ 3 GeV/c and as a Cop-
⁹ per cylinder of the same dimensions for beam momenta > 3 GeV/c. Optimization of the target
¹⁰ dimensions and material is ongoing.

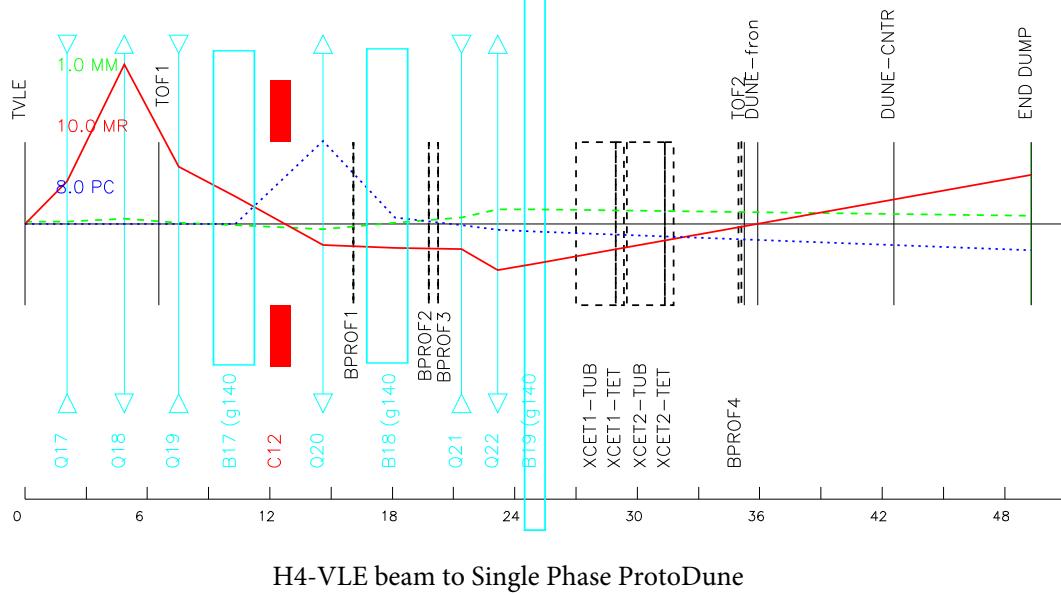
- ¹¹ [tab:beampartcomp](#) Table 5.2 describes the particle composition of the hadron beam at the entrance of the cryostat.
¹² Two features are evident. First, the beam is dominated by positrons at low energies, and secondly,
¹³ the kaon content, and to a lesser extent the pion content, are depleted at lower energies due to
¹⁴ decays of these species along the beam path.

Table 5.2: Beam composition (in percentage) at the cryostat entrance for particles contained in the beam pipe ($R= 10$ cm).

Momentum (GeV/c)	e^{+-}	K^{+-}	μ^{+-}	p^{+-}	π^{+-}
-7	27.4	3.4	1.0	1.3	66.9
-6	33.5	2.9	1.2	1.3	61.2
-5	43.2	1.9	1.3	1.1	52.5
-4	54.6	1.1	1.4	0.6	42.3
-3	28.4	1.1	2.3	1.4	66.8
-2	48.9	0.3	1.8	0.4	48.6
-1	81.7	0.2	1.1	0.2	16.9
-0.4	98.3	0.0	0.4	0.0	1.3
0.4	99.1	0.0	0.0	0.5	0.5
1	69.3	0.0	0.3	15.3	13.9
2	34.9	0.6	1.7	22.9	39.0
3	19.9	2.8	0.6	18.9	56.6
4	47.1	1.6	1.1	8.8	41.3
5	37.0	2.8	0.9	9.4	49.5
6	28.1	4.0	0.9	10.4	56.2
7	20.6	5.1	1.0	10.7	62.6

- ¹⁵ Particle rates, assuming a spill intensity of 10^6 particles on the secondary target and a SPS spill
¹⁶ length of 4.8 seconds, are reported in Table 5.3. The H4 simulation results are documented in
¹⁷ CERN-ACC-NOTE-2016-0052.

- ¹⁸ At momenta larger than about 4 GeV/c, the particle rates are at the limit or beyond the DAQ



H4-VLE beam to Single Phase ProtoDUNE

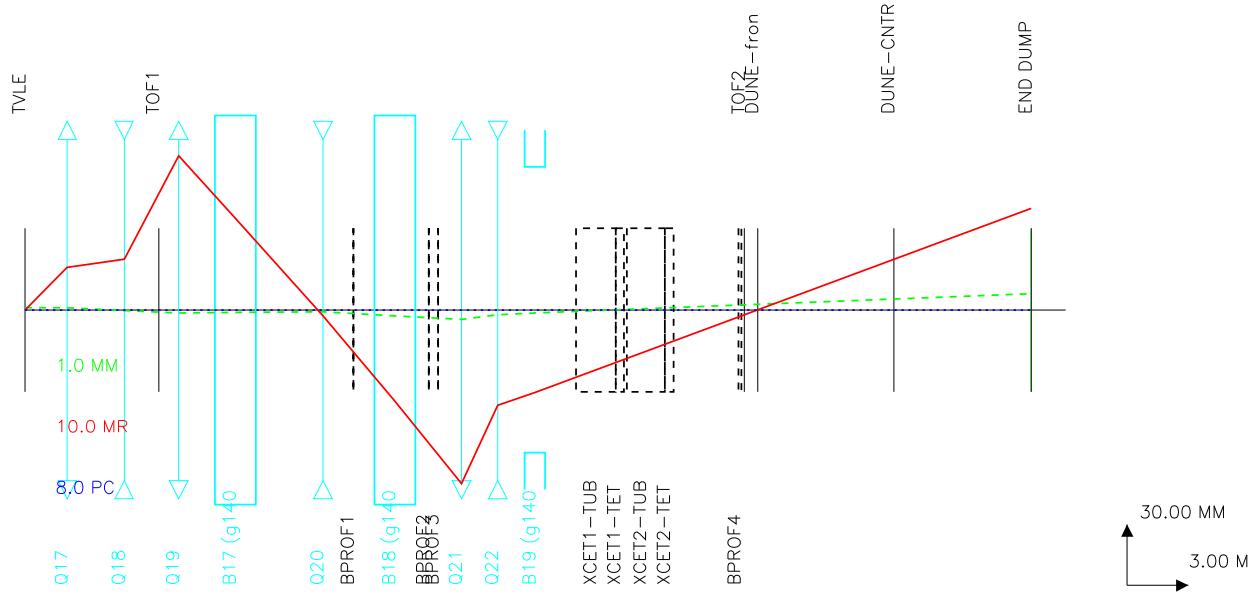


Figure 5.3: H4 beamline extension optics for the horizontal (top) and vertical (bottom) planes. The secondary target is located on the left side of the plots and the front of the ProtoDUNE-SP cryostat is located at the beam focus point, at about 37 m from the secondary target. Q17-Q22 are the quadrupole magnets. B17-B19 are the dipole bending magnets. TOF1-2 are the Time-of-Flight detectors, BPROF1-4 are the beam profile monitors, and XCET1-2 are the threshold Cherenkov counters.

fig:beam

Table 5.3: Particle rates (Hz).

Momentum (GeV/c)	e^{+-}	K^{+-}	μ^{+-}	p^{+-}	π^{+-}	total
-7	57	7	2	3	138	207
-6	62	5	2	2	113	185
-5	72	3	2	2	87	166
-4	93	2	2	1	72	170
-3	11	0.5	1	0.5	26	39
-2	13	0	0.5	0.1	16	27
-1	18	0	0.2	0	4	22
-0.4	8	0	0	0	0.1	8
0.4	7	0	0	0	0	7
1	18	0	0	4	4	27
2	13	0.2	0.5	9	15	38
3	11	1	1	11	31	56
4	92	3	2	17	81	196
5	74	6	3	19	99	200
6	63	9	3	24	127	226
7	52	13	2	27	157	252

¹ capability. At lower energies, the proton and pion rates are much lower, reduced by a factor of 10
² at 1 or 2 GeV/c, and are overwhelmed by the positron rate.

³ The momentum spread of the beam is of the order of 5–7%. At higher energies, where the particle
⁴ rate is higher, the momentum spread can be narrowed by closing the collimators, at the expense
⁵ of the beam intensity. For example, Figure 5.4 shows that at $p = 4$ GeV/c the momentum spread
⁶ can be reduced to $\Delta p/p = 3.6\%$ with a factor of 4 reduction in particle rate.

⁷ 5.2.3 Muon halo

⁸ The secondary beam is mainly composed of 80-GeV pions. In the long path (≈ 600 m) between the
⁹ primary and the secondary target, an intense high-energy muon halo is produced by pion decay.
¹⁰ Muons propagate approximately in the direction of the first section of the H4 beamline, that is
¹¹ slightly upward and sideways of the H4 beamline extension which points at the ProtoDUNE-SP
¹² detector. Therefore the most intense part of the muon halo passes about one meter above the
¹³ left corner of ProtoDUNE-SP cryostat. Figure 5.5 shows the spatial distribution of the muon
¹⁴ halo at the face of the cryostat. Only muons with momentum larger than 4 GeV/c have been
¹⁵ considered. Despite the low statistics of the simulations, the up-down and left-right asymmetry
¹⁶ is clearly visible. The origin of the coordinate system is chosen to coincide with the center of the
¹⁷ cryostat face. The color scale shows the muon intensity in $\mu/0.25\text{ m}^2/\text{spill}$ for 10^6 particles/spill
¹⁸ from the primary target. The muon intensity on the cryostat face, indicated by the black rectangle
¹⁹ in Figure 5.5, ranges up to $\sim 400 \mu/\text{m}^2/\text{spill}$. However, the rate of halo muons impinging on
²⁰ the front side of the TPC active volume (red rectangle) is expected to be significantly lower, in

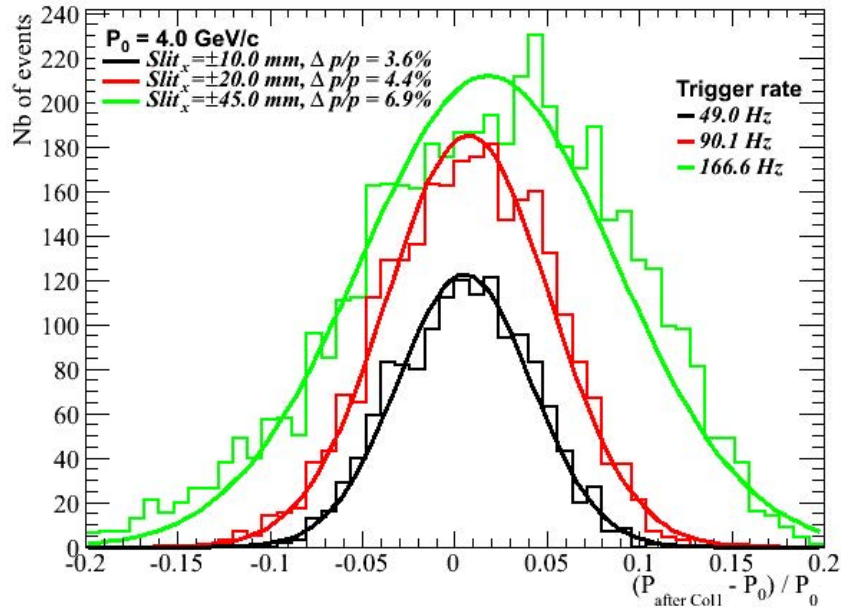


Figure 5.4: Beam momentum spread with different collimator openings at 4 GeV/c.

fig:momo

1 particular on the Saleve side of the TPC where the H4 beamline points. The rate of beam events
 2 with out-of-time halo muon tracks captured in the 2.5 ms time frame of the recorded event is
 3 expected to be limited.

4 [fig:muonhalo HE](#) Figure 5.5 is very preliminary though, not only because of low statistics, but also because shielding
 5 around the low-energy beamline is not included in the simulation, and the muons produced in
 6 neighboring beamlines in EHN1, including the H2 beamline that feeds ProtoDUNE-DP, are not
 7 considered here. Based on these results, the estimated contribution to the total data volume from
 8 beam halo is negligible.

9 5.3 Beamlne instrumentation

10 The H4 beamline will be instrumented with a number of beamline detectors to provide information
 11 about the beam profile, position, momentum, particle identification, and trigger capability. This
 12 section discusses the reference design for the beam instrumentation.

13 5.3.1 Beam profile monitoring, particle tracking and momentum measure- 14 ments

15 Operation of the beamline requires at least one beam monitor, able to provide the beam profile
 16 in two dimensions (x, y) at the entrance point to the NP04 cryostat. The beam monitor can also

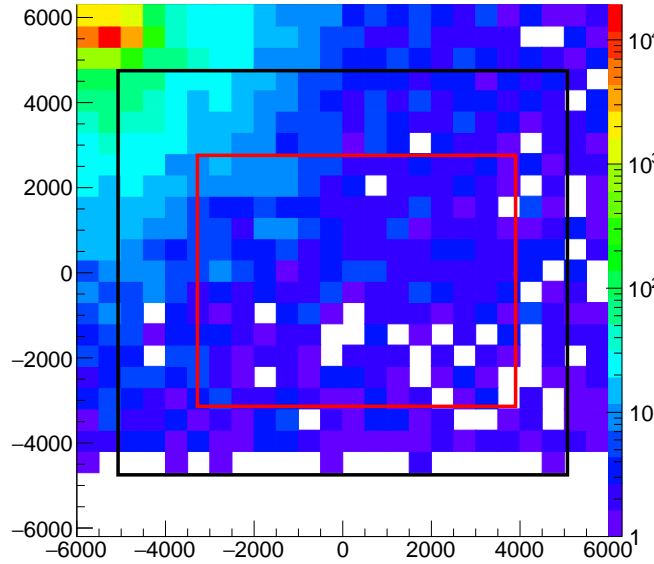


Figure 5.5: Muon halo intensity at the cryostat face for muons originating from the H4 beamline and with $P_\mu \geq 4$ GeV/c. The origin of the $x - y$ coordinate system is centered on the cryostat and dimensions are in mm. Color scale is in units of $\mu/0.25\text{ m}^2/\text{spill}$. The black and red rectangles represent the cryostat face and front face of the active detector volume.

fig:muon

1 be exploited for data analysis, provided that it delivers data on an event-by-event basis. Another
 2 monitor, located immediately downstream of the last bending magnet, is added in the layout in
 3 order to determine the incident particle direction and position at the front face of the cryostat,
 4 and match it with the reconstructed track in the LAr active volume.

5 To reduce the uncertainty due to the momentum spread of the beam around the central selected
 6 value, the momentum can be measured particle by particle with a set of three detectors placed one
 7 upstream and two downstream of the bending magnets B18 (see Figure 5.3). Preliminary results
 8 using full simulations indicate that a momentum resolution on the order of 2% is achievable.
fig:beamoptics

9 **Fiber tracker** The CERN Beam Instrumentation group will produce the beam monitors using
 10 scintillating fiber technology, where the fibers have a polystyrene core surrounded by cladding.
 11 Fibers provide a light yield of ~ 8000 photons/MeV, deposited with fast rise and decay times of 1–
 12 3 ns. The design foresees 1 mm square fibers in two planes to provide x and y coordinates. Fibers
 13 will be mirrored on one end to increase light collection. Every monitor consisting of two planes
 14 of 1 mm thick fibers adds 0.47% of a radiation length (X_0) to the material budget – the amount
 15 of material distributed along the beamline and crossed by the beam particles before entering the
 16 TPC active volume. The three devices for momentum measurement will consist of one layer only,
 17 oriented perpendicularly to the magnet deflection. A fiber plane is made out of 192 fibers with
 18 no space between them. It will cover an area of 192 mm \times 192 mm and fits in the beamline.
 19 Scintillation light will be read out using SiPMs. These detectors for position and momentum
 20 measurement are mounted through special flanges along the beam pipe, without the need to break

¹ the vacuum.

² 5.3.2 Particle identification

³ The H4 beamline is capable of delivering two types of beams, electron and hadron. While the elec-
⁴ tron beam is relatively pure, the hadron beam consists of a mixture of electrons, pions, kaons, and
⁵ protons. Therefore, for the hadron beam, it is essential to have an efficient particle identification
⁶ system to cleanly tag particle types on a particle-by-particle basis. To achieve this goal, a particle
⁷ identification system based on a combination of threshold Cherenkov counters and time-of-flight
⁸ (ToF) system is planned for ProtoDUNE-SP. Cherenkov counters can be placed in the last segment
⁹ of the beamline, between the last bending magnet and the cryostat.

¹⁰ **Threshold Cherenkov counter** Threshold Cherenkov counters have been used extensively in
¹¹ beamlines to discriminate particles. Figure 5.6 shows one of the counters used in the CERN test
¹² beam area. It consists of a gas radiator that is contained in a long cylindrical tube, and a detection
¹³ box in which the Cherenkov light is reflected by a 45° mirror and focused onto a photomultiplier
¹⁴ tube (PMT). A variety of gases (e.g., CO₂, nitrogen, argon, Freon 12, air) are available at CERN for
¹⁵ filling the Cherenkov counter to optimize particle identification. Two threshold Cherenkov counters
¹⁶ will be installed in the beamline, one detecting pions, the other detecting pions and kaons. The
¹⁷ combination of the two signals will allow identification of all hadron species. In order to provide
¹⁸ signals at low beam momenta, either heavier gases or high pressures are needed. Figure 5.7 shows
¹⁹ the gas-pressure threshold for the production of Cherenkov light for various particle types as a
²⁰ function of particle momentum for Freon 12 and CO₂ gases.

²¹ Freon 12 has been selected for its heavier mass, however, to avoid liquefaction it cannot be operated
²² at pressures larger than 3 bars. CO₂ can be used more easily at higher pressures.

²³ Figure 5.7 shows that pions can be tagged with a 3-bars Freon counter for momenta larger than
²⁴ 2 GeV/c, and kaons can be tagged with a high-pressure (15-bars) CO₂ counter above 4 GeV/c.

²⁵ The reference plan for beam instrumentation includes a 2-m-long Cherenkov counter filled with
²⁶ Freon 12 at adjustable pressure up to 3 bars (XCET1), and a 2-m-long Cherenkov counter filled
²⁷ with CO₂ at adjustable pressure up to 15 bars (XCET2).

²⁸ Existing Cherenkov counters at CERN are designed for pressures lower than 3 bar, therefore a
²⁹ new counter has to be manufactured in order to reach the 15 bars needed to efficiently tag kaons.
³⁰ Drawings for such high-pressure Cherenkov counters do exist, as they have been used in the past.
³¹ Since it will not be necessary to use both counters at all energies, the CO₂ counter, filled at low
³² pressure, will be used for electron discrimination at beam momenta lower than 4 GeV/c.

³³ A time-of-flight (ToF) system is necessary to distinguish hadrons below the mentioned thresholds.
³⁴ In summary:

- ³⁵ • **below 2 GeV/c** : one Cherenkov, filled with CO₂ at low pressure, discriminates electrons;
³⁶ ToF needed for hadrons.

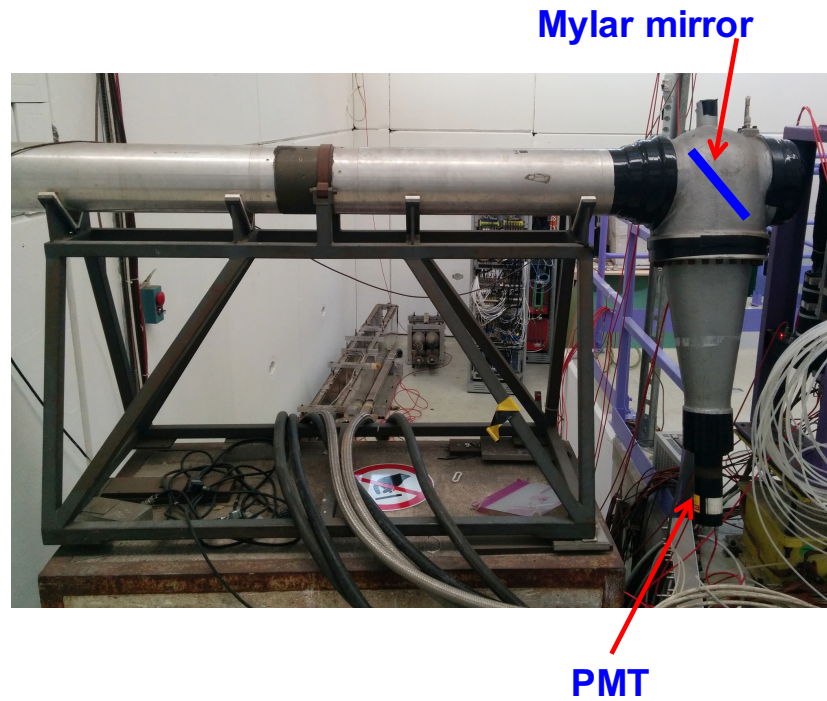
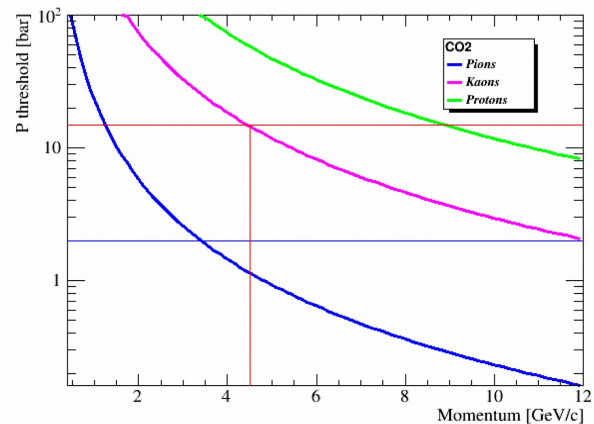
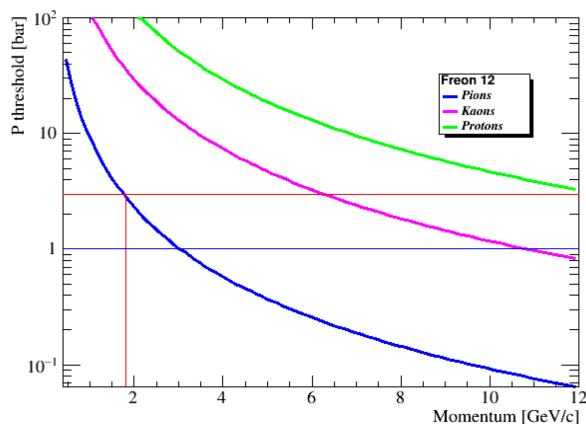


Figure 5.6: CERN threshold Cherenkov counter

fig:ckv

Figure 5.7: Gas pressure threshold for the production of Cherenkov light for various particles as a function of particle momentum for Freon 12² and CO₂ gases.

kv_gases

- **2-3 GeV/c** : one Cherenkov, filled with CO₂ low pressure, discriminates electrons; second Cherenkov, filled with Freon 12, tags pions; kaons content in this range is very low or negligible. ToF is needed to identify protons.
- **3-4 GeV/c** : one Cherenkov, filled with CO₂ at low pressure, discriminates electrons; second Cherenkov, filled with Freon 12, tags pions; ToF is needed for kaon/proton discrimination
- **4-7 GeV/c** : one Cherenkov, filled with CO₂ at high pressure, tags kaons; second Cherenkov, filled with Freon 12, tags pions; electron content of the beam is low and can be discriminated by reconstruction.

From table 5.2 it is evident that the kaon content of the beam is negligible at least below 2 GeV/c, thus only pion-proton separation is needed at low energies. Figure 5.8 shows the ToF resolution needed to distinguish among particle species at the 4σ level as a function of the particle momentum, assuming a 28-m-long path. To distinguish pions from protons below 2 GeV/c, a 1-ns resolution is enough, while 300 ps are necessary for kaon-proton separation up to 4 GeV/c. It should also be noted that a ToF system with a \sim 100-ps resolution would allow identification of protons from other hadrons up to 7 GeV; this would release the need for a high-pressure CO₂ Cherenkov. Conversely, covering the full energy range up to 7 GeV for all hadron types would require a ToF system with a resolution better than 40 ps. In the following, two (possibly complementary) ToF systems are described.

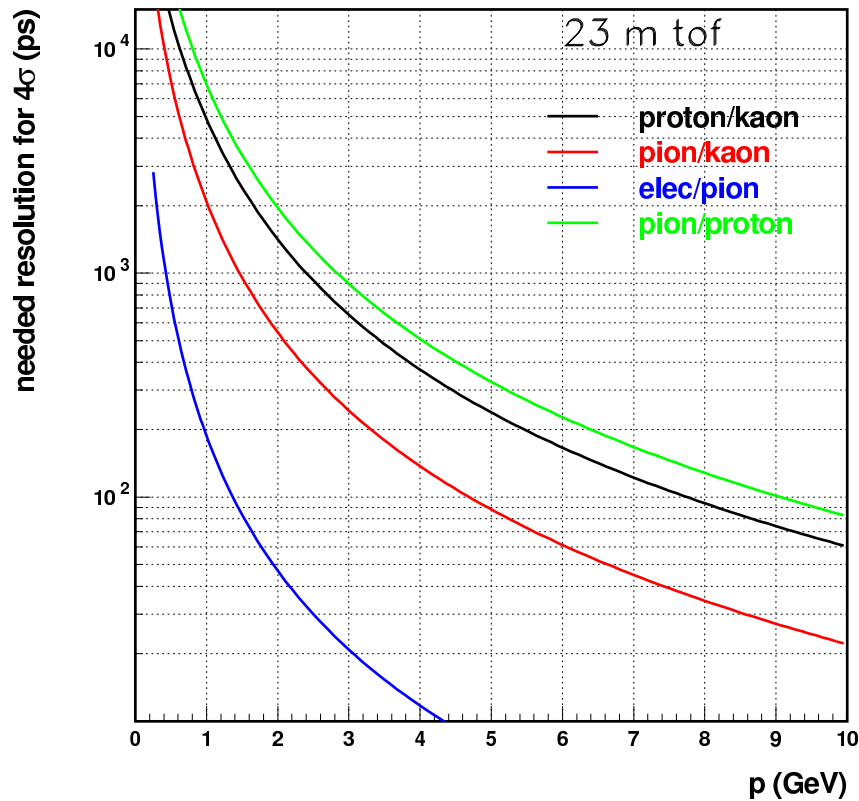


Figure 5.8: Required ToF resolution to distinguish among particle species at the 4σ level as a function of the particle momentum, assuming a 28-m long path. (The figure shows 23 m; it needs to be updated.)

fig:toft

pLAPPD time-of-flight system Fermilab is testing a ToF system from Argonne National Laboratory that would utilize $6 \times 6 \text{ cm}^2$ prototype large-area picosecond photodetectors (pLAPPDs), as shown in Figure 5.9. The microchannel plates based devices are capable of < 50 ps resolution with gains of $10^6 - 10^7$, mm position resolution along one axis, and slightly worse resolution along the other axis. The photodetector is mounted on a readout board, and the relevant exterior dimensions are $165.1 \text{ mm} \times 109.3 \text{ mm}$ and a thickness of 16 mm. The active area is defined by the four squares visible in Figure 5.9, and amounts to about 31 cm^2 . Tests of these devices in the Fermilab test beam facility (FTBF) are underway, to precisely assess the efficiency and timing capabilities of such a system. The pulses from the pLAPPDs will be read out by a fast waveform digitizer and the tests at the FTBF include the development of an artDAQ-based DAQ and potentially a ToF trigger module capable of providing a particle trigger to the ProtoDUNE-SP DAQ. Larger area pLAPPD can be made to match the H4 beam profile.

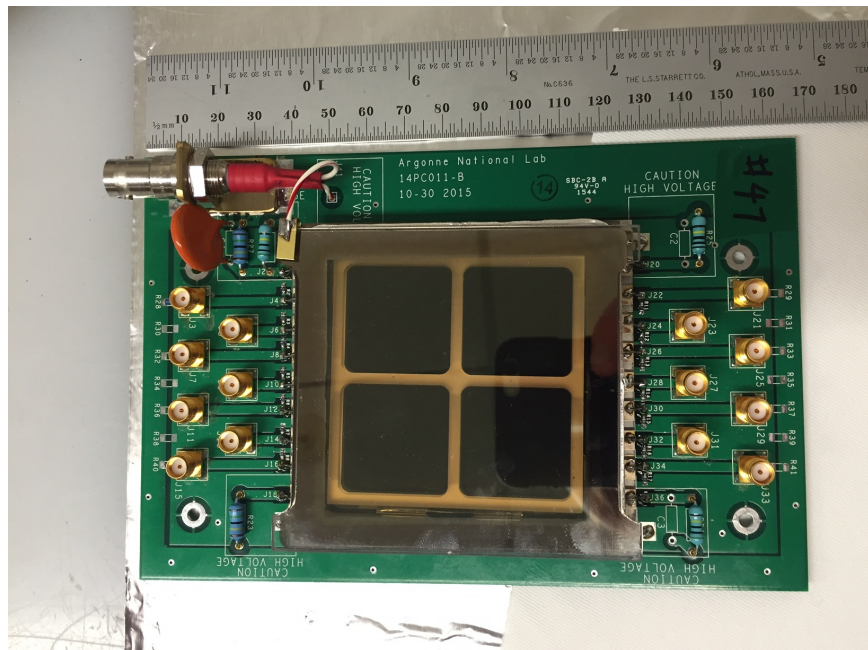


Figure 5.9: Photo of one pLAPPD device as proposed for the H2 and H4 beamlines.

Alternative Time-of-flight system The scintillating-fiber monitors can be used also for ToF purposes with the goal of a 1-ns timing resolution, suitable for low momentum ($< 2 \text{ GeV}/c$) beams. The idea is to read out the detectors with the STiC ASIC [46] for SiPM readout.

Is STiC defined?

In this configuration, the time resolution would be dominated by the fiber response. Monte Carlo simulations estimate a resolution better than 1 ns. A small prototype will be built and tested in the next few months to fully validate this solution.

5.3.3 Material budget and discussion

The set of beam detectors considered for instrumenting the H4 tertiary beamline include five beam monitors (two for tracking and three for spectrometry), two ToF devices, and two high density or pressure gas Cherenkov detectors. The selection of the beam detector configuration in the beamline depends on the type of beam (electron or hadron), and on the beam momentum range. For the electron beam and for low momenta hadron beams the amount of detector material along the beamline may result in particle energy degradation and significant reduction of the beam rate delivered at the active detector due to scattering outside the beam pipe. A FLUKA^[?, 33] simulation was used to evaluate these effects accounting for the detector materials in the beamline, and materials of the beam window, cryostat and beam plug. Figure 5.10 shows the cumulative increase of the material budget along the tertiary beam line from the target to the TPC, expressed in terms of fraction of radiation length (red line - total 0.6 X_0) and of interaction length (black line - total 0.15 λ_I). The average energy loss for a mip is about 28 MeV. The largest contribution to the energy-loss and energy degradation is due to the high pressure Cherenkov detectors and to the pLAPPD. Except for a low-pressure Cherenkov counter for electron discrimination, the high pressure Cherenkov are not necessary at low hadron beam momenta and can be removed or just emptied. Scintillating fiber beam monitors can replace the pLAPPD as ToF devices for the lowest-momentum beam.

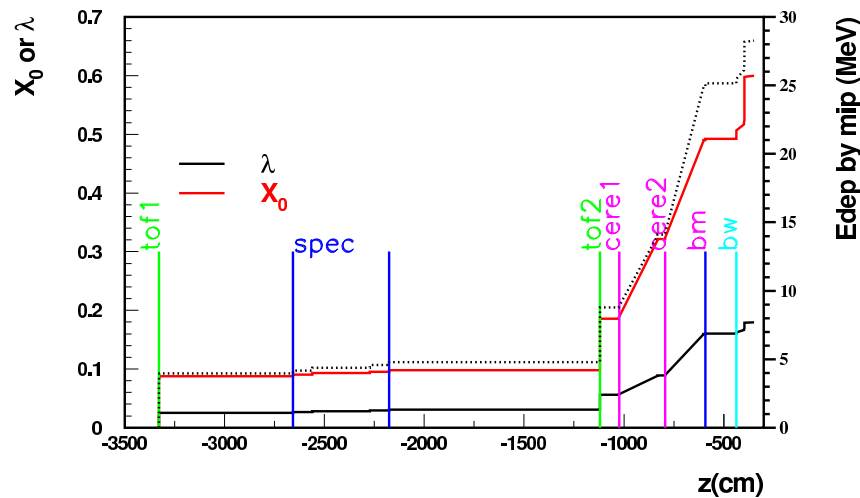


Figure 5.10: Material budget in the beamline, as a function of the distance from the center of the detector (in cm). The red line describes the amount of X_0 , the black line the amount of interaction length, both read on the left axis. The black dotted line is the average energy lost by a mip particle, and is read on the right axis (in MeV). Vertical lines show the positions of the various beam monitors (in between the two blue lines are the 3 devices for spectrometry, “bm” is the last beam monitor, “bw” is the starting point of the beam window).

Scattering of low-energy pions and protons in crossing the detector material significantly reduces their content in the low-momenta hadron beam reaching the detector active volume. For example, at 1 GeV/c the rate of pions arriving at the detector is reduced by a factor of 2.5, and the rate of protons is reduced by a factor of 4.

5.3.4 Trigger and data acquisition

- 2 The beam instrumentation can provide a trigger signal, built from the coincidence of the two last
3 beam monitors, vetoed by the electron-tagging Cherenkov for low-energy beams. A trigger mask,
4 providing the status of the other counters, can also be provided. Synchronization of the detector
5 data acquisition (DAQ) with the beam instrumentation DAQ will be ensured by a common time
6 stamp through a White Rabbit network.
- 7 Beam instrumentation data will be read out independently on a separate DAQ stream. How-
8 ever, the beam data fragments corresponding to events with a valid trigger from both beam and
9 ProtoDUNE-SP will be merged online with the detector data.

1 References

- 2 [1] E.D. Marquardt, J.P. Le, and Ray Radebaugh, “Cryogenic Material Properties Database year
3 = 2010,” tech. rep. http://www.cryogenics.nist.gov/Papers/Cryo_Materials.pdf.
- 4 [2] “Cathode HV Discharge Mitigation Design.” <http://docs.dunescience.org:8080/cgi-bin>ShowDocument?docid=1320>.
- 6 [3] A. A. Machado and E. Segreto, “ARAPUCA a new device for liquid argon scintillation light
7 detection,” *JINST*, vol. 11, no. 02, p. C02004, 2016.
- 8 [4] “Data scenarios spreadsheet.” DUNE DocDB 1086.
- 9 [5] Silicon Labs, *Si5342/5344/5345/5346/5347 Jitter Attenuating Clocks*, 7 2016. Rev. D.
- 10 [6] Avnet, *MicroZed Hardware User’s Guide*, 1 2015. v1.6.
- 11 [7] R. Herbst, “Design of the slac rce platform: A general purpose atca based data acquisition
12 system,” *IEEE*, vol. 978, no. 1-4799-6097-2/14, 2015.
- 13 [8] C. Green, J. Kowalkowski, M. Paterno, M. Fischler, L. Garren, and Q. Lu, “The art frame-
14 work,” *J. Phys. Conf. Ser.*, vol. 396, p. 022020, 2012.
- 15 [9] Elasticsearch, “Kibana - data analytics and visualisation tool,” tech. rep. <https://www.elastic.co/products/kibana>.
- 17 [10] M. Paterno, “artdaq: An event filtering framework for fermilab experiments.” <http://cd-docdb.fnal.gov/0049/004907/003/artdaq-talk.pdf>.
- 19 [11] “XRootD, high performance, scalable fault tolerant access to data repositories.” <http://xrootd.org/>.
- 21 [12] “Design of the data management system for the protodune experiment.” DUNE DocDB 1212.
- 22 [13] “GTT Membrane Technologies.” <http://www.gtt-training.co.uk/gtt-membrane-technologies/>.

- 1 [14] “EHN1-warm cryostat functional specification.” <https://edms.cern.ch/document/1531438/3>.
- 2
- 3 [15] “EHN1-warm cryostat current drawings.” <https://edms.cern.ch/document/1531439/3>.
- 4 [16] “EHN1-protoDUNE-penetrations.” <https://edms.cern.ch/document/1543241/3>.
- 5 [17] “PROTODUNE PENETRATIONS.” <https://edms.cern.ch/document/1581898/0>.
- 6 [18] “LBNF-DUNE Requirements (DUNE doc-db 112).” <http://docs.dunescience.org>

7 need to get proper link

- 8 .
- 9 [19] Montanari, D., “LBNE 35 ton proto Talk at LAr1-ND Meeting,” tech. rep., 2014. <http://lbne2-docdb.fnal.gov/cgi-bin>ShowDocument?docid=8626>.
- 10
- 11 [20] “LAPD Purge and Recirculation Plots.” <http://lartpc-docdb.fnal.gov:8080/cgi-bin>ShowDocument?docid=706>.
- 12
- 13 [21] “Design of the Data Management System for the protoDUNE Experiment (DUNE doc-db 1212).” <http://docs.dunescience.org>
- 14

15 need to get proper link

- 16 .
- 17 [22] “LArSoft Collaboration, Software for LArTPCs.” <http://larsoft.org>.
- 18 [23] “The art Event Processing Framework.” <http://art.fnal.gov>.
- 19 [24] “Scientific Software for Relocatable UPS .” <http://scisoft.fnal.gov/>.
- 20 [25] Chris Hagmann, David Lange, Jerome Verbeke, Doug Wright, “Proton-induced Cosmic-ray Cascades in the Atmosphere,” tech. rep. http://nuclear.llnl.gov/simulation/doc_cry_v1.7/cry.pdf.
- 21
- 22
- 23 [26] Chris Hagmann, David Lange, Doug Wright, “Monte Carlo Simulation of Proton-induced Cosmic-ray Cascades in the Atmosphere year = 2012,” tech. rep. UCRL-TM-229452.
- 24
- 25 [27] D. Heck, G. Schatz, T. Thouw, J. Knapp, and J. N. Capdevielle, “CORSIKA: A Monte Carlo code to simulate extensive air showers,” 1998.
- 26
- 27 [28] C. Andreopoulos *et al.*, “The GENIE Neutrino Monte Carlo Generator,” *Nucl. Instrum. Meth.*,

- ¹ vol. A614, pp. 87–104, 2010.
- ² [29] S. Agostinelli *et al.*, “GEANT4: A Simulation toolkit,” *Nucl. Instrum. Meth.*, vol. A506, pp. 250–303, 2003.
- ⁴ [30] “General Geometry Description (GGD).” <https://github.com/brettviren/gegede>.
- ⁵ [31] J. B. Birks, *The Theory and practice of scintillation counting*. 1964.
- ⁶ [32] M. Szydagis, N. Barry, K. Kazkaz, J. Mock, D. Stolp, M. Sweany, M. Tripathi, S. Uvarov, N. Walsh, and M. Woods, “NEST: A Comprehensive Model for Scintillation Yield in Liquid Xenon,” *JINST*, vol. 6, p. P10002, 2011.
- ⁹ [33] G. Battistoni, T. T. Böhlen, F. Cerutti, P. W. Chin, L. S. Esposito, A. Fassò, A. Ferrari, A. Lechner, A. Empl, A. Mairani, A. Mereghetti, P. G. Ortega, J. Ranft, S. Roesler, P. R. Sala, V. Vlachoudis, and G. Smirnov, “Overview of the FLUKA code,” *Annals of Nuclear Energy*, vol. 82, p. 10, 2015.
- ¹³ [34] A. Ferrari, P. R. Sala, A. Fasso, and J. Ranft, “FLUKA: A multi-particle transport code (Program version 2005),” 2005.
- ¹⁵ [35] G. Battistoni, P. R. Sala, M. Lantz, A. Ferrari, and G. Smirnov, “Neutrino interactions with FLUKA,” *Acta Phys. Polon.*, vol. B40, pp. 2491–2505, 2009.
- ¹⁷ [36] M. Mooney, “The MicroBooNE Experiment and the Impact of Space Charge Effects,” in *Meeting of the APS Division of Particles and Fields (DPF 2015) Ann Arbor, Michigan, USA, August 4-8, 2015*, 2015.
- ²⁰ [37] <http://garfield.web.cern.ch/garfield/>.
- ²¹ [38] “Noise Characterization and Filtering in the MicroBooNE TPC.” <http://www-microboone.fnal.gov/publications/publicnotes/MICROBOONE-NOTE-1016-PUB.pdf>.
- ²³ [39] MicroBooNE noise filtering technot, doc-db:5730 <http://microboone-docdb.fnal.gov:8080/cgi-bin>ShowDocument?docid=5730>.
- ²⁵ [40] “The Cluster Crawler Suite Technical Manual.” <http://microboone-docdb.fnal.gov/cgi-bin>ShowDocument?docid=2831>.
- ²⁷ [41] “TrajCluster: A 2D Cluster Finder .” <https://cdcvns.fnal.gov/redmine/attachments/download/34265/TrajCluster%20Technical%20Note.pdf>.
- ²⁹ [42] <http://larsoft.org/single-record/?pdb=113>.
- ³⁰ [43] J. S. Marshall and M. A. Thomson, “The Pandora Software Development Kit for Pattern Recognition,” *Eur. Phys. J.*, vol. C75, no. 9, p. 439, 2015.

- ¹ [44] <http://larsoft.org/single-record/?pdb=102>.
- ² [45] <http://www.phy.bnl.gov/wire-cell/>.
- ³ [46] T. Harion, K. Briggel, H. Chen, P. Fischer, A. Gil, V. Kiworra, M. Ritzert, H. C. Schultz-Coulon, W. Shen, and V. Stankova, “Stic – a mixed mode silicon photomultiplier readout asic for time-of-flight applications,” *Journal of Instrumentation*, vol. 9, no. 02, p. C02003, 2014.